

*Production of polymer/active
compound composites by
supercritical CO₂ assisted processes*

Paola Franco

UNIVERSITY OF SALERNO



DEPARTMENT OF INDUSTRIAL ENGINEERING

*Ph.D. Course in Industrial Engineering
Curriculum in Chemical Engineering - XXXIII Cycle*

PRODUCTION OF POLYMER/ACTIVE COMPOUND COMPOSITES BY SUPERCRITICAL CO₂ ASSISTED PROCESSES

Supervisor

Prof. Iolanda De Marco

Ph.D. student

Paola Franco

Scientific Referees

Prof. Roberta Campardelli

Eng. Valentina Prosapio, PhD

Ph.D. Course Coordinator

Prof. Francesco Donsì

Publication List

International Journals

1. **P. Franco**, E. Reverchon, I. De Marco, PVP/ketoprofen coprecipitation using supercritical antisolvent process, Powder Technology (2018).
2. **P. Franco**, E. Reverchon, I. De Marco, Zein/diclofenac sodium coprecipitation at micrometric and nanometric range by supercritical antisolvent processing, Journal of CO₂ Utilization (2018).
3. G. Ozkan, **P. Franco**, I. De Marco, J. Xiao, E. Capanoglu, A review of microencapsulation methods for food antioxidants: Principles, advantages, drawbacks and applications, Food Chemistry (2019).
4. **P. Franco**, M. Martino, V. Palma, A. Scarpellini, I. De Marco, Pt on SAS-CeO₂ nanopowder as catalyst for the CO-WGS reaction, International Journal of Hydrogen Energy (2018).
5. **P. Franco**, B. Aliakbarian, P. Perego, E. Reverchon, I. De Marco, Supercritical adsorption of quercetin on aerogels for active packaging applications, Ind. Eng. Chem. Res. (2018).
6. **P. Franco**, E. Reverchon, I. De Marco, Production of zein/antibiotic microparticles by supercritical antisolvent coprecipitation, The Journal of Supercritical Fluids (2019).
7. E. Pessolano, R. Belvedere, V. Bizzarro, **P. Franco**, I. De Marco, A. Porta, A. Tosco, L. Parente, M. Perretti and A. Petrella, Annexin A1 May Induce Pancreatic Cancer Progression as a Key Player of Extracellular Vesicles Effects as Evidenced in the In Vitro MIA PaCa-2 Model System, Int. J. Mol. Sci. (2018).
8. R. Campardelli, **P. Franco**, E. Reverchon, I. De Marco, Polycaprolactone/Nimesulide patches obtained by a one-step supercritical foaming + impregnation process, The Journal of Supercritical Fluids (2019).
9. **P. Franco**, O. Sacco, I. De Marco, V. Vaiano, Zinc Oxide Nanoparticles Obtained by Supercritical Antisolvent Precipitation for the Photocatalytic Degradation of Crystal Violet Dye, Catalysts (2019).
10. **P. Franco**, L. Incarnato, I. De Marco, Supercritical CO₂ impregnation of α -tocopherol into PET/PP films for active packaging applications, Journal of CO₂ Utilization (2019).
11. E. Pessolano, R. Belvedere, V. Bizzarro, **P. Franco**, I. De Marco, F. Petrella, A. Porta, A. Tosco, L. Parente, M. Perretti, A. Petrella, Annexin A1 Contained in Extracellular Vesicles Promotes the Activation of Keratinocytes by Mesoglycan Effects: An Autocrine Loop Through FPRs, Cells (2019).

12. G. Ozkan, **P. Franco**, E. Capanoglu, I. De Marco, PVP/flavonoid coprecipitation by supercritical antisolvent process, *Chemical Engineering and Processing: Process Intensification* (2019).
13. **P. Franco**, I. De Marco, Supercritical Adsorption of Non-Steroidal Anti-Inflammatory Drugs into Biopolymer Aerogels, *Journal of CO₂ Utilization* (2020).
14. **P. Franco**, R. Belvedere, E. Pessolano, S. Liparoti, R. Pantani, A. Petrella, I. De Marco, PCL/Mesoglycan devices obtained by supercritical foaming + impregnation, *Pharmaceutics* (2019).
15. **P. Franco**, E. Pessolano, R. Belvedere, A. Petrella, I. De Marco, Supercritical Impregnation of Mesoglycan into Calcium Alginate Aerogel for Wound Healing, *The Journal of Supercritical Fluids* (2020).
16. **P. Franco**, I. De Marco, Supercritical antisolvent coprecipitation in the pharmaceutical field: different polymeric carriers for different drug releases, *The Canadian Journal of Chemical Engineering* (2020).
17. **P. Franco**, I. De Marco, Eudragit: A Novel Carrier for Controlled Drug Delivery in Supercritical Antisolvent Coprecipitation, *Polymers* (2020).
18. I. De Marco, **P. Franco**, Production of Eudragit/Ampicillin Microparticles by Supercritical Antisolvent Coprecipitation, *Chemical Engineering Transactions* (2020).
19. **P. Franco**, I. De Marco, The Use of Poly(N-vinyl pyrrolidone) in the Delivery of Drugs: A Review, *Polymers* (2020).
20. **P. Franco**, O. Sacco, I. De Marco, D. Sannino, V. Vaiano, Photocatalytic Degradation of Eriochrome Black-T Azo Dye Using Eu-Doped ZnO Prepared by Supercritical Antisolvent Precipitation Route: A Preliminary Investigation, *Topics in Catalysis* (2020).
21. **P. Franco**, I. De Marco, Supercritical Antisolvent Process for Pharmaceutical Applications: A Review, *Processes* (2020).
22. **P. Franco**, I. De Marco, Preparation of non-steroidal anti-inflammatory drug/ β -cyclodextrin inclusion complexes by supercritical antisolvent process, *Journal of CO₂ Utilization* (2021).
23. **P. Franco**, I. De Marco, Formation of rutin/ β -cyclodextrin inclusion complexes by supercritical antisolvent precipitation, *Polymers* (2021).
24. **P. Franco**, I. De Marco, Nanoparticles and nanocrystals by supercritical CO₂ assisted techniques for pharmaceutical applications: A review, *Applied Sciences* (2021).
25. **P. Franco**, I. De Marco, Controlled-release antihistamines using supercritical antisolvent process, *Journal of Supercritical Fluids* (2021).

Book chapter

P. Franco, I. De Marco, Oral Fast and Topical Controlled Ketoprofen Release through Supercritical Fluids Based Processes, *Advances in Bionanomaterials II* (2020). Lecture Notes in Bioengineering. Springer, Cham.

Proceedings

1. De Marco, **P. Franco**, E. Reverchon, Supercritical antisolvent coprecipitation of PVP/ketoprofen microparticles, 12th International Symposium on Supercritical Fluids, April 22-25 2018, Antibes, France.
2. I. De Marco, **P. Franco**, E. Reverchon, Supercritical antisolvent coprecipitation in the pharmaceutical field: different polymers for different drug releases, 17th European Meeting on Supercritical Fluids - 7th European Meeting on High Pressure Technology, April 8-11 2019, Ciudad Real, Spain.
3. **P. Franco**, E. Reverchon, I. De Marco, Starch aerogel loaded with nimesulide through supercritical CO₂ adsorption, 17th European Meeting on Supercritical Fluids - 7th European Meeting on High Pressure Technology, April 8-11 2019, Ciudad Real, Spain.
4. I. De Marco, **P. Franco**, E. Reverchon, Coprecipitazione polimero/farmaco tramite antisolvente supercritico: differenti carrier per diverse forme di rilascio del farmaco, Convegno Gricu 2019, June 30-July 3 2019, Mondello, Palermo, Italy.
5. **P. Franco**, E. Reverchon, I. De Marco, Produzione di microparticelle Eudragit/Ampicillina tramite antisolvente supercritico, Convegno Gricu 2019, June 30-July 3 2019, Mondello, Palermo, Italy.

Contents

Figure Index	V
Table Index.....	XIII
Abstract	XV
Introduction	XVII
Chapter I Aim of the work	1
Chapter II State of the art of the scCO₂ assisted technologies	3
II.1 State of the art of SAS process	3
II.1.1 <i>Fundamentals of SAS technique</i>	4
II.1.2 <i>SAS micronization of active compounds</i>	7
II.1.3 <i>SAS coprecipitation polymer/active compound</i>	10
II.2 State of the art of supercritical impregnation	15
Chapter III Analytical methods	19
III.1 Field Emission Scanning Electron Microscopy	19
III.2 Determination of the specific surface area	19
III.3 Fourier Transform Infrared (FTIR) Spectroscopy	19
III.4 Differential Scanning Calorimetry	20
III.5 X-Ray Diffraction	20
III.6 UV-vis spectroscopy	20
Chapter IV SAS coprecipitation carrier/active compound	23
IV.1 Introduction	23
IV.1.1 <i>Materials</i>	24
IV.1.2 <i>SAS apparatus and procedure</i>	24
IV.2 The use of PVP as polymeric carrier	26
IV.2.1 <i>PVP/ketoprofen coprecipitation</i>	26
IV.2.2 <i>PVP/rutin coprecipitation</i>	33
IV.3 The use of zein as polymeric carrier	39

IV.3.1	<i>Zein micronization by SAS process</i>	39
IV.3.2	<i>Zein/diclofenac coprecipitation</i>	42
IV.3.3	<i>Zein/antibiotic coprecipitation</i>	49
IV.3.4	<i>Zein/antihistamine coprecipitation</i>	58
IV.4	The use of Eudragit as polymeric carrier	69
IV.4.1	<i>SAS micronization of Eudragit L100-55</i>	69
IV.4.2	<i>Eudragit/ampicillin coprecipitation</i>	71
IV.4.3	<i>Eudragit/diclofenac coprecipitation</i>	76
IV.4.4	<i>Eudragit/theophylline coprecipitation</i>	81
IV.5	The use of cyclodextrin as polymeric carrier	88
IV.5.1	<i>Preparation of NSAID/β-CD complexes</i>	88
IV.5.2	<i>Preparation of RUT/β-CD complexes</i>	101
IV.6	Conclusions	109
Chapter V Supercritical impregnation of drugs into polymeric supports.....		111
V.1	Introduction	111
V.1.1	<i>Materials</i>	112
V.1.2	<i>Apparatuses for drying and impregnation by scCO₂</i>	112
V.1.3	<i>Procedures for aerogels preparation</i>	113
V.1.4	<i>Procedures for drug solubility measurements and impregnation tests into polymeric supports</i>	114
V.2	Supercritical impregnation of drugs into aerogels	115
V.2.1	<i>Isotherms of impregnation of NSAIDs into aerogels</i>	115
V.2.2	<i>Kinetics of impregnation of NSAIDs into aerogels</i>	117

V.2.3	<i>Mechanism of NSAID impregnation into aerogels</i>	
		122
V.2.4	<i>Characterization of NSAID/aerogel composites</i>	125
V.2.5	<i>Conclusions</i>	136
V.3	Supercritical impregnation of drugs into polymeric films	137
V.3.1	<i>Solubility measurements of MSG in scCO₂</i>	137
V.3.2	<i>Foaming + MSG impregnation in PCL granules</i>	138
V.3.3	<i>Mechanism of MSG impregnation</i>	141
V.3.4	<i>Foaming + MSG impregnation in PCL films</i>	142
V.2.4	<i>Characterization of MSG/PCL composites</i>	142
V.3.5	<i>Conclusions</i>	145
Conclusions	147
References	151
List of Symbols	173

Figure Index

Figure II.1 VLE of a binary system of type I (Van Konynenburg and Scott, 1980); P: pressure, X_{CO_2} : CO_2 molar fraction.	5
Figure II.2 VLE of the binary system DMSO- CO_2 . From lower to higher pressures, the isotherms correspond to 5, 15, 25, 35, 45, 55, 65, 75 and 85°C (Andreatta et al., 2007a).....	5
Figure IV.1 Schematic representation of SAS laboratory plant. S1: CO_2 supply; S2: liquid solution supply; RB: refrigerating bath; P1, P2: pumps; M: manometer; V: precipitation chamber; MV: micrometering valve; LS: liquid separator; R: rotameter; BPV: back pressure valve.	25
Figure IV.2 FESEM images of SAS precipitated powders from DMSO at 9 MPa and 40°C. (a) PVP microparticles; (b) KET coalescing sub-microparticles.	27
Figure IV.3 FESEM images of PVP/KET 20/1 microparticles coprecipitated from DMSO at 40°C and 20mg/mL. Effect of operating pressure: (a) 9 MPa; (b) 12 MPa; (c) 15 MPa.	28
Figure IV.4 FESEM images of PVP/KET 20/1 microparticles coprecipitated from DMSO at 9 MPa and 40°C. Effect of overall concentration: (a) 10 mg/mL; (b) 50 mg/mL; (c) 100 mg/mL.	29
Figure IV.5 Volumetric cumulative PSDs of PVP/KET particles precipitated at different pressures.	30
Figure IV.6 Volumetric cumulative PSDs of PVP/KET particles precipitated at different polymer/drug ratios.	30
Figure IV.7 FTIR spectra of unprocessed PVP, unprocessed KET, PVP/KET physicalmixture and SAS processed PVP/KET.	31
Figure IV.8 DSC thermograms of unprocessed PVP, unprocessed KET and SAS processed PVP/KET.	32
Figure IV.9 Drug dissolution profiles of KET in HCl solution (pH 2.5).	33
Figure IV.10 FESEM images of PVP/RUT 20/1 particles precipitated from DMSO at 9 MPa, 40°C and (a) 20 mg/mL; (b) 30 mg/mL; (c) 40 mg/mL.....	34
Figure IV.11 Volumetric cumulative PSDs of PVP/RUT particles 20/1 w/w precipitated from DMSO at 9 MPa and 40°C at different overall concentrations.	35
Figure IV.12 Volumetric cumulative PSDs of PVP/RUT particles precipitated from DMSO at 9 MPa, 40°C and 40 mg/mL; effect of PVP/RUT ratio.	36
Figure IV.13 FTIR spectra of unprocessed PVP and RUT, physical mixtures and SAS processed PVP/RUT powders.....	37
Figure IV.14 DSC thermograms of unprocessed PVP and RUT, SAS processed PVP/RUT powders.	37
Figure IV.15 Dissolution profiles for rutin in PBS at 37°C and pH 7.4. 38	

Figure IV.16 FESEM images of zein precipitated from DMSO at 9 MPa and 40°C; (a) nanoparticles at 5 mg/mL; (b) microparticles at 50 mg/mL...	40
Figure IV.17 Effect of zein concentration in DMSO at 40°C and 9 MPa.	41
Figure IV.18 Effect of the operating temperature of zein precipitated from DMSO at 9 MPa and 50 mg/mL.	41
Figure IV.19 FESEM image of zein/DIC 20/1 microparticles obtained at 9 MPa, 40°C, 50 mg/mL.....	43
Figure IV.20 Volumetric cumulative PSDs of zein/DIC particles 20/1 precipitated from DMSO at 9 MPa, 40°C and different total concentrations.	44
Figure IV.21 Volumetric cumulative PSDs of zein/DIC particles precipitated from DMSO at 9 MPa, 40°C and 50 mg/mL; effect of the polymer/drug ratio.	44
Figure IV.22 FTIR spectra for unprocessed and SAS processed DIC and zein, physical mixture ZEIN/DIC 5/1 and SAS processed ZEIN/DIC 5/1. ...	45
Figure IV.23 XRD spectra for unprocessed DIC and ZEIN, SAS processed ZEIN/DIC 5/1 and 20/1 w/w.....	46
Figure IV.24 DSC thermograms of unprocessed DIC, unprocessed zein, and SAS processed zein/DIC 5/1.	47
Figure IV.25 Dissolution profiles of DIC in PBS at 37°C and pH 7.4...47	47
Figure IV.26 FESEM images of zein/AMOXI 20/1 microparticles obtained at 9 MPa, 50 mg/mL and (a) 40°C (run #2); (b) 50°C (run #4).	50
Figure IV.27 FESEM images of zein/AMPI 20/1 precipitated at 9 MPa, 50 mg/mL; (a) submicroparticles at 40°C (run #6); (b) microparticles at 50°C (run #7).	51
Figure IV.28 Volumetric cumulative PSDs of zein/AMPI 20/1 particles precipitated from DMSO at 9 MPa, 50 mg/mL; effect of the temperature...51	51
Figure IV.29 Volumetric cumulative PSDs of zein/AMOXI particles precipitated from DMSO at 40°C, 9 MPa, 50 mg/mL; effect of the polymer/drug ratio.	52
Figure IV.30 FESEM images of zein/AMPI microparticles obtained at 50 °C, 9 MPa, 50 mg/mL. Effect of the polymer/drug ratio: (a) 10/1 w/w (run #8); (b) 5/1 w/w (run #9).	52
Figure IV.31 Volumetric cumulative PSDs of zein/AMPI particles precipitated from DMSO at 50°C, 9 MPa, 50 mg/mL; effect of the polymer/drug ratio.	53
Figure IV.32 FTIR spectra of unprocessed zein and AMOXI, physical mixture zein/AMOXI and SAS processed powders.	54
Figure IV.33 FTIR spectra of unprocessed zein and AMPI, physical mixture zein/AMPI and SAS processed powders.	54
Figure IV.34 DSC thermograms of unprocessed zein, unprocessed and SAS processed AMOXI, SAS processed zein/AMOXI powders.	55

Figure IV.35 DSC thermograms of unprocessed zein, unprocessed and SAS processed AMPI, SAS processed zein/AMPI powders.	56
Figure IV.36 Dissolution profiles of AMOXI in PBS at 37°C and pH 7.4.	57
Figure IV.37 Dissolution profiles of AMPI in PBS at 37°C and pH 7.4.	57
Figure IV.38 FESEM images of zein/CTZ 20/1 particles obtained at 9 MPa, 50 mg/mL and (a) 40°C (run #2); (b) 45°C (run #3); (c) 50°C (run #4).	60
Figure IV.39 Volumetric cumulative PSDs of zein/CTZ 20/1 particles precipitated from DMSO at 9 MPa, 50 mg/mL; effect of the temperature. .	60
Figure IV.40 FESEM images of zein/KTF 20/1 precipitated at 9 MPa, 50 mg/mL; (a) coalescent particles at 40 °C (run #10); (b) microparticles at 45 °C (run #11); (c) aggregates at 50 °C (run #12).	61
Figure IV.41 FESEM images of zein/CTZ precipitated at 9 MPa, 50 mg/mL, (a) 40°C and 10/1 w/w (run #5); (b) 45°C and 10/1 w/w (run #6); (b) 50°C and 10/1 w/w (run #7); (d) 40°C and 10/1 w/w (run #8).	62
Figure IV.42 FESEM images of zein/KTF microparticles obtained at 45 °C, 9 MPa, 50 mg/mL and different polymer/drug ratios: (a) 10/1 w/w (run #13); (b) 5/1 w/w (run #14).	63
Figure IV.43 Volumetric cumulative PSDs of zein/KTF particles precipitated at 45°C, 9 MPa, 50 mg/mL; effect of polymer/drug ratio.	64
Figure IV.44 FTIR spectra of unprocessed CTZ and zein, and SAS processed zein/CTZ powders at different w/w ratios.	65
Figure IV.45 FTIR spectra of unprocessed KTF and zein, and SAS processed zein/CTZ powders at different w/w ratios.	65
Figure IV.46 Dissolution profiles of CTZ in PBS at 37°C and pH 7.4; CTZ released from SAS particles produced at different operating temperatures.	66
Figure IV.47 Dissolution profiles of CTZ in PBS at 37°C and pH 7.4; CTZ released from SAS particles at different polymer/drug ratios.	67
Figure IV.48 Dissolution profiles of KTF in PBS at 37 °C and pH 7.4; KTF released from SAS particles produced at different operating temperatures.	68
Figure IV.49 Dissolution profiles of KTF in PBS at 37 °C and pH 7.4; KTF released from SAS particles at different polymer/drug ratios.	68
Figure IV.50 FESEM images of Eudragit particles precipitated from DMSO at 40°C, 20 mg/mL and (a) 9 MPa; (b) 10 MPa; (c) 12 MPa.	70
Figure IV.51 Volumetric cumulative PSDs of EUD precipitated from DMSO at 40°C and 10 MPa; effect of the polymer concentration in DMSO.	71
Figure IV.52 FESEM images of EUD/AMPI 20/1 particles precipitated from DMSO at 40°C and 40 mg/mL. Effect of the operating pressure: (a) 9 MPa (run #2); (b) 10 MPa(run #3).	72

Figure IV.53 FESEM images of EUD/AMPI 20/1 particles precipitated at 40°C, 10 MPa and (a) 20 mg/mL (run #4); (b) 50 mg/mL (run #5).	73
Figure IV.54 Volumetric cumulative PSDs of EUD/AMPI particles produced at 40°C, 10 MPa and 50 mg/mL; effect of the polymer/drug ratio.	73
Figure IV.55 FTIR spectra for unprocessed AMPI and EUD, physical mixture polymer/drug 10/1 and SAS processed powders EUD/AMPI 10/1. 74	
Figure IV.56 DSC thermograms of unprocessed AMPI and Eudragit L100-55, SAS processed EUD/AMPI composites 10/1.	75
Figure IV.57 Dissolution profiles in PBS at 37°C and pH 7.4.....	75
Figure IV.58 FESEM images of EUD/DIC 20/1 particles precipitated from DMSO at 40°C and 40 mg/mL. Effect of the operating pressure: (a) 9 MPa (run #2); (b) 10 MPa (run #3).	76
Figure IV.59 FTIR spectra for unprocessed and SAS processed EUD, unprocessed DIC, physical mixture and SAS processed EUD/DIC powders.	78
Figure IV.60 DSC thermograms of unprocessed and SAS processed EUD, unprocessed drugs, and SAS processed EUD/drug powders.	79
Figure IV.61 XRD patterns of unprocessed EUD and DIC, and SAS processed EUD/DIC powders.	79
Figure IV.62 Dissolution profiles in PBS at 37 °C and pH 7.4.....	80
Figure IV.63 FESEM images of EUD/THEOP 20/1 powders precipitated from DMSO at 40°C, 20 mg/mL and (a) 10 MPa (run #3) filter; (b) 10 MPa (run #3) precipitating chamber; (c) 12 MPa (run #4); (d) 15 MPa (run #5). 82	
Figure IV.64 Volumetric cumulative PSDs of EUD/THEOP 20/1 particles precipitated from DMSO at 40°C and 20 mg/mL; the effect of pressure.....	83
Figure IV.65 FESEM images of EUD/THEOP 10/1 w/w precipitated from DMSO at 40°C, 12 MPa and 40 mg/mL (run #7): (a) microparticles and (b) expanded microparticles.	83
Figure IV.66 Volumetric cumulative PSDs of EUD/THEOP particles precipitated from DMSO at 40°C, 12 MPa and 40 mg/mL; effect of the polymer/drug ratio.....	84
Figure IV.67 FTIR spectra for unprocessed and SAS processed EUD, unprocessed THEOP, physical mixture polymer/drug and SAS processed EUD/THEOP coprecipitated powders.....	85
Figure IV.68 DSC thermograms of unprocessed and SAS processed EUD, unprocessed THEOP, and SAS processed EUD/THEOP powders. ...	86
Figure IV.69 XRD patterns of unprocessed EUD and THEOP, and SAS processed EUD/THEOP powders.	86
Figure IV.70 Dissolution profiles in PBS at 37°C and pH 7.4.....	87
Figure IV.71 FESEM image of β -CD precipitated from DMSO at 9 MPa, 40°C and 100 mg/mL (run #1).	89

Figure IV.72 FESEM images of particles NIM/ β -CD 1/3 mol/mol precipitated from DMSO at 40°C and 100 mg/mL. Effect of the operating pressure: (a) 9 MPa (run # 3); (b) 12 MPa (run # 4); (c) 15 MPa (run #5). .	90
Figure IV.73 FESEM images of particles KET/ β -CD 1/2 mol/mol precipitated at 40°C and 100 mg/mL. Effect of the operating pressure: (a) 9 MPa (run # 12); (b) 12 MPa (run # 13); (c) 15 MPa (run #14).....	91
Figure IV.74 FESEM images of particles precipitated from DMSO at 40°C and 9 MPa: (a) NIM/ β -CD 1/3 mol/mol at 150 mg/mL (run # 6); (b) KET/ β -CD 1/2 mol/mol at 200 mg/mL (run # 15).....	92
Figure IV.75 Volumetric cumulative PSDs of KET/ β -CD 1/2 mol/mol precipitated from DMSO at 40°C and 9 MPa; effect of the overall concentration in DMSO.	92
Figure IV.76 FESEM images of NIM/ β -CD particles precipitated from DMSO at 40°C, 9 MPa, 200 mg/mL and a NSAID/CD ratio (a) 1/1 mol/mol (run # 9) and (b) 2/1 mol/mol (run # 10); (c) volumetric cumulative PSDs of NIM/ β -CD particles at different NIM/ β -CD molar ratios.	93
Figure IV.77 FESEM images of KET/ β -CD particles precipitated from DMSO at 40°C, 12 MPa, 200 mg/mL and a NSAID/CD ratio (a) 1/1 mol/mol (run # 17) and (b) 2/1 mol/mol (run # 18).	94
Figure IV.78 FTIR spectra of pure NIM, unprocessed and SAS processed β -CD, physical mixture and SAS NIM/ β -CD complexes at various molar ratios.....	95
Figure IV.79 FTIR spectra of unprocessed and SAS processed KET and β -CD, physical mixture and SAS KET/ β -CD complexes at various molar ratios.....	95
Figure IV.80 DSC thermograms of unprocessed NIM and β -CD, and SAS-processed NIM/ β -CD complexes at different molar ratios.	97
Figure IV.81 DSC thermograms of unprocessed KET and β -CD, and SAS-processed KET/ β -CD complexes at different molar ratios.	97
Figure IV.82 XRD patterns of unprocessed NIM and β -CD, and SAS-processed NIM/ β -CD complexes at different molar ratios.....	98
Figure IV.83 XRD patterns of unprocessed KET and β -CD, and SAS-processed KET/ β -CD complexes at different molar ratios.....	98
Figure IV.84 Dissolution profiles in PBS at pH 7.4 and 37°C.	99
Figure IV.85 Dissolution profiles in HCl solution at pH 2.5 and 37°C.	99
Figure IV.86 FESEM images of microparticles RUT/ β -CD 1/2 mol/mol precipitated from DMSO at 40°C, 9 MPa and (a) 100 mg/mL (run #2); (b) 150 mg/mL (run #3); (c) 200 mg/mL (run #4).	103
Figure IV.87 Volumetric PSDs of RUT/ β -CD microparticles 1/2 mol/mol; effect of total concentration in DMSO.	103
Figure IV.88 FESEM image of microparticles RUT/ β -CD 1/2 mol/mol precipitated from DMSO at 40°C, 200 mg/mL and 12 MPa (run #5).....	104
Figure IV.89 Volumetric PSDs of RUT/ β -CD microparticles 1/2 mol/mol; effect of operating pressure.	104

Figure IV.90 FESEM images of (a) microparticles RUT/ β -CD 1/1 mol/mol (run #9), (b) microparticles and crystals at rutin/ β -CD 2/1 mol/mol (run #10), precipitated from DMSO at 40°C, 200 mg/mL and 12 MPa.	105
Figure IV.91 FTIR spectra of unprocessed RUT and β -CD, physical mixture NSAID+ β -CD and SAS processed RUT/ β -CD powders at different molar ratios: a) entire spectra; b) enlargement of the spectra.	106
Figure IV.92 DSC thermograms of unprocessed RUT and β -CD, and SAS processed RUT/ β -CD powders at different molar ratios.	107
Figure IV.93 Dissolution profiles in PBS at pH 7.4 and 37°C.....	108
Figure V.1 Sketches of the plants for (a) drying; (b) impregnation. CO ₂ : carbon dioxide supply; RB: refrigerating bath; P: pump; TC: thermocouple; M: manometer; MV: micrometering valve; LS: liquid separator; BPV: back pressure valve and R: rotameter.	113
Figure V.2 Impregnation isotherms at 18 MPa and 40/60°C for NIM/aerogels.	115
Figure V.3 Impregnation isotherms at 18 MPa and 40 and 60°C for KET/aerogel systems.....	116
Figure V.4 Impregnation isotherms at 18 MPa and 40 and 60°C for DIC/aerogel systems.....	116
Figure V.5 Kinetic curves at 18 MPa and 40 and 60°C for the impregnation of NIM into aerogels.	118
Figure V.6 Kinetic curves at 18 MPa and 40 and 60°C for the impregnation of KET into aerogels.	119
Figure V.7 Kinetic curves at 18 MPa and 40 and 60°C for the impregnation of DIC into aerogels.	119
Figure V.8 Pseudo-second-order kinetics for the impregnation of NIM into aerogels, at 18 MPa and 40 and 60°C.....	121
Figure V.9 Pseudo-second-order kinetics for the impregnation of NIM into aerogels, at 18 MPa and 40 and 60°C.....	122
Figure V.10 Pseudo-second-order kinetics for the impregnation of NIM into aerogels, at 18 MPa and 40 and 60°C.....	122
Figure V.11 Intraparticle diffusion plot for the impregnation of NIM in MSA and CAA.....	123
Figure V.12 Intraparticle diffusion plot for the impregnation of KET in MSA and CAA.....	124
Figure V.13 Intraparticle diffusion plot for the impregnation of DIC in MSA and CAA.....	124
Figure V.14 FESEM images of (a) pure MSA after drying using scCO ₂ , (b) NIM impregnated on MSA, (c) KET impregnated on MSA, (d) DIC impregnated on MSA.	126
Figure V.15 FESEM images of (a) pure CAA after drying using scCO ₂ , (b) NIM impregnated on CAA, (c) KET impregnated on CAA, (d) DIC impregnated on CAA.....	127

Figure V.16 FTIR spectra for pure NIM, pure MSA and CAA, physical mixture aerogel+NIM, NIM impregnated into aerogels.	128
Figure V.17 FTIR spectra for pure KET, pure MSA and CAA, physical mixture aerogel+KET, KET impregnated into aerogels.	128
Figure V.18 FTIR spectra for pure DIC, pure MSA and CAA, physical mixture aerogel+DIC, DIC impregnated into aerogels.	129
Figure V.19 DSC thermograms of pure NIM, pure MSA and CAA, NIM impregnated into aerogels.	130
Figure V.20 DSC thermograms of pure KET, pure MSA and CAA, KET impregnated into aerogels.	130
Figure V.21 DSC thermograms of pure DIC, pure MSA and CAA, DIC impregnated into aerogels.	131
Figure V.22 XRD patterns for pure NIM, pure MSA and CAA, NIM impregnated into aerogels.	131
Figure V.23 XRD patterns for pure KET, pure MSA and CAA, KET impregnated into aerogels.	132
Figure V.24 XRD patterns for pure DIC, pure MSA and CAA, DIC impregnated into aerogels.	132
Figure V.25 Dissolution profiles of NIM in PBS at 37 °C and pH 7.4.	134
Figure V.26 Dissolution profiles of KET in PBS at 37 °C and pH 7.4.	134
Figure V.27 Dissolution profiles of DIC in PBS at 37 °C and pH 7.4.	135
Figure V.28 Kinetic curves at 17 MPa and 35°C for the impregnation of MSG on PCL foams.	139
Figure V.29 Photographs of unprocessed PCL, and foamed + impregnated samples at 17 MPa, 35°C and various contact time (in the range 2 h- 24 h).	139
Figure V.30 Pseudo-second-order kinetics for the impregnation of MSG on PCL at 17 MPa and 35°C.	140
Figure V.31 Pore diffusion plot for the MSG impregnation on foamed PCL.	141
Figure V.32 Photographs of (a) unprocessed PCL film; (b) foamed PCL film after MSG impregnation.	142
Figure V.33 FESEM images of (a) PCL film foamed by scCO ₂ ; (b) MSG impregnated into/on foamed PCL film.	143
Figure V.34 FT-IR spectra for pure MSG and PCL, MSG impregnated on foamed PCL.	143
Figure V.35 DSC thermograms of pure MSG and PCL, MSG impregnated on foamed PCL.	144
Figure V.36 Dissolution kinetics in PBS at pH 7.4 and 37°C.	145

Table Index

Table III.1 <i>Characteristic wavelengths of the selected active compounds.</i>	20
Table IV.1 Summary of SAS experiments performed on PVP/KET (MP:microparticles; cSMP: coalescing sub-microparticles; C: crystals).	26
Table IV.2 Summary of SAS experiments performed on PVP/RUT (MP:microparticles; cMP: coalescing microparticles; C: crystals).	34
Table IV.3 SAS experiments performed on zein (NP: nanoparticles; SMP: sub-microparticles; MP: microparticles).	39
Table IV.4 SAS experiments performed on zein/diclofenac system (NP: nanoparticles; SMP: sub-microparticles; MP: microparticles).	43
Table IV.5 SAS experiments performed on zein/antibiotic systems (SMP: sub-microparticles; MP: microparticles; liq: liquid).	49
Table IV.6 SAS tests performed on zein/antihistamine systems (C: crystals; MP: microparticles; cMP: coalescent microparticles; AGG: aggregates).	59
Table IV.7 A list of SAS experiments performed on Eudragit L100-55 (MP: microparticles; cMP: coalescent microparticles).	70
Table IV.8 SAS experiments performed on Eudragit/ampicillin system (SMP: sub-microparticles; MP: microparticles; cMP: coalescent microparticles).	72
Table IV.9 SAS experiments performed on Eudragit/diclofenac system (NP: nanoparticles; MP: microparticles; cMP: coalescing microparticles)..	76
Table IV.10 SAS experiments performed on Eudragit/theophylline system (C: crystals; MP: microparticles; cMP: coalescing microparticles; EMP: expanded microparticles).	81
Table IV.11 SAS experiments performed on NSAID/ β -CD systems (NP: nanoparticles; cSMP: coalescent sub-microparticles; MP: microparticles; cMP: coalescent microparticles; liq: liquid).	89
Table IV.12 SAS experiments performed on RUT/ β -CD system (MP= microparticles; cMP= coalescent microparticles; C= crystals).	102
Table V.1 <i>Impregnation rate constants obtained from the pseudo-first- order kinetics for NSAID/aerogel systems.</i>	120
Table V.2 <i>Impregnation rate constants obtained from the pseudo- second-order kinetics for NSAID/aerogel systems.</i>	121
Table V.3 <i>Pore diffusion rate parameters for NSAID/aerogel systems.</i>	125
Table V.4 <i>Dissolution parameters obtained by Peppas equation.</i>	136
Table V.5 <i>Solubility of MSG in scCO₂ at 35°C and different pressures.</i>	138

Table V.6 *Impregnation rate constants obtained from the pseudo-first-order and pseudo-second-order models for MSG/PCL system.* 140

Table V.7 *Pore diffusion rate parameters for MSG/PCL system.* 142

Abstract

The interest in the production of novel polymer/active compound composites has increased over time as a response to the main issues encountered in the pharmaceutical field. Nowadays, polymeric carriers are employed to prepare composite systems with several aims, including the protection or stabilization of an active compound, as well as masking its unpleasant taste or odor. However, the main challenge is to reach a control of the drug release rate from innovative pharmaceutical forms, overcoming the drawbacks associated to the use of conventional formulations. The latter ones often provide uncontrolled drug release, sometimes out of the therapeutic range; as a consequence, high and repeated drug dosages are necessary, leading to serious side effects on the patient's health. Different formulations can be fabricated as drug delivery systems, such as granulates, tablets or topical patches. However, the technologies generally used to produce composites suffer from some drawbacks, including the possible degradation of the active compound due to the high operating temperature, or multistage processing required to remove organic solvents, whose residues are often not negligible in the final composites. Supercritical carbon dioxide (scCO₂) assisted techniques are considered a good alternative to overcome all the main limits involved in the use of traditional processes.

In this Ph.D. work, two scCO₂ assisted processes are proposed to produce different polymer/active compound composites:

- Supercritical AntiSolvent (SAS) technique, to produce composite powder with a microparticle-like morphology;
- supercritical impregnation, to obtain orally disintegrating tablets (ODTs) or topical patches.

The main goal is to accelerate or to slow down the dissolution rate of the active principle contained in the composites, depending on the therapeutic effect required by a specific application. In this way, the drug doses or the frequency of administration, as well as side effects, can be reduced, improving the patient's compliance. For this purpose, different polymer/drug systems were studied. Both in case of the microspheres' production by SAS and the drug impregnation into supports, the selection of a proper polymeric carrier according to the desired drug release is particularly important. Specifically, when a hydrophilic carrier is employed, a fast dissolution rate of the active principle is reached. This option is promising to enhance the bioavailability of poorly-water soluble compounds, such as non-steroidal anti-inflammatory drugs (NSAIDs) prescribed for minor inflammations, or natural compounds (e.g., flavonoids) with numerous benefits for human health. On the other hand, the use of hydrophobic polymers promoted a prolonged drug release. This kind of carriers can be combined with drugs

that are highly-water soluble or prescribed for chronic diseases, such as antibiotics, NSAIDs, antihistamines, bronchodilators or anticoagulant drugs.

Regarding SAS technique, the polymer/drug coprecipitation mechanisms in correspondence of different morphologies were also postulated by means of dissolution studies, demonstrating that SAS coprecipitation was fully achieved when microspheres are produced. Until now, one of the weaknesses of the SAS technique was that the coprecipitation had been actually achieved only with a limited number of polymers; i.e., polylactic acid (PLA), poly (L-lactic acid) (PLLA) and polyvinylpyrrolidone (PVP). In this work, the effectiveness of other carriers, namely zein, Eudragit L100-55 and β -cyclodextrin (β -CD), was successfully asserted, optimizing the process conditions to assure an effective coprecipitation in form of composite microparticles. It was proved that both microspheres and guest/host inclusion complexes can be produced by SAS, using a generic polymer or β -CD as oligosaccharides, respectively. The results of dissolution tests highlighted that zein and Eudragit L100-55 tend to prolong the release of the drug embedded into the microspheres. It has to be considered that Eudragit and zein are low cost polymers with respect to lactic acid-based polymers proposed so far to obtain SAS particles that promote a prolonged drug release. Conversely, the preparation of β -CD based complexes allowed to enhance the dissolution rate of active compounds. The use of β -CD also appears to be promising in reducing the amount of carrier in SAS-coprecipitated powders, which is a considerable milestone from a pharmaceutical point of view.

Topical patches and ODTs were prepared by the versatile supercritical impregnation, incorporating different drugs into thin films or aerogels. ODTs both for a rapid or prolonged release of NSAIDs were produced by selecting maize starch aerogel (MSA) and calcium alginate aerogel (CAA), respectively. Peppas mathematical model (Ritger and Peppas, 1987) was applied to identify the dominant factor in the drug release behavior, which is often a combination of solvent diffusion and polymer chain relaxation. In order to produce medicated patches for the wound healing, a single step consisting of the polymer foaming and the drug impregnation into the foam was proposed. The drug release from foamed polycaprolactone (PCL) was significantly prolonged, promoting a proper tissue regeneration. The supercritical impregnation of drugs into polymeric films was suggested for the first time for pharmaceutical applications. The study of the impregnation mechanisms of drugs into all the supports proved that, in general, the impregnation using $scCO_2$ is first governed by the film diffusion, thus the drug is impregnated on the outer surface of the matrix. Then, the impregnation is controlled by pore diffusion, so the drug is also loaded onto the inner pores of the support.

In conclusion, the $scCO_2$ assisted techniques are very versatile and promising to produce different pharmaceutical forms that offer different drug release kinetics, depending on the specific application.

Introduction

Polymer/active compound composites are widely employed in various industrial applications, especially to overcome the main issues encountered in the pharmaceutical field. Different formulations can be fabricated as drug delivery systems, such as capsules, granulates, tablets, and topical patches. The use of polymeric carriers to produce pharmaceutical composites has multiple functions: the protection of an active principle against its oxidation and/or deactivation caused by external agents (light, oxygen, high temperature, pH), as well as masking its unpleasant taste and/or odor in case the drug is orally administered. Currently, the primary reason is the control of the release rate of an active compound. Conventional pharmaceutical forms typically provide undesired release kinetics in which the drug concentration can be below the minimum effective concentration required to have a therapeutic effect or above the maximum safe concentration, in an uncontrolled manner. Thus, high and repeated drug dosages are necessary, leading to serious side effects on the patient's health.

Nowadays, the interest of the pharmaceutical market in novel formulations is continuously growing to improve the therapeutic efficacy of active compounds and the patient's compliance, providing different release profiles within the therapeutic range for different diseases. Indeed, a rapid or prolonged drug release can be necessary depending on the specific pathology, which may require a fast or long-term response. Many prescribed drugs are characterized by a low solubility in water, resulting in a low bioavailability. The particle size reduction of an active compound through micronization processes allows to improve the dissolution rate of poorly water-soluble drugs, by increasing the specific surface area of the powder drug and its contact with the water molecules. The drug dissolution can be further enhanced by developing hydrophilic polymer-based formulations of various types, including microspheres or ODTs. On the contrary, when an active compound has to be released slowly because of its highly water-solubility or chronic use, the selection of a hydrophobic carrier is recommended.

With regards to infections, long-term antibiotic therapies are generally prescribed. Unfortunately, many antibiotics are very soluble in water and

characterized by a short half-life; in these cases, prolonged-release drug delivery systems are desirable to reduce the number of administrations and the side effects, including the antibiotic resistance (Stebbins et al., 2014). Given the existence of many inflammatory conditions, in the case of NSAIDs, both a fast and prolonged release kinetics can be required for the treatment of minor inflammations (e.g., headaches, toothache) or chronic disease (e.g., rheumatoid arthritis, osteoarthritis), respectively (Altman et al., 2015, Gupta and Bah, 2016, Maniar et al., 2018). It has to be considered that, when NSAIDs are frequently taken, serious side effects may occur, such as nausea, vomiting, gastrointestinal bleeding and peptic ulcer. All these issues can be solved by promoting an accelerated or prolonged drug release by properly choosing hydrophilic or hydrophobic carriers, respectively. Other useful applications of pharmaceutical composites concern the treatment of the chronic bronchial asthma or the allergies. Nowadays, the main challenge related to the asthma is to achieve the control of the disease; i.e., to prevent symptoms or asthmatic exacerbations, with the least number of drugs. In this context, as an alternative to drugs often taken by inhalation in case of exacerbations to have a rapid improvement of symptoms, there is a growing interest in drugs to be used daily, which provide a long-term control. Therefore, efficient delivery systems are often required to achieve a prolonged or sustained release of bronchodilator drugs. Similarly, attempts are being made to produce next generation antihistamine formulations that promote a drug prolonged release, to prevent and to treat the allergy symptoms, as well as to reduce side effects, such as sleepiness and daze, in patients with chronic allergy.

Dosing frequency and adverse effects related to drug overuse can also be reduced using topical formulations, which provide constant blood levels, avoiding the first-pass metabolism and the gastrointestinal tract. Indeed, a medicated patch offers a controlled release of the active principle: a specific amount of drug released from a medicine reservoir penetrates the skin, subcutaneous fatty tissue and muscle, without reaching high plasma levels. Thus, topical plasters improve the drug local bioavailability to the specific site of action and, in case of toxicity, the treatment can be stopped by simply removing the patch. Unfortunately, this kind of formulation presents a main drawback; i.e., the molecules of the active principle have to be small enough to penetrate the skin, which is a very effective barrier. Topical systems are considered, for example, a promising approach to wound healing.

It is clear that the development of various innovative polymer/drug systems can provide a valid answer to the main troubles facing pharmaceutical companies. There are different technologies to fabricate polymer/active compound composites in the different forms. However, conventional techniques generally employed suffer from some drawbacks, including low loading efficiencies, possible degradation of the active compound due to high process temperatures, and multistage processing

involved to remove toxic organic solvents, whose residues are often not negligible in the final composites. In addition, morphology, mean particle size and particle size distribution (PSD) are often difficult to control in the case of micronization processes (Wu et al., 2009, Lee et al., 2010, Park et al., 2010, Ha et al., 2020). The attainment of irregular particles with a wide PSD can be a serious limitation when oral or injectable formulations are produced. Instead, in the case of the incorporation of active compounds in porous matrices to obtain for example ODTs, the collapse of porosities or the difficult penetration of the solvent used into the pores often occur.

The scCO₂ assisted techniques are considered a good alternative to traditional processes (Won et al., 2005, Wu et al., 2009, Park et al., 2010, Lee et al., 2010, da Fonseca Machado et al., 2018, Ha et al., 2020, Park et al., 2020). The use of organic solvents is considerably reduced or eliminated, whereas scCO₂ is completely removed from the product by simple depressurization. It is also possible to process thermolabile compounds without degradation, due to scCO₂ moderate critical parameters (T_c=31.1 °C, P_c=7.38 MPa). The scCO₂ based technologies are very versatile, allowing to produce different possible pharmaceutical forms, from oral to topical administration. Microparticles or nanoparticles with narrow PSDs can be created using different supercritical micronization techniques, among which SAS process stands out. The high diffusivity and the quasi-zero surface tension of scCO₂ facilitates its penetration into the pores of polymeric matrices as aerogels, while preserving the porous structure (Kikic and Vecchione, 2003, Tkalec et al., 2015). In addition, its ability to swell or foam various polymers favours the loading of active compounds. The supercritical impregnation process is exactly based on these advantages: the scCO₂ is exploited as a solvent and a swelling or foaming agent to produce drug-loaded supports for oral or topical applications; e.g., ODTs or medicated patches, respectively.

Chapter I

Aim of the work

Considering the current interest in improving the therapeutic efficacy of many active principles and in their safe use, the present work is focused on the production of polymer/active compound composites, mainly:

- to enhance the dissolution rate of poorly-water soluble drugs,
 - to prolong the release of active compounds for chronic diseases,
- in order to reduce the administration dosage/frequency and the side effects associated with the drug overuse.

The goal is to provide the best drug release kinetics for a specific pharmaceutical application, developing polymer/drug composites by two scCO₂ assisted techniques:

- SAS process;
- supercritical impregnation.

These scCO₂ based technologies are proposed to overcome the main limits related to the production of composite systems by conventionally used methods. The key role of the polymeric carrier selected to prepare the pharmaceutical formulations is also highlighted.

In particular, the SAS technique was employed to produce composite microspheres that promote a fast or a prolonged release of the embedded active compound, depending on the desired therapeutic effect. The aim was to produce well-defined composite microparticles with narrow PSDs and zero solvent residue. In the current literature, the polymer/drug coprecipitation by SAS process has been successfully achieved only with a limited number of polymers. Thus, one of the main objectives of this part of the work was also to identify new carriers processable by SAS that allow a proper coprecipitation of the two materials. The novel carriers proposed are not only valid in terms of drug release control, but also allow to overcome some drawbacks related to the use of polymers hitherto considered effective for SAS coprecipitation, such as high costs or high quantities of polymer necessary to achieve a coprecipitation in the form of composite microparticles. The coprecipitation mechanisms in correspondence of different morphologies were also postulated.

The solvent-free supercritical impregnation of drugs into polymeric supports is instead employed to develop topical patches for a controlled drug delivery or ODTs, characterized by a rapid or prolonged drug release depending on the selected carrier. The goal was to exploit the scCO₂ as a solvent to load different categories of active principles into different polymeric supports (i.e., aerogels or film), obtaining various drug delivery systems. It is worth noting that, up to now, the supercritical impregnation of drugs into polymeric films has not been proposed for the production of topical patches. For an appropriate interpretation of the experimental data, the impregnation mechanisms of the active compounds onto/into the polymeric supports were investigated, as well as the release kinetics models.

The final aim is to provide satisfactory results that encourage the use of the two supercritical techniques on an industrial scale to produce different composite systems for the treatment of different clinical pathologies.

Chapter II

State of the art of the scCO₂ assisted technologies

II.1 State of the art of SAS process

Over time, the interest in the production of microparticles, nanoparticles and composite microparticles has widely spread in many industrial applications. In particular, the micronization of active compounds (i.e., food ingredients and drugs) and their incorporation in biocompatible polymer-based particles is largely employed in the nutraceutical and pharmaceutical fields. Nowadays, polymer/active compound composite microparticles attract great interest and can be classified as follows:

- microspheres, a polymeric matrix in which an active principle is homogeneously dispersed, frequently obtained by a simultaneous precipitation of the drug and the polymeric carrier;
- microcapsules, in which a core material (i.e., the active compound) is surrounded by a polymeric shell (i.e., the coating material).

These composite systems, when applied for oral drug delivery, allow a good control of the dissolution rate of the embedded active compounds. There are many conventional micronization techniques used to produce coprecipitates: spray-drying, emulsification/solvent evaporation, centrifugal extrusion, jet-milling, freeze drying, and coacervation. However, these processes suffer from some drawbacks, such as the production of irregular particles often characterized by wide PSDs, the possible degradation of the product due to mechanical or thermal stresses and the difficulty in the complete elimination of the organic solvents used during the process (Won et al., 2005, Wu et al., 2009, Lee et al., 2010, Park et al., 2010, Park et al., 2020, da Fonseca Machado et al., 2018, Ha et al., 2020). These limitations can be overcome by scCO₂-assisted micronization technologies, including the SAS technique that exploits the scCO₂ as antisolvent. SAS process is based on some main prerequisites: the scCO₂ has to be completely miscible with the selected liquid solvent; on the contrary, the solute/solutes to be

processed has/have to be soluble in the liquid solvent, but insoluble in the binary mixture formed in the precipitator consisting of the solvent and the antisolvent. Hence, the precipitation/coprecipitation of solute/solutes occurs because of the fast diffusion of scCO₂ into the liquid solvent and the consequent supersaturation of the solute/solutes.

There are also some modified versions of the SAS technique, in which the scCO₂ acts equally as an antisolvent, such as the supercritical gas antisolvent (GAS) process and the solution enhanced dispersion by supercritical fluids (SEDS). In the SEDS process, the scCO₂ and the liquid solution are both injected through a coaxial nozzle. In the GAS process, the scCO₂ is introduced into the solution consisting of the liquid solvent and solute/solutes to be precipitated. The SAS process was also proposed in the literature with other different acronyms, such as Aerosol Solvent Extraction System (ASES).

II.1.1 Fundamentals of SAS technique

In order to fully understand the SAS process, three main aspects and their interactions have to be considered, namely:

- high-pressure vapor liquid equilibria (VLEs) of the system formed by solvent, antisolvent and solute/solutes;
- fluid dynamics of the injected solution in contact with scCO₂;
- mass transfer to/from the injected solution that causes the particles formation.

Regarding the high-pressure VLEs, the ternary system consisting of solvent/solute/scCO₂ or the quaternary system solvent/drug/polymer/scCO₂ should be considered in case of micronization or coprecipitation, respectively. However, SAS is based on the assumption that the solute is practically insoluble in the mixture consisting of the solvent and the antisolvent. If this main hypothesis is verified, the presence of solute/solutes can be neglected, thus the fluid phase formed in the precipitation chamber can be considered as a binary mixture. For this reason, the 'pressure-CO₂ molar fraction' isothermal diagram of the mixture solvent/antisolvent is generally used to identify the position of the operating point with respect to the binary mixture critical point (MCP). SAS micronization/coprecipitation is typically operated at pressures above the MCP of the binary system solvent/antisolvent.

According to the classification proposed by Van Konynenburg and Scott (Van Konynenburg and Scott, 1980), the CO₂ and an organic solvent usually form type-I systems in term of phase behavior, as shown for example in **Figure II.1**. Since dimethylsulfoxide (DMSO) is considered one of the best solvents for SAS precipitation and being the one employed for the experiments reported in this thesis, the VLE of the binary system DMSO-CO₂ (with isotherms at different temperatures) is also shown in **Figure II.2**.

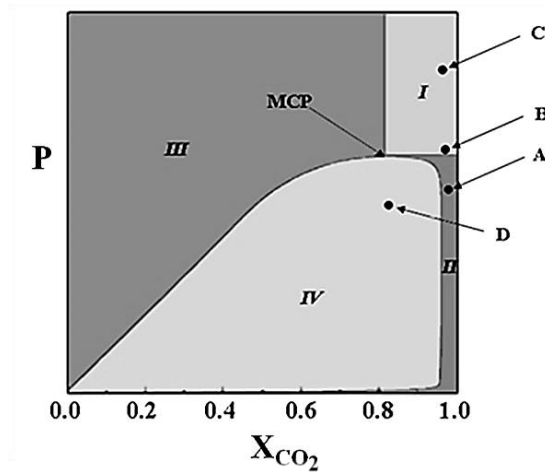


Figure II.1 VLE of a binary system of type I (Van Konynenburg and Scott, 1980); P : pressure, X_{CO_2} : CO₂ molar fraction.

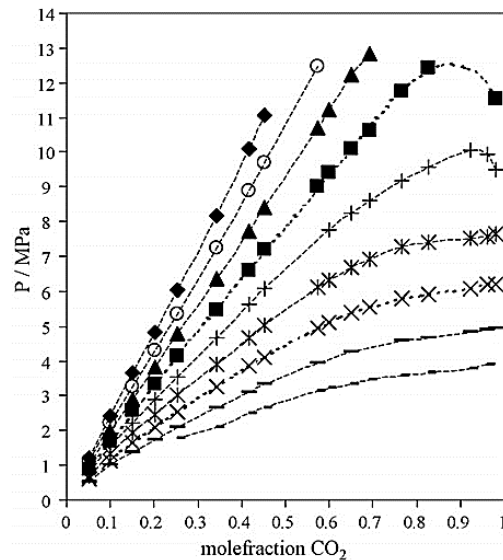


Figure II.2 VLE of the binary system DMSO-CO₂. From lower to higher pressures, the isotherms correspond to 5, 15, 25, 35, 45, 55, 65, 75 and 85°C (Andreatta et al., 2007a).

During a typical SAS experiment, the solvent/antisolvent mixture should be supercritical. Therefore, at a fixed temperature, the operating point has to be above the MCP of the selected couple solvent/antisolvent, as well as at molar fractions on the right of the MCP, to assure the formation of a supercritical mixture (region I). Looking at the diagram in **Figure II.1**, different regions can be explored operating at conditions different from region I: subcritical gaseous conditions located in region II, expanded liquid

conditions located in region III, and two-phase region conditions located in region IV. Depending on the physical state of the binary mixture in the precipitation chamber, different morphologies can be obtained by working in the various regions mentioned (Bouchard et al., 2007, Reverchon et al., 2007, Reverchon et al., 2008a, Reverchon et al., 2008b, Chang et al., 2008a, Reverchon and De Marco, 2011). Generally:

- expanded microparticles are obtained working in subcritical conditions (point A);
- microparticles are produced near above the MCP, in the transition zone between two and single-phase mixing (point B);
- nanoparticles precipitate operating far above the MCP, at fully developed supercritical conditions (point C);
- crystals precipitate if the operating point falls within the miscibility hole (point D).

In the SAS process, the nozzle used as injection device has to induce the jet break-up and the atomization of the liquid solution. The atomization of the liquid phase plays a key role in enhancing the contact and, thus, favoring the mass transfer between the liquid solvent and the antisolvent. The dimensions of the liquid droplets produced depend on the jet fluid dynamics. The influence of the jet velocity and the liquid properties (e.g. viscosity and surface tension) can be studied using following dimensionless numbers:

- the Reynolds number ($Re=Dv\rho/\mu$) that represents the ratio between the inertial and the viscous forces;
- the Ohsenorge number ($Oh=\mu/\sqrt{D\rho\sigma}$) that relates the viscous and the surface tension forces, dividing the square root of Weber number ($We=\rho v^2 D/\sigma$) by the Reynolds number.

It was also demonstrated that the evolution of the liquid jet is controlled by the competition of two main mechanisms: the jet break-up and the surface tension vanishing (Reverchon and De Marco, 2011, Marra et al., 2012). If the time of jet break-up (t_{JB}) is the shortest characteristic time of the process, micrometric droplets are produced at the injector exit as a result of the liquid jet break-up, following by the atomization of the liquid phase. The very fast mass transport of $scCO_2$ into the droplet, due to the high solubility of $scCO_2$ in organic solvents, and the solvent evaporation into the bulk $scCO_2$ lead to the precipitation/coprecipitation of the solute/solutes and the attainment of amorphous spherical microparticles. Considering this precipitation mechanism, each droplet works as a micro-precipitator; the surface tension of the liquid phase forces all the material to maintain its original shape and volume, therefore the diameters of microparticles are similar to the ones of the droplets from which they originate. As previously mentioned, at a fixed temperature, SAS spherical microparticles are obtained only in a limited range of pressures near above the MCP of the binary system solvent/antisolvent. Operating at subcritical gaseous conditions, expanded microparticles generally precipitate, whose formation mechanism can be

considered as a variation of the one proposed for microparticles. In particular, the atomization generates microdroplets; then, mass transfer to/from the liquid droplet occurs, but fluid phase is not at supercritical conditions, thus the surface tension never goes to zero. Therefore, the droplets are forced to maintain the spherical shape and the formed gaseous phase is blocked in the spherical envelope. The mass transfer continues, in the meanwhile the residual surface tension maintains the coherence of the micro-precipitator, so an increase in the droplet volume occurs. The solute begins to precipitate near the internal droplet surface, then it accumulates forming a solid shell (an empty core), leading to the generation of expanded microparticles, also called “balloons”. Instead, performing SAS process far above the MPC of the solvent/antisolvent mixture, it was demonstrated that the time of surface tension vanishing (t_{STV}) is lower than t_{JB} : in this case, nanoparticles are obtained by gas-to-particles nucleation and growth. At these conditions, droplets are not formed at the injector exit, but the liquid solution mixes with the gas phase (gas mixing), from which solids can nucleate and grow. Many experimental evidences supported this hypothesis, firstly the irregular shape of the nanoparticles, compared to the perfectly spherical shape of microparticles generated from the drying of spherical droplets confined by the surface tension. Moreover, Lengsfeld et al. (Lengsfeld et al., 2000) demonstrated that, operating in completely developed supercritical conditions, the time scale of the surface tension disappearance of the jets of miscible fluids (solvent+antisolvent) determines the jet evolution as a gas mixing, thus no droplets are formed. Lastly, it is well known that the surface tension tends to zero faster the more the pressure increases; thus, at very high pressures, far above the MPC of the solvent/antisolvent mixture, the surface tension of the injected liquid goes rapidly to zero and no droplets are formed.

II.1.2 SAS micronization of active compounds

SAS technique is one of the most effective micronization techniques based on the use of scCO₂. So far, several active compounds, such as antibiotics, anti-inflammatory drugs, antioxidants, anticancer drugs, and corticosteroids, were successfully micronized in form of nanoparticles, sub-microparticles and microparticles by SAS (Kalogiannis et al., 2005, Reverchon and De Marco, 2006, Tenorio et al., 2007a, Zhao et al., 2011b, Zu et al., 2012, Zhao et al., 2012, Park et al., 2013, Montes et al., 2016a).

Many literature studies demonstrated that SAS process allows to overcome the main drawbacks of conventional micronization techniques, such as spray drying, freeze-drying, jet-milling, solvent evaporation and grinding (Park et al., 2010, Ha et al., 2020). Rogers et al. (Rogers et al., 2001) compared scCO₂-based processes, including the SAS, and cryogenic spray-freezing technologies in the micronization of active principles. Both

the approaches were presented as potential solution for the production of particles of active compounds that cannot be processed by more conventional micronization techniques, such as spray drying and jet-milling. In the specific case of SAS technique, the authors highlighted the advantage of using an environmentally-friendly antisolvent as the scCO₂ with respect to the toxic organic antisolvents conventionally employed. The gas-like and liquid-like properties of scCO₂, such as the high diffusivity and the high solvent power, lead to the attainment of dry particles without solvent residues in one step. Conversely, lyophilization or antisolvent extraction are needed to dry the powders prepared by the cryogenic micronization technologies. The study of Park et al. (Park et al., 2010) demonstrated the superiority of the SAS process with respect to spray drying in the micronization of cefdinir (a model drug). Microparticles characterized by a mean size equal to $2.32 \pm 1.76 \mu\text{m}$ and a specific surface area of $35.01 \pm 0.63 \text{ m}^2/\text{g}$ were obtained by spray drying, whereas nanoparticles with a narrow PSD ($0.15 \pm 0.07 \mu\text{m}$) and a higher surface area ($55.79 \pm 0.06 \text{ m}^2/\text{g}$) were produced by the SAS technology. As a result of the increase in the surface area, which led to a better contact between the drug and the water molecules, the dissolution of the SAS-processed cefdinir was faster than the spray-dried drug particles. According to the results obtained by Ha et al. (Ha et al., 2020), SAS micronization also proved to be more effective than milling techniques. SAS nanoparticles and sub-microparticles (size in the range: $0.15\text{--}0.50 \mu\text{m}$) allowed to speed up the dissolution of resveratrol, with respect to crystals ($18.75 \mu\text{m}$) or crystals/irregular coalescent particles ($1.94 \mu\text{m}$) produced by Fritz milling and jet-milling, respectively. Similarly, in other works (Kim et al., 2007, Kim et al., 2008, Chang et al., 2008b, Chen et al., 2010, Zhao et al., 2011b, Zu et al., 2012, Montes et al., 2016a, Hiendrawan et al., 2016), SAS micronization led to an enhancement of the drug dissolution rate. Therefore, it is ascertained that SAS micronization provides benefits in the final pharmaceutical product in terms of morphology/dimensions of the particles that constitute it and, consequently, in terms of dissolution and bioavailability. It is well known that different factors can influence the oral bioavailability of an active compound, including the first-pass metabolism, the drug permeability, and its solubility and dissolution rate in water. In particular, poor solubility and slow dissolution rates are the main causes of the low bioavailability for most of the active principles (Abuzar et al., 2018). Consequently, a low drug amount, often at an insufficient concentration, is available at the specific site of action.

SAS technique offers the possibility of obtaining both crystalline and amorphous materials, by modulating the operating conditions of pressure and temperature. Considering the P–x isothermal diagram of the solvent/antisolvent mixture (**Figure II.1**), if the working point is above the MCP of the drug/solvent/scCO₂ system, the possibility of producing an

amorphous material by an effective micronization increases by increasing the pressure. It is obvious that the attainment of amorphous powders involves numerous benefits, including the enhancement of the drug dissolution rate in an aqueous environment.

However, as emerged from several papers, the selection of the proper liquid solvent is crucial. The success of SAS precipitation strongly depends on the affinity between the solvent and the antisolvent; i.e., the solubility of the liquid solvent in the scCO₂ and the fast gas-like diffusion of the scCO₂ in the solvent. These fundamental aspects assure the attainment of small particles. Many studies showed that DMSO is one of the best solvents for SAS micronization (Kalogiannis et al., 2005, Tenorio et al., 2007a, Zhao et al., 2011b, Zu et al., 2012, Montes et al., 2016a), as it often allows to produce particles with good morphology and small size, in addition to being the most used solvent. Respecting the basic prerequisites of SAS precipitation, up to now, DMSO allowed micronizing a wide variety of active principles in the form of nanometric and micrometric particles. Ethanol (EtOH) (Cardoso et al., 2008b, Cardoso et al., 2008a, Zhao et al., 2011a, Visentin et al., 2012, Zhao et al., 2012, Ha et al., 2020) and acetone (Chen et al., 2010, Widjojokusumo et al., 2013) also emerged as good solvents for the SAS micronization of active compounds. Besides, some active principles were effectively micronized using methanol (Kim et al., 2008, Park et al., 2010, Ha et al., 2020) and N-methyl-2-pyrrolidone (NMP) (Reverchon et al., 2000, Tenorio et al., 2007b, Liu et al., 2020). Acetone belongs to the category of solvents that have a narrow pressure range to switch from the two-phase to the single-phase mixing with scCO₂; using this kind of solvents, nanoparticles are generally obtained (De Marco et al., 2013). On the other hand, microparticles usually precipitate from DMSO, EtOH and NMP, which are solvents that present a broad transition zone from the two-phase to the single-phase mixing with scCO₂. For the latter category of solvents, high operating pressures are necessary to produce nanoparticles.

Another critical parameter for a successful micronization is the molar fraction of CO₂, which should allow the complete miscibility between the solvent and the antisolvent at the selected pressure and temperature. For this purpose, in most of the reported papers, CO₂ molar fractions higher than 0.95 were used. The operating pressure and the concentration of the active compound in the liquid solution also influence the morphology and the size of the precipitated powders. In particular, when spherical particles are produced, a decrease of the pressure or an increase of the drug concentration often results in an increase of particles' dimensions. However, it is possible that large crystals significantly precipitate, increasing drug concentration. This result can be explained considering that the presence of the active compound can modify the high-pressure VLEs of the solvent/antisolvent binary system. Consequently, the MCP of the drug/solvent/scCO₂ ternary system shifts towards higher pressures with respect to the MCP of the

solvent/scCO₂ binary system (Campardelli et al., 2017b, Campardelli et al., 2019b). Therefore, the operating point could lie below the MCP; i.e., in the biphasic region. This effect is accentuated by increasing the drug concentration in the liquid solvent.

The morphology and the dimensions of SAS-processed particles obviously influence the dissolution of the active compound. As highlighted in various papers (Kim et al., 2008, Montes et al., 2016c, Ha et al., 2020, Liu et al., 2020), smaller particle size, having higher surface area, lead to an increase in the drug dissolution rate. However, many active compounds are not processable by SAS technique. In some cases, SAS micronization substantially fails since crystals precipitate (Miguel et al., 2006, Chang et al., 2008b, Wu et al., 2009, Bagratashvili et al., 2012, Zahran et al., 2014, Prosapio et al., 2016a) or, even, the active compound can be extracted by the solvent/antisolvent mixture formed in the precipitator (Prosapio et al., 2016b, Prosapio et al., 2017), not respecting the fundamental prerequisites of the SAS process. Nevertheless, different studies proved that it is possible to force the morphology and, consequently, modify the processability of these compounds not suitable for SAS micronization by their coprecipitation with a proper selected polymeric carrier (Zhang et al., 2009, Wu et al., 2009, Zhao et al., 2011a, Zahran et al., 2014, Prosapio et al., 2016b, Prosapio et al., 2017).

II.1.3 SAS coprecipitation polymer/active compound

Until now, the production of composite polymer/active compound particles was attempted by SAS process to treat different diseases or clinical conditions, including inflammations (Prosapio et al., 2016b, Zahran et al., 2014, Montes et al., 2014b), infections (Barrett et al., 2007, Montes et al., 2011, Uzun et al., 2011, Montes et al., 2012, Montes et al., 2013, Djerafi et al., 2017), asthma and allergies (Martin et al., 2002, Lee et al., 2010, Prosapio et al., 2016a), diabetes (Elvassore et al., 2001, Majerik et al., 2007, Jin et al., 2012), hypertension (Park et al., 2013, Ha et al., 2015a), and many others (Chen et al., 2006, Argemí et al., 2009, Kalantarian et al., 2011, Prosapio et al., 2015a, Ha et al., 2015c, Ha et al., 2015b, Alias et al., 2017). Different kinds of active principles, both with synthetic and natural origin, have been incorporated into polymeric particles. In particular, SAS particles loaded with natural active compounds have been often proposed as alternative therapies to conventional ones; e.g., for the prevention and treatment of tumors or cardiovascular diseases (Hu et al., 2012, Fernández-Ponce et al., 2015, Huang et al., 2016, Lestari et al., 2019, Chen et al., 2020). Carotenoids, phenols, and flavonoids belong to this category of compounds that offer numerous benefits for human health, given their antioxidant, anticancer, antimicrobial, and anti-inflammatory properties.

As occurs for the drug micronization, the coprecipitation of a polymer and an active principle by SAS technique offers many advantages if compared with conventional techniques, both in terms of morphology, mean size and PSD, as well as the control of drug dissolution (Won et al., 2005, Wu et al., 2009, Lee et al., 2010, da Fonseca Machado et al., 2018, Park et al., 2020).

Polymer/drug composites are produced for various purposes, but the main challenge is to suitably modify the dissolution kinetics of the active principles, aiming for excellent therapies. Depending on the medical application, different drug release kinetics can be required. The choice of the right polymeric carrier is strategic to release the drug at the desired time/speed and/or to a specific site of action. When a hydrophilic polymer is used as the carrier, the dissolution of the active principle contained in the SAS composite particles is enhanced. PVP belongs to this category of polymers; its use allowed to increase the dissolution rate of various poorly-water soluble active compounds (Park et al., 2013, Zahran et al., 2014, Prosapio et al., 2015a, Prosapio et al., 2015b, Prosapio et al., 2016a, Prosapio et al., 2016b, Park et al., 2017, Prosapio et al., 2017, Lestari et al., 2019, Chen et al., 2020, Machmudah et al., 2020). Conversely, the drug release is generally prolonged using a polymer with a hydrophobic behavior, as occurs by selecting PLA and PLLA (Martin et al., 2002, Chen et al., 2006, Patomchaivivat et al., 2008, Argemí et al., 2009, Wang et al., 2013, Montes et al., 2014a, Montes et al., 2014c, Yoshida et al., 2015, Lin et al., 2017, Cuadra et al., 2019), which, until now, have been mostly employed to deliver anticancer drugs.

However, it is necessary to identify and to use carriers that can be processed by the SAS technique. In addition to respecting the essential prerequisites of the SAS process, it has to be considered that the SAS coprecipitation seems to be effective when composite microspheres are obtained (Prosapio et al., 2018). As previously mentioned, the liquid jet break-up and the subsequent atomization quickly occur with respect to the surface tension vanishing in the case of the microparticles generation. As a consequence, the polymer and the active compound are entrapped in the same droplet, which behaves like an isolated reactor. The droplet drying by scCO₂ leads to the attainment of the composite microsphere. On the contrary, because of the very fast surface tension vanishing, nanoparticles precipitate by gas-to-particles nucleation and growth. In this case, it is highly likely that a sort of physical mixture at the nanometric level is obtained; i.e., polymer nanoparticles mixed with drug nanoparticles. Hence, the achievement of an effective coprecipitation polymer/active compound seems to be strongly influenced by the size and the morphology of the particles produced, as well as by their shape. Indeed, the coprecipitation basically fails also in the case of the attainment of crystals, which occurs by operating in the miscibility gap between the solvent and the antisolvent, where the two

compounds tend to precipitate separately resulting in polymer crystals and drug crystals.

Several papers showed that the selection of a proper carrier could force even the morphology of active principles that cannot be processed alone by the SAS technique (Wu et al., 2009, Zhang et al., 2009, Zhao et al., 2011a, Zahran et al., 2014, Prosapio et al., 2016b, Prosapio et al., 2017). Moreover, the entrapment of the active compound into the amorphous polymeric matrix can also favor the inhibition of the drug recrystallization (Lee et al., 2019).

Satisfactory results have been reached so far only with a reduced number of polymers, which are therefore identified as effective carriers for the SAS coprecipitation. PVP is currently the most used polymer and is considered one of the best carrier, since it often allowed to obtain regular and spherical composite particles and to inhibit the drug recrystallization (Majerik et al., 2007, Uzun et al., 2011, Park et al., 2013, Zahran et al., 2014, Prosapio et al., 2015a, Prosapio et al., 2015b, Machmudah et al., 2020, Prosapio et al., 2016a, Prosapio et al., 2016b, Prosapio et al., 2017, Park et al., 2017, Chhouk et al., 2018, Matos et al., 2019, Lestari et al., 2019, Chen et al., 2020). PVP is followed by PLA and PLLA that are also suitable carriers often employed (Elvassore et al., 2001, Chen et al., 2006, Kalogiannis et al., 2006, Miguel et al., 2008, Patomchaivivat et al., 2008, Argemí et al., 2009, Guha et al., 2011, Li et al., 2012, Jung et al., 2012, Wang et al., 2013, Montes et al., 2014a, Montes et al., 2014c, Yoshida et al., 2015, Lin et al., 2017, Alias et al., 2017, Liu et al., 2019). SAS coprecipitation was attempted with other categories of polymers, such as polyethylene glycol, poly(lactide-co-glycolide), ethyl cellulose, hydroxypropylmethyl cellulose and poly(hydroxybutyrate-co-hydroxyvalerate), however showing unsatisfactory results (Barrett et al., 2007, Majerik et al., 2007, Franceschi et al., 2010, Montes et al., 2011, Lang et al., 2012, Montes et al., 2012, Jin et al., 2012, Montes et al., 2013, Boschetto et al., 2013, Park et al., 2013, Boschetto et al., 2014, Fernández-Ponce et al., 2015, Ha et al., 2015a, Ha et al., 2015c, Machado et al., 2016, Djerafi et al., 2017). Conversely, although they need to be further investigated, some carriers were identified as interesting for SAS coprecipitation, namely zein (Zhong et al., 2008, Zhong et al., 2009, Liu et al., 2016), Eudragit (Montes et al., 2014a, Montes et al., 2014c, Montes et al., 2016b) and β -CD (Lee et al., 2010, Nerome et al., 2013, Jia et al., 2018).

Zhong et al. (Zhong et al., 2008) reported SAS experiments on zein, a storage protein in corn endosperm classified as 'Generally Recognized as Safe' (GRAS) by the US Food and Drug Administration. Mixtures ethanol-water (water 10 % v/v) and methanol were used for the zein micronization. In the first case, they obtained very large collapsed microparticles; in the second case they produced nanoparticles. In a subsequent work, Zhong et al. (Zhong et al., 2009) used zein as a carrier to try to coprecipitate lysozyme by SAS using 90% ethanol in water as the liquid solvent. The presence of 10% w/w water at the adopted SAS conditions does not allow complete

miscibility between the liquid mixture and scCO₂; therefore, conditions for a fully successful SAS were not obtained, and irregular particles with internal pores were produced. However, the authors observed an improvement in the drug release rate, which appears to be prolonged/sustained. Liu et al. (Liu et al., 2016) tried to apply SAS process to incorporate 10-hydroxycamptothecin in zein microspheres, but coprecipitation failed. Field Emission Scanning Electron Microscopy (FESEM) showed that crystals of active compound and zein precipitated separately. Summarizing the previous works (Zhong et al., 2008, Zhong et al., 2009, Liu et al., 2016), some attempts to use zein in SAS coprecipitation were substantially unsuccessful, but zein alone seems to be processable (Zhong et al., 2008).

Very few studies were also focused on the use of Eudragit polymers, although they are really interesting from a pharmaceutical point of view. They offer moisture protection, odor/taste masking, in addition to their versatility that offer a targeted drug release, being pH-sensitive polymers that dissolve at specific pH values. Among the various kinds of Eudragits on the market, Eudragit RS100 and Eudragit RL100 revealed to be not suitable for SAS process (Duarte et al., 2007). Instead, Montes et al. tried to coprecipitate Eudragit L100 with ibuprofen (Montes et al., 2014a) and naproxen (Montes et al., 2014c) by SAS process. They obtained particles Eudragit L100/ibuprofen and Eudragit L100/naproxen with mean size respectively in the range 0.08 - 0.51 μm and 0.08 - 0.31 μm . Because of the nanometric/sub-micrometric particle size that did not allow a massive coprecipitation polymer/drug, low loading efficiencies were achieved (0.94-7.88 % for ibuprofen and 4.45-25.55 % for naproxen). Similar results were obtained in another study (Montes et al., 2016b), coprecipitating ellagic acid and Eudragit L100 at different polymer/drug ratios. It was observed that crystals precipitated working with Eudragit L100/ellagic acid ratios equal to 1/1 and 2/1, whereas coalescent sub-microparticles precipitated using a polymer/drug ratio of 4/1. It is clear that SAS coprecipitation using Eudragits as carriers is still not satisfactory, but Eudragit L100 seems to be processable. Similar to Eudragit L100, Eudragit L100-55 differs from the previous one only for the presence of a methyl group instead of an ethyl group, which influences the slightly different dissolution pH threshold of the two polymers. Eudragit L100-55 is soluble at pH higher than 5.5, corresponding to the first intestinal tract (duodenum), thus the active compound is protected against the acid gastric fluid; in the meanwhile, the side effects on the gastric tract are also avoided.

In the case of the coprecipitation, the polymer/drug ratio plays a crucial role in the attainment of composite particles. In addition to particles morphology, the polymer content strongly affects the dissolution rate; in general, the release of the active compound is mostly modified by increasing the polymer/drug ratio (Ha et al., 2015b, Won et al., 2005, Patomchaivivat et al., 2008, Jung et al., 2012, Montes et al., 2014a, Machmudah et al.,

2020). Aiming to obtain spherical microspheres that guarantee an effective coprecipitation, in some cases, it is not possible to reduce the amount of polymer in the composite particles beyond a specific value. A high polymer content in the pharmaceutical formulations can be a limitation of the SAS coprecipitation when some carriers are employed. Alternatively, a high amount of carrier in the SAS coprecipitated powders seems to be avoided by selecting cyclodextrins (CDs), which are oligosaccharides (Lee et al., 2010, Nerome et al., 2013, Jia et al., 2018, Jun et al., 2007, Zhou et al., 2012, Huang et al., 2016, Sun et al., 2019).

In general, CDs are characterized by a hydrophilic external surface, which makes them very soluble in water, and a hydrophobic internal cavity, in which various molecules can be incorporated to form guest/host inclusion complexes by non-covalent interactions. A limited number of papers has been focused on the application of the SAS technique to prepare inclusion complexes by using CDs as the carrier (Lee et al., 2010, Nerome et al., 2013, Jia et al., 2018, Jun et al., 2007, Zhou et al., 2012, Huang et al., 2016, Sun et al., 2019). The production of CDs-based inclusion complexes by SAS technique has been proposed mainly to mask the bitter taste and/or to increase the dissolution of various active compounds, such as antioxidants, antihistamine drugs, antibiotics, and others. Lee et al. (Lee et al., 2010) chose the β -CD to mask the bitter taste of an antihistamine drug; i.e., cetirizine dihydrochloride. They compared the large and irregular crystals produced by the freeze-drying method with the regular and spherical particles prepared by the SAS technique, at cetirizine/ β -CD molar ratios equal to 1/3, 1/2 and 1/1. Nevertheless, the dissolution kinetics of the cetirizine released from all the obtained complexes, including the ones obtained using the SAS process, were similar to those of the unprocessed drug. Nerome et al. (Nerome et al., 2013) produced spherical nanoparticles/submicroparticles by coprecipitating lycopene and β -CD using $scCO_2$ as antisolvent in the SEDS process. However, no dissolution studies were performed to highlight the eventual possible differences in the dissolution kinetics of lycopene when pure and when released from the β -CD-based complexes. Jia et al. (Jia et al., 2018) used SEDS to obtain microparticles and nanoparticles of berberine/ β -CD with improved dissolution properties. Crystals and big particles with holes (size up to about 80 μ m) were instead obtained by Sun et al. (Sun et al., 2019) by preparing tosylloxacin tosylate/hydroxypropyl- β -cyclodextrin (HP- β -CD) complexes with the supercritical antisolvent technique. Similarly, HP- β -CD was employed to prepare inclusion complexes by SAS also in other papers (Jun et al., 2007, Huang et al., 2016, Zhou et al., 2012), in order to increase the dissolution rate of the simvastatin (an anti-cholesterol agent), apigenin (a flavonoid), and resveratrol (a phenol). In all these cases, the results were not good in terms of morphology; indeed, aggregated or coalescent drug/HP- β -CD particles were produced. However, in these studies, an improvement in

the dissolution rate was shown with respect to the unprocessed drugs. In general, in these papers, the formation of complexes was demonstrated by the shift, the total or the partial disappearance of the characteristic bands/peaks of the drug in the Fourier-transform infrared (FTIR) spectra (Jun et al., 2007, Lee et al., 2010, Zhou et al., 2012, Huang et al., 2016, Sun et al., 2019) or differential scanning calorimetry (DSC) thermograms (Jun et al., 2007, Zhou et al., 2012, Huang et al., 2016) of the composite powders drug/CDs. Any changes in the X-ray diffraction (XRD) patterns were also associated with the interactions between the active compound and the CD in the inclusion complexes (Lee et al., 2010).

In summary, irregular and coalescent particles or even aggregates/crystals were obtained by coprecipitating an active compound with HP- β -CD as carrier via the SAS process. On the contrary, in the papers of Lee et al. (Lee et al., 2010), Nerome et al. (Nerome et al., 2013), and Jia et al. (Jia et al., 2018), regular drug-loaded particles using β -CD as the carrier were produced. Therefore, although it is practically unexplored, the use of β -CD seems to be more promising to obtain a regular and spherical morphology. However, a marked improvement in the dissolution rate of the active compounds from β -CD was reported only in one of the papers published using β -CD as the carrier (Jia et al., 2018). Therefore, a key role of β -CD in increasing the dissolution of drugs from SAS complexes has only been sporadically proven; thus, its application as an effective carrier for SAS coprecipitation has to be validated.

It is worth nothing that the use of cyclodextrine derivatives (HP- β -CD for instance) has been often proposed because β -CD can be toxic for the kidney and can show nephrotoxicity in case of parenteral administration or by nasal route (Stella and Rajewski, 1997, Mammucari et al., 2006). However, β -CD is considered safe, and therefore approved, for oral administration.

II.2 State of the art of supercritical impregnation

Among the different techniques employed to fabricate polymer/active compound composites, the impregnation using scCO₂, also known as supercritical impregnation, is an innovative environmentally friendly technology. Briefly, the active compound is firstly dissolved in scCO₂, then this mixture is put in contact with a polymeric support, which has to be impregnated.

Conventional techniques used to incorporate drugs into matrices have some drawbacks, mainly related to the use of organic solvents and high process temperatures employed to remove them, leading to a possible thermal degradation of thermosensitive compounds. As a result, the functional properties of the active compounds can be compromised. Moreover, the partial volatilization of the active principle with the solvent used and the low penetration of the liquid solutions (organic solvent+drug)

in the polymeric substrate often lead to low loading efficiencies. These limitations can be overcome by solvent-free supercritical impregnation (Caputo et al., 2012, García-González and Smirnova, 2013). Indeed, scCO₂ features allow to operate at low temperatures, without altering the drug properties. In addition, its near-zero surface tension and high diffusivity enable its rapid penetration within polymeric matrices, avoiding pore collapse that generally occurs using liquid solvents, due to the capillary stress caused by the liquid-vapour meniscus within each pore. In the supercritical impregnation, scCO₂ acts as solvent for the solute to impregnate and as plasticizing and swelling agent for polymers (Kikic and Vecchione, 2003). These latter characteristics further favor the loading of the active compound in the polymeric matrix. Another interesting aspect in the use of scCO₂ is its ability to foam some kinds of polymers under certain conditions (Reverchon and Cardea, 2007, Tsivintzelis et al., 2007, Tsivintzelis et al., 2016). The scCO₂-assisted foaming promotes the formation of porosities in the polymeric support, favoring the loading of the active compound in the solid substrate and prompting the use of polymeric foams for drug controlled release formulations (Di Maio and Kiran, 2018). Dimensions and morphology of the produced pores depend on the gas concentration, the diffusivity of scCO₂ in the polymer, the interfacial tension of the polymer/CO₂ solutions in contact with scCO₂, and how the transition temperatures of the polymer, its plasticization/vitrification or melting/crystallization processes and its rheological properties are affected both during the sorption and during the decompression step (Curia et al., 2015). At a fixed temperature, a faster depressurization promotes the formation of smaller pore sizes or higher cell number densities. On the other hand, fixing a certain depressurization rate, higher temperatures generally lead to the formation of larger pores (Kiran, 2010).

It is clear that the supercritical impregnation of a certain active principle into a polymeric matrix is strongly affected by the interaction between active compound/scCO₂/polymeric substrate (Kikic and Vecchione, 2003). The first fundamental pre-requisite is obviously the drug solubility in scCO₂, followed by the structure/morphology of the support and the polymeric materials it is made of.

Different kinds of materials have been incorporated into various solid substrates, ensuring the effectiveness of the supercritical impregnation (Guney and Akgerman, 2002, Smirnova et al., 2003, Smirnova et al., 2005b, Yoda et al., 2011, Masmoudi et al., 2011, Caputo et al., 2012, Champeau et al., 2015, De Marco and Reverchon, 2017, Mir et al., 2017, Bastante et al., 2017). Polymeric aerogels are among the best supports for the impregnation of active compounds, since the very high porosity and the high specific surface area allow high drug loadings. Unlike other drying techniques (Glenn and Irving, 1995, García-González et al., 2011, Cardea et al., 2013, De Marco et al., 2015a, Baldino et al., 2016), the gel drying using scCO₂

stands out to produce aerogels that preserve the native porous structure, avoiding its collapse. Caputo et al. improved the dissolution rate of nimesulide (Caputo et al., 2012) and domperidone (Caputo, 2013), two poorly water soluble drugs, through their supercritical impregnation in silica aerogel, producing orodispersible tablets. Similarly, Smirnova et al. (Smirnova et al., 2003, Smirnova et al., 2005b) studied the supercritical impregnation of ketoprofen and griseofulvin in hydrophilic silica aerogels for the drug delivery by oral route. A rapid release of both the active principles was reached. In another study, Smirnova et al. (Smirnova et al., 2005a) enhanced the dissolution rate of other active principles (i.e., miconazole, dithranol, flurbiprofen and ibuprofen) by loading them in hydrophilic silica aerogels. The impregnation of ketoprofen was investigated both in hydrophilic and in hydrophobic silica aerogels. When hydrophobic aerogels were used as supports, after an initial burst-like effect, due to the dissolution of the drug molecules on/near the aerogel surface, a slower release of the active principle located into the aerogel pores was observed. The slow drug dissolution was attributed to the diffusion mechanism, which, in this case, is the controlling phenomenon due to the high stability of the hydrophobic aerogels in water. The release rate of an active compound from aerogel-based formulations seems to be influenced by the hydrophobicity of the aerogel, in addition to the dimensions of pores.

Recently, the use of biocompatible materials that are also biodegradable, such as polysaccharides, is increasingly required. In this context, biodegradable aerogels were applied as matrices for the supercritical impregnation of active compounds in some studies (De Marco and Reverchon, 2017, Pantić et al., 2016). For example, the bioavailability of some fat-soluble vitamins, namely α -tocopherol (vitamin E) and menadione (vitamin K3), was enhanced by adsorbing them onto MSA (De Marco and Reverchon, 2017). In particular, the dissolution rate was increased up to 16 times and 3.5 times for vitamin K3 and vitamin E, respectively and 16 times. In another study (Pantić et al., 2016), vitamin K3 and cholecalciferol (vitamin D3) were incorporated in alginate aerogels. The contact time between the drug dissolved in scCO₂ and the polymeric support was indicated as one of the most critical and important parameters of the supercritical impregnation process. From the literature studies (Caputo et al., 2012, De Marco and Reverchon, 2017, Smirnova et al., 2005a), it emerged that the loading of the active compound into the aerogels also depends on the support features, the drug concentration in the supercritical phase, the temperature and the pressure. In particular, these last two parameters have an influence on the solubility of the active principle in the scCO₂, which is fundamental for an effective supercritical impregnation. Indeed, it has always to be considered that both the thermodynamics and the kinetics control the impregnation process.

In summary, the literature focused on the supercritical impregnation of active principles into biodegradable matrices, such as polysaccharide-based aerogels, for the oral drug delivery is still limited to a few papers. Moreover, the role of aerogels based on hydrophilic or hydrophobic polymers in modifying the drug release kinetics has to be further investigated. However, the drug impregnation into polysaccharide-based aerogels seems to be really interesting for the production of drug-loaded ODTs without solvent residues. For this purpose, among various polysaccharides, starch and alginate are promising.

Another poorly explored aspect is the supercritical impregnation of active compounds into polymeric films. This topic was attempted in a few studies mainly for food packaging applications (Rojas et al., 2015, Medeiros et al., 2017, Villegas et al., 2017, Cejudo Bastante et al., 2017, Belizón et al., 2018, Milovanovic et al., 2018), but sporadically in the pharmaceutical field; e.g., recently for the production of antibacterial films (Zizovic, 2020).

However, the thin films have gained increasing interest as emerging support for the development of transdermal patches. Drug-loaded films allow a targeted release, which is often not possible with liquid formulations, tablets, or traditional oral administration (Mandeep et al., 2013, Karki et al., 2016). Medicated patches are well-accepted by patients, due to their flexibility as well as the reduced thickness and encumbrance of the polymeric films. These non-invasive formulations offer numerous advantages, such as easy handling during manufacture and transportation and moderate costs in the development of the formulations. However, an ideal film has to possess some peculiar properties, such as sufficient drug loading capacity, formulation stability, and relatively long residence time in the site of administration. It has obviously to be non-toxic and biocompatible. Considering these premises, it would be worth combining the advantages of using the thin films and the supercritical impregnation to produce excellent and eco-friendly topical formulations, characterized by a controlled drug release and reduced side effects associated with the oral administration.

Chapter III

Analytical methods

III.1 Field Emission Scanning Electron Microscopy

The morphology of the composite systems was observed by a field emission-scanning electron microscope (FESEM, mod. LEO 1525, Carl Zeiss SMT AG). The samples were dispersed on a carbon tab, previously stuck on an aluminum stub (Agar Scientific, Stansted), and coated with gold (layer thickness 250Å) using a sputter coater (mod. B7341, Agar Scientific Stansted). PSDs of SAS-produced particles were determined by FESEM photomicrographs using Sigma Scan Pro Software (release 5.0 Aspire Software international, Ashburn, VA, USA). The diameters of about 1000 particles were measured for each PSD. The obtained data were statistically analyzed by Microcal Origin Software (release 8.0, Microcal Software, Inc., Northampton, MA). FESEM photomicrographs, Sigma Scan Pro Software and Microcal Origin Software were also used to determine the pore size distributions of aerogels and foams, in terms of mean pore size and standard deviation.

III.2 Determination of the specific surface area

Brunauer, Emmett and Teller (BET) surface areas of the aerogels were calculated from dynamic N₂ adsorption measurement at -196 °C by using a Costech Sorptometer 1042 (Costech International S.p.A., Milan, Italy); the samples (about 0.2 g) were previously degassed at 40 °C for 16 h.

III.3 Fourier Transform Infrared (FTIR) Spectroscopy

The FTIR spectra of the samples were obtained by a FTIR spectrophotometer (IR-Tracer100, Shimadzu). The samples (about 1 mg) were ground and mixed thoroughly with 100 mg of potassium bromide (KBr) and pressed through a manual press. The analyses were performed on previously prepared discs in a range of wavenumbers between 4000 and 450

cm^{-1} , at a resolution of 1 cm^{-1} ; 32 scan signals were averaged to reduce the noise of the measurements.

III.4 Differential Scanning Calorimetry

The thermal behavior of the composite samples was studied by a Differential Scanning Calorimeter (DSC, model TC11, Mettler Toledo, Inc., Columbus, USA), using Mettler STARe system. Approximately 5 mg of each sample were crimped into an aluminum pan, then heated from 25°C to the desired temperature at $10^\circ\text{C}/\text{min}$, under a nitrogen purge (flow rate 50 mL/min).

III.5 X-Ray Diffraction

Solid state analyses were performed on the samples using a X-ray diffractometer (XRD, mod. D8 Discover, Bruker AXS, Inc., Madison, WI) with a Cu sealed tube source. Samples were placed in the holder and flattened with a glass slide, to assure a good surface texture. The measuring conditions were as follows: Ni-filtered $\text{CuK}\alpha$ radiation, $\lambda=1.54 \text{ \AA}$, with a scan rate of 0.5 s/step and a step size of 0.08° .

III.6 UV-vis spectroscopy

The drug loadings and the dissolution tests of the active compounds from composite systems were performed by a UV-vis spectrophotometer (model Cary 50, Varian, Palo Alto, CA). The absorbance was measured at the characteristic wavelength of each active compound, reported in **Table III.1**.

Table III.1 *Characteristic wavelengths of the selected active compounds.*

Active compound	Characteristic wavelength
Amoxicillin	224 nm
Ampicillin sodium	220 nm
Cetirizine dihydrochloride	230 nm
Diclofenac sodium	276 nm
Ketoprofen	262 nm
Ketotifen fumarate	297 nm
Mesoglycan	206 nm
Nimesulide	245 nm
Rutin	257 nm
Theophylline	271 nm

A calibration curve was previously determined to convert the absorbance into drug concentration. Dilute solutions, which consisted of the drug

dissolved into the selected dissolution medium, were used to determine the calibration curve, in order to be able to apply the Beer–Lambert law in the following form:

$$A = \varepsilon l c \quad (1)$$

where A is the absorbance, ε is the characteristic molar attenuation coefficient for each substance, l is the optical path length (cm), c is the solution concentration.

Consequently, the dissolution tests were also conducted using solutions at low concentrations of active compound, to determine the improvement in terms of the dissolution rate of the drug in pure form or released from composite systems produced by the supercritical techniques.

Based on the specific pharmaceutical application and the active compound studied, the release tests were conducted in phosphate buffer solution (PBS) at pH 7.4 or hydrochloric acid (HCl) 0.1 M solution (pH 2.5), as dissolution media. The dissolution medium selected for each active compound was in agreement with the literature. Accurately weighted samples containing an equivalent amount of active compound (in the range 5-20 mg) were suspended in 3 mL of PBS/HCl solution into a dialysis membrane (12-14000 Daltons) or placed in a filter paper, based on the size of the drug molecules. Then, the system containing the composite was immersed in 250-300 mL of the dissolution medium, continuously stirred at 150 rpm and heated at 37°C. The specific amounts of active compound and dissolution medium for the drug release tests were chosen based on calibration curves previously determined for each system drug/dissolution medium. Each dissolution test was carried out in triplicate and the mean release profiles are reported in this work. The drug loadings were evaluated considering the absorbance measured at the end of the dissolution test; i.e., when all the active compound was released from the composites to the external dissolution medium. The absorbance was converted to the drug concentration using the calibration curve. In the specific case of SAS particles, the entrapment efficiency (EE%) was calculated as the ratio between the effective loading evaluated by UV-vis spectroscopy and the theoretical loading, namely the amount of active principle in the solution injected into the SAS plant, as follows:

$$EE\% = \frac{\text{mg drug in the SAS sample}}{\text{mg drug in the initial solution}} \cdot 100 \quad (2)$$

Chapter IV

SAS coprecipitation carrier/active compound

IV.1 Introduction

Nowadays, the main challenge in the pharmaceutical field is to tune the release of an active compound depending on the specific medical application, improving the therapeutic efficacy and reducing the side effects.

About 40% of the active compounds on the market is classified as “poorly water-soluble” (Jermain et al., 2018). Among the different approaches mentioned in the Introduction section, particle size reduction with the aid of hydrophilic polymeric carriers is a valid answer to enhance the dissolution rate and, consequently, the bioavailability of poorly water-soluble compounds.

Another current issue with many drugs that are taken orally is that they only work for a limited time or pass quickly through the body. In some cases, repeated doses are required for the drug to be effective, thus the difficulty is getting patients to take medication daily. It is well known that only about 50% of patients take their medication as prescribed; a trivial example is remembering to take medicine. Hence, one of the goals is also to make it easier. The strategy of producing composite microparticles is a useful tool to prolong the dissolution rate of frequently taken drugs, for which long-term therapies are generally prescribed.

The aim of this part of work was to assert the role of some polymers as novel effective carrier for SAS coprecipitation. Firstly, some sets of experiments with the well-established PVP were also performed. Then, the applicability of zein, Eudragit L100-55 and β -cyclodextrin in the production of coprecipitates by SAS process was tested. The role of hydrophilic or hydrophobic carriers to accelerate or to prolong the drug release was also highlighted. In this context, the dissolution of antibiotics, such as amoxicillin and ampicillin, which generally require long-term therapies, was prolonged using hydrophobic carriers. Similarly, alternative extended-release

formulations containing bronchodilators (i.e., theophylline) or antihistamines (i.e., cetirizine and ketotifen) were also proposed. On the other hand, NSAIDs-based microparticles, both at fast and prolonged release, were produced to treat inflammations like headaches or toothache (e.g., using ketoprofen or nimesulide), or chronic rheumatoid arthritis or osteoarthritis (e.g., using diclofenac). In the framework of proposing alternative formulations, SAS coprecipitation was also attempted with a “natural drug” namely rutin, a flavonoid also defined as vitamin P. This natural compound offers numerous benefits for the human health, including antioxidant, anti-inflammatory, antiviral, antidiabetic and anticancer activities, in addition to being useful in the treatment of cardiovascular disease, venous insufficiency and capillary impairment (Erlund et al., 2000, Yang et al., 2008a, Cazarolli et al., 2008, Ganeshpurkar and Saluja, 2017). Rutin is also widely exploited against the hair follicle degeneration (preventing the causes of baldness), for the promotion of the collagen synthesis and its anti-fatigue activity, as well as the sunscreen effect (Carelli et al., 2012, Ganeshpurkar and Saluja, 2017).

With regards to the particles produced by SAS process, the classification of powders as nanoparticles for mean diameters less than 0.2 μm , sub-microparticles for mean diameters ranging from 0.2 and 0.4 μm and microparticles for mean diameters larger than 0.4 μm was proposed.

IV.1.1 Materials

Ampicillin sodium salt (AMPI, average molecular weight 371.39 g/mol), cetirizine dihydrochloride (CTZ, purity $\geq 98\%$), diclofenac sodium salt (DIC, average molecular weight 318.13 g/mol), ketoprofen (KET, purity $\geq 98\%$), ketotifen fumarate salt (KTF, purity $\geq 99\%$), nimesulide (NIM, purity 98%), rutin hydrate (RUT, purity 95%), anhydrous theophylline (THEOP, average molecular weight 180.16 g/mol), polyvinylpyrrolidone (PVP, average molecular weight 10,000 g/mol), zein (CAS Number: 9010-66-6, water content $< 8\%$), and dimethylsulfoxide (DMSO, purity 99.5 %) were supplied by Sigma-Aldrich (Italy). Amoxicillin trihydrate (AMOXI, average molecular weight 419.45 g/mol) was supplied by Virbac (Milan, Italy). Eudragit L100-55 (EUD) was generously donated by Degussa (Darmstadt, Germany). Hydrochloric acid (HCl, 37%) was purchased from Carlo Erba Reagents. Distilled water was obtained using a laboratory water distiller supplied by ISECO S.P.A. (St. Marcel, AO, Italy). Carbon dioxide (CO_2 , purity 99 %) was purchased from Morlando Group s.r.l. (Italy).

IV.1.2 SAS apparatus and procedure

The homemade SAS laboratory plant is sketched in **Figure IV.1**. It consists of two high pressure pumps to feed the CO_2 and the liquid solution containing the solute/solutes to be micronized, respectively. The

precipitation chamber is a cylindrical vessel with an internal volume of 500 cm³. The temperature control is assured by a proportional integral derivative (PID) controller connected with electrically thin bands, whereas the pressure in the vessel is measured using a test gauge manometer and regulated by a micrometering valve. The liquid solution is injected in the precipitator through a thin wall, 100 μm internal diameter stainless steel nozzle. The CO₂ is instead pre-cooled through a refrigerating bath and, after a preheating, it is delivered to the chamber through another port. A stainless steel filter with a pore diameter of 0.1 μm, located at the bottom of the precipitator, is used to collect the produced powder and allows the CO₂-solvent mixture to pass through. The liquid solvent is then recovered in a second collection vessel, which is located downstream the precipitator at a lower pressure (about 2 MPa) regulated by a backpressure valve. At the exit of the second vessel, the CO₂ flow rate and the total quantity of antisolvent delivered are measured by a rotameter and a dry test meter, respectively.

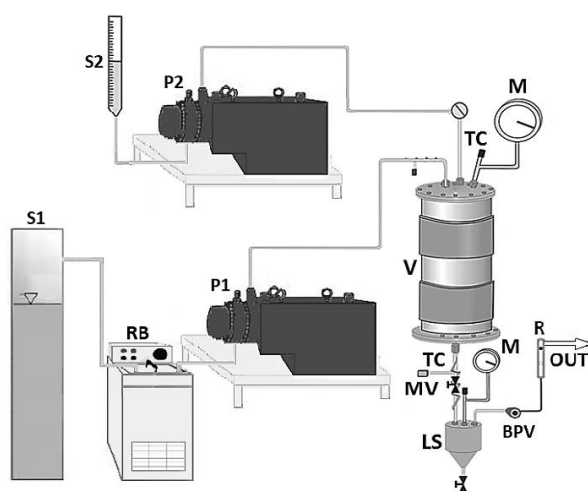


Figure IV.1 Schematic representation of SAS laboratory plant. S1: CO₂ supply; S2: liquid solution supply; RB: refrigerating bath; P1, P2: pumps; M: manometer; V: precipitation chamber; MV: micrometering valve; LS: liquid separator; R: rotameter; BPV: back pressure valve.

A typical SAS test starts pressurizing the precipitator with CO₂ until the desired pressure and temperature are reached. Then, the pure solvent is sent through the nozzle to obtain a quasi-steady state composition of solvent and antisolvent inside the chamber. Afterwards, the liquid solution is delivered to the precipitator, producing the precipitation of the solute/solutes. At the end of the solution injection, scCO₂ continues to flow to completely remove the solvent residues. When the washing step is completed, CO₂ flow is stopped, the precipitator is depressurized down to atmospheric pressure and the precipitated powder can be collected and characterized.

IV.2 The use of PVP as polymeric carrier

To date, PVP is considered one of the best polymeric carriers for SAS coprecipitation, as highlighted in the ‘Introduction’ section. In the first part of this Ph.D. work, PVP was applied to increase the dissolution rate of a model NSAID and of a natural compound; i.e., KET and RUT, respectively.

For all the following SAS tests focused on the use of PVP, DMSO was used as liquid solvent and temperature, liquid solution flow rate and CO₂ flow rate were fixed at 40°C, 1 mL/min and 30 g/min, respectively. As mentioned in the ‘State of the art’ section, these conditions were chosen according to previous studies conducted on PVP, in order to assure the supercritical mixture conditions working at molar fractions on the right of the MCP of the selected couple solvent-antisolvent (i.e., about 0.98). The effect of other parameters on the morphology and size of the particles produced was investigated.

IV.2.1 PVP/ketoprofen coprecipitation

The operating pressure (P), concentration of solutes in the liquid solution (C_{tot}) and polymer/drug (w/w) ratio were varied to investigate the influence of these parameters on morphology and size of PVP/KET coprecipitates. In **Table IV.1**, a summary of the most significant tests performed is reported, indicating the PVP/KET ratio, the pressure, the total concentration in DMSO, as well as the morphology (M), mean diameter (m.d.) and standard deviation (s.d.) of particles produced.

Table IV.1 Summary of SAS experiments performed on PVP/KET (MP: microparticles; cSMP: coalescing sub-microparticles; C: crystals).

#	PVP/KET (w/w)	P (MPa)	C _{tot} (mg/mL)	M	m.d.±s.d. (µm)
1	1/0	9	40	MP	4.05±2.67
2	0/1	9	20	cSMP	0.30±0.12
3	20/1	9	20	MP	3.60±1.99
4	20/1	12	20	MP	2.97±1.65
5	20/1	15	20	MP	2.41±1.29
6	20/1	9	10	MP	3.09±1.38
7	20/1	9	50	MP	3.81±2.01
8	20/1	9	100	C	-
9	3/1	9	50	MP	3.10±1.51
10	5/1	9	50	MP	3.21±1.77
11	10/1	9	50	MP	3.44±1.88

Preliminary experiments (runs # 1 and #2 in **Table IV.1**) were performed precipitating the polymer and the drug separately, at 9 MPa and 40°C. In the case of the polymer, well-separated microparticles (**Figure IV.2a**) with a mean diameter equal to $4.05 \pm 2.67 \mu\text{m}$ were precipitated. In the case of KET, a small amount of powder in form of coalescing sub-microparticles (**Figure IV.2b**) was recovered from the filter at the bottom of the precipitation chamber, whereas the remaining part of the drug was extracted by the mixture formed by the scCO₂/DMSO.

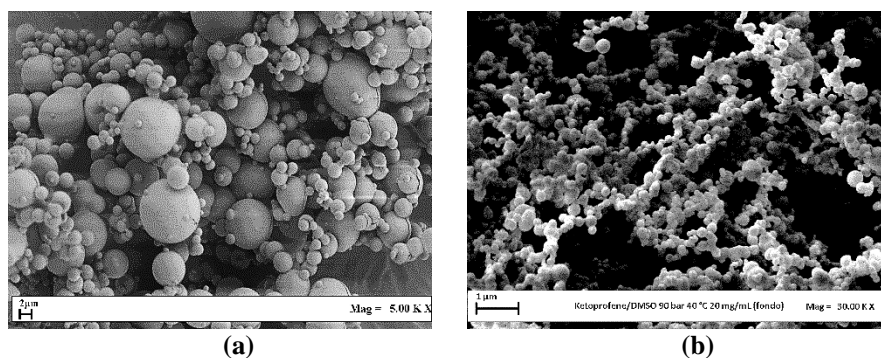


Figure IV.2 FESEM images of SAS precipitated powders from DMSO at 9 MPa and 40°C. (a) PVP microparticles; (b) KET coalescing sub-microparticles.

Then, PVP/KET coprecipitation was attempted in correspondence of different operating conditions of pressure, overall concentration and polymer/drug ratio, as follows.

Effect of the operating pressure

For the first set of coprecipitation experiments, PVP/KET ratio was fixed at 20/1 and the total concentration in DMSO at 20 mg/mL. Three values of pressure were investigated: 9, 12 and 15 MPa (runs #3, #4 and #5 in **Table IV.1**). At all the pressure values, spherical microparticles were obtained, as shown in **Figure IV.3**, where three exemplificative FESEM images are reported. From the comparison between the volumetric cumulative PSDs obtained at different pressures, it was possible to deduce that, increasing the pressure, the mean diameter decreased whereas the PSD shrank.

A consideration can be immediately made observing these results: the attainment of microparticles at 9 MPa was expected, because this pressure value is in the proximity of the MCP of the binary system solvent-antisolvent; in the range 12-15 MPa, nanoparticles would have been precipitated (De Marco and Reverchon, 2011). Indeed, the operating point should be located well above the MCP; consequently, the solutes were expected to precipitate for nucleation and growth, in analogy with the gas-to-particle formation in form of nanoparticles. However, PVP tends to force the

overall coprecipitation and produces micrometric particles, even if the operating pressure is well above the binary mixture MCP (Prosapio et al., 2018), as observed also when it was coprecipitated with other active compounds (De Marco et al., 2015b).

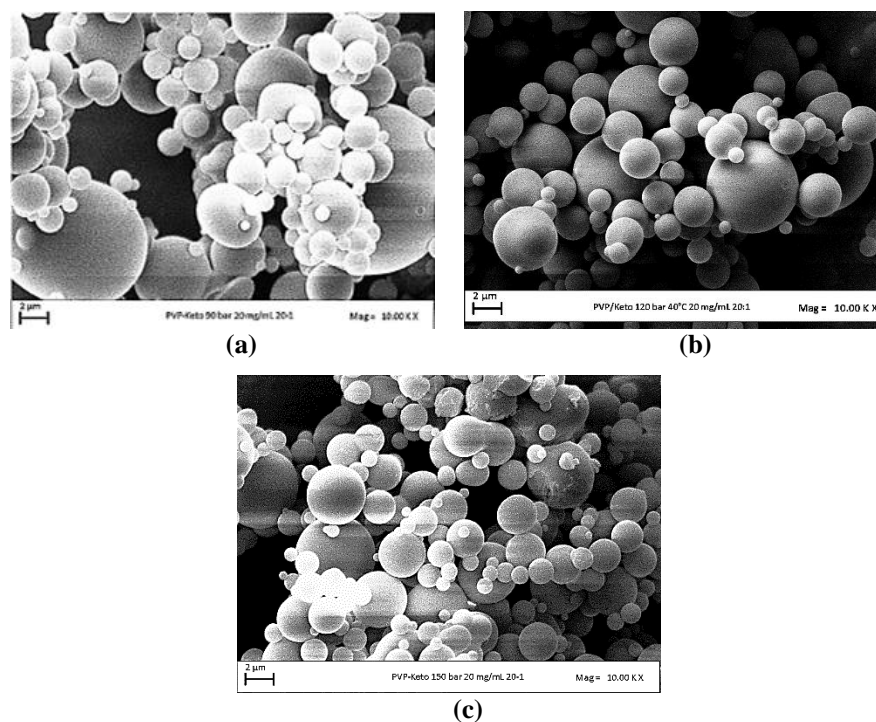


Figure IV.3 FESEM images of PVP/KET 20/1 microparticles coprecipitated from DMSO at 40°C and 20 mg/mL. Effect of operating pressure: (a) 9 MPa; (b) 12 MPa; (c) 15 MPa.

Effect of the overall concentration

The effect of the total concentration of solutes dissolved in DMSO was evaluated, in this set of experiments; the PVP/KET ratio, as in the previous set of experiments, was fixed at 20/1, whereas the chosen pressure was 9 MPa. The overall concentration was varied in the range 10-100 mg/mL (runs #6, #3, #7 and #8 in **Table IV.1**). At 10, 20 and 50 mg/mL, well-separated microparticles with mean diameters in the range 3.09-3.81 µm were produced, whereas irregular crystals were obtained at 100 mg/mL. FESEM images of PVP/KET system precipitated from solutions at various concentrations are shown in **Figure IV.4**.

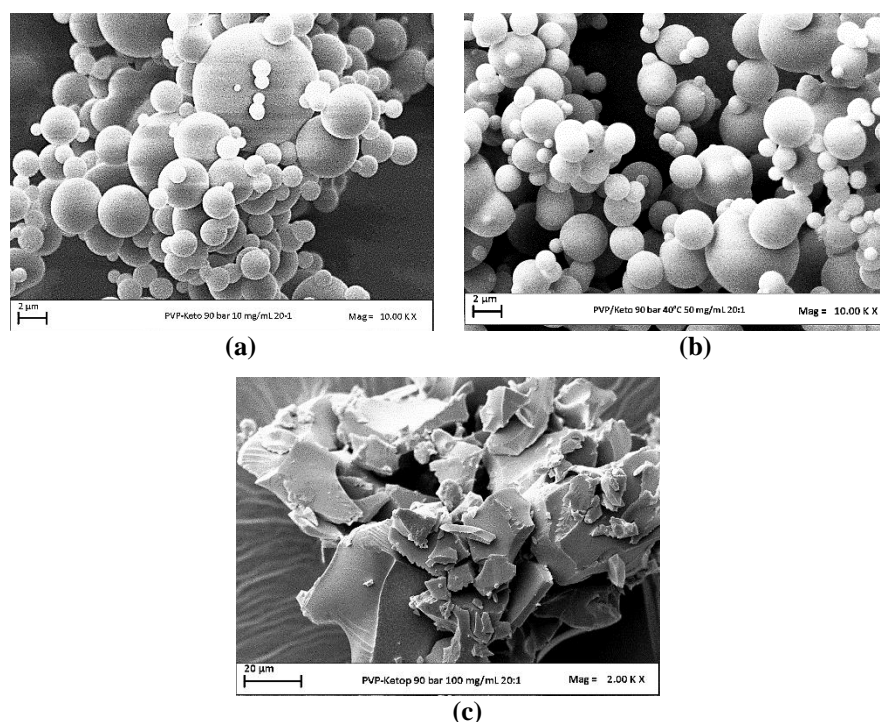


Figure IV.4 FESEM images of PVP/KET 20/1 microparticles coprecipitated from DMSO at 9 MPa and 40°C. Effect of overall concentration: (a) 10 mg/mL; (b) 50 mg/mL; (c) 100 mg/mL.

The presence of crystals in correspondence of 100 mg/mL may be explained using thermodynamic considerations. The MCP of the binary system DMSO/CO₂ is located at 8.6 MPa at 40°C (Andreatta et al., 2007a); thus, the operating point at 9 MPa was theoretically above the MCP. However, the addition of one or more solutes can modify the high-pressure VLEs of the system; therefore, the MCP of the quaternary system PVP/KET/DMSO/scCO₂ could shift towards higher pressures (Campardelli et al., 2017a, Campardelli et al., 2019b). This effect will be the more pronounced, the larger is the concentration of solutes into the liquid solution. Therefore, considering a shift of the VLEs curve at 100 mg/mL, in this case, the operating point at 9 MPa could lie in the biphasic region where crystals commonly precipitated (De Marco et al., 2015b).

A comparison between the volumetric cumulative PSDs obtained at different concentration of solutes in DMSO is reported in **Figure IV.5**; it is possible to observe that, increasing the overall concentration, the mean diameter increased and the PSD enlarged.

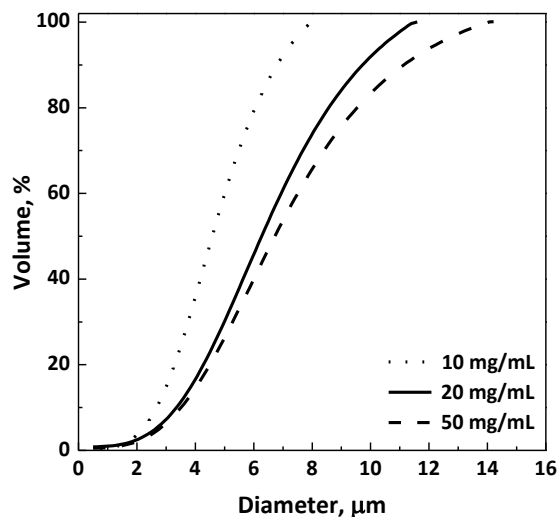


Figure IV.5 Volumetric cumulative PSDs of PVP/KET particles precipitated at different pressures.

Effect of PVP/KET ratio

The effect of PVP/KET ratio was studied, setting again the pressure at 9 MPa and using a total concentration of 50 mg/mL. The ratio was varied from 3/1 to 20/1 (runs # 9, 10, 11 and 7 in **Table IV.1**). In correspondence of all PVP/KET ratios, well-separated microparticles were obtained. Increasing the polymer/drug ratio, the mean diameter increased and the PSDs enlarged, as it is possible to observe in **Figure IV.6**.

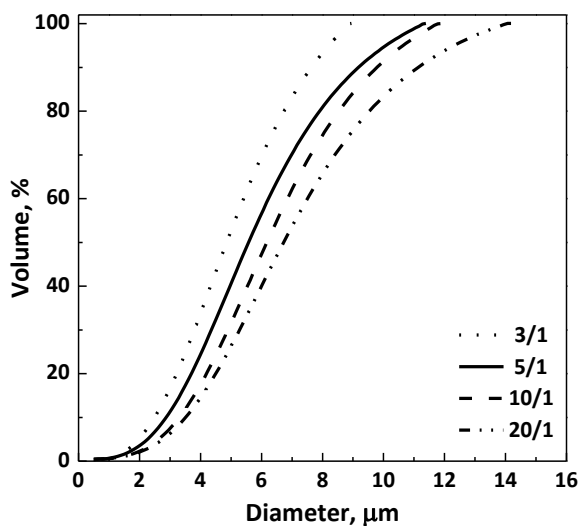


Figure IV.6 Volumetric cumulative PSDs of PVP/KET particles precipitated at different polymer/drug ratios.

Characterization of PVP/KET samples

FTIR analyses were performed on different samples to identify the characteristic peaks of the drug and the carrier and any chemical interactions between the two materials in the coprecipitates. FTIR spectra of unprocessed drug and PVP were compared to the PVP/KET 10/1 physical mixture and to SAS processed PVP/KET 10/1 spectra. As it is possible to observe from **Figure IV.7**, the spectrum of the unprocessed drug shows: (a) in the range $1600\text{-}1700\text{ cm}^{-1}$, the bands related to the stretching vibration of C=O carbonyl groups; (b) at 1440 and 1370 cm^{-1} , two characteristic absorption bands due to the C-H group stretching vibration. The spectrum of the polymer shows: (a) an absorption band at 1653 cm^{-1} , due to the stretching vibration of C=O groups; (b) C-H stretching vibration at 2873 cm^{-1} ; (c) -OH stretching vibration at 3469 cm^{-1} . The characteristic bands of the polymer dominate the spectra of both the physical mixture and SAS powders, being the PVP present in larger quantities than the NSAID. The existence of an interaction between PVP and KET was not detected by FTIR analyses.

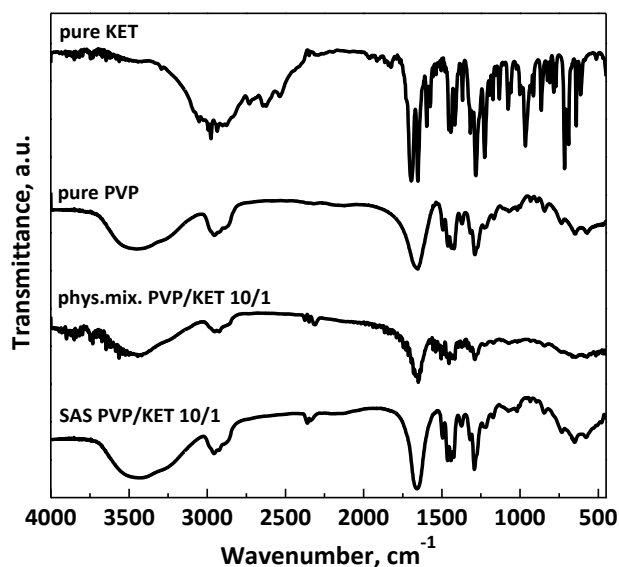


Figure IV.7 FTIR spectra of unprocessed PVP, unprocessed KET, PVP/KET physical mixture and SAS processed PVP/KET.

DSC thermograms of four samples (unprocessed drug, unprocessed polymer, PVP/KET coprecipitated at 3/1 and 10/1 w/w ratios) are compared in **Figure IV.8**. In the thermogram of the unprocessed KET, an endothermic peak in correspondence of about $93\text{ }^{\circ}\text{C}$ is detectable, due to the drug melting. The thermogram of the unprocessed PVP is characterized by a broad endothermic peak ranging from 80 to $110\text{ }^{\circ}\text{C}$ related to the loss of water. SAS processed PVP/KET coprecipitates, in correspondence of 3/1 and 10/1 ratios, do not show the peak characteristic of the drug. This behavior can be

ascribed to the fact that the drug was hidden in the amorphous polymer matrix, which is present in greater quantities.

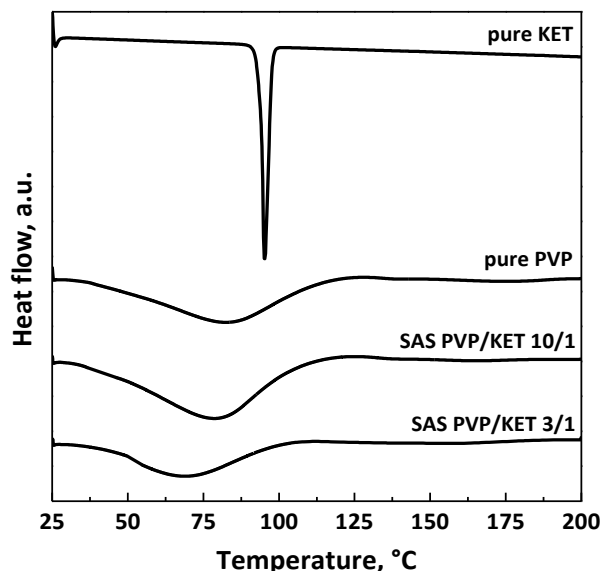


Figure IV.8 DSC thermograms of unprocessed PVP, unprocessed KET and SAS processed PVP/KET.

In order to prove the coprecipitation of the drug and the polymer and to verify the increase of KET dissolution rate, UV-vis spectroscopy analyses were performed for the unprocessed KET, the physical mixture PVP/KET, SAS micronized KET and SAS coprecipitates 10/1 and 3/1 w/w (**Figure IV.9**). When KET is orally administered, it passes through the stomach where KET is largely absorbed; for this reason, the dissolution studies were performed in a HCl 0.1 M solution at pH 2.5 and 37°C, to simulate the gastric acidity. From **Figure IV.9**, it can be observed that unprocessed KET completely dissolved in the dissolution medium in about 8 h, while the physical mixture PVP/KET took about 6 h. All SAS coprecipitated PVP/KET powders took about 3 h, therefore KET released from PVP-based microparticles is almost 3 times faster than pure KET. It can be noted that SAS-micronized KET completely dissolved 1.7 times faster than the pure drug, demonstrating the drug dissolution was accelerated not only because of the particle size reduction, but also as a result of the effective coprecipitation of KET with the hydrophilic carrier in form of microspheres.

For all the coprecipitated samples, encapsulation efficiency (EE%) was also calculated by UV/vis analysis. For the sample PVP/KET 3/1 (run #9), EE% is equal to 66.1%, which implies that part of the drug was extracted during SAS process. For all the other samples, the EE% ranged from 96.3 to 99.6%, indicating that KET solubilized with PVP in the starting SAS solution was present in the recovered powder.

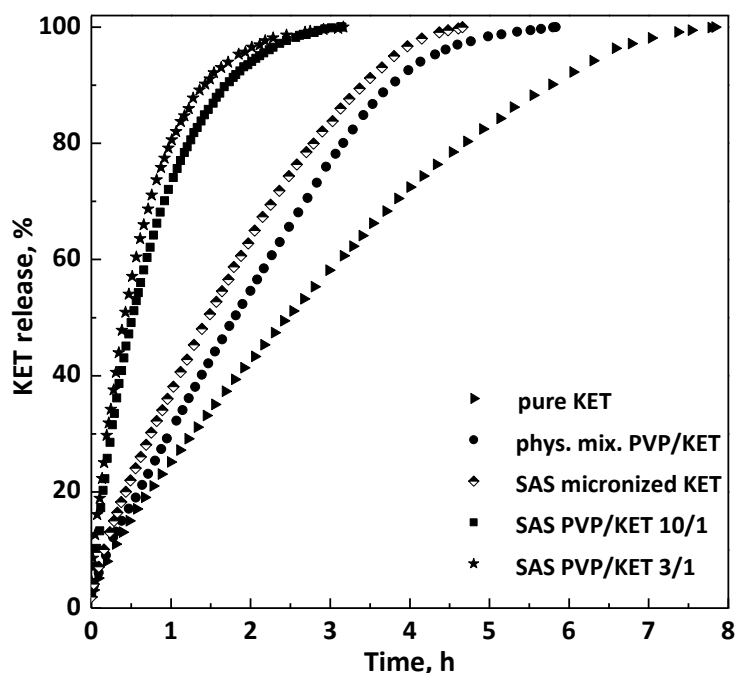


Figure IV.9 Drug dissolution profiles of KET in HCl solution (pH 2.5).

Discussion

As highlighted in the ‘State of the art’, PVP is an effective carrier to increase the drug bioavailability. It was demonstrated that KET dissolution can be enhanced coprecipitating it with PVP, up to be 3 times faster than the dissolution of the pure drug. This outcome allow to decrease the amount of drug supplied in patients, avoiding the side effects due to high dosages.

IV.2.2 PVP/rutin coprecipitation

SAS experiments were carried out at an operating temperature of 40°C and a pressure of 9 MPa. The operating pressure was chosen higher than the critical pressure of the binary system DMSO/CO₂, which is approximately 8.5 MPa (Andreatta et al., 2007a) at 40°C; i.e., above the MCP. The effect of the total concentration of solutes and the PVP/RUT weight ratio were investigated. In **Table IV.2**, a summary of some performed tests is reported, specifying the morphology of precipitated powders, the mean diameter and the standard deviation of the particles on a volumetric basis.

As previously observed, well-separated microparticles precipitated by micronizing PVP alone (**Figure IV.2a**). A preliminary test was also performed by processing only RUT at 40°C, 9 MPa and a solute concentration in DMSO equal to 20 mg/mL (run #2 in **Table IV.2**). A small amount of powder was found in the precipitator at the end of the test,

because RUT was extracted by the scCO₂/DMSO mixture. FESEM analysis revealed the presence of large and irregular RUT crystals. Therefore, rutin is not a good candidate for SAS micronization. Since PVP is an effective carrier for the SAS coprecipitation in form composite microspheres, the following experiments were performed with the system PVP/rutin.

Table IV.2 Summary of SAS experiments performed on PVP/RUT (MP: microparticles; cMP: coalescing microparticles; C: crystals).

#	PVP/RUT (w/w)	C _{tot} (mg/mL)	Morphology	m.d.±s.d. (µm)
1	1/0	40	MP	4.05±2.67
2	0/1	20	C	-
3	20/1	20	cMP	0.84 ± 0.26
4	20/1	30	MP	1.15 ± 0.34
5	20/1	40	MP	8.17 ± 2.29
6	10/1	40	cMP	0.94 ± 0.25

Effect of the overall concentration in DMSO

The effect of the total concentration of solutes in the liquid solution was investigated at 9 MPa, 40 °C and a PVP/rutin ratio of 20/1 w/w, varying the overall concentration of solutes in DMSO from 20 mg/mL to 40 mg/mL (runs #3-#5 in **Table IV.2**).

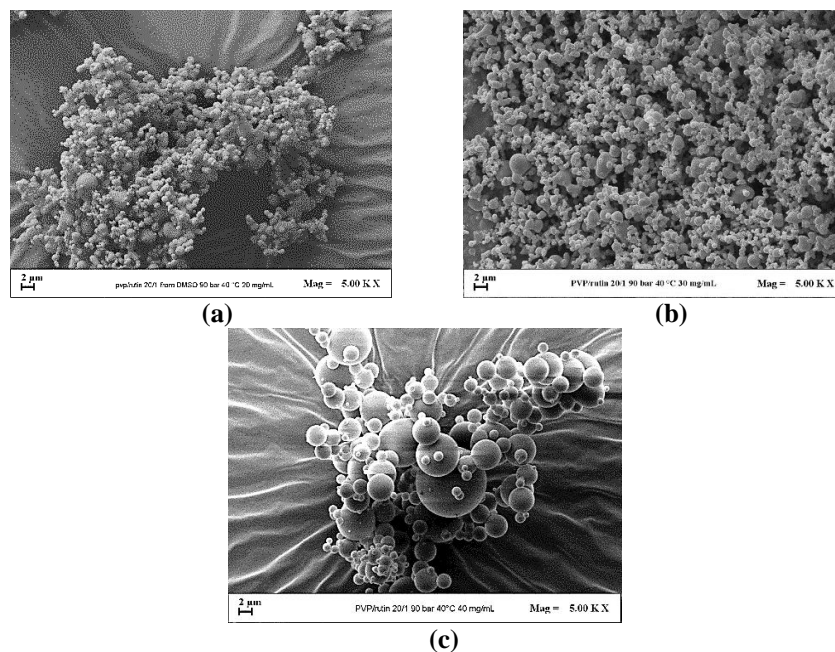


Figure IV.10 FESEM images of PVP/RUT 20/1 particles precipitated from DMSO at 9 MPa, 40°C and (a) 20 mg/mL; (b) 30 mg/mL; (c) 40 mg/mL.

Coalescing microparticles (**Figure IV.10a**) were obtained operating with a total concentration of 20 mg/mL (run #12), whereas slightly coalescing microparticles were formed at 30 mg/mL (run #13), as shown in **Figure IV.10b**. On the other hand, increasing the total concentration of PVP/rutin at 40 mg/mL (run #14), well-defined spherical microparticles were produced, as shown in **Figure IV.10c**.

The comparison between the volumetric cumulative PSDs, reported in **Figure IV.11**, showed that the particle size increased and the PSD enlarged by increasing the overall concentration of PVP and rutin in DMSO.

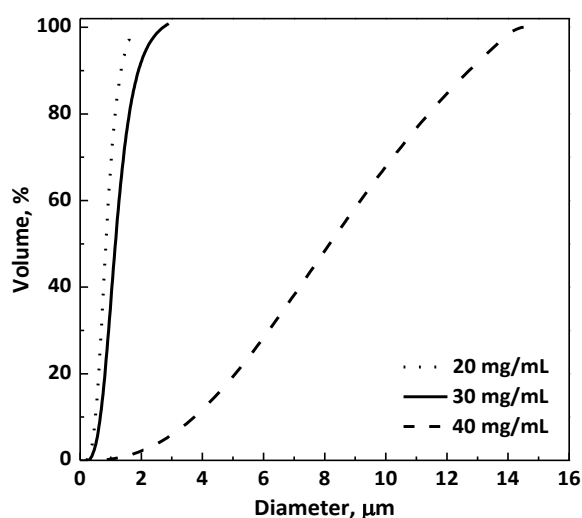


Figure IV.11 Volumetric cumulative PSDs of PVP/RUT particles 20/1 w/w precipitated from DMSO at 9 MPa and 40°C at different overall concentrations.

Effect of PVP/RUT ratio

The decrease of the PVP/rutin ratio from 20/1 to 10/1 w/w was investigated by fixing the total concentration in DMSO at 40 mg/mL, which seemed to be the most suitable to obtain microparticles from the previous set of experiments. Slightly coalescing microparticles were produced with a PVP/rutin ratio equal to 10/1 w/w. Therefore, it was decided not to further reduce the PVP/RUT ratio, because aggregates of particles would surely have been obtained for weight ratios lower than 10/1. As it can be noted in **Figure IV.12**, where the volumetric cumulative PSDs at the two different PVP/RUT ratios are reported, a decrease in particle size was observed by reducing the polymer/RUT ratio. Indeed, the mean diameter \pm standard deviation varied from $8.17 \pm 2.29 \mu\text{m}$ in the case of the ratio 20/1 to $0.94 \pm 0.25 \mu\text{m}$ at ratio 10/1.

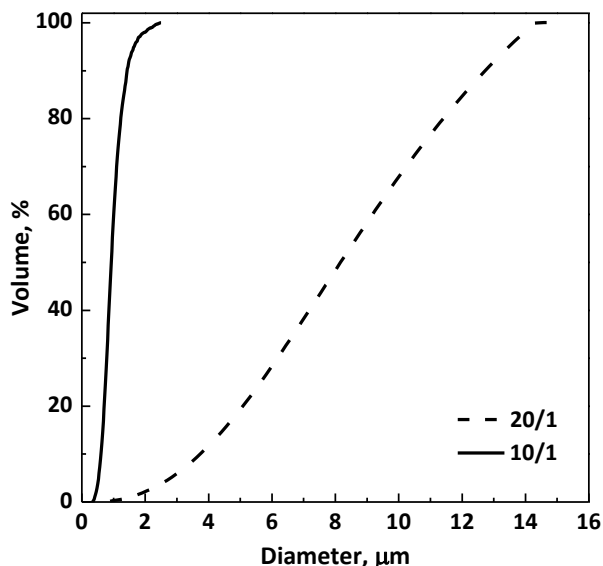


Figure IV.12 Volumetric cumulative PSDs of PVP/RUT particles precipitated from DMSO at 9 MPa, 40°C and 40 mg/mL; effect of PVP/RUT ratio.

Characterization of PVP/RUT samples

FTIR analyses were performed to identify the presence of possible interactions between rutin and PVP in the composite microparticles. FTIR spectra of unprocessed rutin and PVP, physical mixtures PVP/rutin, SAS processed PVP/rutin 20/1 and 10/1 w/w are reported in **Figure IV.13**. The spectrum of unprocessed rutin showed characteristic absorption bands at 3425 cm^{-1} (–OH), $2930\text{--}2912\text{ cm}^{-1}$ (C–H), 1655 cm^{-1} (C=O), 1600 cm^{-1} (aromatic structure), as well as a characteristic fingerprint in the region $1500\text{--}400\text{ cm}^{-1}$ (Montes et al., 2016a). The PVP spectrum shows characteristic absorption bands at 1653 cm^{-1} (C=O), 2873 cm^{-1} (C–H) and 3469 cm^{-1} (–OH) (Prosapio et al., 2017). Some of these characteristic bands were observed in the spectra of the physical mixtures PVP/RUT and of SAS composites PVP/RUT, indicating the presence of both the polymer and RUT. However, as expected, the spectra of SAS coprecipitates were more similar to the PVP spectrum, because of the high amount of polymer in the SAS powders. Moreover, no chemical interaction between PVP and RUT in the SAS powders was observed.

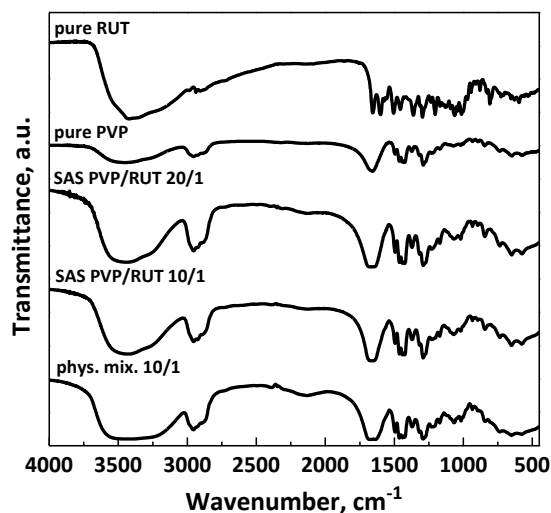


Figure IV.13 FTIR spectra of unprocessed PVP and RUT, physical mixtures and SAS processed PVP/RUT powders.

DSC thermograms of unprocessed RUT and PVP, and SAS processed PVP/RUT 10/1 were reported in **Figure IV.14**. The curve of pure PVP showed a broad endothermic peak corresponding to the dehydration. The thermogram of pure RUT exhibited a peak at 174°C caused by its molecular rearrangement (Muthurajan et al., 2015); i.e., the melting point (Asfour and Mohsen, 2018). The subsequent peaks provide evidence of the phase transition of RUT. SAS composites PVP/rutin showed an amorphous structure similar to the one of the polymer.

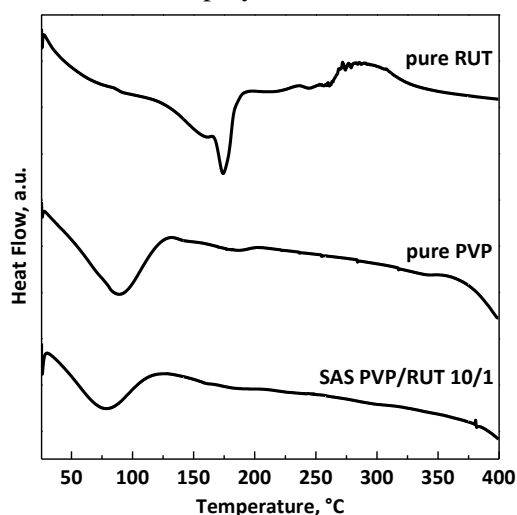


Figure IV.14 DSC thermograms of unprocessed PVP and RUT, SAS processed PVP/RUT powders.

Dissolution tests in PBS at pH 7.4 were performed to verify that the coprecipitation occurred. The dissolution profiles of unprocessed rutin and SAS coprecipitated powders PVP/RUT 10/1 w/w were reported in **Figure IV.15**. Unprocessed RUT completely dissolved in about 73.7 h, whereas the active compound took about 22 h to be released from SAS PVP/RUT 10/1 particles. Therefore, the RUT dissolution rate was about 3 times faster in the case of SAS powders PVP/RUT compared to unprocessed active compound.

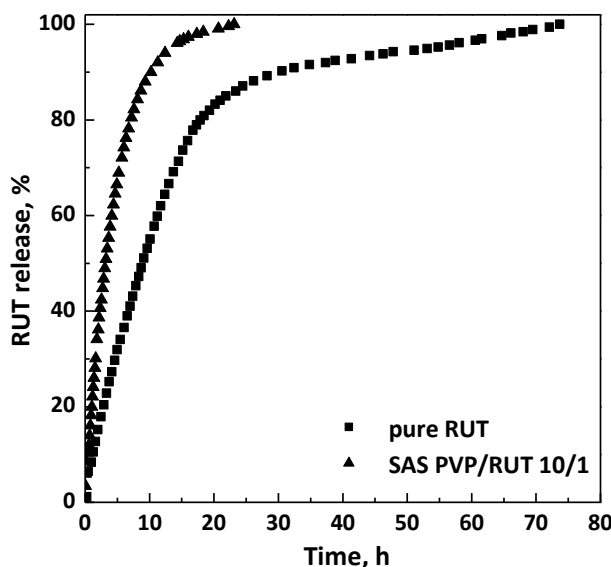


Figure IV.15 Dissolution profiles for rutin in PBS at 37°C and pH 7.4.

Encapsulation efficiency (EE%) was determined for all SAS samples by UV-vis analyses. The EE% was found to be equal to 35% when an overall concentration of 20 mg/mL was employed. In this case, the amount of polymer was probably not enough to trap all the rutin in the solution. The maximum EE% (in the range 90.1-99.8%) was obtained with PVP/rutin 20/1 samples, both using an overall concentration of 30 mg/mL and 40 mg/mL, as well as PVP/rutin 10/1 at 40 mg/mL, indicating a successful coprecipitation.

Discussion

Although PVP is a well-established carrier for the SAS process, an effective coprecipitation in form of microspheres could not be reached with some active compounds and/or under certain operating conditions. The experimentation conducted on the system rutin/PVP has revealed a possible limiting factor that could be found using this carrier: an effective coprecipitation in form of composite microparticles could not be possible with low polymer/drug ratios, as occurred with rutin. This means that large PVP amounts are sometimes required to ensure the desired morphology of the SAS coprecipitated powders.

IV.3 The use of zein as polymeric carrier

To date, some previous attempts using zein in SAS coprecipitation were substantially unsuccessful, but zein alone seems to be processable, as highlighted in the Introduction section. Therefore, in order to ensure that zein was effectively a novel polymeric carrier processable by SAS, a preliminary study focused on zein micronization was firstly carried out. Zein morphologies obtainable by SAS technique were investigated in detail, at different process conditions. Then, DIC was used as model compound to study SAS coprecipitation using zein as carrier. An interpretation of the coprecipitation in correspondence of different morphologies was postulated by dissolution tests. Due to the zein ability to prolong the drug release, it was also used to control the release kinetics of two commonly prescribed antibiotics, namely AMOXI and AMPI, as well as of two antihistamine drugs, namely CTZ and KTF.

IV.3.1 Zein micronization by SAS process

A preliminary study about zein micronization was carried out using DMSO as the liquid solvent, a CO₂ flow rate of 30 g/min and a solution flow rate of 1 mL/min, to assure the supercritical mixture conditions (Vega Gonzalez et al., 2002, Reverchon and De Marco, 2011). It should be specified that the same solvent, as well as CO₂ and liquid solution flow rates, were also used for the coprecipitation tests with zein shown below.

As regards the study of the zein micronization, the pressure, the zein concentration in DMSO and the temperature (T) were varied to investigate their influence on the morphology and size of particles. **Table IV.3** reports a list of the tests, with the indication of the obtained morphology, mean diameter of particles and standard deviation on a volumetric basis.

Table IV.3 SAS experiments performed on zein (NP: nanoparticles; SMP: sub-microparticles; MP: microparticles).

#	T (°C)	P (MPa)	C _{tot} (mg/mL)	Morphology	m.d.±s.d. (µm)
1	40	9	5	NP	0.109±0.041
2	40	15	5	NP	0.105±0.048
3	40	9	10	NP	0.154±0.080
4	40	9	20	SMP	0.238±0.094
5	40	9	50	MP	0.419±0.264
6	35	9	50	SMP	0.398±1.776
7	50	9	50	MP	2.953±1.776
8	60	9	50	-	-

Effect of the operating pressure

The first set of experiments was performed to investigate the effect of operating pressure, fixing the temperature at 40°C and the zein concentration into the liquid solution at 5 mg/mL. The pressure was increased from 9 MPa to 15 MPa (runs #1 and #2 in **Table IV.3**). Nanoparticles with mean size of around 100 nm precipitated at both pressure conditions.

Effect of the zein concentration

Aiming at obtaining microparticles, for the reasons explained in depth in ‘the state of the art’ section, zein concentration was varied in the range 5-50 mg/mL (runs #1, #3, #4 and #5 in **Table IV.3**). The highest value of concentration to operate with was chosen considering the maximum solubility of zein in DMSO, which was experimentally determined, and it is about 60 mg/mL at room temperature. For this set of experiments related to the influence of zein concentration on morphology and particle size, the pressure and the temperature were set at 9 MPa and 40°C, respectively.

When zein concentration was increased from 5 mg/mL to 20 mg/mL sub-microparticles were produced, whereas microparticles were observed at 50 mg/mL. A FESEM image of zein nanoparticles precipitated at 9 MPa, 40°C and 5 mg/mL is reported in **Figure IV.16a**. Zein microparticles produced at at 9 MPa, 40 °C and 50 mg/mL were instead shown in **Figure IV.16b**. The comparison of the volumetric PSDs at different concentrations of liquid solution (**Figure IV.17**) revealed that mean particle size increased and PSDs enlarged, especially at the largest concentration used (50 mg/mL).

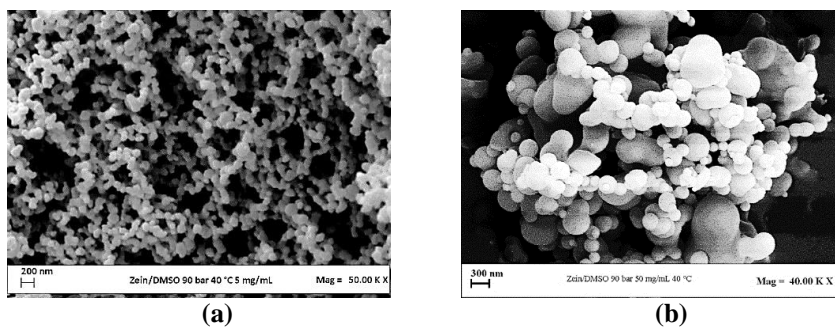


Figure IV.16 FESEM images of zein precipitated from DMSO at 9 MPa and 40°C; (a) nanoparticles at 5 mg/mL; (b) microparticles at 50 mg/mL.

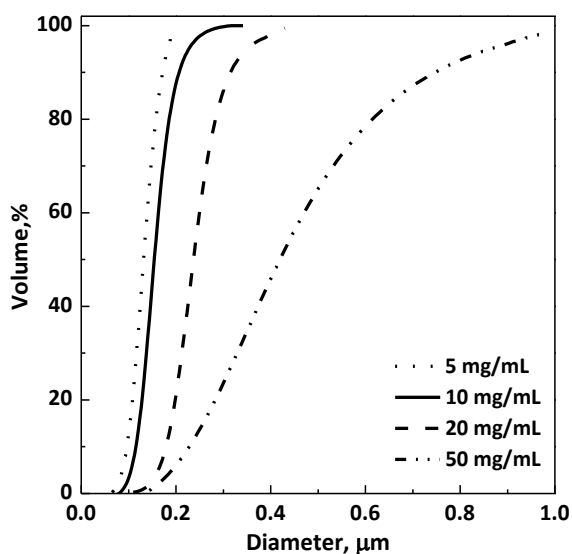


Figure IV.17 Effect of zein concentration in DMSO at 40°C and 9 MPa.

Effect of the operating temperature

Setting the pressure at 9 MPa and the polymer concentration in DMSO at 50 mg/mL, the effect of temperature was investigated (runs #5-#8 in **Table IV.3**). In **Figure IV.18**, the comparison of volumetric PSDs reveals that, increasing the temperature from 35°C to 50°C, a large increase of mean particle size and an enlargement of PSDs occurred. In detail, the mean diameter of microparticles at 50°C was around 2.95 μm.

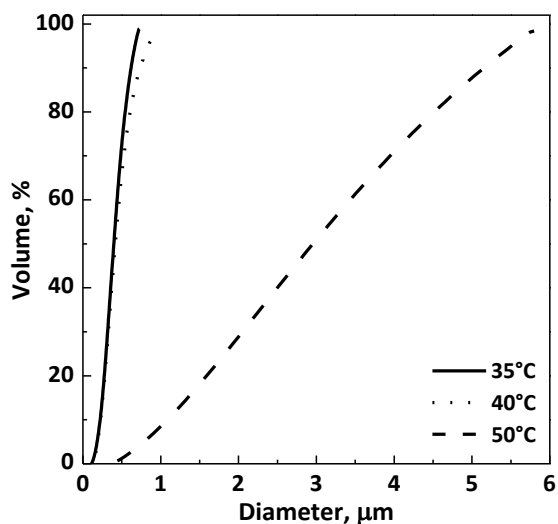


Figure IV.18 Effect of the operating temperature of zein precipitated from DMSO at 9 MPa and 50 mg/mL.

However, when the temperature was set at 60°C, liquid was found in the precipitation chamber at the end of the experiment. The failure of this last test was due to the non-complete miscibility of DMSO and CO₂ at these process conditions: the corresponding SAS operating point should be located inside the miscibility hole for the system DMSO-CO₂. Therefore, no further experiments were performed at this temperature.

Discussion

An interpretation of the experimental results obtained micronizing zein needs to recall the general explanation of SAS precipitation. As also discussed in the state of the art of SAS process, it was demonstrated that the evolution of the liquid jet is controlled by the competition between the jet break-up and the surface tension vanishing. When t_{JB} is the shortest characteristic time of the process, droplets are formed, which are dried by scCO₂, producing microparticles. If t_{STV} is lower than t_{JB} , nanoparticles are obtained by gas-to-particles nucleation and growth. When zein alone was used as the solute, at all the pressures (even very close to the MCP) and at low concentrations in DMSO, nanoparticles were obtained. It can be assumed that, in all these cases, the time necessary for the complete vanishing of the surface tension between the injected solution and the surrounding gas is lower than the time of jet break-up. Consequently, gas mixing prevails, no droplets are formed and the precipitation is obtained by gas-to-particles nucleation and growth. Increasing the zein concentration, higher concentration gradients between the scCO₂ and the liquid solution are formed during mixing, because of a larger quantity of solute molecules. In addition, the viscosity of the solution increases as the concentration of the solution increases. Therefore, t_{STV} increases and can be larger than t_{JB} ; as a consequence, sub-microparticles and microparticles are obtained.

IV.3.2 Zein/diclofenac coprecipitation

Once identified the operating conditions to produce preferably zein microparticles, coprecipitation experiments were carried out. The first coprecipitation study using zein as a carrier was performed by selecting DIC as the model drug. For these experiments, it was decided to work at a fixed temperature of 40°C and a pressure of 9 MPa. Indeed, from the preliminary tests processing zein alone, it emerged that this pressure value allows to produce microparticles when associated with a total concentration in DMSO greater than 20 mg/mL. **Table IV.4** reports a list of the experiments performed on the system zein/DIC, with the indication of the process parameters, namely the total concentration of solutes in DMSO and the polymer/drug w/w ratio, and the obtained morphology, mean diameter and standard deviation of particles produced, on a volumetric basis.

Table IV.4 SAS experiments performed on zein/diclofenac system (NP: nanoparticles; SMP: sub-microparticles; MP: microparticles).

#	Zein/DIC (w/w)	C _{tot} (mg/mL)	Morphology	m.d.±s.d. (µm)
1	0/1	20	NP	0.138±0.051
2	20/1	30	SMP	0.309±0.205
3	20/1	40	MP	0.476±0.343
4	20/1	50	MP	0.848±0.703
5	5/1	50	MP	0.416±0.228
6	10/1	50	MP	0.458±0.240
7	15/1	50	MP	0.547±0.468
8	25/1	50	MP	0.850±0.703
9	30/1	50	MP	1.308±0.762

A preliminar experiment was performed processing DIC alone at an operating pressure of 9 MPa and a drug concentration in DMSO equal to 20 mg/mL (run #1 in **Table IV.4**). The FESEM analysis of SAS processed DIC showed that the drug precipitated in form of nanoparticles with a mean diameter of about 130 nm.

Effect of the overall concentration in DMSO

The effect of the total concentration of solutes in the solution was studied at 9 MPa and 40 °C, fixing a polymer/drug ratio equal to 20/1 w/w. The overall concentration in DMSO was varied from 30 mg/mL to 50 mg/mL (runs #2-#4 in **Table IV.4**). At the lower concentration of 30 mg/mL, sub-microparticles with a mean size of 0.309 µm were observed. Increasing the concentration to 40 mg/mL and then 50 mg/mL, microparticles (as shown in **Figure IV.19** for 50 mg/mL) with a mean diameter of 0.476 µm and 0.848 µm were produced, respectively. Hence, increasing the overall concentration of the solution, the mean particle size enhanced, as evident in **Figure IV.20**.

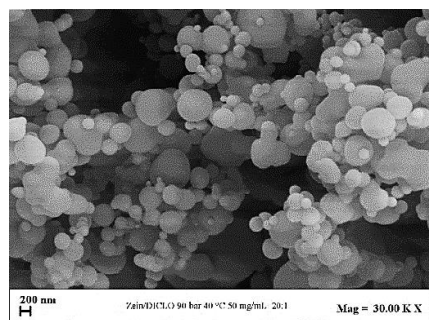


Figure IV.19 FESEM image of zein/DIC 20/1 microparticles obtained at 9 MPa, 40°C, 50 mg/mL.

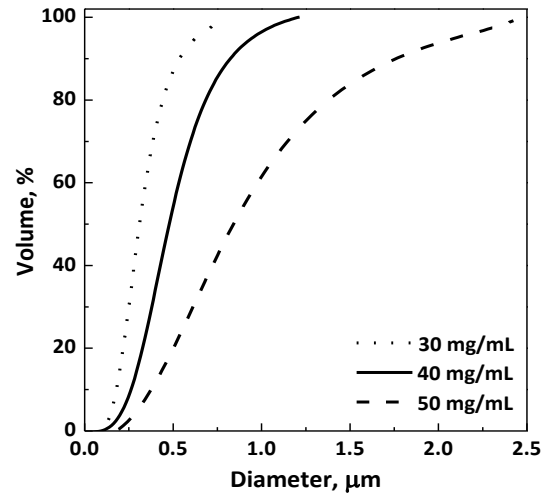


Figure IV.20 Volumetric cumulative PSDs of zein/DIC particles 20/1 precipitated from DMSO at 9 MPa, 40°C and different total concentrations.

Effect of zein/DIC ratio

Aiming at obtaining preferentially micrometric size, the total concentration in DMSO of 50 mg/mL was selected to study the effect of polymer/drug ratio, varying it from 5/1 to 30/1 w/w (runs #4-#9 in **Table IV.4**). Microparticles were obtained for all the tests, with mean size in the range 0.42-1.31 μm. By increasing zein/DIC ratio, the mean particle diameter increased and the PSD enlarged, as shown by volumetric cumulative PSDs reported in **Figure IV.21**.

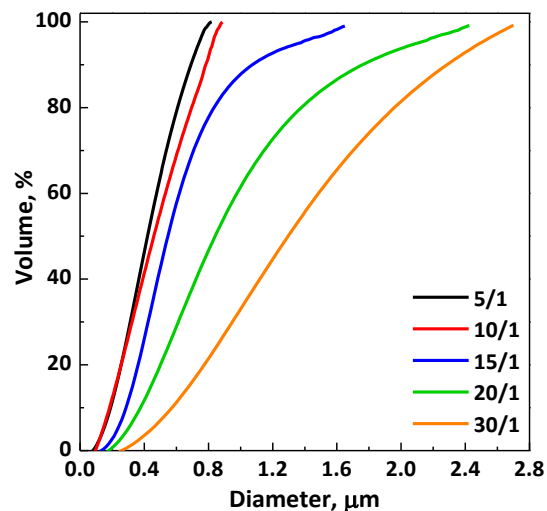


Figure IV.21 Volumetric cumulative PSDs of zein/DIC particles precipitated from DMSO at 9 MPa, 40°C and 50 mg/mL; effect of the polymer/drug ratio.

Characterization of zein/DIC samples

FTIR spectra of unprocessed and SAS processed zein and DIC, physical mixture zein/DIC 5/1 and SAS processed zein/DIC 5/1 w/w are reported in **Figure IV.22**. FTIR spectrum of pure DIC exhibited characteristic bands at 3385 cm^{-1} (N–H stretching of the secondary amine), 1574 cm^{-1} (C=O stretching of the carboxyl ion), 1557 cm^{-1} (C=C ring stretching), 1445 cm^{-1} (C–H bend), 1087 cm^{-1} (C–N stretching) and at 774 and 746 cm^{-1} (C–Cl stretching) (Kebebe et al., 2010, Edavalath et al., 2011). SAS processed DIC spectrum showed the same peaks, indicating that neither the presence of DMSO nor the one of scCO_2 altered the drug structure. Both the unprocessed and SAS processed zein spectrum showed distinctive bands at around 1645 cm^{-1} , 1541 cm^{-1} , and 1236 cm^{-1} corresponding to amide I, II, and III, respectively (Karthikeyan et al., 2012), evidencing the absence of the protein denaturation due to the presence of DMSO or scCO_2 during the SAS process. Zein peaks, with a minor contribution of the DIC bands, dominated the spectra of the physical mixtures and of SAS processed zein/DIC. The spectrum of SAS coprecipitate zein/DIC showed some of the characteristic peak of the drug; specifically, the peak at 1574 cm^{-1} , corresponding to the C=O stretching of the carboxyl ion, the peak at 1445 cm^{-1} corresponding to the C–H bend, and the two peaks at 774 and 746 cm^{-1} corresponding to the C–Cl stretching revealed the presence of DIC in the coprecipitates.

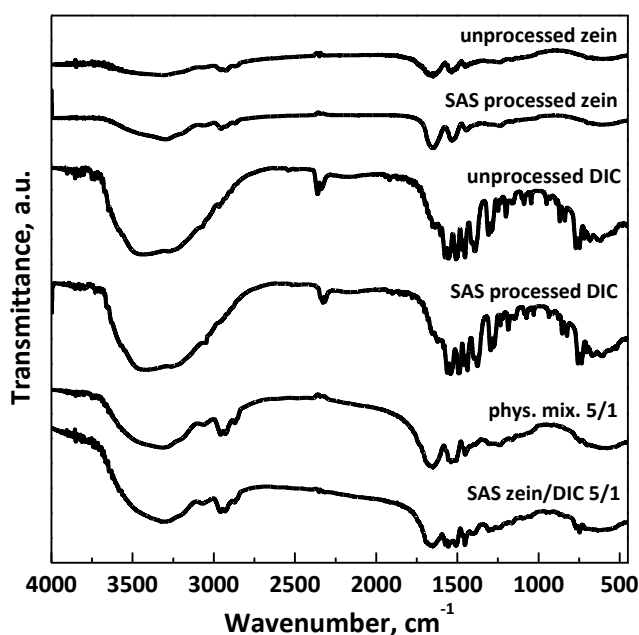


Figure IV.22 FTIR spectra for unprocessed and SAS processed DIC and zein, physical mixture ZEIN/DIC 5/1 and SAS processed ZEIN/DIC 5/1.

XRD analyses were performed on unprocessed zein and diclofenac, SAS processed zein/diclofenac 5/1 and 20/1, to evaluate the crystallization behavior of the different samples. XRD spectra are reported in **Figure IV.23**. XRD analyses showed that unprocessed diclofenac was characterized by a crystalline structure; whereas, unprocessed zein and coprecipitates showed an amorphous structure. Therefore, the coprecipitated powder seems to be amorphous like zein.

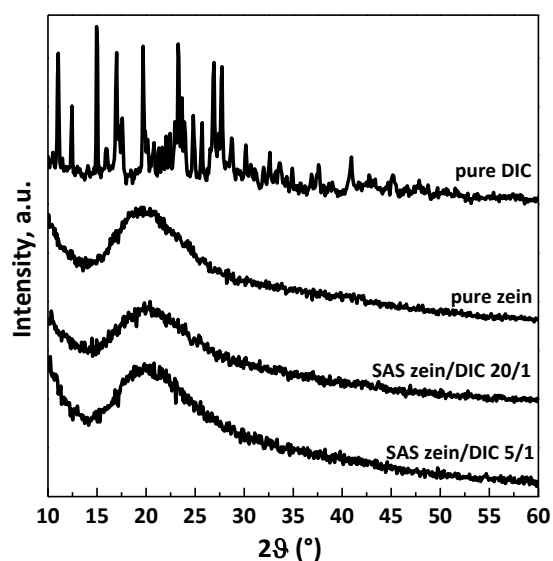


Figure IV.23 XRD spectra for unprocessed DIC and ZEIN, SAS processed ZEIN/DIC 5/1 and 20/1 w/w.

Considering that the crystalline structure of the drug might be hidden by the zein amorphous form, DSC analyses (**Figure IV.24**) were performed for unprocessed DIC and zein, and SAS processed zein/DIC 5/1 w/w. The DSC curve of pure crystalline DIC showed two endothermic peaks, the first related to the dehydration and the other (at about 288 °C) corresponding to the melting point (Tita et al., 2011, Killedar and Nale, 2014). Zein thermogram exhibited a broad endothermic peak ranging from 50 to 150°C, attributed to the loss of volatile components, whereas the glass transition temperature (T_g) was at around 170 °C, in agreement with the literature (Müller et al., 2011). The thermogram of the SAS process powder zein/DIC 5/1 showed a trend similar to the one of the zein curve, without the endothermic melting peak of crystalline DIC. Therefore, DSC analyses confirmed the amorphous form of zein/DIC SAS coprecipitated powders.

Dissolution tests in PBS at pH 7.4 (**Figure IV.25**) were performed for unprocessed drug and SAS processed zein/DIC at different weight ratio, also to understand the coprecipitation mechanisms in correspondence of various particle morphologies.

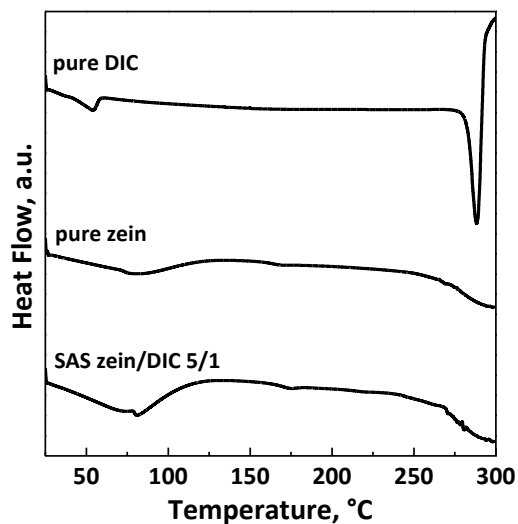


Figure IV.24 DSC thermograms of unprocessed DIC, unprocessed zein, and SAS processed zein/DIC 5/1.

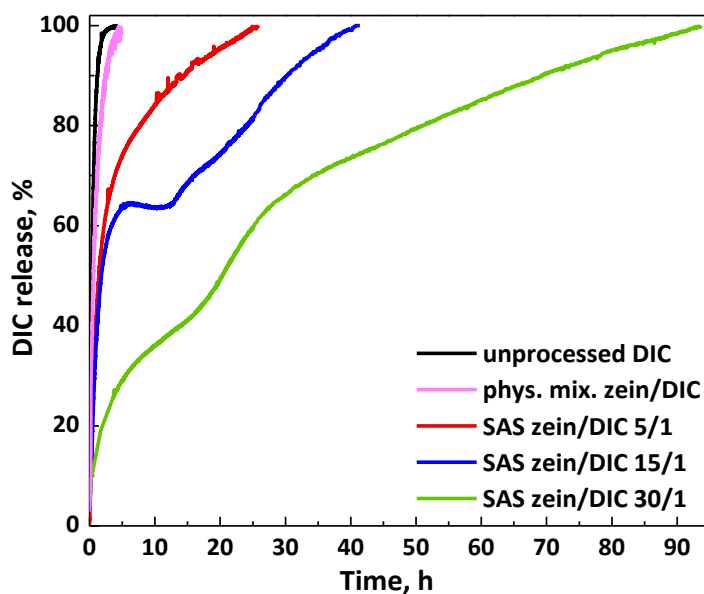


Figure IV.25 Dissolution profiles of DIC in PBS at 37°C and pH 7.4.

It was observed that pure DIC and the physical mixture zein/DIC achieved 90% of the dissolution in about 1.2 and 2.4 h, respectively. The systems zein/DIC 5/1, 15/1, and 30/1 w/w reached 90% of drug release in about 14.9, 31.8 and 85 h, respectively. Therefore, the higher the polymer/drug ratio, the slower is the release. Looking at **Figure IV.25**, it is possible to state that drug release rate depends also on particles

morphology/diameter. In the case of 5/1 ratio, at which particles with mean size of about 0.4 μm precipitated, a large part of dissolution (about 60%) is characterized by a burst-like effect. This result means that a sort of nano-physical mixture was prevalently obtained and the polymer and the drug, at least in part, precipitated separately. As the particle size increases, the percentage of drug located on/near the particle surface decreases and the burst-like effect reduced, as proved by the coprecipitated powder zein/DIC 30/1, consisting of microparticles (mean size: 1.3 μm). Indeed, at the highest polymer/drug ratio investigated, which corresponds to micrometric particles, the physiological burst is about 10%, calculated on surface exposed DIC, whereas the drug complete dissolution is further delayed.

Discussion

For a correct interpretation of the results obtained by coprecipitating zein and DIC, the competition of the jet break-up phenomenon and the surface tension vanishing has to be considered (Reverchon and De Marco, 2011, Marra et al., 2012). If t_{JB} is the shorter characteristic time of the process, composite zein/DIC microparticles can be produced, since the two compounds are entrapped in the same droplet that behaves like an isolated reactor. It should be noted that also sub-microparticles are formed by the drying of sub-micrometric droplets obtained as a result of jet break-up. On the other hand, when t_{STV} is the shorter characteristic time of the process, the liquid jet disappears before the jet break-up; a gaseous system is formed. In this case, the polymer and the drug precipitate separately by homogeneous nucleation and coprecipitation fails at least partly (Reverchon and De Marco, 2011). Indeed, in the latter case, a portion of the precipitated powder is constituted by polymer nanoparticles, a portion by drug nanoparticles, and the residual powder amount can be formed by nanoparticles of the materials precipitated together, with an irregular distribution of the drug into the polymer.

In case of zein/DIC ratios 5/1, 10/1 and 15/1 w/w, coprecipitation is only in some measure achieved, since a large aliquot of drug dissolution is characterized by a burst effect: the active compound is somewhat freely soluble. In particular, the dissolution tests show the presence of an initial burst-like effect that decreases as the polymer/drug ratio increases, up to an approximately constant value (about 10 %), probably corresponding to drug molecules/particles located near/on composite microparticles surface. As the particle size increases, a larger amount of drug is captured and dispersed within the polymeric matrix formed after droplets drying. Furthermore, the drug release is slower as zein/diclofenac ratio increases.

In conclusion, zein/DIC coprecipitates were obtained, but the process parameters have to be accurately selected to produce microspheres, which can assure a massive coprecipitation of the two compounds. In particular, at the process conditions employed (40°C/9 MPa), also the polymer/drug ratio

needs to be accurately selected to produce microparticles. Indeed, in correspondence of zein/DIC 30/1 weight ratio, a successful coprecipitation with a prolonged drug release can be achieved. Therefore, it was proved that the use of zein allowed to control the drug release, thus reducing the frequency of administration and adverse effects caused by drug overuse. This result is relevant from a pharmaceutical point of view, since high dosages and chronic use of diclofenac sodium is often prescribed to treat a large number of connective tissue disorders, resulting in many side effects.

IV.3.3 Zein/antibiotic coprecipitation

SAS coprecipitation using zein as polymeric carrier was also studied with two model antibiotics, namely AMOXI and AMPI. Based on the previous obtained results, in order to produce preferentially microspheres, the pressure and the overall concentration in DMSO were fixed at 9 MPa and 50 mg/mL for all the tests performed on both the zein/antibiotic systems. However, in this part of the work, the attention was focused on the effect of the operating temperature on morphology/size of zein-based coprecipitates, at different zein/antibiotic mass ratio. A summary of the experiments performed on zein/AMOXI and zein/AMPI systems is shown in **Table IV.5**, where the particle morphology (M), mean diameter and standard deviation on a volumetric basis were indicated.

Table IV.5 SAS experiments performed on zein/antibiotic systems (SMP: sub-microparticles; MP: microparticles; liq: liquid).

#	Antibiotic	zein/antibiotic (w/w)	T (°C)	M	m.d.±s.d. (µm)
1	AMOXI	0/1	40	SMP	0.26±0.15
2		20/1	40	MP	0.65±0.51
3		20/1	50	MP+liq	12.0±8.20
4		30/1	40	MP	0.85±0.53
5	AMPI	0/1	40	SMP	0.23±0.15
6		20/1	40	SMP	0.36±0.30
7		20/1	50	MP	19.47±9.07
8		10/1	50	MP	11.32±6.17
9		5/1	50	MP	9.05±5.71

Some preliminary tests were carried out, processing the antibiotics alone at 40°C, 9 MPa and an antibiotic concentration in DMSO equal to 20 mg/mL (runs #1 and #5 in **Table IV.5**). In both cases, operating under these conditions, sub-microparticles with a mean diameter of 0.26 µm and 0.23 µm precipitated in the case of AMOXI and AMPI, respectively. With the aim of verifying if the zein capability of producing composite microspheres is also applicable to the selected antibiotics, SAS experiments with the systems zein/AMOXI and zein/AMPI were performed.

Effect of the operating temperature

Fixing the polymer/drug ratio at 20/1 w/w, the effect of temperature on particle morphology, particle mean size and PSD was studied for each antibiotic at 40°C and 50°C.

As concerns the system zein/AMOXI, working at the temperature of 40°C (run #2 in **Table IV.5**) spherical microparticles with a mean diameter of 0.65 μm were obtained, as shown in the **Figure IV.26a**. Increasing the temperature at 50 °C (run #3 in **Table IV.5**), a certain amount of liquid was found at the end of the experiment inside the precipitation chamber, whereas an exiguous amount of powder was recovered from the filter. When analyzed by FESEM, this powder was constituted by very large microparticles (**Figure IV.26b**) with a mean size of 12 μm . The formation of a liquid phase may be considered a failure of the experiment, which can be ascribed to the possible modification of the high-pressure VLEs of the binary system CO_2/DMSO (Andreatta et al., 2007a), due to the presence of zein and AMOXI. If the binary region of the VLEs is enlarged, the SAS operating point should be located inside this two-phase region. For this reason, no further experiments were performed at 50°C and the temperature of 40°C was selected for the following experiments with the system zein/AMOXI.

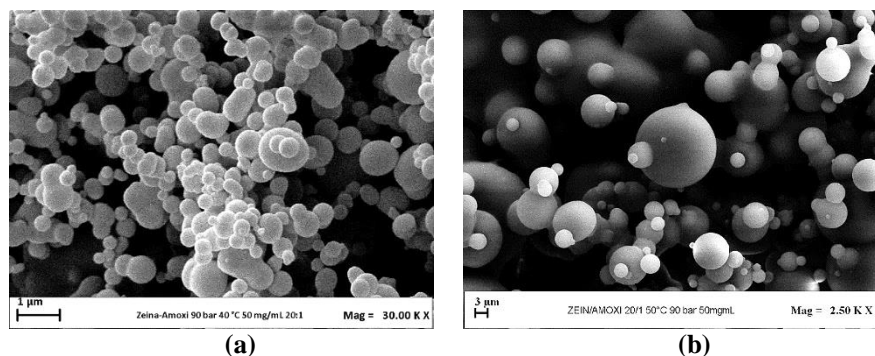


Figure IV.26 FESEM images of zein/AMOXI 20/1 microparticles obtained at 9 MPa, 50 mg/mL and (a) 40°C (run #2); (b) 50°C (run #4).

Regarding the system zein/AMPI, slightly coalescent sub-microparticles (**Figure IV.27a**) were obtained at 40°C (run #6 in **Table IV.5**), whereas well-defined microparticles were produced at 50°C (run #7 in **Table IV.5**), as shown in the FESEM image reported in **Figure IV.27b**. The remarkable increase of particle size by increasing the temperature can be noted from the comparison of the volumetric cumulative PSDs reported in **Figure IV.28**. For this reason, the subsequent tests on the influence of zein/AMPI ratio (w/w) were performed setting the temperature at 50°C to produce preferentially well-separated microspheres.

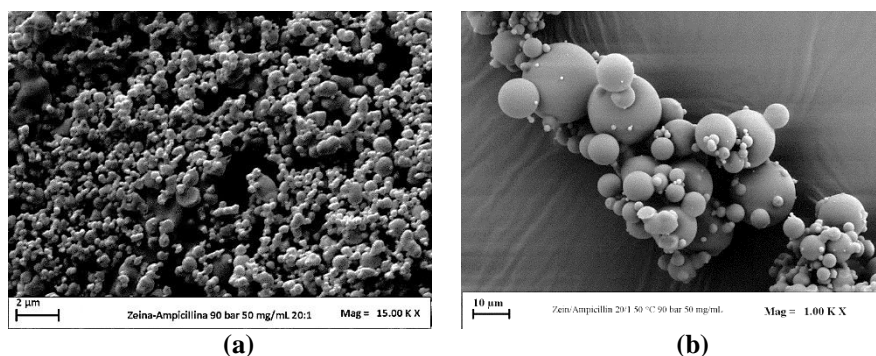


Figure IV.27 FESEM images of zein/AMPI 20/1 precipitated at 9 MPa, 50 mg/mL; (a) submicroparticles at 40°C (run #6); (b) microparticles at 50°C (run #7).

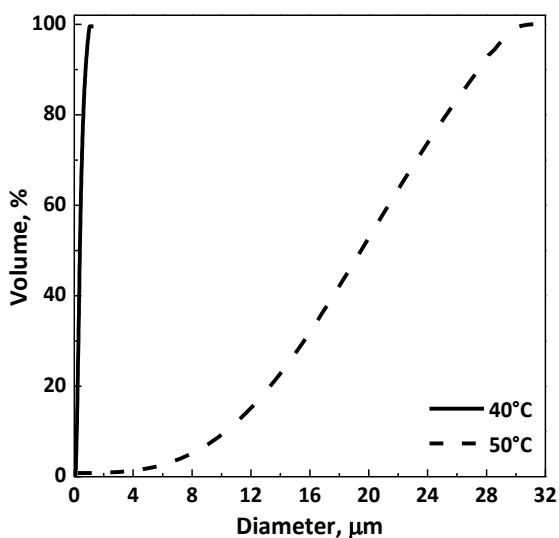


Figure IV.28 Volumetric cumulative PSDs of zein/AMPI 20/1 particles precipitated from DMSO at 9 MPa, 50 mg/mL; effect of the temperature.

Effect of zein/antibiotic ratio

As explained above, the effect of polymer/drug ratio (w/w) for the system zein/AMOXI was studied at 40 °C (runs #2 and #4 in **Table IV.5**). According to the previous results and the literature study reported in the ‘State of the art of SAS process’, the mean size of SAS produced particles often decreases by increasing the polymer/drug ratio. Taking into account this consideration and the fact that particles with mean size of 0.65 μm precipitated at 40°C and a zein/AMOXI ratio of 20/1 (run #2), it was decided to increase the polymer/drug ratio at 30/1 (run #4) to study the influence of this last parameter. Comparing the volumetric cumulative PSDs reported in **Figure IV.29**, an increase of the mean particle size was observed.

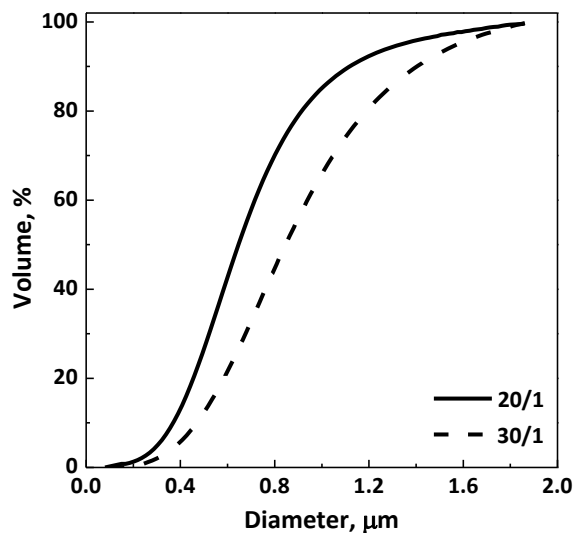


Figure IV.29 Volumetric cumulative PSDs of zein/AMOXI particles precipitated from DMSO at 40°C, 9 MPa, 50 mg/mL; effect of the polymer/drug ratio.

Regarding the system zein/AMPI, the polymer/drug ratio was gradually decreased from 20/1 to 5/1 (runs #7-#9 in **Table IV.5**), at the optimized temperature of 50°C. In all cases, well separated microparticles were produced, as can be observed in the FESEM images reported in **Figure IV.30**. Moreover, it was observed that, decreasing the polymer/drug ratio, the mean particle size decreased, as demonstrated in **Figure IV.31**, where the volumetric cumulative PSDs are compared.

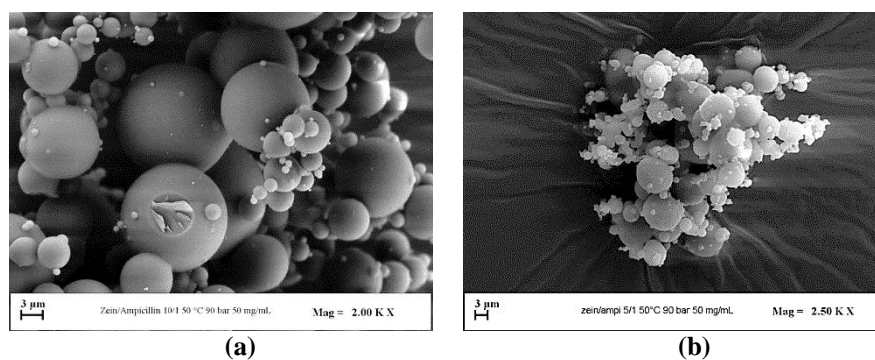


Figure IV.30 FESEM images of zein/AMPI microparticles obtained at 50 °C, 9 MPa, 50 mg/mL. Effect of the polymer/drug ratio: (a) 10/1 w/w (run #8); (b) 5/1 w/w (run #9).

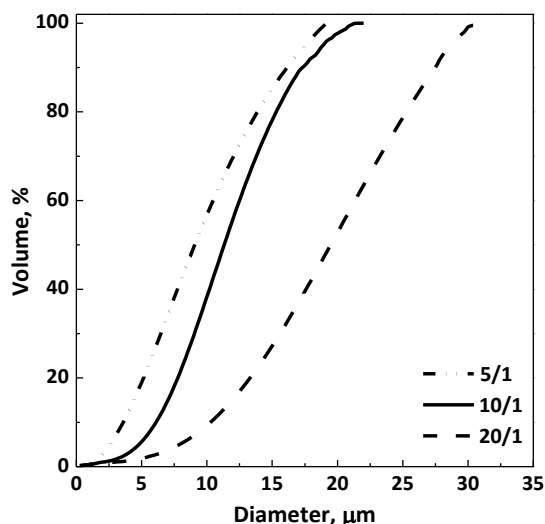


Figure IV.31 Volumetric cumulative PSDs of zein/AMPI particles precipitated from DMSO at 50°C, 9 MPa, 50 mg/mL; effect of the polymer/drug ratio.

Characterization of zein/antibiotic samples

FTIR spectra of pure antibiotics and zein, physical mixtures and SAS processed zein/antibiotic 20/1 w/w are shown in **Figure IV.32** and **Figure IV.33** for AMOXI and AMPI, respectively. The spectrum of zein showed characteristic bands at about 1645 cm^{-1} , 1541 cm^{-1} and 1236 cm^{-1} assigned to amide I, II and III, respectively (Karthikeyan et al., 2012). The spectrum of pure AMOXI (in **Figure IV.32**) exhibited bands at 3463 cm^{-1} related the N-H stretching of primary amine, at 1777 cm^{-1} and 1687 cm^{-1} attributed to the C=O stretching of carbonyl and carboxylic group, respectively; moreover, a peak at 1590 cm^{-1} , assigned to the C-C stretching of the thiazole ring, was also observed (Chullasat et al., 2018). The spectrum of pure AMPI (in **Figure IV.33**) showed the characteristic band of the -OH stretching at around 3400 cm^{-1} , two peaks at 2969 e 2930 cm^{-1} assigned to the asymmetric stretching vibrations of C-H, an absorption band at 1774 cm^{-1} corresponding to carbonyl vibrations, whereas the bands in the range 1625-1530 cm^{-1} were related to the C-C stretching vibrations of the aromatic ring (Gunasekaran et al., 1996). A peak at about 1320 cm^{-1} was related to the C-O stretching of carboxylic group and the band at 697 cm^{-1} was assigned to heterocyclic S-C stretching vibration. For both the zein/antibiotic systems, the zein peak dominated the spectra of the physical mixtures and of SAS processed composites, with a minor contribution of those of antibiotics, probably due to the greater amount of polymer than drug. In particular, the spectrum of coprecipitates zein/AMOXI showed a shoulder at 1777 cm^{-1} related to the respective peak of AMOXI as well as the peak at 1236 cm^{-1} . In the spectrum

of SAS processed zein/AMPI, instead, the presence of the peaks at 697 cm^{-1} and 1320 cm^{-1} , attributed to the antibiotic, was evident. In any case, no interactions occurred between the carrier and the drug after SAS process.

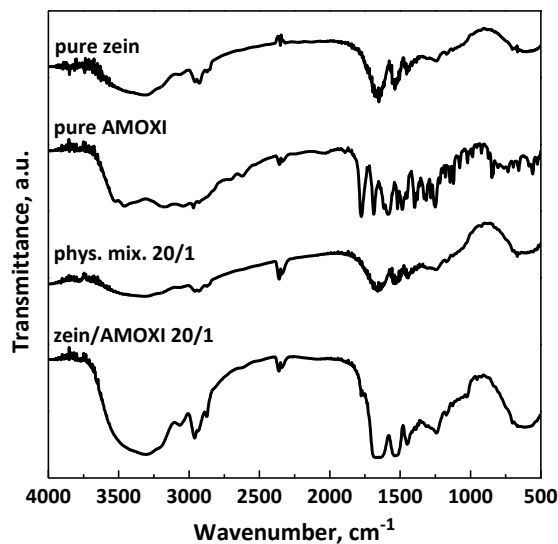


Figure IV.32 FTIR spectra of unprocessed zein and AMOXI, physical mixture zein/AMOXI and SAS processed powders.

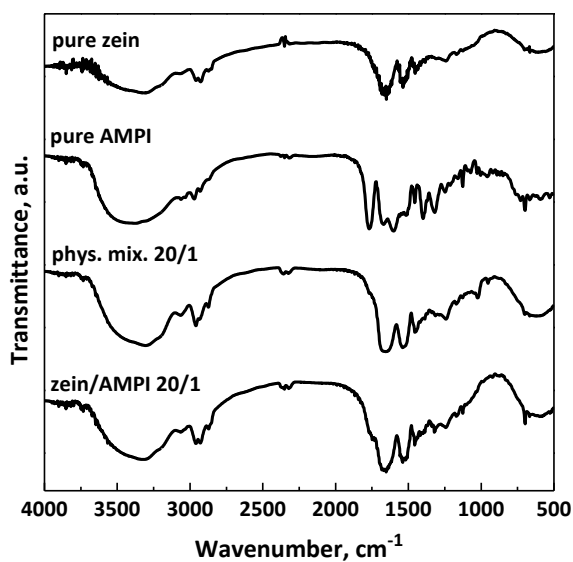


Figure IV.33 FTIR spectra of unprocessed zein and AMPI, physical mixture zein/AMPI and SAS processed powders.

DSC thermograms of pure antibiotics, pure zein and SAS processed zein/antibiotics at different temperature and polymer/drug ratio are reported in **Figure IV.34** and **Figure IV.35** for AMOXI and AMPI, respectively. A broad endothermic peak ranging from 50 to 150°C related to the loss of volatile components was observed in zein thermogram, whereas the glass transition temperature (T_g) was at about 170°C (Müller et al., 2011). DSC thermogram of pure AMOXI (**Figure IV.34**) showed two endothermic peaks, the first at around 120 °C due to the loss of water and the last at 195°C indicating the melting point (Marciniec et al., 2002). The exothermic peak at about 178°C, instead, showed the re-crystallization from trihydrate to anhydrate. DSC thermogram of pure AMPI (**Figure IV.35**) showed an endothermic curve due to the dehydration and an endothermic peak at about 233°C corresponding to the melting point (Marciniec et al., 2002). Both antibiotics micronized by SAS technique seemed to have an amorphous structure, because the precipitation process occurs so fast that the drug molecules do not have time to organize into an ordered structure. Composite systems zein/antibiotic showed thermograms similar to the one of zein, except for the coprecipitate zein/AMPI 5/1, slightly different, probably because of the higher amount of the antibiotic. In any case, SAS coprecipitates are amorphous as well as the polymeric carrier.

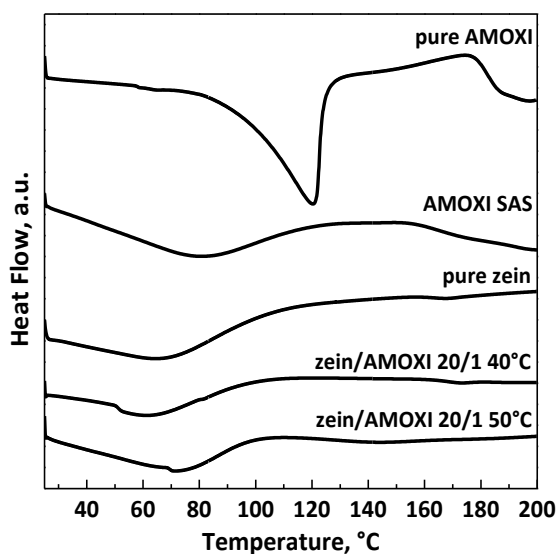


Figure IV.34 DSC thermograms of unprocessed zein, unprocessed and SAS processed AMOXI, SAS processed zein/AMOXI powders.

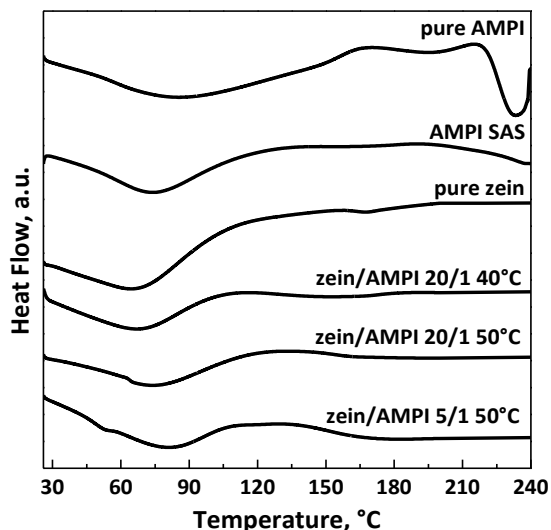


Figure IV.35 DSC thermograms of unprocessed zein, unprocessed and SAS processed AMPI, SAS processed zein/AMPI powders.

Dissolution tests were performed for both the pure antibiotics and SAS processed powders to compare the drug dissolution rate in PBS and to verify the occurred coprecipitation. In **Figure IV.36**, it can be observed that pure AMOXI reached 90% of the dissolution in about 3 h, while the physical mixture zein/AMOXI took about twice the time. The AMOXI dissolution rate was slower for all the composite systems obtained by SAS. As an example, the sample zein/AMOXI 20/1 w/w processed at 40°C achieved 90% of drug release in about 49 h. Therefore, zein/AMOXI coprecipitates showed a dissolution rate about 16 times slower than pure antibiotic. Moreover, an initial burst effect (around 33%) was observed, due to the percentage of AMOXI located on/near the particles surface. The dissolution profiles of AMPI samples are instead reported in **Figure IV.37**. Pure ampicillin and the physical mixture zein/ampicillin achieved 90% of the dissolution in about 3 h and 4 h, respectively. The antibiotic dissolution was significantly delayed for all SAS coprecipitates zein/AMPI. As an example, the system zein/AMPI 5/1 w/w obtained at 50 °C achieved 90% of drug release in about 14 h. Hence, the dissolution rate was about 5 times slower than unprocessed antibiotic, whereas the burst-like effect was about 10%.

Regarding the antibiotic entrapment efficiency, it was 99.5-99.8% for all the SAS samples.

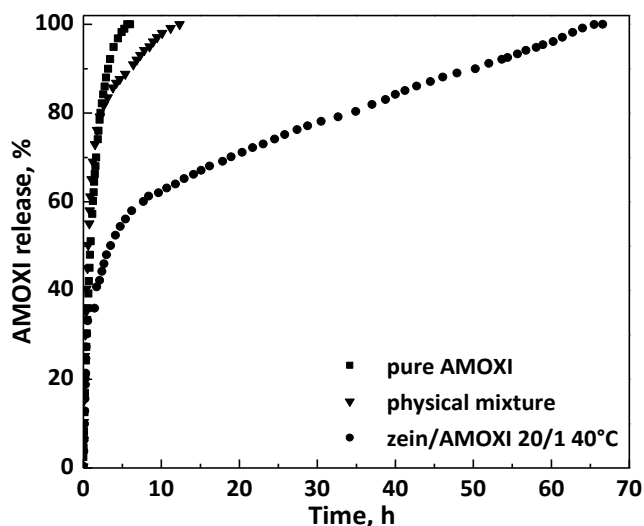


Figure IV.36 Dissolution profiles of AMOXI in PBS at 37°C and pH 7.4.

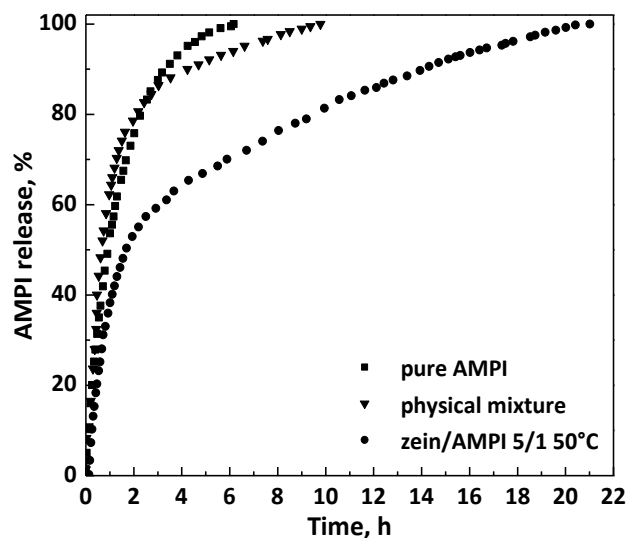


Figure IV.37 Dissolution profiles of AMPI in PBS at 37°C and pH 7.4.

Discussion

The difficulty of obtaining composite microspheres by SAS technique using zein as carrier was successfully overcome, since, as desired, well separated microparticles were produced, accurately selecting the process conditions to ensure a massive coprecipitation. The coprecipitation was also confirmed by means of in vitro dissolution tests, since both the systems zein/AMOXI and zein/AMPI showed a significant increase in the time necessary for the complete drug dissolution with respect to the pure

antibiotics. This change in the dissolution rate of the antibiotic is due to the fact that AMOXI and AMPI were entrapped in the zein matrix.

Considering the results achieved, two different antibiotic delivery applications can be proposed:

- zein/AMOXI systems, whose complete dissolution was achieved in almost 3 days, can be used for a “long-term antibiotic therapy” against severe infections, such as Lyme disease, some urinary tract infections, possible complications after surgery, etc.;
- zein/AMPI systems, whose complete release was achieved in almost one day, can be used for a “short-term antibiotic therapy”; i.e., common infections of respiratory, gastrointestinal and urinary tracts.

IV.3.4 Zein/antihistamine coprecipitation

Zein was also employed as polymeric carrier with the aim of prolonging the release of two model antihistamine drugs, namely CTZ and KTF.

For all the tests related to zein/antihistamine coprecipitation, the pressure and the overall concentration in DMSO were fixed at 9 MPa and 50 mg/mL, since it was proved that micrometric particles generally tend to precipitate at these conditions, both in the case of zein micronization and zein/drug coprecipitation. From the previous study on zein/antibiotic coprecipitation, it emerged that the variation of the temperature could favor the attainment of microspheres in the case of some zein/drug systems. Since the temperature seemed to play a key role on morphology/size of particles produced using zein, the effect of temperature was further studied with zein/antihistamine systems; its influence on the drug dissolution was also investigated. The polymer/drug ratio was also varied with the aim of reducing the amount of zein in coprecipitates, while maintaining the microparticle morphology.

A summary of the experiments performed on zein/CTZ and zein/KTF systems is shown in **Table IV.6**, where the particle morphology, mean diameter and standard deviation on a volumetric basis were indicated.

Some preliminary tests were carried out, processing the two antihistamine drugs separately, at 40°C, 9 MPa and a drug concentration in DMSO equal to 20 mg/mL (runs #1 and #9 in **Table IV.6**). In both cases, at the end of the experiment, no powder was found in the precipitation chamber, because the drug was probably extracted by the mixture DMSO/scCO₂. Therefore, it could be asserted that the two antihistamine drugs are not good candidates for the SAS micronization. The following SAS coprecipitation tests were also conducted to verify if zein could force the processability and the morphology of the two active principles.

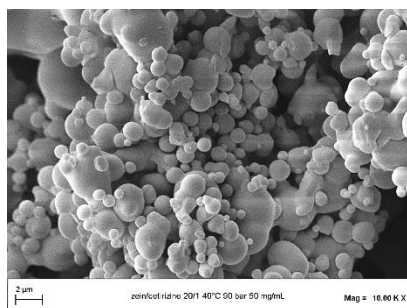
Table IV.6 SAS tests performed on zein/antihistamine systems (C: crystals; MP: microparticles; cMP: coalescent microparticles; AGG: aggregates).

#	Antihistamine	zein/drug (w/w)	T (°C)	Morphology	m.d.±s.d. (µm)
1		0/1	40	-	-
2		20/1	40	MP	2.75±0.85
3		20/1	45	MP	2.92±0.91
4	CTZ	20/1	50	MP	3.84±1.08
5		10/1	40	cMP	-
6		10/1	45	cMP+MP*	*4.02±1.24
7		10/1	50	MP	8.77±2.72
8		5/1	50	C	-
9		0/1	40	-	-
10		20/1	40	cMP	0.72±0.20
11	KTF	20/1	45	MP	1.93±0.57
12		20/1	50	AGG	-
13		10/1	45	MP	2.23±0.65
14		5/1	45	MP	1.85±0.54

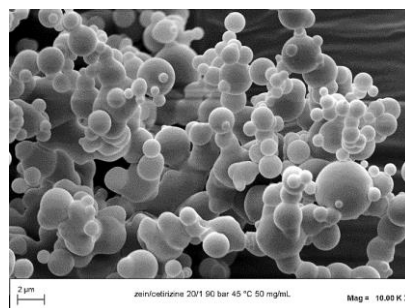
Effect of the operating temperature

Fixing the zein/antihistamine ratio at 20/1 w/w, the effect of temperature was studied by gradually increasing it from 40°C to 50°C.

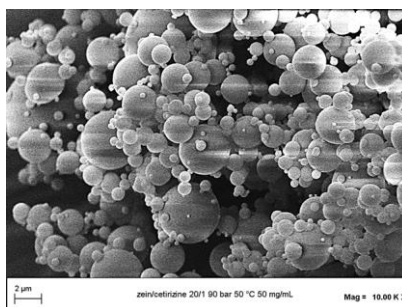
As concerns the system zein/CTZ, spherical microparticles were produced in all the conditions investigated (run #2-#4 in **Table IV.6**), namely 40°C, 45°C and 50°C, as observable in **Figure IV.38a**, **Figure IV.38b** and **Figure IV.38c**, respectively. However, as can be noted from the FESEM images, the microparticles produced at 50°C seemed to have a better morphology, in terms of sphericity and regularity, than the particles obtained under the other temperature conditions. From the comparison of the volumetric cumulative PSDs at different temperatures as reported in **Figure IV.39**, it was possible to deduce that the mean diameter increased by increasing the temperature up to 50°C, whereas the PSD widened.



(a)



(b)



(c)

Figure IV.38 FESEM images of zein/CTZ 20/1 particles obtained at 9 MPa, 50 mg/mL and (a) 40°C (run #2); (b) 45°C (run #3); (c) 50°C (run #4).

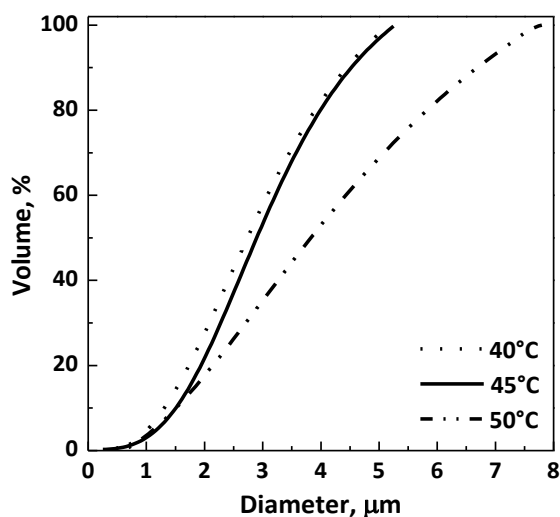


Figure IV.39 Volumetric cumulative PSDs of zein/CTZ 20/1 particles precipitated from DMSO at 9 MPa, 50 mg/mL; effect of the temperature.

Regarding the system zein/KTF, coalescent microparticles (**Figure IV.40a**) were obtained at 40°C (run #10 in **Table IV.6**), whereas well-defined microparticles were produced at 50°C (run #11 in **Table IV.6**), as shown in the FESEM image reported in **Figure IV.40b**. It should be noted that, in addition to the disappearance of coalescence, increasing the temperature from 40 to 45°C, an increase in the mean particle size was also observed, as evident in **Table IV.6**. However, by further increasing the temperature to 50°C (run #12 in **Table IV.6**), aggregates precipitated, as shown in **Figure IV.40c**. For this reason, the subsequent experiments on the influence of zein/KTF ratio (w/w) were performed by setting the temperature at 45°C in order to produce preferentially well-separated microspheres.

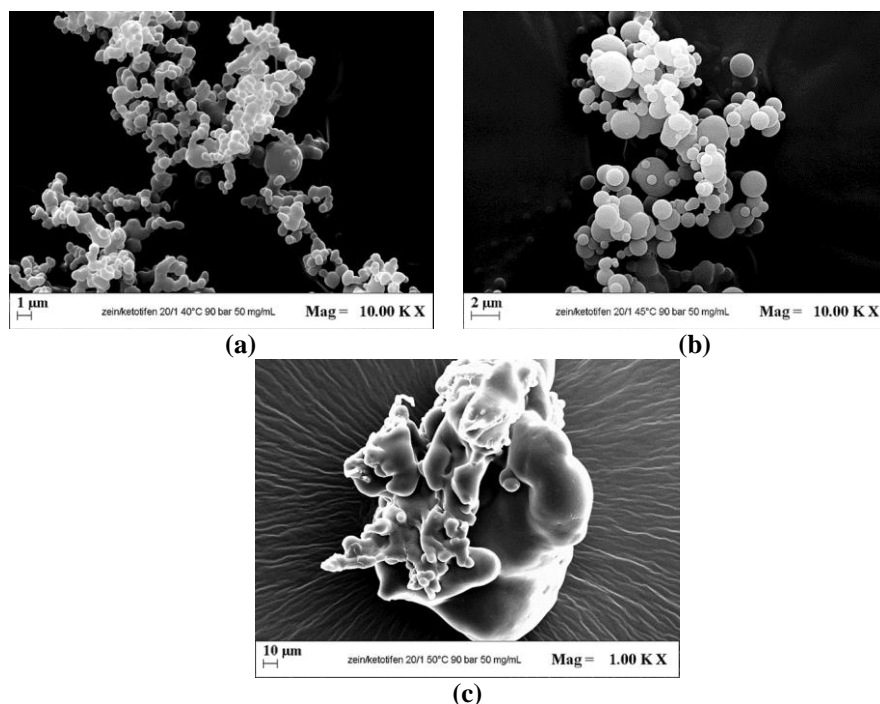


Figure IV.40 FESEM images of zein/KTF 20/1 precipitated at 9 MPa, 50 mg/mL; (a) coalescent particles at 40 °C (run #10); (b) microparticles at 45 °C (run #11); (c) aggregates at 50 °C (run #12).

Effect of zein/antihistamine ratio

Since roughly zein/CTZ micrometric particles were obtained at all temperatures previously investigated, it was decided to conduct a first set of experiments by reducing the polymer/drug ratio from 20/1 to 10/1 w/w at all the three different temperatures (runs #5, #6 and #7 in **Table IV.6**).

The first test was carried out operating at 40°C for a zein/CTZ ratio equal to 10/1 w/w; however, highly coalescing particles (**Figure IV.41a**) were obtained. From the second test conducted at 45°C and zein/CTZ ratio 10/1 w, coalescing particles along with spherical microparticles with mean size 4.02 µm were produced (**Figure IV.41b**). On the other hand, the third experiment, conducted at 50°C and 10/1 w/w, led to the attainment of very well-defined microspheres (**Figure IV.41c**) with an average diameter of 8.77 µm. This result confirmed that the temperature of 50°C is the optimum one for the system zein/CTZ.

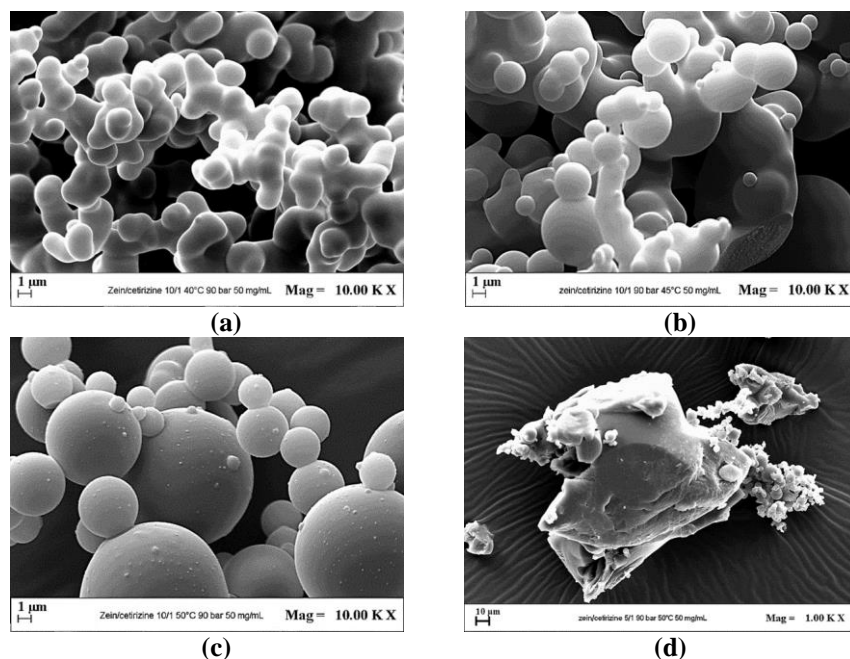


Figure IV.41 FESEM images of zein/CTZ precipitated at 9 MPa, 50 mg/mL, (a) 40°C and 10/1 w/w (run #5); (b) 45°C and 10/1 w/w (run #6); (c) 50°C and 10/1 w/w (run #7); (d) 40°C and 10/1 w/w (run #8).

Comparing the volumetric cumulative PSDs obtained at the fixed temperature of 50°C and polymer/drug ratios of 20/1 and 10/1 w/w (runs #4 and #7 in **Table IV.6**), for which only distinct microparticles precipitated, an increase in the mean particle size was observed as the polymer/drug ratio decreased. Based on most of the literature studies mentioned in the ‘State of the art’ section, an opposite trend in terms of size was generally observed as the polymer/drug ratio increases. The increase in particle size with the increase of zein/CTZ ratio; i.e., decreasing the amount of polymer that generally forces the morphology of the composite system, can be explained by considering some thermodynamic aspects of the SAS process. Under the process conditions 50°C/9 MPa, SAS operating point of the system is located above the MCP of the binary system DMSO/CO₂ (Andreatta et al., 2007a). However, the presence of one or more solutes can modify the high pressure VLEs of the system. In the specific case studied, cetirizine seems to have a greater influence on phase equilibria compared to zein. Hence by increasing the CTZ amount, the MCP of the quaternary system zein/CTZ/DMSO/CO₂ may have moved to higher pressures compared to the MCP of the binary system solvent/antisolvent. In general, the shift of the MCP towards higher pressure values is more evident the higher the concentration of the solute that affects VLEs, namely cetirizine (Campardelli et al., 2017b, Campardelli et al., 2019b). Therefore, when the test was

conducted at zein/CTZ 10/1 w/w (50°C/9 MPa), the operating point was located closer to the MPC with respect to the operating point at a ratio 20/1 w/w (50°C/9 MPa). As a consequence, larger particles precipitated working at a zein/CTZ ratio equal to 10/1 w/w, since it is well known that the particle size generally increases or decreases by approaching or moving away from the MCP, respectively (Reverchon et al., 2007, Reverchon et al., 2008b). The hypothesis of the influence of cetirizine on the high pressure VLEs was confirmed by conducting another test at 50°C and 9 MPa, further increasing the polymer/drug ratio to 5/1 w/w (run #8 in **Table IV.6**). Under these conditions, large crystals with very few particles precipitated, as shown in **Figure IV.41d**. The further increase in the quantity of antihistamine drug in the liquid solution has considerably altered the VLEs of the quaternary system zein/CTZ/DMSO/CO₂, so the operating point was in proximity or even below the MCP (i.e., inside the miscibility gap), condition that generally leads to the precipitation of crystals.

Regarding the system zein/KTF, the polymer/drug ratio was gradually decreased from 20/1 to 5/1 (runs #11, #13 and #14 in **Table IV.6**), at the optimized temperature of 45°C. In all cases, well-separated microparticles were produced, as can be observed in **Figure IV.42**. By comparing the cumulative volumetric PSDs at the different zein/KTF ratios (**Figure IV.43**), it was possible to observe that the variation of this parameter did not have a significant influence on the average size of the zein/KTF microspheres.

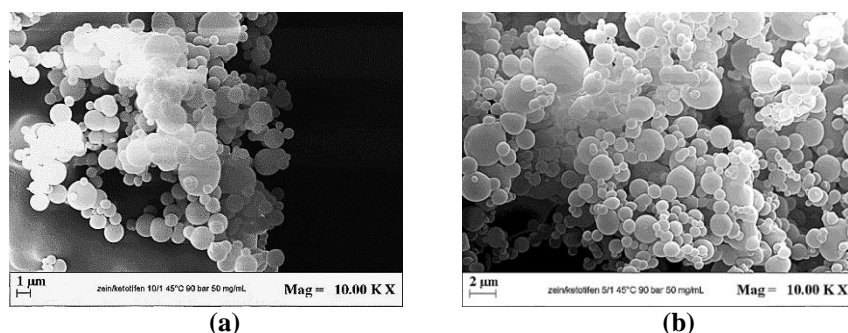


Figure IV.42 FESEM images of zein/KTF microparticles obtained at 45 °C, 9 MPa, 50 mg/mL and different polymer/drug ratios: (a) 10/1 w/w (run #13); (b) 5/1 w/w (run #14).

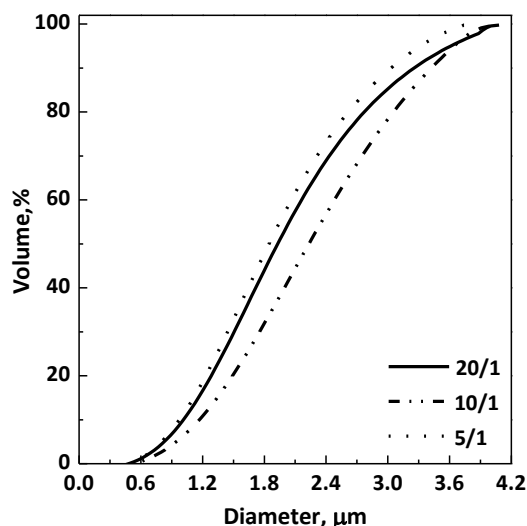


Figure IV.43 Volumetric cumulative PSDs of zein/KTF particles precipitated at 45°C, 9 MPa, 50 mg/mL; effect of polymer/drug ratio.

Characterization of zein/antihistamine samples

FTIR analyses were performed on unprocessed antihistamine drugs and zein, SAS processed powders at different zein/antihistamine w/w ratios. The FTIR spectra of samples were shown in **Figure IV.44** and **Figure IV.45** for CTZ and KTF, respectively. The spectrum of zein showed characteristic peaks at about 1645 cm^{-1} , 1541 cm^{-1} and 1236 cm^{-1} assigned to amide I, II and III, respectively (Karthikeyan et al., 2012). The spectrum of pure CTZ (**Figure IV.44**) exhibited many absorption bands, including that at 3044-3023 cm^{-1} due to C-H stretching of the aromatic ring, bands at 2984-2949 cm^{-1} attributed to CH_2 stretching, a strong band at 1740 cm^{-1} about the C=O stretching related to the carboxylic group, the band at 1602 cm^{-1} caused by the substitution at the para position on the benzene ring. The C-Cl stretching also appeared at 1457 cm^{-1} , in addition to bands at 1435 and 1319 cm^{-1} attributed to the C-O carboxylic bond, three different absorption bands at 1496, 1077 and 758 cm^{-1} related to the monosubstitution on the benzene ring, and bands at 846-809 cm^{-1} again associated to benzene rings (Hasan et al., 2012). The characteristic bands of zein predominated in the spectra of zein/CTZ coprecipitates, although the presence of some CTZ peaks (highlighted by thin vertical lines) confirmed the presence of drug in SAS powders, such as those associated with the CO stretching or benzene rings. The spectrum of KTF (**Figure IV.45**) showed bands at about 3425 cm^{-1} due to the N-H stretching vibration, at 16450 cm^{-1} because of the C=C aromatic stretching vibration, at 1477 cm^{-1} associated to the CH_3 bending vibration, at 1397 cm^{-1} due to the phenolic OH bending vibration, at 754 cm^{-1} for CH bending vibrations in -C=CH- group (Soltani et al., 2016). Many

characteristic bands of the drug can be noted in the spectra of SAS coprecipitated zein/KTF powders at different ratios. Furthermore, for both the systems zein/antihistamine, new bands or band shifts were not detected, thus no interaction between drug and polymer occurred after SAS process.

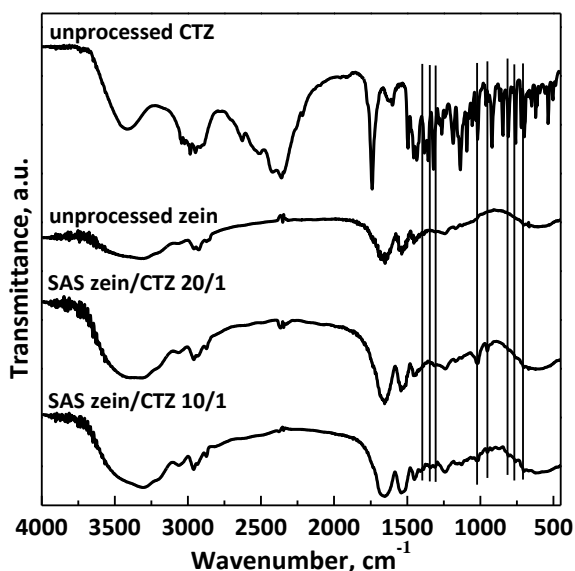


Figure IV.44 FTIR spectra of unprocessed CTZ and zein, and SAS processed zein/CTZ powders at different w/w ratios.

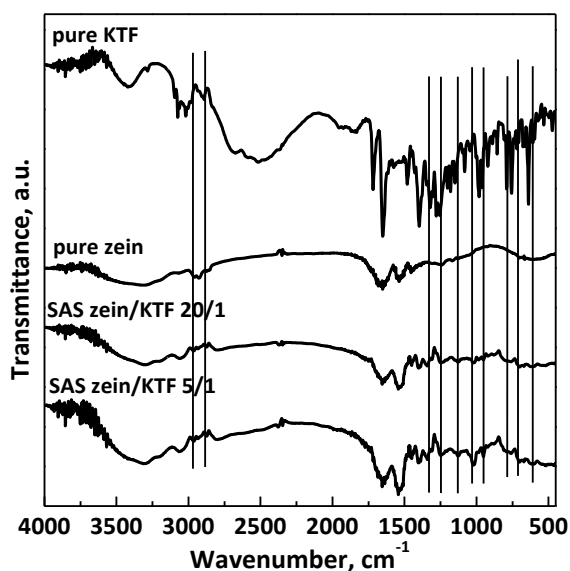


Figure IV.45 FTIR spectra of unprocessed KTF and zein, and SAS processed zein/KTF powders at different w/w ratios.

Dissolution tests were performed in PBS for the pure antihistamine drugs and SAS processed powders. For each zein/antihistamine system, both the influence of the polymer/drug ratio and of the operating temperature on the drug release rate from SAS composites was investigated.

In **Figure IV.46**, the dissolution profiles of CTZ from particles obtained at the same polymer/drug ratio of 20/1 w/w and different temperature were compared (runs #2-#4 in **Table IV.6**). Pure CTZ dissolved fairly quickly in PBS, in about 5 h. In the case of SAS processed powders, the CTZ release was prolonged about 5-6 times compared to pure drug, taking about a day. The complete dissolution of the antihistamine was reached in about 24-25 h in the case of the zein/CTZ 20/1 particles obtained at 40 and 45°C, whereas CTZ was completely released in about 30 h from SAS composites produced at 50°C. The presence of a burst effect of about 20%, caused by the fast dissolution of CTZ located near/on the particle surface, is evident in the case of composites produced at 40°C and 45°C. The burst-like effect is almost negligible (<5%) in the case of zein/CTZ microparticles produced at 50°C, probably due to the more regular morphology and larger size of these particles, which allow to trap a greater quantity of drug in the zein matrix, with respect to particles obtained at 40°C and 45°C.

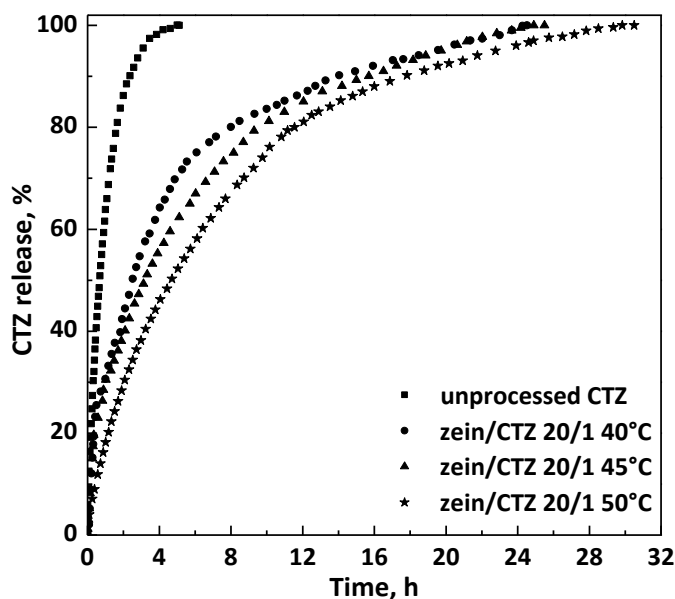


Figure IV.46 Dissolution profiles of CTZ in PBS at 37°C and pH 7.4; CTZ released from SAS particles produced at different operating temperatures.

In **Figure IV.47**, the dissolution profiles of CTZ from particles obtained at a temperature of 50°C and at different zein/CTZ ratios, namely 20/1 and 10/1, were compared (runs #4 and #7 in **Table IV.6**). The antihistamin drug was completely released in about 30 h both from zein-based microparticles

at 20/1 and 10/1 w/w ratio. However, in this last case, the burst effect (about 35%) was more pronounced compared to that observed in the case of microparticles zein/CTZ 20/1 w/w.

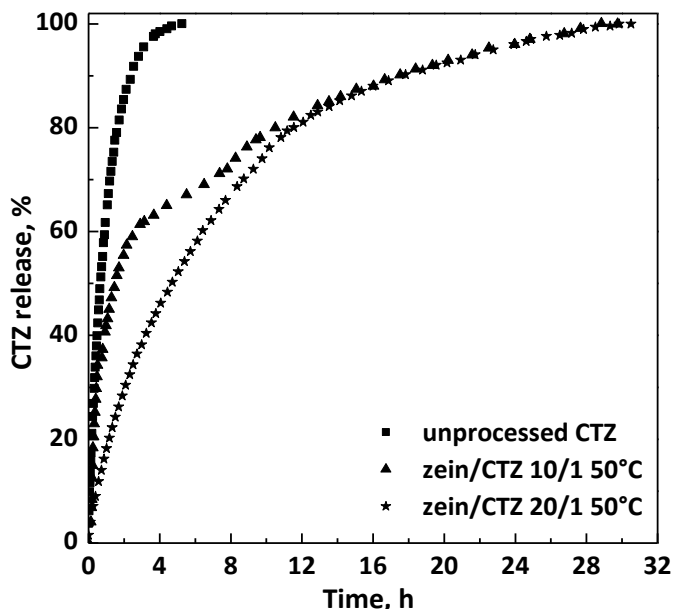


Figure IV.47 Dissolution profiles of CTZ in PBS at 37°C and pH 7.4; CTZ released from SAS particles at different polymer/drug ratios.

In **Figure IV.48**, the dissolution profiles of KTF from particles obtained at polymer/drug ratio 20/1 w/w and different operating temperatures (i.e.; 40°C and 45°C) were compared (runs #10 and #11 in **Table IV.6**). The samples obtained at the temperature of 50°C were excluded from the study, since only large aggregates precipitated. Pure KTF completely dissolved in PBS in just 30 minutes; whereas the antihistamine was released after about 5 h and 42 h from SAS powders obtained at 40°C and at 45°C, respectively. This difference in the dissolution kinetics can be explained taking into account the different morphology of composites. Indeed, coalescing particles of small dimensions (about 0.7 μm) were obtained at 40°C, consequently the coprecipitation failed at least in part; i.e., part of KTF could not be entrapped in the zein matrix. Spherical microparticles with mean size of about 2 μm were produced at 45°C; in this case it was possible to reach a more prolonged release, thanks to an effective coprecipitation that allowed to trap all KTF into the microspheres. In this case, the presence of the burst effect is less than 10%. In **Figure IV.49**, the dissolution profiles of KTF from particles obtained at 45°C and at different zein/KTF ratios, namely 20/1 and 5/1, were compared (runs #12 and #14 in **Table IV.6**). The antihistamin was completely released in about 36 h from microparticles at zein/KTF ratio equal to 5/1 w/w, whereas the burst effect was about 22%.

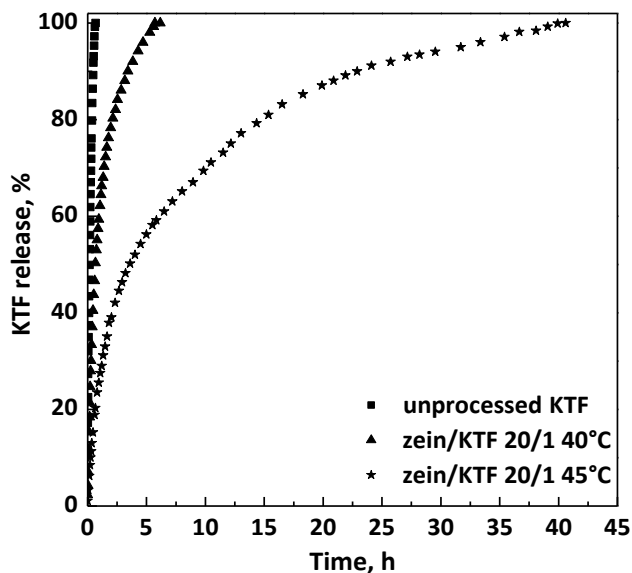


Figure IV.48 Dissolution profiles of KTF in PBS at 37 °C and pH 7.4; KTF released from SAS particles produced at different operating temperatures.

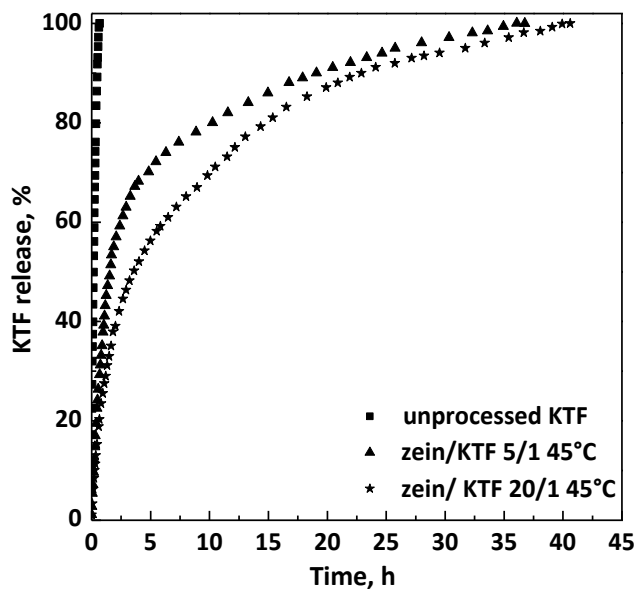


Figure IV.49 Dissolution profiles of KTF in PBS at 37 °C and pH 7.4; KTF released from SAS particles at different polymer/drug ratios.

Discussion

SAS coprecipitation with zein is an effective route to prolong the release rate of antihistamine drugs. The results achieved with zein/antihistamine

systems are very relevant because, nowadays, the attention of many pharmaceutical companies is focused on the production of next generation formulations, which extends the antihistamine release at least within a day. As required, SAS coprecipitates zein/CTZ and zein/KTF allow to reduce the administration frequency and, consequently, side effects associated to antistamine overdose. In the case of the allergy treatment, a low burst effect in the drug release kinetics is also a valid option, as an immediate response against allergens. Indeed, in the context of new prolonged-release formulations, a novel goal is to achieve a bimodal release of the antihistamine: an immediate release of a small amount of the drug, to quickly relieve symptoms associated with allergy, followed by a prolonged release of the remaining drug dose, to avoid repeated administration throughout the day. SAS-produced powders zein/CTZ and zein/KTF satisfy these prerequisites. Bimodal release formulations as those obtained in this part of the work are recently coveted by pharmaceutical companies for the allergy treatment.

IV.4 The use of Eudragit as polymeric carrier

Given the presence on the market of different types of Eudragits, an initial screening by processing some of them was carried out, namely Eudragit RSPO, Eudragit RLPO, Eudragit EPO and Eudragit L100-55. All preliminary tests were performed using DMSO as solvent, at 40°C, 12 MPa and a polymer concentration of 20 mg/mL. Eudragit RSPO and Eudragit RLPO were completely extracted from the solvent/antisolvent mixture formed into the precipitation chamber, not allowing the powder recovery. Few crystals precipitated by processing Eudragit EPO, which was mostly extracted, whereas, a particle morphology was observed only by micronizing Eudragit L100-55. Based on the preliminary results obtained and the considerations emerged from the literature studies as mentioned in the ‘State of the art of the SAS process’, Eudragit L100-55 (EUD) was selected as the most promising Eudragit for SAS process.

Firstly, EUD micronization was studied to know in detail the morphology obtainable by SAS technique, at different process conditions. Then, coprecipitation tests were performed to assert that EUD is a novel carrier for a controlled drug delivery. An antibiotic, a NSAID and a bronchodilator drug were selected as model compounds for SAS coprecipitation with EUD, namely DIC, AMPI and THEOP, respectively.

IV.4.1 SAS micronization of Eudragit L100-55

A preliminary study was carried out by micronizing EUD alone. For this set of experiments, DMSO was used as the liquid solvent, the temperature was fixed at 40°C, as well as a CO₂ flow rate of 30 g/min and a solution flow

rate of 1 mL/min, in order to ensure the supercritical mixture conditions. These conditions were also employed for the subsequent coprecipitation tests performed on the different EUD/drug systems. **Table IV.7** reports a list of some experiments performed by micronizing EUD alone, at different pressure and EUD concentration in DMSO; the morphology and the dimensions of particles on a volumetric basis were indicated.

Table IV.7 A list of SAS experiments performed on Eudragit L100-55 (MP: microparticles; cMP: coalescent microparticles).

#	P (MPa)	C _{tot} (mg/mL)	Morphology	m.d.±s.d. (μm)
1	9	20	MP	1.99±0.49
2	10	20	MP	1.69±0.51
3	12	20	cMP	1.64±0.72
4	10	40	MP	1.95±0.54

Effect of the operating pressure

The effect of the operating pressure was investigated setting a polymer concentration in DMSO equal to 20 mg/mL and gradually increasing the pressure from 9 to 12 MPa (runs #1-#3 in **Table IV.7**).

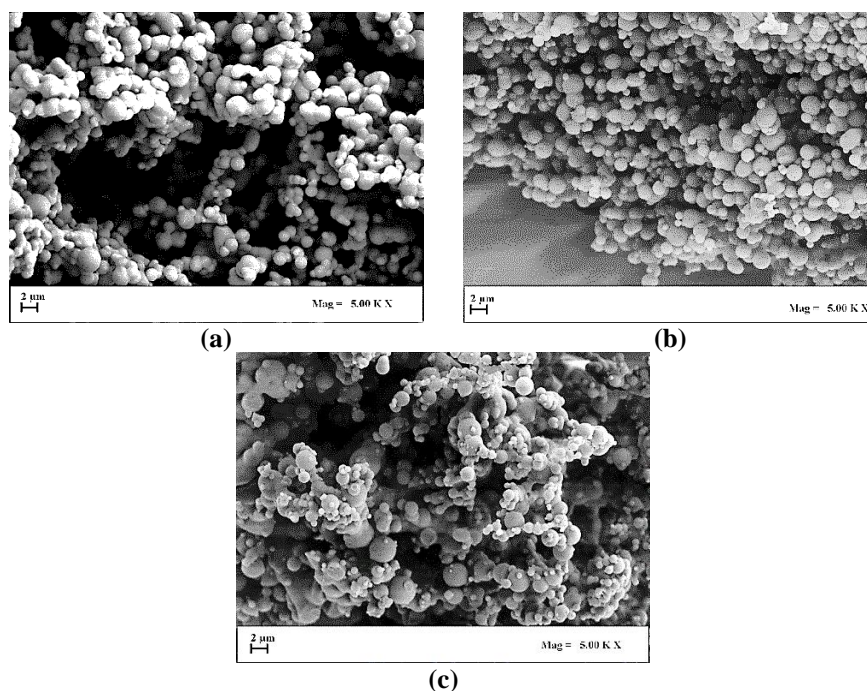


Figure IV.50 FESEM images of Eudragit particles precipitated from DMSO at 40°C, 20 mg/mL and (a) 9 MPa; (b) 10 MPa; (c) 12 MPa.

FESEM analyses revealed that well-separated spherical microparticles were obtained working at 9 and 10 MPa (**Figure IV.50a** and **Figure IV.50b**, respectively), whereas coalescing and more irregular in shape and dimensions microparticles were formed at 12 MPa (**Figure IV.50c**). Moreover, a slight increase of the particle dimensions was observed by decreasing the pressure, as shown in the last column of **Table IV.7**.

Effect of the polymer concentration

Fixing the pressure at 10 MPa, which seemed to allow the production of microparticles with the best morphology, the polymer concentration in DMSO was increased at 40 mg/mL (run #4 in **Table IV.7**). This concentration value was chosen considering the maximum EUD solubility in DMSO equal to about 55 mg/mL, experimentally determined at room temperature. Spherical microparticles of EUD were produced at 40 mg/mL; the comparison of the volumetric cumulative PSDs in **Figure IV.51** (related to runs #2 and #4 in **Table IV.7**) demonstrated that the mean particle size increased and PSD widened by increasing the EUD concentration in DMSO.

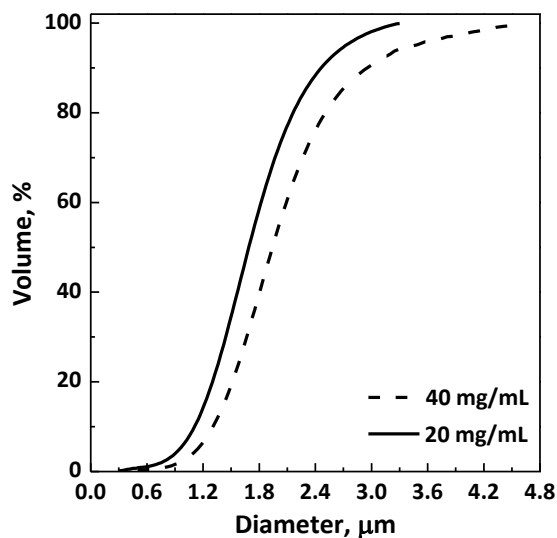


Figure IV.51 Volumetric cumulative PSDs of EUD precipitated from DMSO at 40°C and 10 MPa; effect of the polymer concentration in DMSO.

IV.4.2 Eudragit/ampicillin coprecipitation

After optimizing the EUD micronization, SAS coprecipitation was firstly attempted using AMPI as model drug. Based on the previous results, 9 and 10 MPa were selected as optimum pressures to perform the following coprecipitation tests, at a temperature of 40°C. The effect of the overall concentration in DMSO and polymer/drug ratio w/w on composites were

also investigated. In **Table IV.8**, the morphology, mean diameter and standard deviation of particles are indicated for each test.

Table IV.8 SAS experiments performed on Eudragit/ampicillin system (SMP: sub-microparticles; MP: microparticles; cMP: coalescent microparticles).

#	EUD/AMPI (w/w)	P (MPa)	C _{tot} (mg/mL)	M	m.d.±s.d. (µm)
1	0/1	9	20	SMP	0.23±0.15
2	20/1	9	40	MP*+cMP	*2.82±0.94
3	20/1	10	40	MP	1.99±0.57
4	20/1	10	20	cMP	-
5	20/1	10	50	MP	2.52±0.73
6	10/1	10	50	MP	1.53±0.47

Effect of the operating pressure

Fixing the overall concentration in DMSO at 40 mg/mL and the polymer/drug ratio at 20/1 w/w, the effect of the pressure on Eudragit/AMPI system was investigated varying it from at 9 and 10 MPa (runs #2 and #3 in **Table IV.8**). A high degree of coalescence was observed in particles obtained at 9 MPa (**Figure IV.52a**) than that produced at 10 MPa (**Figure IV.52b**). In particular, more-defined EUD/AMPI microparticles with a mean diameter of about 2 µm were produced working at 10 MPa.

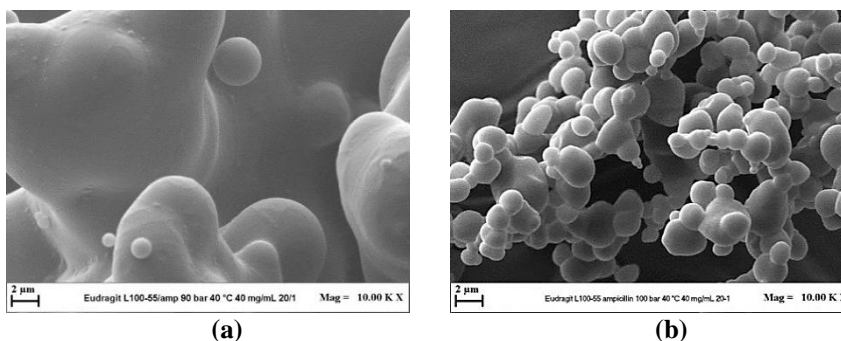


Figure IV.52 FESEM images of EUD/AMPI 20/1 particles precipitated from DMSO at 40°C and 40 mg/mL. Effect of the operating pressure: (a) 9 MPa (run #2); (b) 10 MPa (run #3).

Effect of the overall concentration in DMSO

Since the pressure of 10 MPa led to obtaining microparticles, this value was set to study the influence of the overall concentration in DMSO on EUD/AMPI composites, at a polymer/drug ratio of 20/1 w/w. Very coalescing particles (**Figure IV.53a**) precipitated at 20 mg/mL (run #4 in

Table IV.8); whereas, microparticles were produced by increasing the total concentration at 40 and 50 mg/mL (runs #2 and #5 in **Table IV.8**), as shown in **Figure IV.53b** and **Figure IV.53c**, respectively.

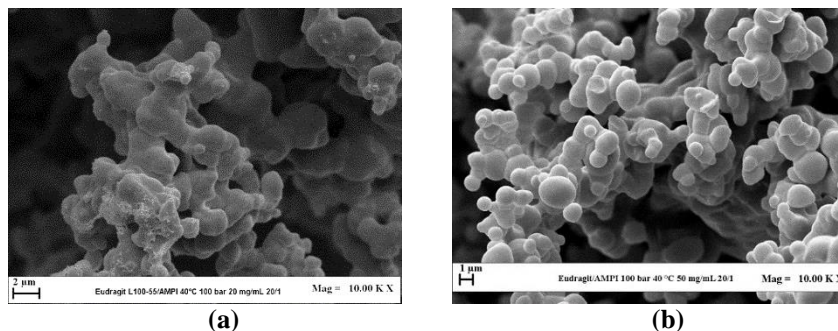


Figure IV.53 FESEM images of EUD/AMPI 20/1 particles precipitated at 40°C, 10 MPa and (a) 20 mg/mL (run #4); (b) 50 mg/mL (run #5).

Effect of EUD/AMPI ratio

The optimized pressure and overall concentration; i.e., 100 MPa and 50 mg/mL, were selected to investigate the effect of the EUD/AMPI ratio. Decreasing the polymer/drug ratio at 10/1 w/w (run #6 in **Table IV.8**), microparticles were produced; a reduction of mean particle size was noted with respect to 20/1 ratio, as highlighted by the comparison of PSDs in **Figure IV.54**. Since a worsening the particle morphology slightly was observed by varying the ratio from 20/1 to 10/1, it was decided not to further reduce the EUD/AMPI ratio.

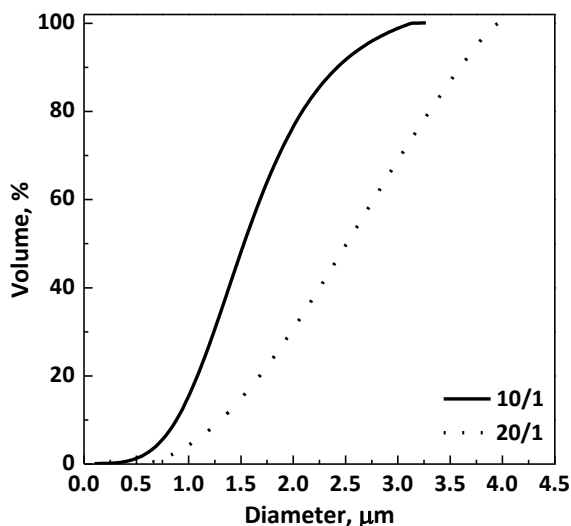


Figure IV.54 Volumetric cumulative PSDs of EUD/AMPI particles produced at 40°C, 10 MPa and 50 mg/mL; effect of the polymer/drug ratio.

Characterization of EUD/AMPI samples

FTIR spectra of unprocessed AMPI and Eudragit L100-55, physical mixture EUD/AMPI 10/1 w/w and SAS processed EUD/AMPI 10/1 are reported in **Figure IV.55**. FTIR spectrum of pure EUD was characterized by absorption bands at around 1157 cm^{-1} , 1184 cm^{-1} e 1261 cm^{-1} due to the ester vibrations, peaks at about 1701 cm^{-1} and at 1736 cm^{-1} attributed to the C=O stretching of the carboxylic acid and the vibrations of the esterified carboxyl groups, respectively; moreover, the presence of peaks at 1387 cm^{-1} , 1479 cm^{-1} e 2979 cm^{-1} corresponded to CHX vibrations (Majeed et al., 2017). The spectra of physical mixture and SAS coprecipitated powders EUD/AMPI exhibited all the bands related to the polymer, due to its higher amount, and some characteristic peaks of the drug, such as peaks at about $646\text{ e }697\text{ cm}^{-1}$ attributed to the stretching of S-C bond (Gunasekaran et al., 1996).

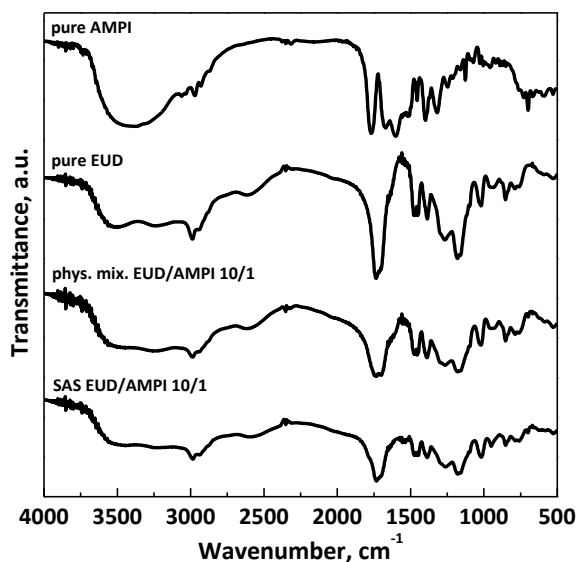


Figure IV.55 FTIR spectra for unprocessed AMPI and EUD, physical mixture polymer/drug 10/1 and SAS processed powders EUD/AMPI 10/1.

Thermal analyses (**Figure IV.56**) were performed on unprocessed AMPI and Eudragit L100-55 and SAS processed EUD/AMPI 10/1 w/w. EUD has a glass transition temperature (T_g) at around 110°C ; two endothermic peaks appeared in its DSC thermogram, the first due to the dehydration and the second peak at about 200°C , related to the melting of the crystalline portion of the polymer (Ceballos et al., 2005). DSC thermogram of pure AMPI showed a first endothermic peak due to the loss of volatile compounds and another at about 233°C corresponding to the melting point (Marciniec et al., 2002). The SAS coprecipitated powders had a thermal behavior similar to the polymer one, with a slightly higher degree of amorphism, probably due to the particle size reduction after SAS process.

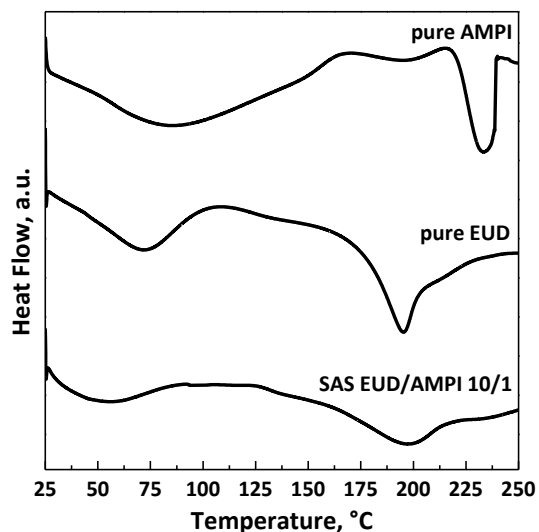


Figure IV.56 DSC thermograms of unprocessed AMPI and Eudragit L100-55, SAS processed EUD/AMPI composites 10/1.

The dissolution profiles of AMPI in pure form and released from SAS EUD/AMPI 20/1 and 10/1 w/w were compared in **Figure IV.57**.

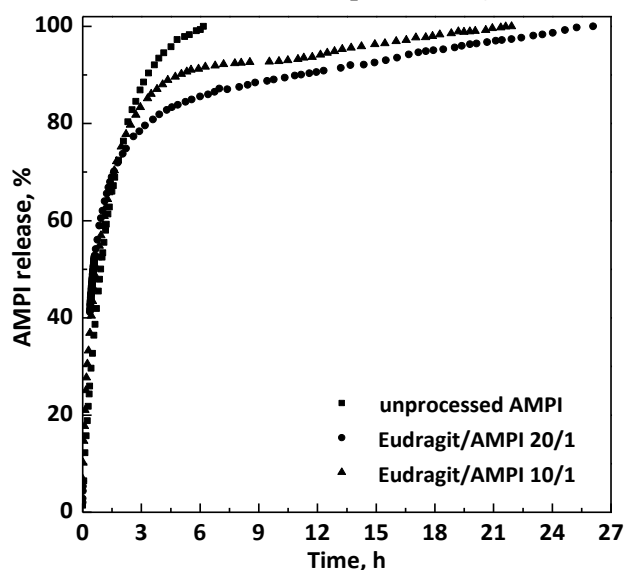


Figure IV.57 Dissolution profiles in PBS at 37°C and pH 7.4.

Unprocessed AMPI completely dissolved in about 6.5 h, whereas SAS processed EUD/AMPI 20/1 and 10/1 took about 26 and 22 h, respectively, therefore their complete dissolution was respectively 4 and 3 times slower than that of the pure drug. Unfortunately, a very high burst effect was observed, equal to about 65% and 80% in the case of 20/1 and 10/1 particles,

respectively. This result means that only a small part of AMPI is incorporated in the internal area of the composite particles.

IV.4.3 Eudragit/diclofenac coprecipitation

The influence of pressure, overall concentration of solutes in DMSO and polymer/drug ratio was also studied on EUD/DIC systems. A summary of some experiments performed at the different process conditions is reported in **Table IV.9**, indicating the obtained morphology, the mean diameter and the standard deviation on a volumetric basis. In particular, some results reported.

Table IV.9 SAS experiments performed on Eudragit/diclofenac system (NP: nanoparticles; MP: microparticles; cMP: coalescing microparticles).

#	EUD/DIC (w/w)	P (MPa)	C _{tot} (mg/mL)	M	m.d.±s.d. (µm)
1	0/1	9	20	NP	0.14±0.05
2	20/1	9	40	MP*+cMP	*2.16±0.69
3	20/1	10	40	MP	2.47±0.71
4	20/1	10	20	cMP	-
5	20/1	10	50	MP	2.92±0.81
6	10/1	10	50	MP	1.53±0.45

Effect of the operating pressure

Firstly, the effect of the pressure was investigated for the system EUD/DIC by selecting 9 and 10 MPa as pressures, according to the previous results obtained by studying EUD micronization. An overall concentration in DMSO of 40 mg/mL and a polymer/drug ratio of 20/1 w/w were also fixed.

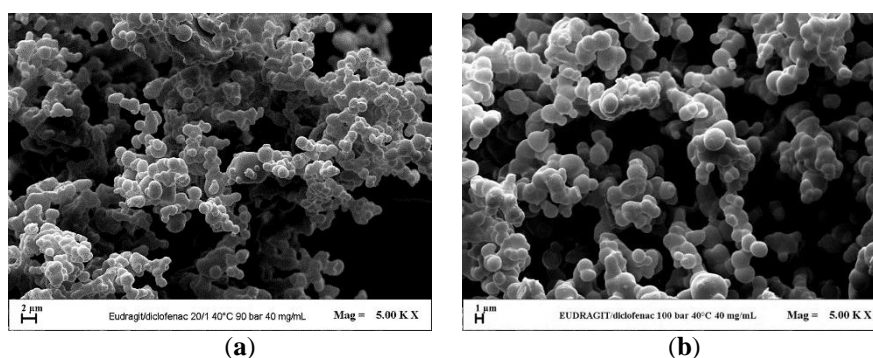


Figure IV.58 FESEM images of EUD/DIC 20/1 particles precipitated from DMSO at 40°C and 40 mg/mL. Effect of the operating pressure: (a) 9 MPa (run #2); (b) 10 MPa (run #3).

Similarly to EUD/AMPI system, a less degree of coalescence of EUD/DIC particles was observed operating at 10 MPa (run #3 in **Table IV.9**) with respect to 9 MPa (run #2 in **Table IV.9**), as observable from the FESEM images reported in **Figure IV.58**.

Effect of the overall concentration in DMSO

Since the pressure of 10 MPa allows the attainment of more-defined EUD/DIC particles, the influence of the overall concentration in DMSO at a polymer/drug ratio of 20/1 w/w was evaluated in correspondence of that pressure. Very coalescing particles precipitated at 20 mg/mL (run #4 in **Table IV.9**), whereas an improvement in morphology was observed by increasing the total concentration up to 50 mg/mL (run #5 in **Table IV.9**). Moreover, an increase in particle size was determined by the increase of the total concentration; indeed, the mean diameter of microparticles obtained at 50 mg/mL (about 2.9 μm) was higher than that of particles formed at 40 mg/mL (about 2.5 μm).

Effect of EUD/DIC ratio

The EUD/DIC ratio was decreased from 20/1 to 10/1 w/w (runs #5 and #6 in **Table IV.9**), at the selected conditions of pressure and overall concentration of 10 MPa and 50 mg/mL. Slightly irregular and coalescing microparticles were produced working at 10/1 w/w; a decrease of the mean particle size was also observed by decreasing the polymer/drug ratio.

Characterization of EUD/DIC samples

FTIR spectra of pure DIC, unprocessed and processed EUD, physical mixture EUD/DIC 10/1 w/w and SAS processed EUD/DIC 20/1 and 10/1 are reported in **Figure IV.59**. The spectra of pure and unprocessed EUD showed absorption bands at around 1157 cm^{-1} , 1184 cm^{-1} e 1261 cm^{-1} due to the ester vibrations, peaks at about 1701 cm^{-1} and at 1736 cm^{-1} attributed to the C=O stretching of the carboxylic acid and the vibrations of the esterified carboxyl groups, respectively; moreover, the presence of peaks at 1387 cm^{-1} , 1479 cm^{-1} e 2979 cm^{-1} corresponded to CHX vibrations (Majeed et al., 2017). No changes were observed in the polymer at the level of the functional group after SAS processing. FTIR spectra of the physical mixture and SAS processed EUD/DIC powders clearly showed the characteristic bands of the polymer since it is present in more quantity, and few peaks related to DIC as the stretching of C-Cl bond at about 720 cm^{-1} (Edavalath et al., 2011).

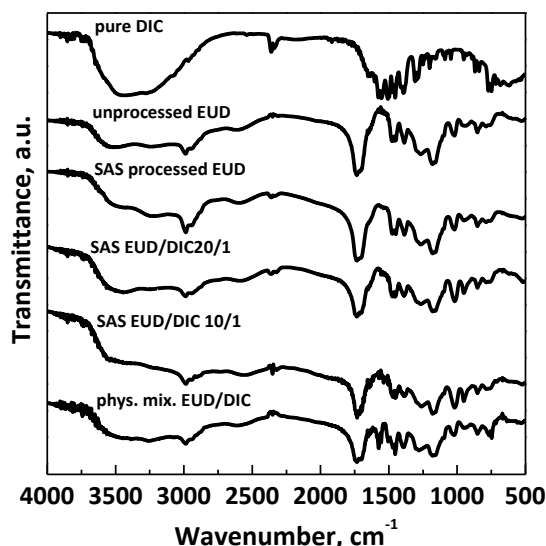


Figure IV.59 FTIR spectra for unprocessed and SAS processed EUD, unprocessed DIC, physical mixture and SAS processed EUD/DIC powders.

DSC thermograms of unprocessed DIC, unprocessed and processed EUD and SAS processed EUD/drug 20/1 and 10/1 w/w are reported in **Figure IV.60**. The DSC curve of pure DIC showed two endothermic peaks, the first one related to the dehydration and the second one at about 288°C corresponding to the melting point (Tița et al., 2011). The thermogram of unprocessed EUD had two endothermic peaks, the first one due to the loss of water and the other one at about 200°C related to the melting of the crystalline portion of the polymer (Ceballos et al., 2005). Moreover, in agreement with the literature (Jadhav et al., 2014), unprocessed EUD is characterized by a glass transition temperature (T_g) at around 119°C, slightly shifted at lower temperature (around 112°C) for SAS processed EUD due to the scCO₂ plasticizing effect in presence of semicrystalline polymers (Lian et al., 2006, Campardelli et al., 2019a). The thermal behavior of SAS coprecipitated powders is similar to the polymer one. The absence of the melting point of the drug in the thermograms of the coprecipitated powders can be ascribed to the amorphization. Moreover, because of the particle size reduction, a slightly higher degree of amorphism is detected both in SAS processed polymer and SAS coprecipitated powders with respect to unprocessed EUD, as observable from the less pronounced melting peak linked to the crystalline portion of the polymer.

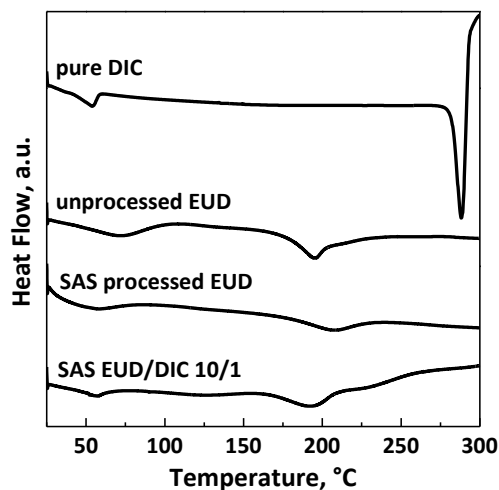


Figure IV.60 DSC thermograms of unprocessed and SAS processed EUD, unprocessed drugs, and SAS processed EUD/drug powders.

XRD patterns of pure DIC, unprocessed EUD and SAS processed EUD/drug 10/1 w/w are reported in **Figure IV.61**. XRD analyses confirmed the outcomes deduced by DSC thermograms; i.e., the pure drugs were in a crystalline state, the pure EUD showed a semi-crystalline pattern, whereas the coprecipitated powders were characterized by an amorphous behavior.

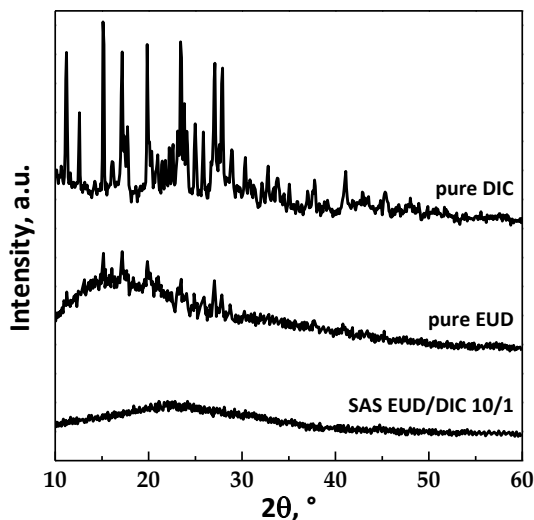


Figure IV.61 XRD patterns of unprocessed EUD and DIC, and SAS processed EUD/DIC powders.

Dissolution tests were performed using UV-vis spectroscopy to compare the dissolution rate of unprocessed drug with the drug coprecipitated with EUD. The dissolution profiles in PBS of the unprocessed DIC, physical

mixture EUD/DIC 10/1 w/w and SAS processed EUD/DIC 20/1 and 10/1 are reported in **Figure IV.62**. Pure DIC and DIC present in the physical mixture were completely released in about 4 h and 10 h, respectively. The delayed effect of the drug release due to the coprecipitation with the polymer is evident since the complete dissolution is achieved for both SAS coprecipitated powders 20/1 and 10/1 in about 100 h with a similar burst effect (about 45%), which is ascribable to the drug portion located near/on the surface of the particles. In summary, the dissolution of DIC coprecipitated with EUD was about 28 times slower with respect to the unprocessed NSAID.

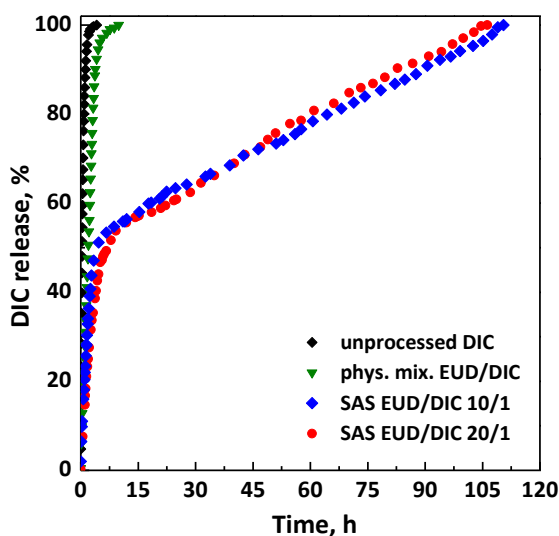


Figure IV.62 Dissolution profiles in PBS at 37 °C and pH 7.4.

Discussion

Summarizing the results related to the use of Eudragit L100-55 as carrier for AMPI and DIC, namely the first two active principles selected, it can be asserted that the coprecipitation was achieved only in part, since small and sometimes irregular microparticles generally precipitated. The UV-vis dissolution tests highlighted that a very high burst effect in the range 65-80% was obtained in the case of EUD/AMPI particles (size in the range 1.5-2.5 μm), indicating that the coprecipitation failed at least to some extent. The burst-like effect slightly decreased in the case of EUD/DIC composites (about 45%), which were characterized by larger particle size (in the range 1.5-2.9 μm) with respect to those obtained with the other system. Once again it is possible to correlate the particle size to the percentage of drug that can actually be trapped in the polymeric matrix, as verified in the previous paragraph using zein as carrier.

IV.4.4 Eudragit/theophylline coprecipitation

In order to achieve a control of the chronic bronchial asthma, THEOP was selected as model bronchodilator drug to be coprecipitated with EUD. A summary of several experiments performed at different process conditions is reported in **Table IV.10**, indicating the obtained morphology, the mean diameter and the standard deviation on a volumetric basis.

Table IV.10 SAS experiments performed on Eudragit/theophylline system (C: crystals; MP: microparticles; cMP: coalescing microparticles; EMP: expanded microparticles).

#	EUD/THEOP (w/w)	P (MPa)	C _{tot} (mg/mL)	M	m.d.±s.d. (µm)
1	0/1	9	20	C	-
2	20/1	10	40	C	-
3	20/1	10	20	C+MP*	*6.79±1.84
4	20/1	12	20	MP	5.93±1.62
5	20/1	15	20	cMP	1.64±0.32
6	20/1	12	40	MP	5.65±1.66
7	10/1	12	40	MP*+EMP	*3.75±1.08

A preliminary test was performed by processing THEOP alone at 40°C, 9 MPa and a drug concentration in DMSO equal to 20 mg/mL (run #1 in **Table IV.10**). At the end of SAS test, no powder was found in the precipitation chamber, because it was probably extracted by the mixture formed by the organic solvent and scCO₂. Long crystals of THEOP were observed by analyzing at FESEM the very few granules that were recovered. It was possible to conclude that THEOP is not a good candidate for SAS micronization. In order to successfully coprecipitate the model bronchodilator drug with EUD, the effect of the pressure, the overall concentration of EUD/THEOP in DMSO and the polymer/drug ratio on the morphology and size of the produced composite particles was investigated.

Effect of the operating pressure

Considering that the pressure of 10 MPa gave the best results in terms of sphericity and mean diameter of the powders both in the case of EUD/AMPI and EUD/DIC coprecipitation, preliminary tests with the system EUD/THEOP 20/1 w/w at 40 mg/mL (run #2 in **Table IV.10**) and 20 mg/mL (run #3 in **Table IV.10**) were performed in correspondence of this pressure. Using this system, crystals and crystals precipitated with coalescing microparticles (as shown in **Figure IV.63a** and **Figure IV.63b** for run #3) were obtained at 40 mg/mL and 20 mg/mL, respectively. This outcome may be explained taking into account the thermodynamic aspects. Considering the temperature of 40°C, the MCP of the binary system

DMSO/CO₂ is located at 8.61 MPa (Andreatta et al., 2007b); it means that the operating point at 10 MPa is above the MCP. However, the presence of the solutes can modify the high-pressure VLEs of the system, and the MCP of the quaternary system EUD/THEOP/DMSO/scCO₂ could shift towards higher pressures with respect to the one of the binary system solvent-antisolvent. This shift of the MCP towards higher pressures is generally more evident by increasing the concentration of the solutes in the liquid solution (Campardelli et al., 2017b, Campardelli et al., 2019b). In this specific case, the presence of THEOP probably modified the high-pressure VLEs, thus the operating point at 10 MPa could be below the MCP and lie in the biphasic region, from which a split of the precipitated solute in two morphologies may occur; i.e., crystals and microparticles as in case of run #3. In the following set of experiments, with the aim of shifting the operating point above the MCP, the total concentration in DMSO was fixed at 20 mg/mL, and the effect of pressure in the range 10-15 MPa (runs #3-5 in **Table IV.10**) was evaluated. Well-defined spherical microparticles (**Figure IV.63c**) were obtained in correspondence of a pressure of 12 MPa, whereas slightly coalescing microparticles precipitated at 15 MPa (**Figure IV.63d**). Moreover, it was observed that the particles mean diameter decreased by increasing the pressure, as shown by the comparison of the volumetric cumulative PSDs reported in **Figure IV.64**.

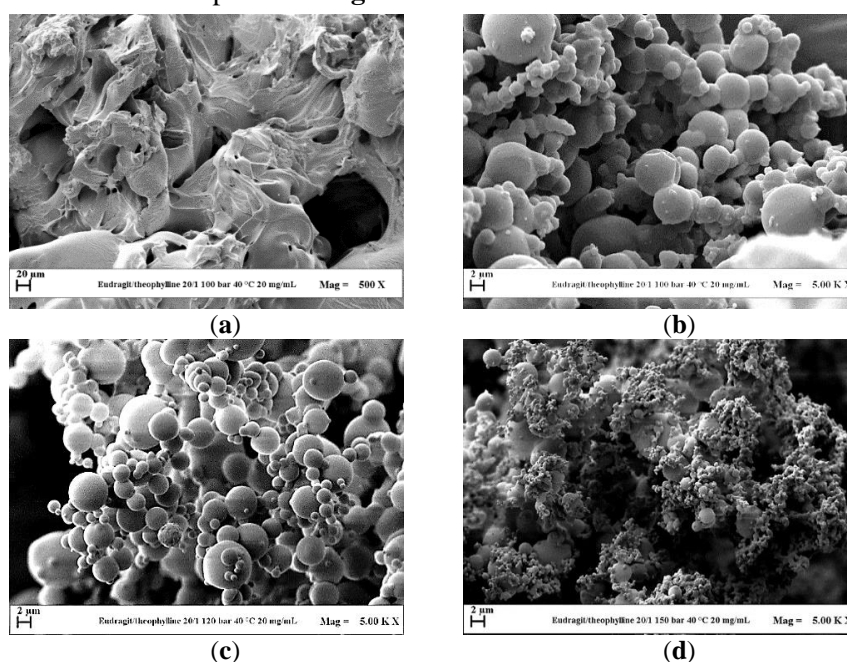


Figure IV.63 FESEM images of EUD/THEOP 20/1 powders precipitated from DMSO at 40°C, 20 mg/mL and (a) 10 MPa (run #3) filter; (b) 10 MPa (run #3) precipitating chamber; (c) 12 MPa (run #4); (d) 15 MPa (run #5).

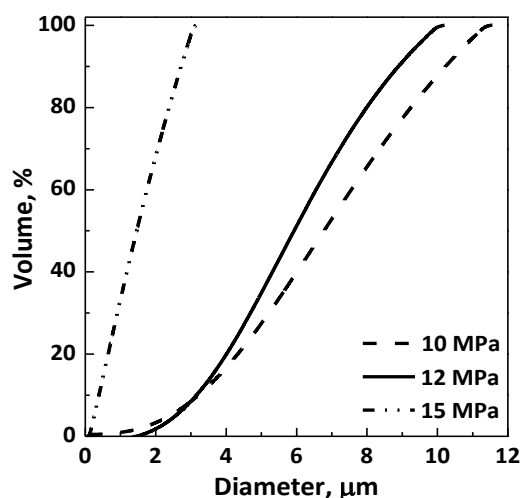


Figure IV.64 Volumetric cumulative PSDs of EUD/THEOP 20/1 particles precipitated from DMSO at 40°C and 20 mg/mL; the effect of pressure.

Effect of the overall concentration in DMSO

For the system EUD/THEOP 20/1 w/w, the effect of the overall concentration in DMSO was evaluated at the optimized pressure of 12 MPa in the range 20-40 mg/mL (runs #4 and #6 in **Table IV.10**). Well-defined microparticles were obtained at 40 mg/mL as well as at 20 mg/mL, and no significant changes in terms of particle size occurred.

Effect of EUD/THEOP ratio

EUD/THEOP ratio was decreased from 20/1 to 10/1 w/w, fixing the pressure at 12 MPa and the total concentration at 40 mg/mL. Well-defined microparticles (**Figure IV.65a**) were obtained at 10/1 w/w (run # 7 in **Table IV.10**), with lower average size than the particles produced at 20/1, as shown from the comparison of the volumetric cumulative PSDs in **Figure IV.66**.

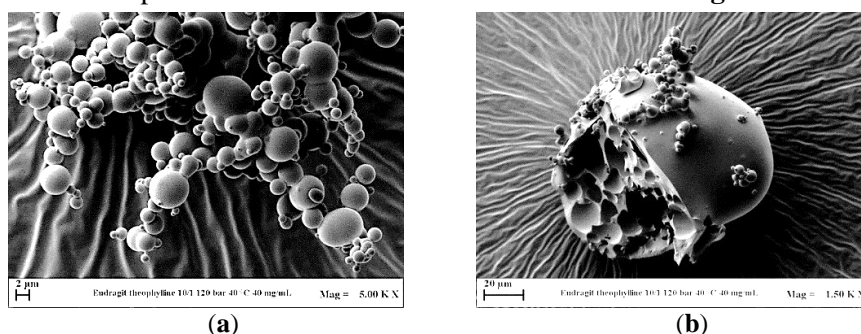


Figure IV.65 FESEM images of EUD/THEOP 10/1 w/w precipitated from DMSO at 40°C, 12 MPa and 40 mg/mL (run #7): (a) microparticles and (b) expanded microparticles.

The presence of few larger particles (**Figure IV.65b**) with an internal structure characterized by holes was also noted working at 10/1 w/w. This outcome can be ascribed to the higher influence of theophylline on the VLEs, since a higher concentration in the liquid solution can cause the MCP shift at higher pressures.

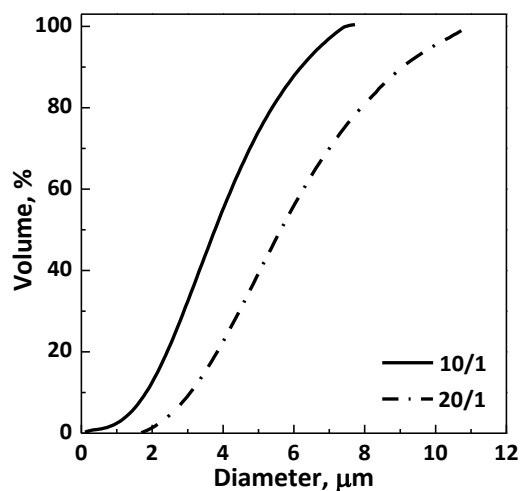


Figure IV.66 Volumetric cumulative PSDs of EUD/THEOP particles precipitated from DMSO at 40°C, 12 MPa and 40 mg/mL; effect of the polymer/drug ratio.

Characterization of EUD/DIC samples

FTIR spectra of unprocessed THEOP, unprocessed and processed EUD, physical mixture EUD/ THEOP 10/1 w/w and SAS processed EUD/ THEOP 20/1 and 10/1 are reported in **Figure IV.67**. FTIR spectra of pure and unprocessed EUD is characterized by absorption bands at around 1157 cm^{-1} , 1184 cm^{-1} e 1261 cm^{-1} due to the ester vibrations, peaks at about 1701 cm^{-1} and at 1736 cm^{-1} attributed to the C=O stretching of the carboxylic acid and the vibrations of the esterified carboxyl groups, respectively; moreover, the presence of peaks at 1387 cm^{-1} , 1479 cm^{-1} e 2979 cm^{-1} corresponded to CHX vibrations (Majeed et al., 2017). No changes were observed in the polymer at the level of the functional group after SAS processing. In addition to EUD characteristic peaks, FTIR spectra of physical mixture and SAS processed EUD/THEOP powders exhibited several absorption bands attributed to THEOP, such as at 3120 cm^{-1} assigned to the N-H stretching, at 3060 and 2989 cm^{-1} related to the C-H stretching, at about 1718 and 1667 cm^{-1} assigned to the carbonyl stretching and at 1307 cm^{-1} due to the C–O stretching (Kesavan and Peck, 1996, Kumar Singh Yadav and Shivakumar, 2012, Lin et al., 2013).

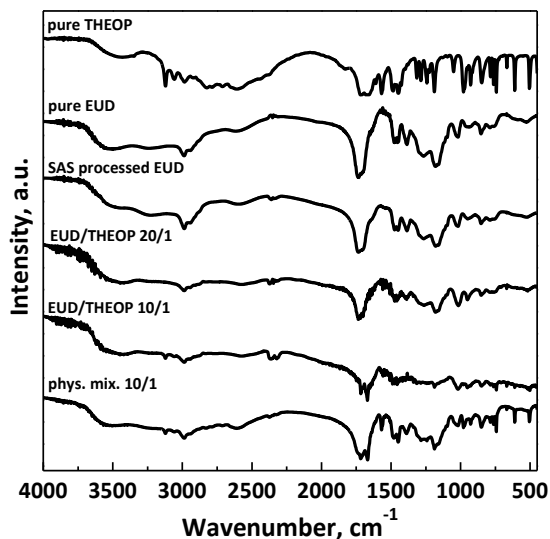


Figure IV.67 FTIR spectra for unprocessed and SAS processed EUD, unprocessed THEOP, physical mixture polymer/drug and SAS processed EUD/THEOP coprecipitated powders.

DSC thermograms of unprocessed THEOP, unprocessed and processed EUD and SAS processed EUD/THEOP 20/1 and 10/1 w/w are reported in **Figure IV.68**. The DSC thermogram of pure THEOP showed an endothermic peak at around 272°C, which is its melting point (Ochoa et al., 2005). The thermogram of unprocessed EUD had two endothermic peaks, the first one due to the loss of water and the other one at about 200°C related to the melting of the crystalline portion of the polymer (Ceballos et al., 2005). Moreover, in agreement with the literature (Jadhav et al., 2014), unprocessed EUD is characterized by a glass transition temperature (T_g) at around 119°C, slightly shifted at lower temperature (around 112°C) for SAS processed EUD due to the $scCO_2$ plasticizing effect in presence of semicrystalline polymers (Lian et al., 2006, Campardelli et al., 2019a). The thermal behavior of SAS coprecipitated powders is similar to the polymer one. The absence of the melting point of the drug in the thermograms of the coprecipitated powders can be ascribed to the amorphization. Moreover, because of the particle size reduction, a slightly higher degree of amorphism is detected both in SAS processed polymer and SAS coprecipitated powders with respect to unprocessed EUD, as observable from the less pronounced melting peak linked to the crystalline portion of the polymer.

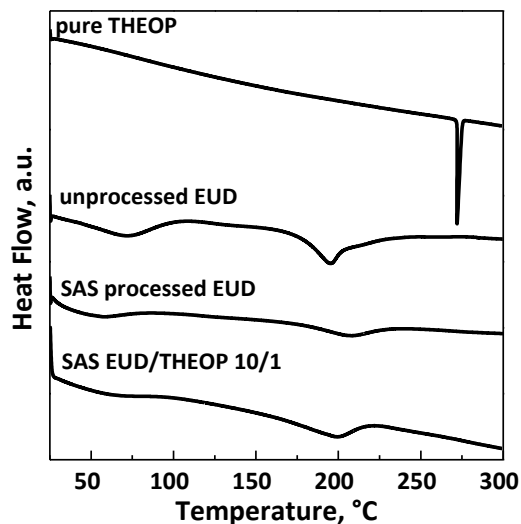


Figure IV.68 DSC thermograms of unprocessed and SAS processed EUD, unprocessed THEOP, and SAS processed EUD/THEOP powders.

XRD patterns of pure THEOP and EUD, and SAS processed EUD/THEOP 10/1 w/w are reported in **Figure IV.69**. XRD analyses confirmed the outcomes deduced by DSC ones; i.e., the pure drugs were in a crystalline state, the pure EUD showed a semi-crystalline pattern, whereas the coprecipitated powders were characterized by an amorphous behavior.

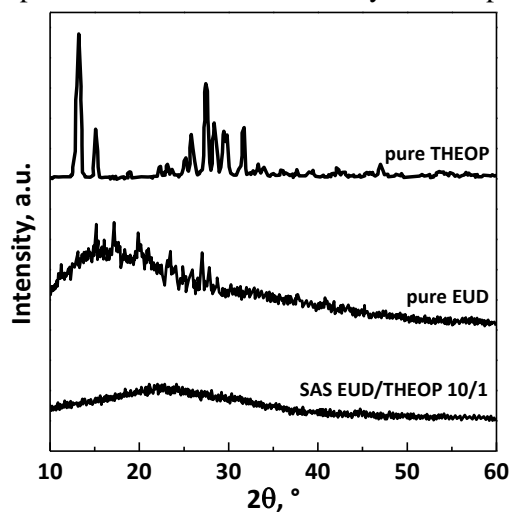


Figure IV.69 XRD patterns of unprocessed EUD and THEOP, and SAS processed EUD/THEOP powders.

Dissolution tests in PBS of pure THEOP, physical mixture EUD/THEOP 10/1 w/w and SAS processed EUD/THEOP 20/1 and 10/1 are reported in

Figure IV.70. As for pure THEOP e and the physical mixture, the time taken for the complete release is practically the same (about 2.3 e 2.6 h, respectively). Differently, SAS coprecipitated EUD/ THEOP 10/1 and 20/1 w/w powders require for the complete drug dissolution about 118 h and 130 h, respectively; therefore, also in this case, the release was considerably prolonged using EUD, up to about 57 times. Moreover, by increasing the polymer/drug ratio from 10/1 to 20/1 w/w, the drug release burst decreased from 60% to 20%. The difference in the release of EUD/THEOP 10/1 and 20/1 w/w can be explained, according to the literature (Brzeziński et al., 2019), to the size of the microparticles. Indeed, increasing the powders' diameter, the portion of the drug finely dispersed in the polymer microparticle increased and, correspondingly, the portion of drug disposed on the polymer surface decreased. This corresponds to a reduction of the initial drug release burst observed in the case of EUD/THEOP 20/1 w/w.

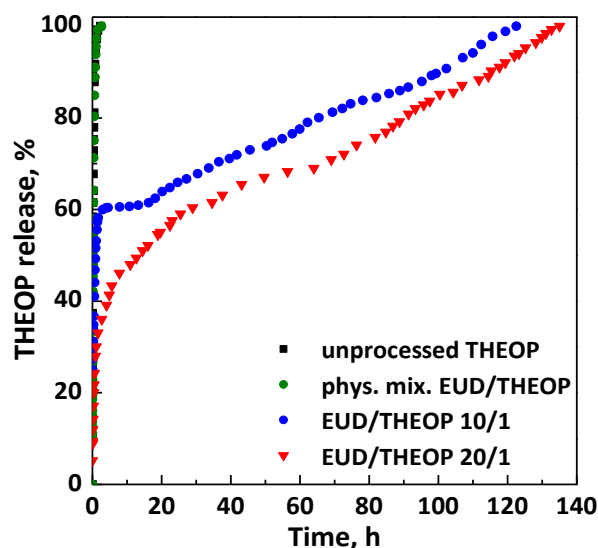


Figure IV.70 Dissolution profiles in PBS at 37°C and pH 7.4.

Discussion

Unlike the two previous systems investigated using Eudragit L100-55 as carrier, well-defined microspheres were produced for EUD/THEOP system, assuring a massive coprecipitation with a burst effect that reduced up to a value of 20% for EUD/THEOP 20/1 w/w. It was also proved that EUD can have a great influence on the morphology of coprecipitates, making the coprecipitation possible even with active compounds that are bad candidates for SAS micronization, as occurred with THEOP. The whole experimentation conducted on Eudragit L100-55 showed that different results can be reached with different drugs even using the same carrier, proving once again that the interactions between polymer, active principle,

scCO₂, and liquid solvent can affect the high-pressure VLEs and modify the processability of materials. Accurately selecting the process conditions based on the couple EUD-drug, composite microspheres can be produced. It can be asserted that Eudragit L100-55 is an effective carrier for SAS coprecipitation to formulate controlled drug delivery systems.

IV.5 The use of cyclodextrin as polymeric carrier

SAS micronization of cyclodextrins was fully investigated in a previous work, by changing the operating pressure, the temperature and the CD concentration in DMSO (De Marco and Reverchon, 2008). However, the preparation of inclusion complexes coprecipitating the active compound with these oligosaccharides by SAS has to be further explored, as mentioned in the ‘State of the art’ section. Among various, β -cyclodextrin emerged as the most promising one for SAS process, due to its tendency to precipitate in the form of spherical particles. However, its use is limited to very few SAS works, in which a remarkable enhancement of the dissolution rate of the drug incorporated in the β -CD cavity did not emerge (Lee et al., 2010, Nerome et al., 2013, Jia et al., 2018). Therefore, aiming at ensuring that β -CD was an effective carrier to obtain inclusion complexes by SAS technique, its coprecipitation was studied firstly with two NSAIDs, namely NIM and KET, and then RUT as natural active compound.

In agreement with the literature studies focused on guest/host inclusion complexes, the nomenclature drug/ β -CD was used in this part of the work, as well as the mol/mol ratio was specified. Inclusion complexes were often obtained at guest/ β -CD ratios equal to 1/2 mol/mol and 1/1 mol/mol, and even, although in few cases, 2/1 mol/mol; other ratios like 1/3 mol/mol were also proposed in the literature, as mentioned in the ‘State of the art’. For all SAS experiments performed on guest/ β -CD systems, DMSO as the liquid solvent, a temperature of 40°C, CO₂ flow rates of 30 g/min and liquid solution equal to 1 mL/min were employed to ensure that the operating point lies in the supercritical mixture region (Andreatta et al., 2007b).

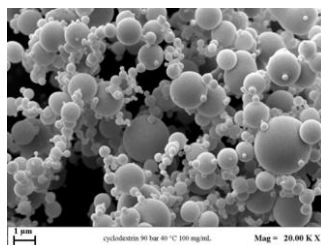
IV.5.1 Preparation of NSAID/ β -CD complexes

Firstly, two model NSAIDs, namely NIM and KET, were coprecipitated with β -CD, to obtain inclusion complexes. The effect of the pressure, the concentration of solutes in DMSO and the drug/carrier mol/mol ratio was investigated on the morphology/size of composite particles produced. A list of the tests performed at different conditions is reported in **Table IV.11**, specifying the morphology of the obtained particles, along with the mean diameter and standard deviation on a volumetric basis. It is worth noting that the NSAID/ β -CD molar ratios studied, gradually increased from 1/3 or 1/2 to 2/1 mol/mol, approximately correspond to 1/10, 1/5 and 1/2 w/w.

Table IV.11 SAS experiments performed on NSAID/ β -CD systems (NP: nanoparticles; cSMP: coalescent sub-microparticles; MP: microparticles; cMP: coalescent microparticles; liq: liquid).

#	NSAID	NSAID/CD (mol/mol)	P (MPa)	C _{tot} (mg/mL)	M	m.d. \pm s.d. (μ m)
1	-	0/1	9	100	MP	1.91 \pm 0.54
2		1/0	9	20	-	-
3		1/3	9	100	MP	0.59 \pm 0.28
4		1/3	12	100	MP	0.59 \pm 0.20
5		1/3	15	100	MP+NP	-
6	NIM	1/3	9	150	MP	3.39 \pm 1.05
7		1/3	9	200	cMP	-
8		1/1	9	150	MP	2.14 \pm 0.60
9		1/1	9	200	MP	2.31 \pm 1.02
10		2/1	9	200	MP	1.90 \pm 0.55
11		1/0	9	20	cSMP	0.30 \pm 0.12
12		1/2	9	100	MP	3.26 \pm 0.93
13		1/2	12	100	cMP	0.55 \pm 0.20
14	KET	1/2	15	100	NP	-
15		1/2	9	200	MP	4.76 \pm 1.44
16		1/1	9	200	liq+cMP	-
17		1/1	12	200	MP	2.47 \pm 0.72
18		2/1	12	200	MP	0.65 \pm 0.20

A preliminary test performed by micronizing NIM alone at 40°C, 9 MPa and a drug concentration in DMSO of 20 mg/mL (run #2 in **Table IV.11**) revealed that NIM was completely extracted by the mixture scCO₂/DMSO. Conversely, as reported in the paragraph IV.2.1, a part of KET precipitated in form of coalescing sub-microparticles (**Figure IV.2b**), whereas the remaining part was extracted. On the other hand, when it is micronized by SAS, β -CD has the tendency to precipitate in form of microparticles at various process conditions (De Marco and Reverchon, 2008); for example, in **Figure IV.71**, β -CD microparticles obtained at 40°C, 9 MPa and a oligosaccharide concentration in DMSO of 100 mg/mL (run #1) are shown.

**Figure IV.71** FESEM image of β -CD precipitated from DMSO at 9 MPa, 40°C and 100 mg/mL (run #1).

Effect of the operating pressure

Firstly, the influence of the pressure was evaluated by gradually increasing it from 9 MPa up to 15 MPa. The total concentration of solutes in DMSO was fixed at 100 mg/mL.

Regarding the system NIM/ β -CD, by selecting a NSAID/carrier molar ratio of 1/3, well-defined microparticles were produced at 9 MPa (**Figure IV.72a**) and 12 MPa (**Figure IV.72b**); whereas, working at 15 MPa, slightly coalescent nanoparticles (**Figure IV.72c**) precipitated.

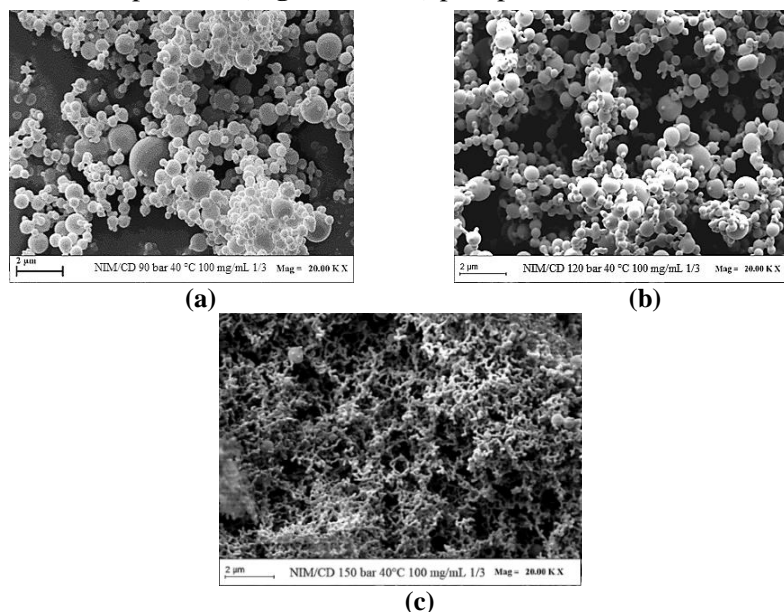


Figure IV.72 FESEM images of particles NIM/ β -CD 1/3 mol/mol precipitated from DMSO at 40°C and 100 mg/mL. Effect of the operating pressure: (a) 9 MPa (run # 3); (b) 12 MPa (run # 4); (c) 15 MPa (run #5).

Concerning the system KET/ β -CD at a molar ratio 1/2, microparticles (**Figure IV.73a**) and coalescent microparticles (**Figure IV.73b**) were produced at 9 MPa and 12 MPa, respectively; whereas, nanoparticles precipitated at 15 MPa, as observable in **Figure IV.73c**.

For both the NSAIDs, a decrease of the particles' dimensions was noted by increasing the operating pressure.

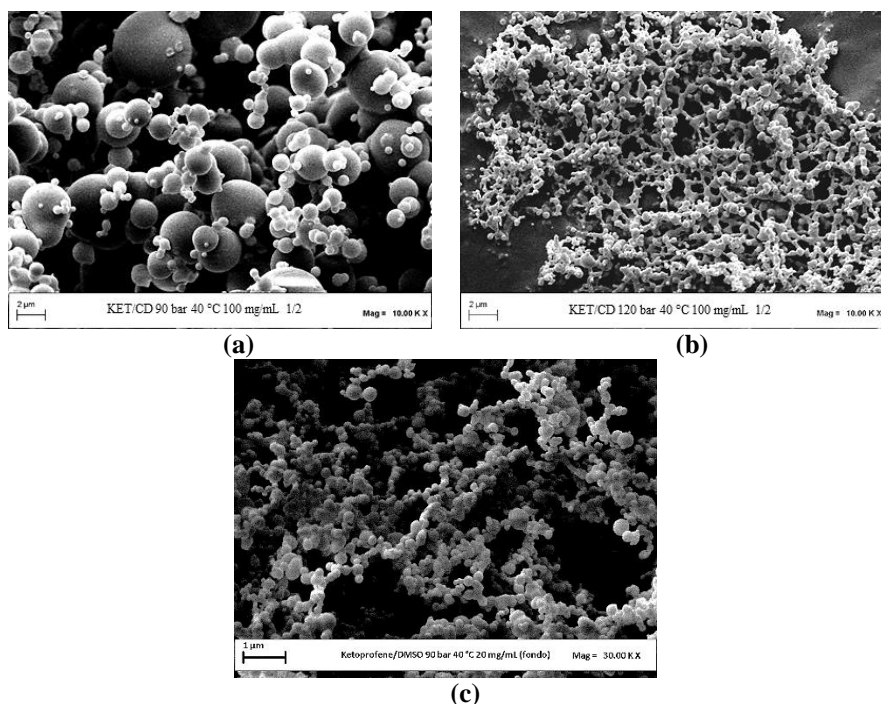


Figure IV.73 FESEM images of particles KET/ β -CD 1/2 mol/mol precipitated at 40°C and 100 mg/mL. Effect of the operating pressure: (a) 9 MPa (run # 12); (b) 12 MPa (run # 13); (c) 15 MPa (run #14).

Effect of the overall concentration in DMSO

The pressure of 9 MPa, which led to regular microparticles at 100 mg/mL, was fixed to study the effect of the overall concentration in DMSO for both the NSAIDs. For the system NIM/ β -CD 1/3 mol/mol, well-defined microparticles (**Figure IV.74a**) precipitated at 150 mg/mL (run #6 in **Table IV.11**), characterized by larger size than the particles obtained at 100 mg/mL. By increasing the total concentration up to 200 mg/mL (run #7 in **Table IV.11**), coalescent and irregular microparticles were instead obtained.

The effect of the overall concentration on the morphology of the obtained powders was different when KET is used as the active principle. Indeed, in correspondence of an overall concentration of solutes in DMSO equal to 200 mg/mL (run #15 in **Table IV.11**), well-separated microparticles KET/ β -CD 1/2 mol/mol were produced (**Figure IV.74b**).

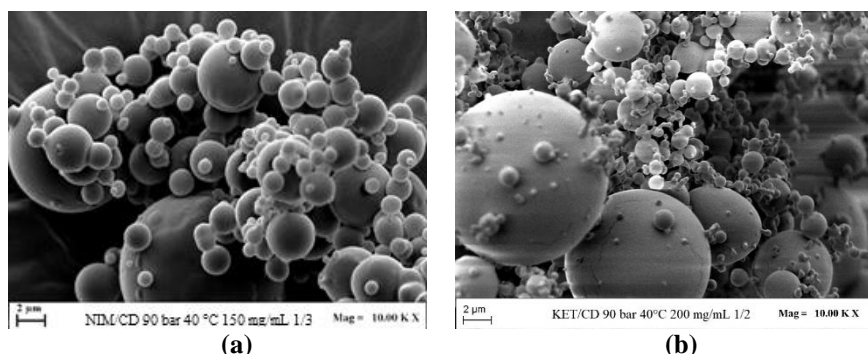


Figure IV.74 FESEM images of particles precipitated from DMSO at 40°C and 9 MPa: (a) NIM/β-CD 1/3 mol/mol at 150 mg/mL (run # 6); (b) KET/β-CD 1/2 mol/mol at 200 mg/mL (run # 15).

The mean diameter of the NSAID/β-CD particles increased and the PSD enlarged by increasing the overall concentration of solutes in DMSO, as shown, for example, in **Figure IV.75** through the comparison of the volumetric cumulative PSDs at different KET+CD concentration in DMSO.

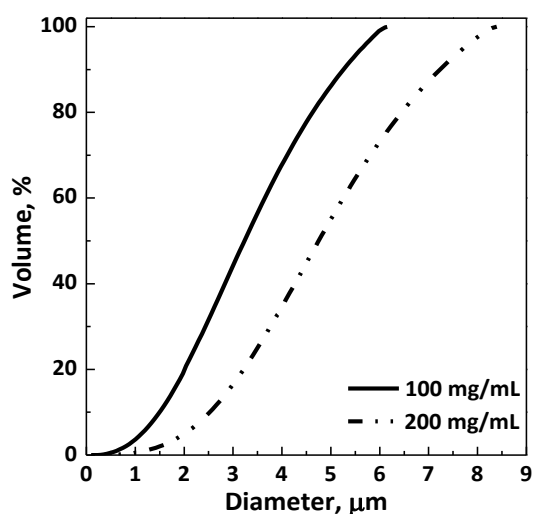


Figure IV.75 Volumetric cumulative PSDs of KET/β-CD 1/2 mol/mol precipitated from DMSO at 40°C and 9 MPa; effect of the overall concentration in DMSO.

Effect of NSAID/β-CD molar ratio

Since the drug/β-CD molar ratio can strongly affect the complex inclusion formation, the effect of this parameter on the morphology, and the dimensions of the particles was evaluated.

Regarding the system NIM/β-CD, two tests at a molar ratio equal to 1/1 were performed by setting the pressure at 9 MPa, but fixing the total

concentration in DMSO at 150 mg/mL (run #8 in **Table IV.11**) and 200 mg/mL (run #9 in **Table IV.11**). NIM/ β -CD 1/1 mol/mol microparticles were obtained in both cases, but they were well-defined by working with the higher value of concentration (**Figure IV.76a**). Therefore, the NIM/ β -CD ratio was further increased up to 2/1 mol/mol by fixing 200 mg/mL as the concentration (run #10 in **Table IV.11**), again producing microparticles (**Figure IV.76b**). Comparing the volumetric cumulative PSDs obtained at different NIM/ β -CD molar ratios (**Figure IV.76c**), it can be observed that the particle size increased by reducing the NIM/ β -CD molar ratio.

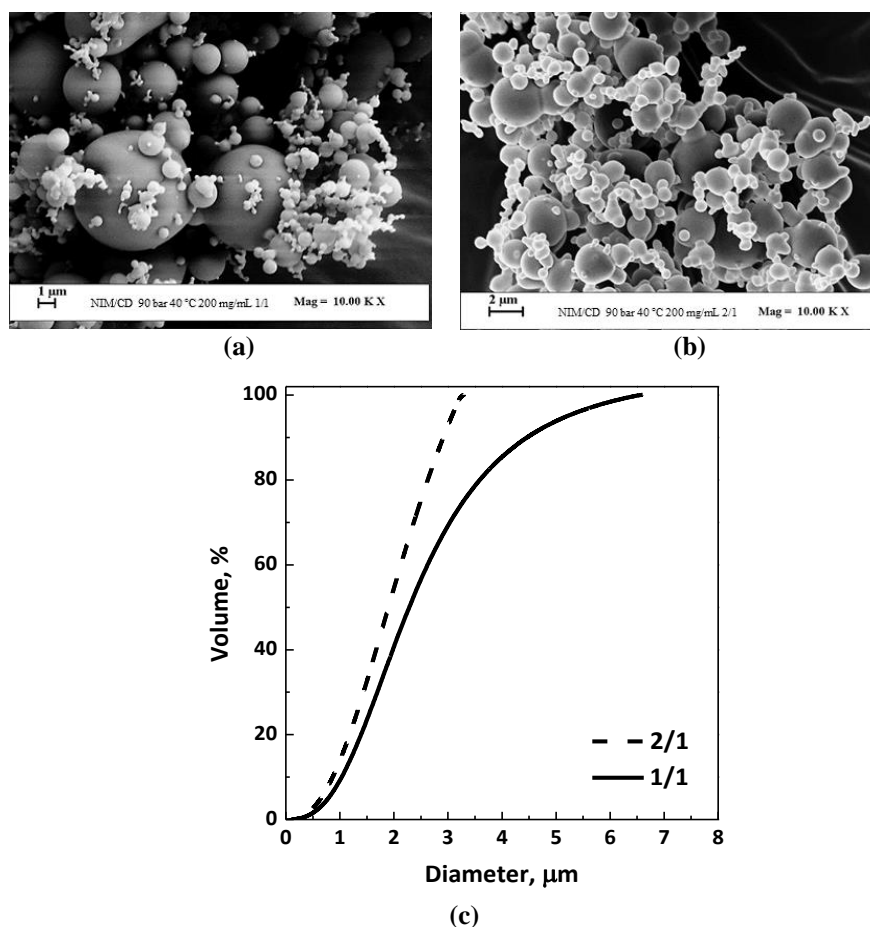


Figure IV.76 FESEM images of NIM/ β -CD particles precipitated from DMSO at 40°C, 9 MPa, 200 mg/mL and a NSAID/CD ratio (a) 1/1 mol/mol (run # 9) and (b) 2/1 mol/mol (run # 10); (c) volumetric cumulative PSDs of NIM/ β -CD particles at different NIM/ β -CD molar ratios.

Considering the system KET/ β -CD, the molar ratio was fixed at 1/1, working at a pressure of 9 MPa and a concentration in DMSO equal to 200 mg/mL (run #16 in **Table IV.11**). At the end of this test, some liquid was

found in the precipitator; very little powder was recovered and analyzed by FESEM, revealing the attainment of very coalescent microparticles. The presence of liquid into the precipitation chamber can be explained, taking into account thermodynamic aspects. At the operating conditions of 40°C/9 MPa, the working point is theoretically above the MCP of the binary system DMSO/scCO₂ (i.e; 40°C/8.6 MPa). However, the presence of a high KET content could have modified the high-pressure VLEs of the system; as a consequence, the MCP of the quaternary system DMSO/KET/ β -CD/scCO₂ would have shifted towards higher pressures compared to the MCP of the binary system DMSO/scCO₂. Therefore, the operating point could be below the MCP and lie in the biphasic region in case of run #16.

According to this consideration, the following tests about the influence of the KET/ β -CD ratio (runs #17 and #18 in **Table IV.11**) were conducted at 200 mg/mL and 12 MPa, to assure that the operating point is above the MCP of the quaternary system. Indeed, spherical microparticles were produced both at a KET/ β -CD molar ratio of 1/1 (**Figure IV.77a**) and 2/1 (**Figure IV.77b**), with particle size that decreased by increasing the NSAID amount.

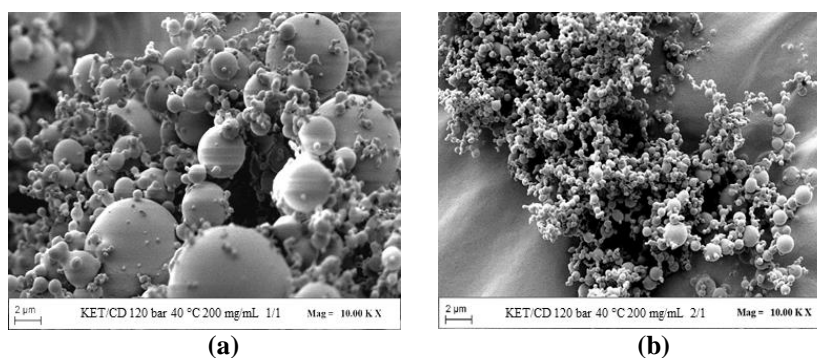


Figure IV.77 FESEM images of KET/ β -CD particles precipitated from DMSO at 40°C, 12 MPa, 200 mg/mL and a NSAID/CD ratio (a) 1/1 mol/mol (run # 17) and (b) 2/1 mol/mol (run # 18).

Characterization of NSAID/ β -CD samples

The samples produced by SAS were characterized by different analytic techniques in order to prove the successful complexation.

Firstly, FTIR analyses were conducted. FTIR spectra of unprocessed and processed NSAIDs and β -CD, physical mixtures NSAID+ β -CD (1/1 mol/mol), and SAS processed NSAID/ β -CD at different molar ratios were reported in **Figure IV.78** and **Figure IV.79** for NIM and KET, respectively.

The spectrum of unprocessed β -CD exhibited the characteristic bands attributed to the C-O stretching vibrations of glycosidic bond, primary alcohol, and cyclic alcohol at 1022 cm⁻¹, 1638 cm⁻¹ and 1156 cm⁻¹, respectively (Mahmood et al., 2016). FTIR spectra of unprocessed and processed β -CD are similar, therefore the material did not undergo chemical changes in presence of the supercritical CO₂, such as carbonation reactions.

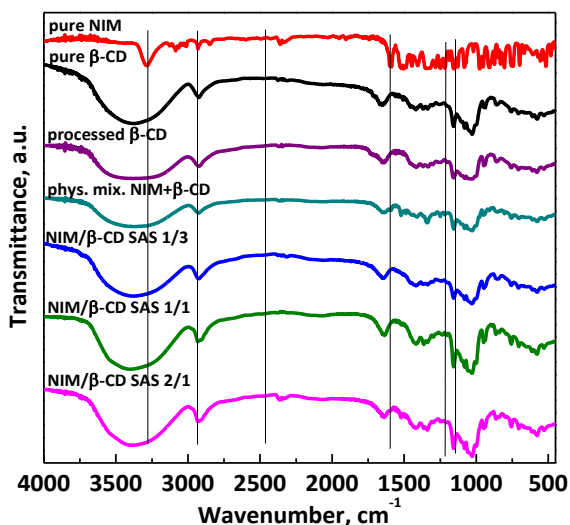


Figure IV.78 FTIR spectra of pure NIM, unprocessed and SAS processed β -CD, physical mixture and SAS NIM/ β -CD complexes at various molar ratios.

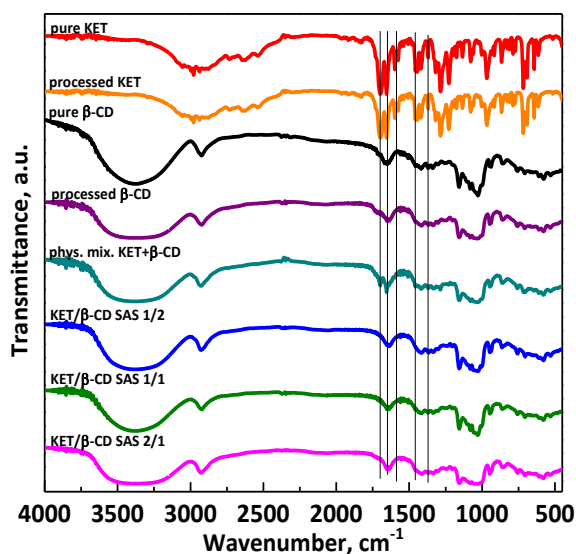


Figure IV.79 FTIR spectra of unprocessed and SAS processed KET and β -CD, physical mixture and SAS KET/ β -CD complexes at various molar ratios.

The FTIR spectrum of pure NIM showed different characteristic bands such as the peaks at 3283 cm⁻¹ and 2928 cm⁻¹ due to the N-H vibrations and the aliphatic C-H stretching, respectively; bands at about 1590 cm⁻¹ and 1250 cm⁻¹ indicating the asymmetric and symmetric stretching of NO₂; peaks at about 1150 cm⁻¹ attributed to SO₂ stretching and the C-O-C ether linkage at about 1210 cm⁻¹ (Begum et al., 2015). The spectrum of pure KET was

characterized by absorption bands at 1598 cm^{-1} , 1580 cm^{-1} and 1455 cm^{-1} due to the C=C stretching of the aromatic ring; at 1440 cm^{-1} and 1370 cm^{-1} attributed to the C-H asymmetric and symmetric deformation of CH_3 ; at 1693 cm^{-1} and 1650 cm^{-1} , also observed in the spectrum of the physical mixture KET + β -CD, indicating the C=O stretching of acid and ketone, respectively (Yadav et al., 2013). No substantial changes occurred after SAS processing the KET, since the FTIR spectra of unprocessed and processed KET are similar. Some of these characteristic bands of each NSAID were observed in the spectra of the physical mixtures NSAID+ β -CD. Instead, the NSAID absorption bands were not detected in the spectra of NSAID/ β -CD complexes precipitated by SAS, whose spectra were similar to the oligosaccharide one. In many papers (Jun et al., 2007, Cannavà et al., 2008, Al-Marzouqi et al., 2009, Lee et al., 2010, Zhou et al., 2012, Mohan et al., 2012, Huang et al., 2016, Chen et al., 2017, Sun et al., 2019), any changes in the FTIR spectra, such as the shift or the disappearance of absorption bands or the reduction in peak intensity, were attributed to the formation of inclusion complexes due to weak intermolecular interactions. Therefore, the disappearance of the peaks of NSAIDs into inclusion complexes obtained by SAS, even at high molar ratio NSAID/ β -CD equal to 2/1, demonstrated that the NSAID was incorporated into the β -CD cavity, by forming the guest/host inclusion complex. Moreover, it was noted that the characteristic NIM band at 2928 cm^{-1} shifted/stretched towards lower wavenumbers in the case of the inclusion complexes. This modification was probably due to the formation of hydrogen bonds with the primary and secondary hydroxyl groups of β -CD (Attoui-Yahia et al., 2015, Moyers-Montoya et al., 2016, Di Capua et al., 2017a). Further analyzes, reported below, were carried out to assert the effective complexation (DSC, XRD, UV-vis), but also the presence of the drug in the SAS-processed powders (UV-vis).

DSC thermograms of unprocessed NSAIDs and β -CD and SAS processed NSAID/ β -CD at different molar ratios were reported in **Figure IV.80** and **Figure IV.81** for NIM and KET, respectively. The thermograms of unprocessed NSAIDs are characterized by an endothermic peak related to the melting point at about 150°C and 96°C for pure NIM and KET, respectively. The curve of the pure β -CD showed a broad peak in the range $75\text{-}115^\circ\text{C}$, corresponding to the loss of water molecules. It is possible to note a reduction in the peak intensity related to the dehydration in the case of all SAS coprecipitated powders compared to those of unprocessed β -CD. According to the literature (Olaru et al., 2009), the water molecules located in the β -CD cavity were replaced by the hydrophobic “guest” (the NSAID), to reach a lower and more stable energy state with the formation of the inclusion complex. Additionally, the partial or complete disappearance of the NSAID melting peak in the thermograms of the SAS powders also indicated that the complexation occurred (Jun et al., 2007, Zhou et al., 2012, Huang et al., 2016); i.e., the NSAID is hidden into the cavity of the amorphous β -CD.

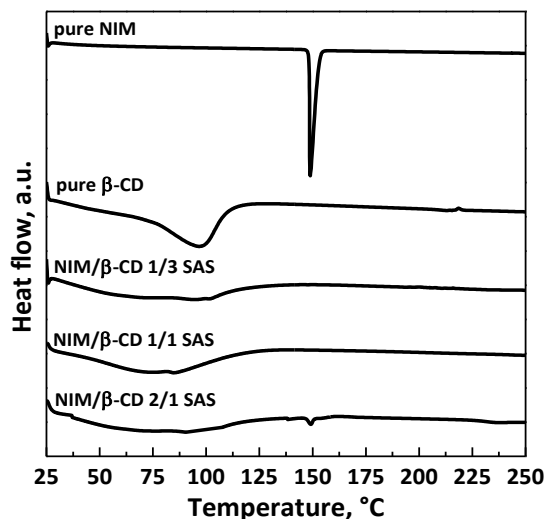


Figure IV.80 DSC thermograms of unprocessed NIM and β -CD, and SAS-processed NIM/ β -CD complexes at different molar ratios.

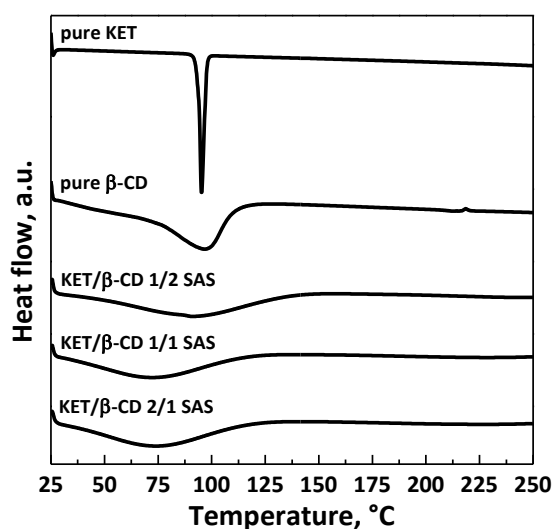


Figure IV.81 DSC thermograms of unprocessed KET and β -CD, and SAS-processed KET/ β -CD complexes at different molar ratios.

XRD analysis was also carried out to validate the results obtained from the previous analyses about the complexes formation. The XRD patterns of unprocessed NSAIDs and β -CD, and SAS processed NSAID/ β -CD at different molar ratios were reported in **Figure IV.82** and **Figure IV.83** for NIM and KET samples, respectively. The diffractograms of unprocessed NIM, KET, and β -CD showed the strong sharp peaks characteristic of each material, proving their crystalline nature. However, the CD micronization therefore led to a loss of the oligosaccharide crystallinity. Indeed, the

patterns of SAS NIM/ β -CD and KET/ β -CD powders at all the molar ratios indicated an amorphous state of the structure. In the literature, this change in the solid phase was also attributed to an interaction between the drug and β -CD when inclusion complexes are formed (Jun et al., 2007). In detail, the characteristic peaks of the drugs disappeared in the patterns of SAS complexes, since the NSAID molecules were incorporated and hidden in the cavity of the amorphous micronized CDs.

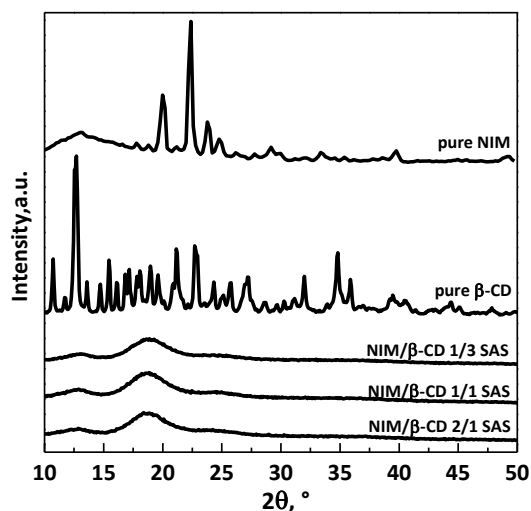


Figure IV.82 XRD patterns of unprocessed NIM and β -CD, and SAS-processed NIM/ β -CD complexes at different molar ratios.

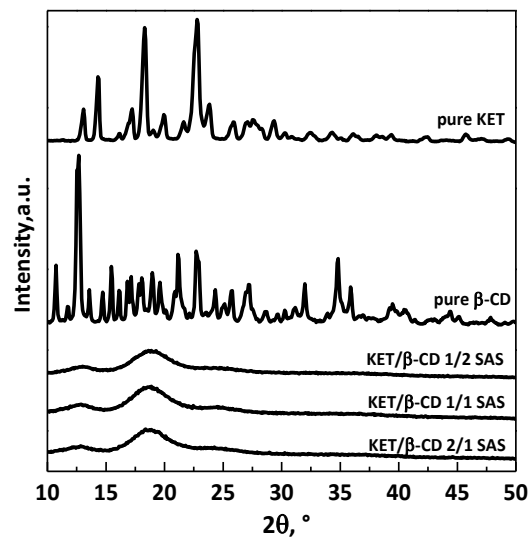


Figure IV.83 XRD patterns of unprocessed KET and β -CD, and SAS-processed KET/ β -CD complexes at different molar ratios.

Dissolution tests, performed to compare the dissolution rate of each NSAID in pure form and from SAS particles at different NSAID/ β -CD molar ratios, are reported in **Figure IV.84** and **Figure IV.85** for NIM and KET, respectively. In agreement with the literature, the dissolution tests of NIM samples were achieved in PBS at pH 7.4 (Prosapio et al., 2016b); a HCl 0.1 M solution (pH 2.5) was instead chosen as dissolution medium for KET samples to simulate the gastrointestinal stomach acidity (Yang et al., 2008b, Sultanova et al., 2016), because it is a more acidic drug than NIM. Thus, a large part of KET is already absorbed in the gastric tract (Singh et al., 1999).

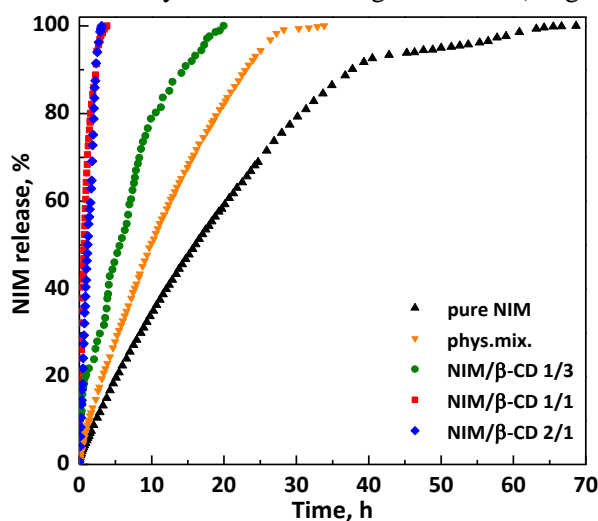


Figure IV.84 Dissolution profiles in PBS at pH 7.4 and 37°C.

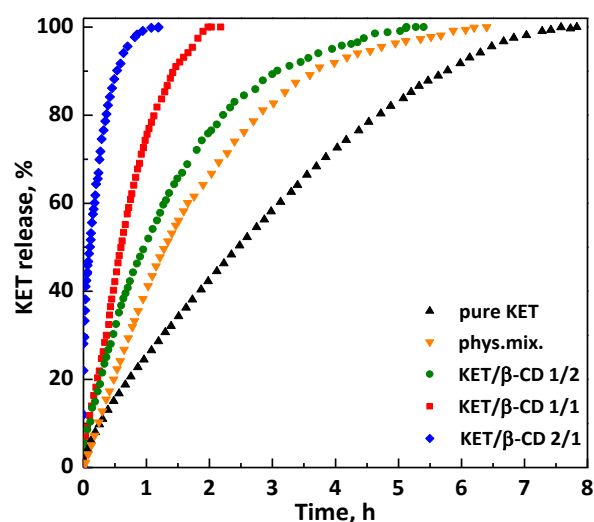


Figure IV.85 Dissolution profiles in HCl solution at pH 2.5 and 37°C.

As can be observed in **Figure IV.84**, the complete dissolution of NIM in PBS was reached in about 67 h and 30 h as unprocessed drug and from physical mixture NIM+CD, respectively. NIM from SAS particles produced at a molar ratio equal to 1/2 completely dissolved in about 20 h. The dissolution profiles of SAS NIM/ β -CD 1/1 and 2/1 mol/mol are similar, achieving the complete dissolution in 3.8 h and 3.2 h, respectively. The time of NIM dissolution was decreased in the case of NIM/ β -CD inclusion complexes, up to approximately 21 times for NIM/ β -CD 2/1 mol/mol compared to pure NIM. Unprocessed KET completely dissolved in HCl solution in almost 8 h, whereas the drug from the physical mixture KET+CD dissolved in about 6 h. KET released from inclusion complexes took about 5.2 h, 2 h, and 1.1 h for KET/ β -CD molar ratio of 1/2, 1/1 and 2/1, respectively. KET dissolution rate was enhanced because of the formation of inclusion complexes, up to be about 7 times faster in the case of KET/ β -CD 2/1 mol/mol with respect to the unprocessed KET. In the case of the complexes containing both NIM and KET, the NSAID dissolution rate enhanced as the NSAID/ β -CD ratio increased. This trend may seem unusual if compared with the results obtained in other papers focused on the production of composite particles by SAS technique or other processes, in which the drug dissolution kinetics are more strongly influenced by increasing the amount of the carrier (Ha et al., 2015b, Won et al., 2005, Patomchaivivat et al., 2008, Jung et al., 2012, Montes et al., 2014a, Machmudah et al., 2020). However, the trend obtained in the case of the NSAID/ β -CD complexes was already observed, for example, in the study of Di Capua et al. (Di Capua et al., 2017a). In this paper, the observed trend in release kinetics was affected by the formation of weak intermolecular interactions, which positively influence the dissolution rate, as occurs in the case of the formation of drug/ β -CD complexes. This outcome is, therefore, a further demonstration that the formation of NIM/ β -CD and KET/ β -CD inclusion complexes occurred. Moreover, unlike KET, from **Figure IV.84** it can be noted that the dissolution profiles of NIM/ β -CD 1/1 and 2/1 mol/mol are very similar, probably indicating an incomplete inclusion in the case of NIM/ β -CD ratio 2/1 mol/mol (Lu et al., 2009). This result can be also confirmed by considering the outcomes of DSC analyses (**Figure IV.80**). In particular, in the thermogram of complexes NIM/ β -CD 2/1 mol/mol, the characteristic melting peak of NIM can be noted at least in a small part, meaning that part of NIM molecule was not incorporated in the CD cavity. Therefore, by increasing the NIM/ β -CD molar ratio from 1/1 to 2/1, a partial inclusion complex probably begins to occur; thus, the 1/1 molar ratio can be considered as a limit for a complete complexation NIM/ β -CD. On the contrary, the inclusion complexation is total in the case of KET even at NSAID/ β -CD ratio 2/1 mol/mol, since the KET melting peak completely disappeared (**Figure IV.81**), as a symptom that KET was wholly incorporated and hidden into the CD cavity. As a consequence, the

dissolution of KET was further accelerated with the formation of KET/ β -CD 2/1 inclusion complex. This explanation can be also asserted by the size of NIM molecule (308 Da), which is larger than KET (254 Da).

Discussion

The preparation of inclusion complexes containing NSAIDs, namely NIM and KET, was achieved by SAS coprecipitation using β -CD as the carrier. The attainment of well-defined composite microparticles is possible by optimizing the process condition for each couple NSAID/ β -CD. The FTIR and DSC analyses proved the formation of NSAID/ β -CD inclusion complexes at all the studied molar ratios. Indeed, the characteristic bands/peaks of each drug disappeared in the FTIR spectra/DSC thermograms of inclusion complexes. The attainment of inclusion complexes was also confirmed by changes in the solid-state emerged from XRD analyses, comparing the inclusion complexes and the unprocessed materials. It was also demonstrated that β -CD is an effective carrier to be used for SAS coprecipitation, in order to improve the dissolution and, consequently, the bioavailability of active principles. Indeed, SAS inclusion complexes increased the NSAIDs' dissolution rate up to about 21 and 7 times compared to the unprocessed NIM and KET, respectively. Besides, the formation of cyclodextrin-based inclusion complexes allowed to reduce the amount of carrier significantly, down to a NSAID/ β -CD molar ratio equal to 2/1. The outcomes of UV-vis analyses also highlighted the probable formation of non-covalent interactions characteristic of the inclusion complexes. The results obtained by using β -CD as carrier are relevant, since a higher amount of carrier is often necessary to coprecipitate active compounds by SAS process when other polymers are employed. On the other hand, the formation of inclusion complexes allowed to reduce the amount of the carrier into the coprecipitated powders with respect to the composite microspheres usually obtained by SAS coprecipitation. A striking example is provided by the comparison of SAS KET/PVP coprecipitates (reported in the Paragraph IV.2.1) and SAS KET/ β -CD complexes. Specifically, well-defined microparticles were obtained for KET/PVP system and KET/ β -CD system at ratio equal to 1/3 w/w and 1/2 w/w (2/1 mol/mol), respectively. Moreover, the formation of complexes KET/ β -CD allowed to further increase the drug dissolution rate with respect to the KET/PVP coprecipitation. Indeed, KET was released completely in 1 h and 3 h from SAS KET/ β -CD and KET/PVP powders, respectively.

IV.5.2 Preparation of RUT/ β -CD complexes

Since the preparation of CD-based inclusion complexes seemed to allow the reduction of the carrier amount in the coprecipitated powders, tests about RUT/ β -CD were also performed. Unfortunately, the coprecipitation of RUT

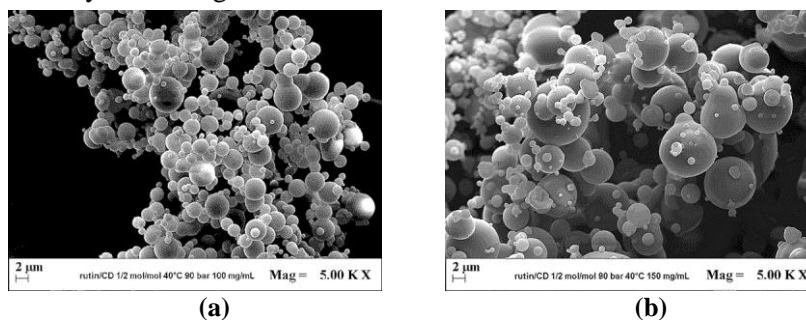
and PVP (reported at the paragraph 2.2) did not allow to increase the active compound/polymer ratio above 1/10 w/w, which revealed to be the limit ratio for the production of RUT/PVP particles. Moreover, RUT is extracted by the mixture DMSO/scCO₂ when it is processed alone; instead, β -CD tends to precipitate in the form of microparticles when SAS micronized, as well as it can force the morphology of composite particles produced by SAS coprecipitation. Taking into account all these considerations, the RUT/ β -CD coprecipitation was studied. A list of the tests performed at various conditions is reported **Table IV.12**, indicating the particles' morphology, mean size and standard deviation on a volumetric basis. It is specified that different RUT/ β -CD ratios were studied: 1/2 mol/mol (1/4 w/w), 1/1 mol/mol (1/2 w/w) and 1/1 mol/mol (2/1 w/w).

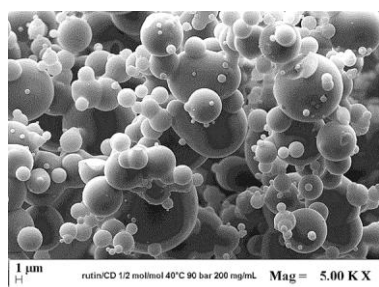
Table IV.12 SAS experiments performed on RUT/ β -CD system (MP= microparticles; cMP= coalescent microparticles; C= crystals).

#	RUT/CD (mol/mol)	P (MPa)	C _{tot} (mg/mL)	M	m.d. \pm s.d. (μ m)
1	1/0	9	20	C	-
2	1/2	9	100	MP	2.88 \pm 0.88
3	1/2	9	150	MP	6.72 \pm 1.74
4	1/2	9	200	MP	7.94 \pm 2.12
5	1/2	12	200	MP	4.12 \pm 1.14
6	1/2	15	200	MP	3.63 \pm 1.09
7	1/1	9	200	-	-
8	1/1	12	200	MP	1.45 \pm 0.88
9	2/1	12	200	MP+C	-

Effect of the overall concentration in DMSO

The effect of the concentration of solutes in DMSO was studied at a fixed pressure of 9 MPa and a RUT/ β -CD ratio equal to 1/2 mol/mol (runs #2-#4 in **Table IV.12**). Increasing the concentration from 100 to 200 mg/mL, spherical microparticles were produced in all cases (**Figure IV.86**). The influence of the total concentration in the solution is highlighted by the comparison of the PSDs reported in **Figure IV.87**: the microparticles size increased by increasing the total concentration in DMSO.





(c)

Figure IV.86 FESEM images of microparticles RUT/β-CD 1/2 mol/mol precipitated from DMSO at 40°C, 9 MPa and (a) 100 mg/mL (run #2); (b) 150 mg/mL (run #3); (c) 200 mg/mL (run #4).

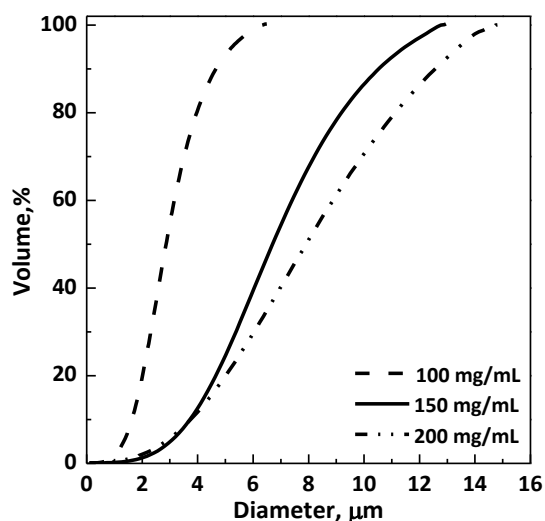


Figure IV.87 Volumetric PSDs of RUT/β-CD microparticles 1/2 mol/mol; effect of total concentration in DMSO.

Effect of the operating pressure

Total concentration of 200 mg/mL and RUT/β-CD ratio equal to 1/2 mol/mol were fixed to study the influence of pressure on particle size. The pressure was gradually increased from 9 MPa to 15 MPa (runs #4-#6 in **Table IV.12**). Well-separated microparticles were obtained in correspondence of all the tested pressure; exemplificative FESEM images of particles obtained at 9 MPa and 12 MPa are reported in **Figure IV.86c** and **Figure IV.88**, respectively.

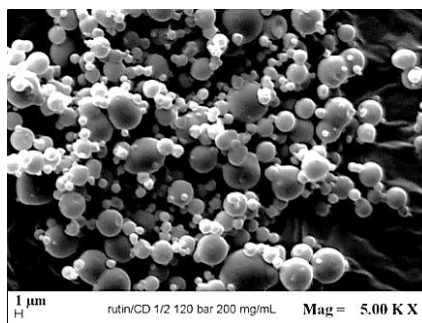


Figure IV.88 FESEM image of microparticles RUT/ β -CD 1/2 mol/mol precipitated from DMSO at 40°C, 200 mg/mL and 12 MPa (run #5).

The volumetric cumulative PSDs of particles precipitated at 40°C and 200 mg/mL are compared in **Figure IV.89** to highlight the effect of the operating pressure. It was noted that, by decreasing it, the mean particle size increased and the PSD enlarged.

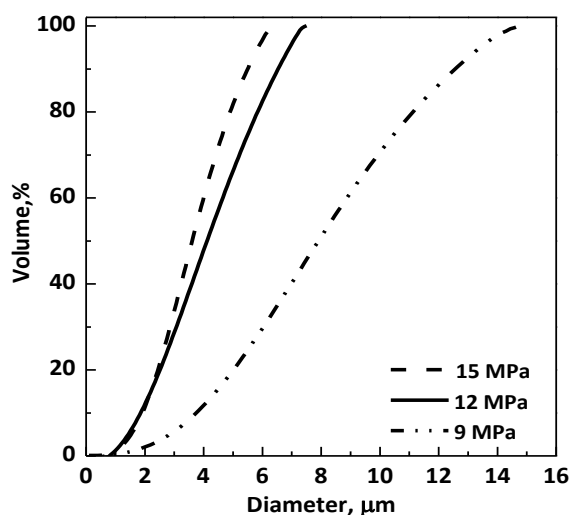


Figure IV.89 Volumetric PSDs of RUT/ β -CD microparticles 1/2 mol/mol; effect of operating pressure.

Effect of RUT/ β -CD molar ratio

The influence of RUT/ β -CD molar ratio was also studied, because it seems to mostly affect the complexation process (Davis and Brewster, 2004). In order to further reduce the amount of carrier in the composites, the RUT/ β -CD ratio was gradually increased from 1/2 to 2/1 mol/mol. Since working under the conditions of the previous test #5 (9 MPa, 40°C, 200 mg/mL) well-defined microparticles rutin/ β -CD 1/2 mol/mol were obtained, firstly the reduction of the guest/host molar ratio at 1/1 was attempted keeping the other parameters unchanged (run #7 in **Table IV.12**). However,

operating under these conditions, liquid was found in the precipitator at the end of the experiment. This outcome could be explained considering the high-pressure VLEs. At the selected temperature of 40°C, the MCP of the binary system DMSO/scCO₂ is located at 8.61 MPa; therefore, the operating point at 9 MPa was theoretically above the MCP of the binary system solvent/antisolvent. However, the presence of a high quantity of rutin could have altered the high-pressure VLEs of the system, meaning that the MCP of the quaternary system rutin/ β -CD/DMSO/scCO₂ could shift towards higher pressures compared to the MCP of the binary system solvent/antisolvent. Consequently, in case of run #7, the operating point at 9 MPa/ 40°C could be below the MCP and located in the biphasic region. For this reason, the following test performed with a RUT/ β -CD ratio 1/1 mol/mol was conducted at 12 MPa (run #8 in **Table IV.12**), with the aim to shift the operating point above the MCP of the quaternary system. Microparticles (**Figure IV.90a**) at molar ratio guest/host 1/1 were finally produced at 12 MPa. Given the positive result, it was attempted to further increase the RUT/ β -CD ratio at 2/1 mol/mol, working at 12 MPa and 200 mg/mL (run #9 in **Table IV.12**). However, under these condition, large crystals and microparticles precipitated from DMSO (**Figure IV.90b**). This outcome means that the coprecipitation was not effective at RUT/ β -CD ratio 2/1 mol/mol, since the operating point was near/below the MCP due to the influence of a high amount of RUT on VLEs.

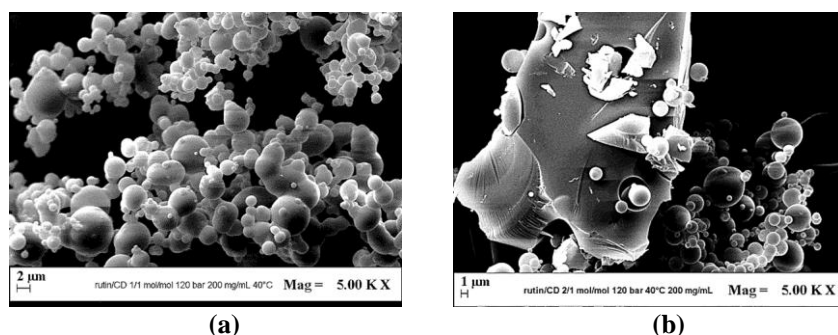


Figure IV.90 FESEM images of (a) microparticles RUT/ β -CD 1/1 mol/mol (run #9), (b) microparticles and crystals at rutin/ β -CD 2/1 mol/mol (run #10), precipitated from DMSO at 40°C, 200 mg/mL and 12 MPa.

Characterization of RUT/ β -CD samples

In order to verify the formation of inclusion complexes, SAS powders were characterized by different analytical techniques.

The FTIR spectra of unprocessed rutin and β -CD, physical mixture RUT+ β -CD (1/1 mol/mol) and SAS processed RUT/ β -CD at different molar ratios were reported in **Figure IV.91**.

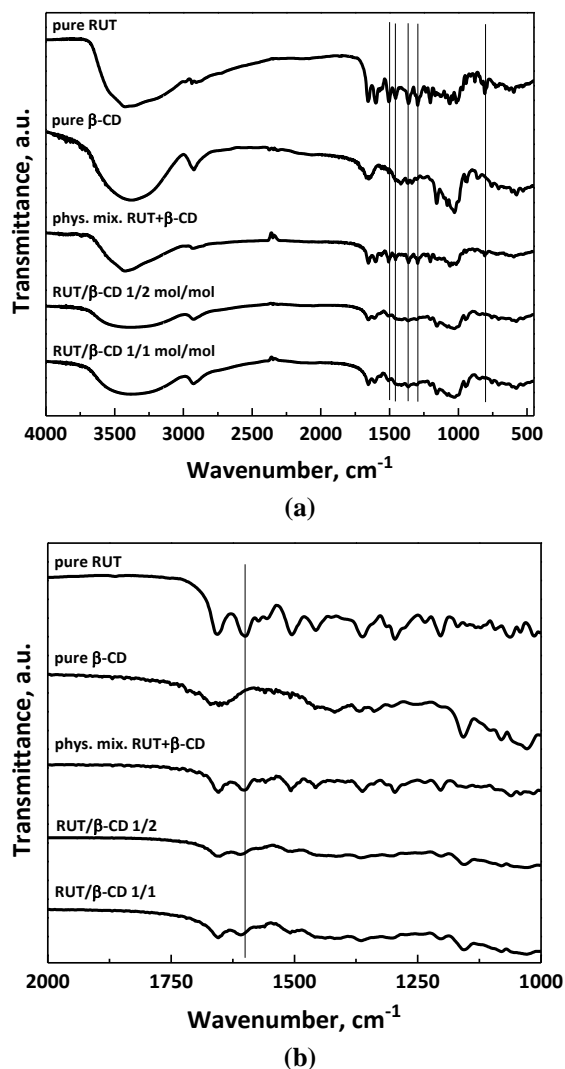


Figure IV.91 FTIR spectra of unprocessed RUT and β -CD, physical mixture NSAID+ β -CD and SAS processed RUT/ β -CD powders at different molar ratios: a) entire spectra; b) enlargement of the spectra.

The spectrum of pure RUT showed various characteristic bands, including the stretching carbonyl group at 1654 e 1600 cm^{-1} , that of the ether group at 1362 e 1169 cm^{-1} and the characteristic absorption band of Ar at 1507 cm^{-1} (Montes et al., 2016a). The FTIR spectrum of pure β -CD showed the absorption bands attributed to the C=O stretching vibrations of the glycosidic bond, the primary alcohol and the cyclic alcohol at 1022 cm^{-1} , 1638 cm^{-1} and 1156 cm^{-1} , respectively (Mahmood et al., 2016). The characteristic bands of RUT are evident in the spectrum of the physical

mixture, unlike the spectra of SAS processed powders RUT/ β -CD both at 1/2 mol/mol and 1/1 mol/mol. The disappearance of the RUT absorption bands or the reduction in peak intensity in the FTIR spectra of RUT/ β -CD samples was attributed to the formation of inclusion complexes (Jun et al., 2007, Cannavà et al., 2008, Al-Marzouqi et al., 2009, Lee et al., 2010, Zhou et al., 2012, Mohan et al., 2012, Huang et al., 2016, Chen et al., 2017, Sun et al., 2019), since the active compound (guest) was incorporated into the β -CD cavity (host). In addition to the partial or complete disappearance of RUT bands, like those at 1169, 1362, 1654 cm^{-1} , a shift of the RUT characteristic band at 1600 cm^{-1} towards slightly higher wavenumbers was also noted, as observable in the enlargement of FTIR spectra reported in **Figure IV.91b**. According to the literature (Di Capua et al., 2017b, Moyers-Montoya et al., 2016), this shift was due to the formation of hydrogen bonds between the carbonyl group and the hydroxyl group of RUT and β -CD, proving again the attainment of inclusion complexes.

DSC thermograms of pure RUT and β -CD and SAS processed RUT/ β -CD at different ratios (1/2 and 1/1 mol/mol) were reported in **Figure IV.92**.

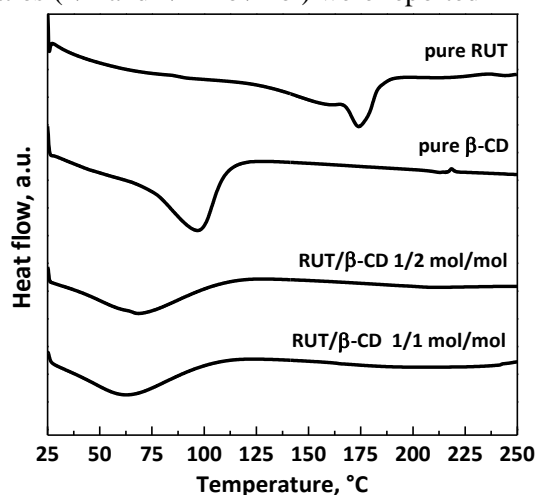


Figure IV.92 DSC thermograms of unprocessed RUT and β -CD, and SAS processed RUT/ β -CD powders at different molar ratios.

The DSC thermogram of pure RUT exhibited an endothermic peak in the range 143°C-190°C, which is related to the RUT melting point. It is possible to note that this characteristic peak of RUT disappeared in the thermograms of SAS processed RUT/ β -CD powders, because RUT was encapsulated in the β -CD cavity due to the formation of weak interactions between the host and the guest (Jun et al., 2007, Zhou et al., 2012, Huang et al., 2016). Moreover, the thermogram of the pure β -CD showed a broad endothermic peak in the range 75°C-115°C because of the dehydration. The intensity of this β -CD peak reduced in the case of all SAS RUT/ β -CD powders, due to the loss of water molecules in the β -CD cavity replaced by the hydrophobic

RUT (Olaru et al., 2009). Indeed, this replacement allowed to reach a lower and more stable energy state with the formation of inclusion complexes.

Dissolution tests (**Figure IV.93**) were performed to compare the dissolution rate of unprocessed RUT and the release of the active compound from SAS complexes at different molar ratios RUT/ β -CD (1/2 mol/mol and 1/1 mol/mol). It was observed that 90% of pure RUT dissolved in PBS in about 30.4 h, whereas it took about 7.7 and 12.7 h in the case of SAS complexes RUT/ β -CD 1/2 and 1/1 mol/mol, respectively. Therefore, the dissolution rate of rutin was increased up to about 3.9 and 2.4 times with the formation of icomplexes RUT/ β -CD 1/2 and 1/1 mol/mol, respectively.

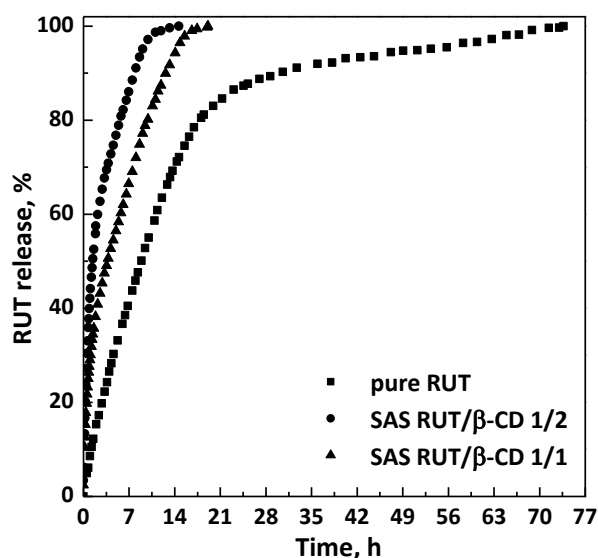


Figure IV.93 Dissolution profiles in PBS at pH 7.4 and 37°C.

Discussion

SAS coprecipitation revealed to be suitable to prepare inclusion complexes RUT/ β -CD. Indeed, the FTIR and DSC analyses proved the formation of guest/host inclusion complexes at RUT/ β -CD ratios equal to 1/2 and 1/1 mol/mol, due to the formation of non-covalent interactions during SAS precipitation. This led to a significant increase in the dissolution rate of RUT, which was about 3.9 and 2.4 times faster compared to pure rutin in the case of the inclusion complexes RUT/ β -CD 1/2 and 1/1 mol/mol, respectively.

The obtained results are very satisfactory, since the coprecipitation of RUT with β -CD allows to successfully process the RUT that is otherwise extracted by the CO₂/DMSO mixture; a significant improvement of the RUT dissolution was also achieved at very low active compound/ β -CD ratios. In the Paragraph 2.2, composite microparticles RUT/PVP were produced by at ratios 1/20 e 1/10 w/w; therefore, the main drawback previously encountered

by coprecipitating RUT with PVP is related to the impossibility of reducing the PVP amount with respect to the active compound in composite microspheres. On the contrary, RUT/ β -CD microparticles 1/4 w/w (1/2 mol/mol) and 1/2 w/w (1/1 mol/mol) were produced in case of inclusion complexation. This means that the formation of inclusion complexes with β -CD allowed to reduce significantly the amount of the carrier into the coprecipitated powders, with respect to the composite microspheres often obtained by SAS coprecipitation with other generic polymers. The use of β -CD revealed to be even better than PVP, which is considered one of the best carriers for SAS coprecipitation.

IV.6 Conclusions

The application of the SAS technique in the pharmaceutical field is strategic to produce composite particles in a controlled manner, with a narrow PSD, which are toxic for human health. In this part of the work, SAS coprecipitation has been proposed for several purposes. The main goal of identifying new polymeric carriers suitable for SAS coprecipitation has been successfully achieved. Indeed, the experimental studies proved that, in addition to the well-known PVP, PLA and PLLA, other polymers can be defined as valid for a successful SAS coprecipitation in the form of microspheres, namely zein, Eudragit L100-55 and β -CD. Based on the couple polymer/active principle, the process conditions must be carefully selected to obtain preferentially composite microparticles. The key role of the selected polymeric carrier in modifying the dissolution kinetics of an active compound, according to the the polymer's properties, emerged. The opportunity of modulating the drug release by choosing a specific carrier based on the required therapy is particularly impressive. In this way, it is possible to release the active principle at the desired dissolution rate, therefore reducing the side effects caused by drug overdoses and improving the patient's compliance. In particular, it is advisable to use zein and Eudragit L100-55 when a prolonged release of the active compound embedded in the composite particles is desired. Antibiotics and NSAIDs prescribed for chronic inflammations belong to this category of drugs. The use of these hydrophobic carriers is also promising to produce particles containing antihistamine or bronchodilator drugs, to propose alternative formulations that allow to achieve the disease control. In these latter cases, a bimodal drug release kinetics with a burst-like effect can also be a valid answer to immediately relieve the symptoms of the disease, in addition to reduce the frequency of administration thanks to the prolonged release of the remaining drug dose. Although lactic acid-based polymers (i.e., PLA and PLLA) proposed so far for SAS coprecipitation allow to prolong the drug release, it has to be considered that they are more expensive with respect to the hydrophobic carriers proposed in this work; i.e., zein and Eudragit,

which are considered low cost polymers (Ki and Park, 2001, Vert et al., 1995, Gough et al., 2020, Gazi and Krishnasailaja, 2019). On the contrary, β -CD allows to increase the dissolution rate and, consequently, the bioavailability of poorly-water soluble active compounds, such as rutin or NSAIDs prescribed for minor inflammations. Moreover, the production of CDs-based inclusion complexes revealed to be a useful tool to reduce the amount of the carrier into SAS coprecipitated powders. As observed for RUT and KET, in some cases, β -CD makes it possible to produce composite particles at very low carrier/drug ratios, even lower than those employed with PVP, one of the best SAS carriers. The formation of CD-based complexes has also further accelerated the dissolution of the poorly-water soluble drugs with respect to PVP-based coprecipitates.

Generally speaking, the composite systems produced using the SAS technique can give an answer to the main issues still existing in the medical field. The results achieved in this part of the work encourage an industrial-scale production of SAS pharmaceutical composites.

Chapter V

Supercritical impregnation of drugs into polymeric supports

V.1 Introduction

Nowadays, different drug delivery systems are manufactured, also to give the patients the possibility to choose the formulation that suit them the best.

In this part of the work, orally disintegrating tablets (ODTs) containing various NSAIDs (namely nimesulide, ketoprofen and diclofenac sodium) were prepared by the supercritical impregnation. The challenge was to produce ODTs that promoted a rapid or prolonged drug release depending on the desired effect. For this purpose, two different aerogels were selected as polymeric supports, namely Maize Starch Aerogel (MSA) and Calcium Alginate Aerogel (CAA), because of the high porosity and high specific surface areas of these matrices. The aerogels used for the experiments were prepared by supercritical gel drying to preserve the native porous structure, as mentioned in the Introduction section. The role of the different polymer used for the production of the aerogels on the drug release kinetics was investigated. The controlling steps involved in the impregnation process were also identified, as well as a modeling of the drug release kinetics in aqueous environment was proposed.

Given the advantages highlighted in the Introduction section about the topical drug delivery, the supercritical impregnation of a heparin-based drug, namely mesoglycan (MSG), was attempted into thin polycaprolactone films, to produce medicated patches for the wound healing. In this case, the foaming of polycaprolactone in contact with the $scCO_2$ was exploited to favor the drug loading into the films. Therefore, a single step “polymer foaming + drug impregnation” using $scCO_2$ was proposed to develop medicated patches for the wound care. In this context, it was proved that mesoglycan favors re-epithelialization process, but long-term therapies and, consequently, repeated dosages are needed, inducing many side effects on patient’s health. Thus, in the recent years, new pharmaceutical approaches

were searched for a proper epithelium repair, including the development of innovative topical devices. The production of new wound dressings with a drug controlled release, to be applied on wounds, lesions and chronic skin ulcers, is still a challenge. These medical patches often represent a protective barrier that assures a favorable environment for the wound healing and, at the same time, the tissue formation is favored by a direct action of the drug.

V.1.1 Materials

Nimesulide (NIM, purity 98%), ketoprofen (KET, purity $\geq 98\%$), diclofenac sodium salt (DIC, average molecular weight 318.13 g/mol), calcium chloride (CaCl_2 , purity $\geq 96\%$), sodium alginate, and high molecular weight polycaprolactone (PCL, average $M_n \sim 80,000$ by GPC) were supplied by Sigma-Aldrich (Italy). Ethanol (EtOH, purity 99.9 %) was bought from Carlo Erba. Maize starch 85652 was supplied by Fluka (Italy). Mesoglycan (MSG) was supplied by Laboratori Derivati Organici SpA, (Italy). Carbon dioxide (CO_2 , purity 99 %) was purchased from Morlando Group s.r.l. (Italy). All materials were used as received. Distilled water was produced using a water distiller supplied by ISECO S.P.A. (St. Marcel, AO, Italy). PCL films (thickness of 100 μm) used for a set of impregnation experiments were produced by Compression Molding in a laboratory of the Industrial Engineering Department of the University of Salerno.

V.1.2 Apparatuses for drying and impregnation by $sc\text{CO}_2$

Aerogels were prepared in a homemade laboratory plant (sketched in **Figure V.1a**), which consists of a 316 stainless steel cylindrical high-pressure vessel with an internal volume of 500 cm^3 , equipped with a high-pressure pump (Milton Roy, mod. Milroyal B, France) used to feed CO_2 . Pressure in the vessel was measured by a test gauge (Salmoiraghi, model SC-3200, Italy) and regulated by a micrometering valve (Hoke, mod. 1315G4Y, Spartanburg, SC), whereas temperature was set by a proportional-integral-derivative (PID) controller (Watlow, mod. 93, USA) connected with electrically controlled thin bands. The liquid solvent was recovered in a second collection vessel located downstream the micrometering valve, whose pressure was regulated by a backpressure valve (Tescom, model 26-1723-44, Italy). At the exit of the second vessel, a rotameter was used to measure the CO_2 flow rate, while a dry test meter allowed to estimate the total quantity of carbon dioxide.

Impregnation experiments were performed in an autoclave (sketched in **Figure V.1b**), consisting of a stainless steel high-pressure cylinder (NWA GmbH, Germany) with an internal volume of 100 cm^3 , closed on the bottom and on the top with two finger tight clamps. CO_2 was delivered by a diaphragm piston pump (Milton Roy, mod. Milroyal B, France) and a

cooling bath connected to the pump head allowed the cooling of CO₂ before compression. Mixing was provided by an impeller mounted on the top cap and driven by a variable velocity electric motor. The autoclave was heated by thin band heaters, whose thermal control was assured by a PID controller (Watlow, mod. 93, USA). The temperature inside the cylinder was measured by a K-type thermocouple with an accuracy of ± 0.1 °C. Pressure was measured by a digital gauge manometer (Parker, Minneapolis, MN). At the exit of the autoclave, CO₂ flow rate was measured by a rotameter. Depressurization was obtained through a micrometering valve (Hoke, mod. 1315G4Y, Spartanburg, SC).

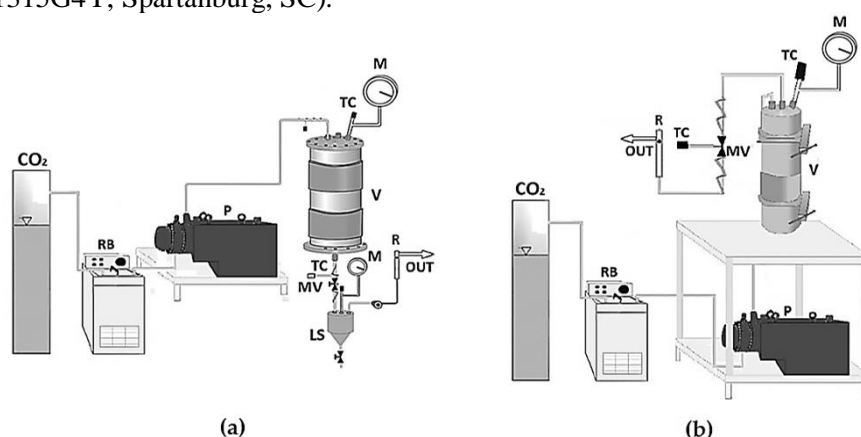


Figure V.1 Sketches of the plants for (a) drying; (b) impregnation. CO₂: carbon dioxide supply; RB: refrigerating bath; P: pump; TC: thermocouple; M: manometer; MV: micrometering valve; LS: liquid separator; BPV: back pressure valve and R: rotameter.

V.1.3 Procedures for aerogels preparation

The experimental procedure to obtain aerogels in the case of MSA and CAA substantially differs only for the achievement of the hydrogel.

Briefly, the production of maize starch aerogel, optimized in a previous work (De Marco et al., 2015a), started with the preparation of a hydrogel through the starch gelation, which involved two steps: gelatinization and retrogradation. The gelatinization step consisted of the preparation of a solution at 15 % w/w in distilled water, stirring for about 24 h and heating up to 110 °C; afterwards, this mixture was poured into cylindrical moulds. The retrogradation step, necessary for the rearrangement of the structure, was reached by placing the samples in a refrigerator at 4°C for three days.

The production of calcium alginate aerogels, optimized in a previous work (Baldino et al., 2016), started with the attainment of an hydrogel through the preparation of a solution at 5 % w/w of sodium alginate in distilled water, stirring for about 24 h at 200 rpm and afterwards pouring into

cylindrical moulds. The gelation was promoted by immersing the samples in a coagulation bath of CaCl_2 (5 % w/w in distilled water) for about 24h. During this step, sodium alginate was converted to calcium alginate. Then the hydrogels were washed with distilled water to eliminate Ca^{2+} residues.

The second step for the aerogel preparation is the attainment of an alcogel, by a gradual replacement of the water filling the pores of the gel structure by batch equilibration with a series of ethanol baths at increasing concentration (30%, 70%, 90% and two times 100% v/v) at room temperature, 24 h each (De Marco et al., 2015a, Baldino et al., 2016).

Then, the alcogels have to be dried to obtain the aerogels using scCO_2 . In detail, the samples were placed in the vessel sketched in **Figure V.1a**, which was then filled with scCO_2 to achieve the operating pressure (20 MPa) and temperature (45°C or 35°C for MSA and CAA, respectively) (2015a, Baldino et al., 2016). Drying was performed for 5 h, using a scCO_2 flow rate of about 1 kg/h. A slow depressurization was used to bring back the system at atmospheric pressure and recover the aerogels from the vessel.

V.1.4 Procedures for drug solubility measurements and impregnation tests into polymeric supports

The MSG solubility in scCO_2 was experimentally determined according to a procedure set in previous papers (Smirnova et al., 2003, Caputo et al., 2012). A small stainless steel cylinder containing a weighed amount of drug was wrapped with paper filter to avoid the drug entrainment and, then, placed on the bottom of the autoclave described for the impregnation tests. Once the autoclave was closed, it was heated up to the desired temperature, whereas CO_2 was delivered to reach the desired pressure. In order to ensure the equilibrium conditions, the system was stored for 24 h under mechanical stirring. At the end of the experiment, CO_2 was slowly vented out (about 1 MPa/min); the not-dissolved MSG contained in the cylinder was weighed, so obtaining the amount of the dissolved drug by the weight difference.

Impregnation experiments were performed using a static method (Smirnova et al., 2003, Zhang et al., 2005). A weighed amount of polymeric support (i.e., aerogel, granules or film) was wrapped in filter paper to avoid its contact with the solid drug. Then, the sample was placed on the bottom of the autoclave. In order to allow contact with scCO_2 , a weighed amount of drug was placed in a small container opened on the top mounted axially on the impeller. Finally, the autoclave was closed, heated to the fixed temperature (in the range 35-60°C) and CO_2 was slowly fed to the system. When the working pressure (in the range 17-18 MPa) was reached, the system was stored for a fixed time (in the range 2-72 h). The amount of CO_2 in the autoclave was determined from the density value, calculated at the operating temperature and pressure through the Bender equation (Bender, 1970). Then, CO_2 was vented out at flow rate of about 1 MPa/min. When the

atmospheric conditions were reached, the impregnated support was recovered and weighed. The weight increase of the sample was related to the amount of loaded drug, which was checked by UV/vis spectrophotometer.

V.2 Supercritical impregnation of drugs into aerogels

The supercritical impregnation of various NSAIDs was studied in different aerogels (i.e., MSA and CAA) to formulate ODTs with a rapid or controlled drug release, for the treatment of both minor and chronic inflammations. In particular, NIM, KET and DIC were selected as model NSAIDs. The experimental results can be divided into three parts:

1. the thermodynamics of impregnation was studied through the isotherms, which correlate the concentration of each NSAID in the scCO₂ phase with the concentration of the drug in the aerogel at equilibrium;
2. the impregnation kinetics of each NSAID in MSA and CAA were studied to know the time required for the drug to reach the equilibrium concentration under certain operating conditions;
3. NSAID/aerogel systems were analyzed by different techniques.

V.2.1 Isotherms of impregnation of NSAIDs into aerogels

The impregnation isotherms of each NSAID in MSA and CAA were determined at 40°C/18 MPa and 60°C/18 MPa, for a fixed time of 24 h in order to ensure equilibrium. The isotherm curves obtained are shown in **Figure V.2**, **Figure V.3** and **Figure V.4**, respectively for NIM, KET and DIC.

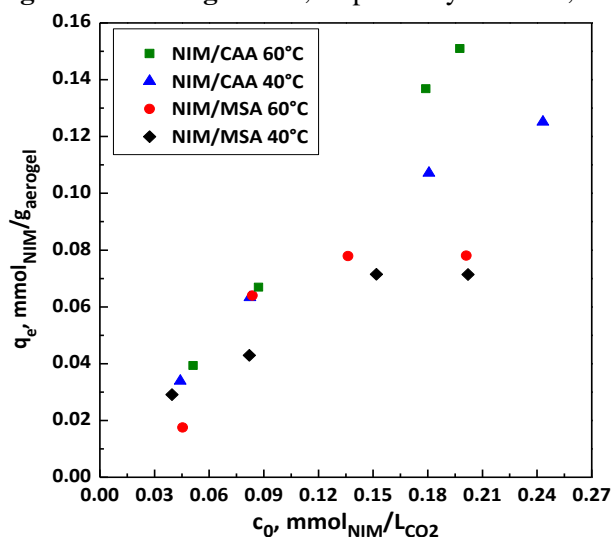


Figure V.2 Impregnation isotherms at 18 MPa and 40/60°C for NIM/aerogels.

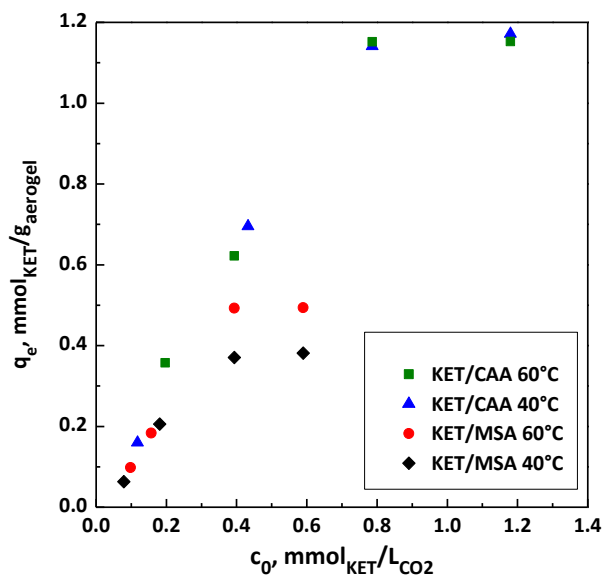


Figure V.3 Impregnation isotherms at 18 MPa and 40 and 60°C for KET/aerogel systems.

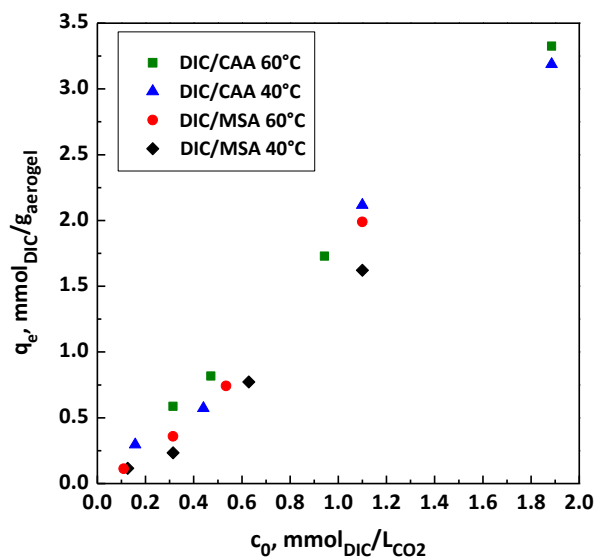


Figure V.4 Impregnation isotherms at 18 MPa and 40 and 60°C for DIC/aerogel systems.

In all the systems studied, it can be noted that the amount of NSAID impregnated in the aerogel increased by increasing the drug concentration in scCO₂ and is higher at the highest studied temperature. Working at 60°C, the maximum amount of impregnated NIM was approximately 0.02 and 0.05 mg_{NIM}/mg_{aerogel} in MSA and CAA, respectively; while KET was impregnated

in MSA and CAA up to a maximum value of 0.13 and 0.29 mg_{KET}/mg_{aerogel}, respectively. The highest loadings were achieved for DIC, since the maximum amount of DIC loaded in MSA and CAA at 60°C was approximately 0.63 e 1.06 mg_{DIC}/mg_{aerogel}, respectively. For each NSAID, it can be noted that the amount of drug impregnated in CAA is generally higher than that loaded in MSA.

On the basis of the Brunauer classification (Brunauer et al., 1940), the isotherms showing an upward convexity are defined “favorable” (type I) to solute uptake; while, they are classified as “unfavorable” (type III) when concave upwards to solute uptake. According to this classification, the isotherms obtained for NIM/MSA at both temperatures, NIM/CAA at 40 °C, KET/MSA and KET/CAA at both temperatures, and DIC/CAA at 40 °C are favorable; while the isotherms for DIC/MSA at both temperatures are “unfavorable”. Instead, the isotherms obtained for NIM/CAA and DIC/CAA at 60°C appear to be linear.

V.2.2 Kinetics of impregnation of NSAIDs into aerogels

The impregnation kinetics was determined to know the time required for the complete impregnation of each NSAID in MSA and CAA. Uptake was expressed as q ; i.e., mmol of NSAID per gram of aerogel. Kinetic data were obtained by loading a constant weighted quantity of drug, which was then dissolved in scCO₂ and kept in contact with each aerogel for various times (from 2 to 72 h) at a fixed pressure of 18 MPa. The impregnation kinetics obtained at temperatures of 40 and 60°C for MSA and CAA are reported in **FigureV.5**, **FigureV.6** and **FigureV.7** respectively for NIM, KET and DIC, in order to study the effect of temperature and the possible difference in terms of NSAIDs impregnation between the two aerogels studied.

For all the composite systems examined, it was shown that the quantity of impregnated NSAID increased by increasing the operating temperature, also due to the higher solubility at the pressure of 18 MPa (Macnaughton et al., 1996). Furthermore, the comparison of kinetic curves for both temperatures suggested that the amount of drug loaded into the CAA was higher than that into the MSA. The best impregnation of all NSAIDs in CAA is probably due to its higher specific surface area compared to MSA. Indeed, the specific surface areas, determined experimentally, were equal to 80 and 277 m²/g for MSA and CAA, respectively. It is also possible to note that the maximum amount of drug is impregnated between 24 h and 48 h for all NSAID/aerogel systems, except in the case of KET impregnated in CAA (between 60 and 72 h). Furthermore, the amount of drug impregnated in both aerogels is higher in the case of DIC, also thanks to its greater solubility in scCO₂ at a pressure of 18 MPa (Bettini et al., 2004), followed by KET (Macnaughton et al., 1996); instead, NIM showed the lowest impregnation values, since it has the lowest solubility in scCO₂ (Macnaughton et al., 1996, Caputo et al., 2012).

Summing up, in terms of aerogel/NSAID weight ratio, the maximum amount of drug loaded into CAA at 60°C was about 0.04, 0.42 and 1.09 $\text{mg}_{\text{drug}}/\text{mg}_{\text{aerogel}}$ for NIM, KET and DIC, respectively. The amount of drug impregnated in the aerogels in the case of KET and especially of DIC is remarkable. This confirms the potential of supercritical impregnation to overcome the main drawbacks of conventional impregnation techniques based on the use of liquid solvents; i.e., low loadings of active principle on/in polymeric matrices (Kikic and Vecchione, 2003). Indeed, the penetration of a liquid (used as a carrier) in porous materials is limited both by the liquid molecular/bulk properties (e.g., surface tension of the liquid) and by the geometry and surface properties of the polymeric matrices (e.g., pore size) (Ahuja and Pathak, 2009).

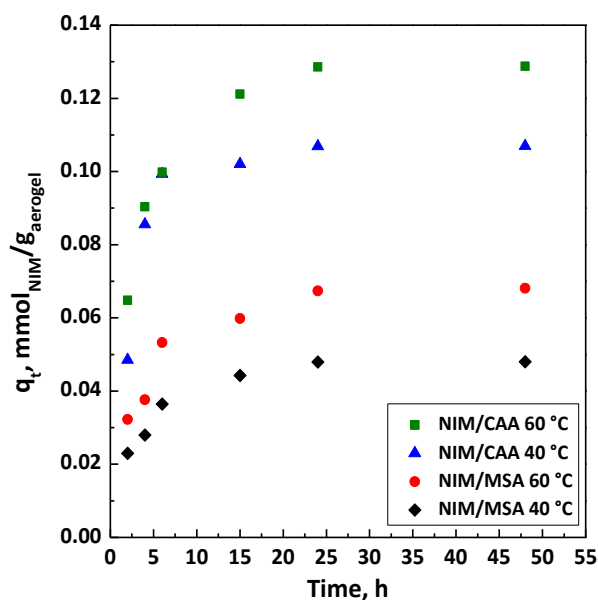


Figure V.5 Kinetic curves at 18 MPa and 40 and 60°C for the impregnation of NIM into aerogels.

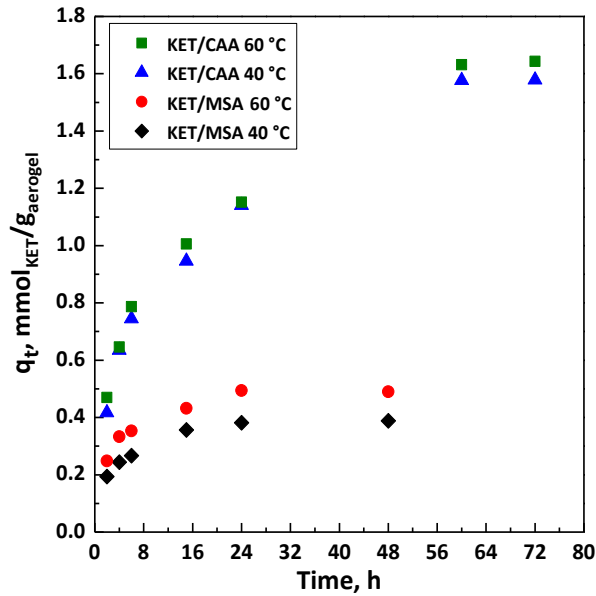


Figure V.6 Kinetic curves at 18 MPa and 40 and 60°C for the impregnation of KET into aerogels.

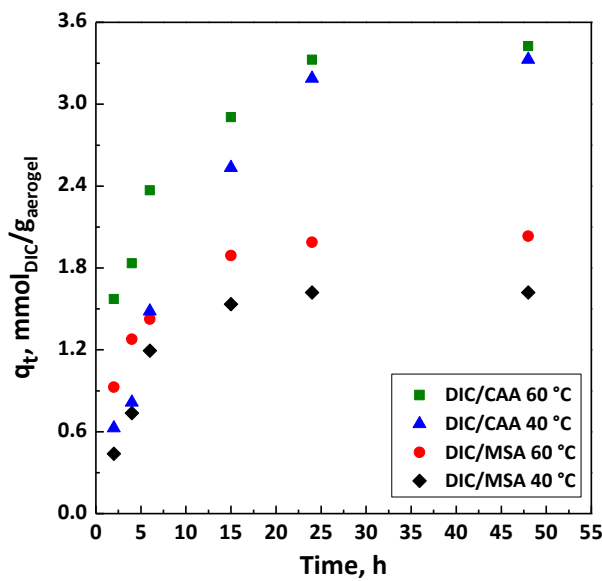


Figure V.7 Kinetic curves at 18 MPa and 40 and 60°C for the impregnation of DIC into aerogels.

In order to verify if the experimental and theoretical loadings are in good agreement and to study the specific rate constants of each support/drug system, the kinetic data were fitted with pseudo-first-order and pseudo-

second-order equations, which were obtained by integrating the following equation (Ho, 2006):

$$\frac{d\left(1 - \frac{q_t}{q_e}\right)}{dt} = -k\left(1 - \frac{q_t}{q_e}\right)^n \quad (3)$$

where q_t is the quantity of drug loaded into the polymeric support after the contact time “ t ” (mmol/g) and q_e is the adsorption capacity at equilibrium (mmol/g); i.e., the maximum amount of drug loaded in the support.

The impregnation rate constants obtained from the pseudo-first-order and pseudo-second-order models are reported in **Table V.1** and in **Table V.2**, respectively. In all the cases studied, it can be observed in **Table V.2** that the pseudo-second-order kinetics fitted better the experimental data with respect to the pseudo-first-order kinetics, since the values of R^2 are closer to unity. According to the literature (Ho, 2006), the pseudo-second-order model is related to a possible chemisorption involving valency forces or weak interactions between the two materials.

The pseudo-second-order equation (Ho, 2006) was expressed as:

$$\frac{t}{q_t} = \frac{t}{q_e} + \frac{1}{k_2 q_e^2} \quad (4)$$

where k_2 is the pseudo-second-order rate constant (g/mmol h).

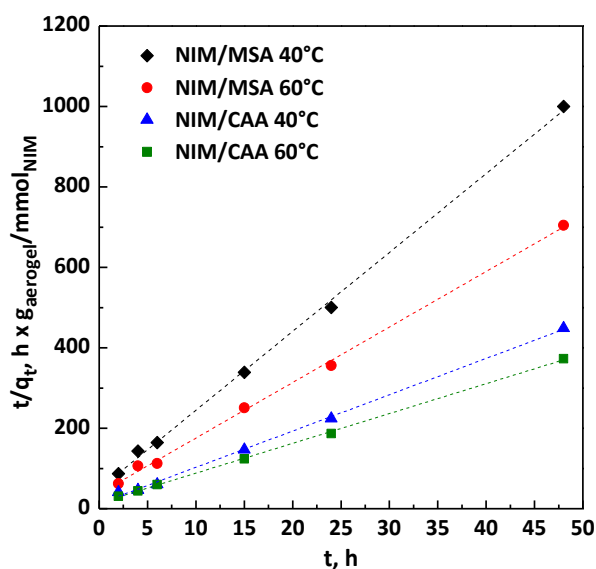
Plotting t/q_t vs t , q_e and k_2 were determined by the slope and the intercept of the fitting, as in **Figure V.8**, **Figure V.9** and **Figure V.10** for NIM, KET and DIC, respectively.

Table V.1 Impregnation rate constants obtained from the pseudo-first-order kinetics for NSAID/aerogel systems.

Sample	T °C	Pseudo-first-order kinetics		
		q_e mmol/g	k_1 1/h	R^2
NIM/MSA	40	0.048	0.261	0.9207
	60	0.068	0.181	0.9207
NIM/CAA	40	0.107	0.313	0.9121
	60	0.129	0.253	0.9539
KET/MSA	40	0.388	0.173	0.9782
	60	0.490	0.162	0.7675
KET/CAA	40	1.579	0.099	0.9392
	60	1.644	0.077	0.9611
DIC/MSA	40	1.621	0.196	0.9885
	60	1.989	0.207	0.9814
DIC/CAA	40	3.328	0.120	0.9615
	60	3.425	0.145	0.9587

Table V.2 Impregnation rate constants obtained from the pseudo-second-order kinetics for NSAID/aerogel systems.

Sample	T °C	Pseudo-second-order kinetics		
		q_e mmol/g	k_2 g/mmol h	R^2
NIM/MSA	40	0.051	7.920	0.9988
	60	0.073	5.058	0.9984
NIM/CAA	40	0.111	6.487	0.9985
	60	0.135	3.903	0.9995
KET/MSA	40	0.411	0.956	0.9992
	60	0.517	0.834	0.9986
KET/CAA	40	1.772	0.061	0.9903
	60	1.833	0.060	0.9888
DIC/MSA	40	1.813	0.125	0.9908
	60	2.110	0.201	0.9988
DIC/CAA	40	4.352	0.018	0.9686
	60	3.677	0.081	0.9987

**Figure V.8** Pseudo-second-order kinetics for the impregnation of NIM into aerogels, at 18 MPa and 40 and 60°C.

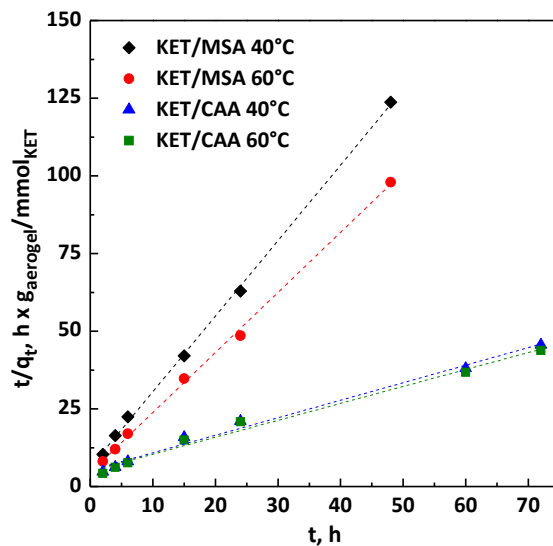


Figure V.9 Pseudo-second-order kinetics for the impregnation of NIM into aerogels, at 18 MPa and 40 and 60°C.

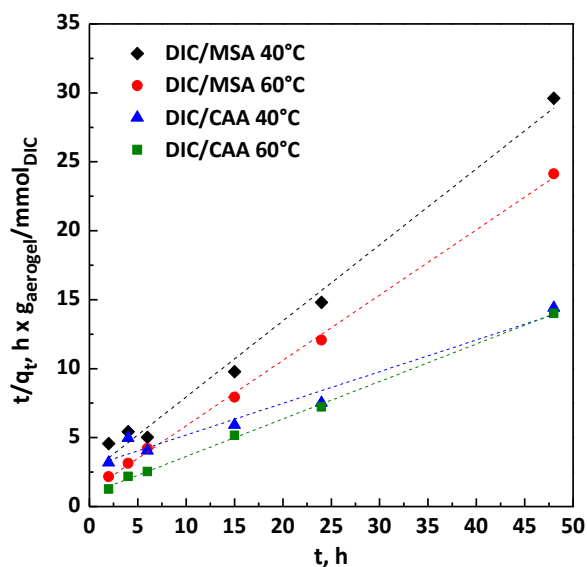


Figure V.10 Pseudo-second-order kinetics for the impregnation of NIM into aerogels, at 18 MPa and 40 and 60°C.

V.2.3 Mechanism of NSAID impregnation into aerogels

Once the impregnation kinetics were determined, the impregnation mechanisms were studied by identifying the controlling steps of the process among the following ones (Lazaridis and Asouhidou, 2003):

- *film diffusion*, due to the transport of the drug on the external surface of the adsorbent;
- *intraparticle or pore diffusion*, related to drug transport within the pores of the adsorbent;
- *drug release* on active adsorbent sites.

In general, the rate-limiting step of the impregnation process is the slowest one between film and intraparticle diffusion, since the last step is commonly very fast so its resistance can be neglected (Kalavathy et al., 2005). If the adsorbent is an aerogel, the impregnation of the drug is often governed initially by film diffusion, followed by pore diffusion (De Marco and Reverchon, 2017). According to the Weber and Morris approach (Weber and Morris, 1963), the intraparticle diffusion coefficient K_{id} can be defined through the following equation:

$$q_t = K_{id} t^{0.5} + C \quad (5)$$

If $C=0$ and K_{id} is constant, q_t is a straight line with intercept equal to zero and intraparticle diffusion is the only limiting step; otherwise, the film diffusion has also to be taken into consideration.

Plotting q_t versus $t^{0.5}$ as shown in **FigureV.11**, **FigureV.12** and **FigureV.13** respectively for NIM, KET and DIC, a multi-linearity was observed in all the cases studied, indicating that several steps governed the impregnation process (Weber and Morris, 1963, Sun and Yang, 2003, Kalavathy et al., 2005).

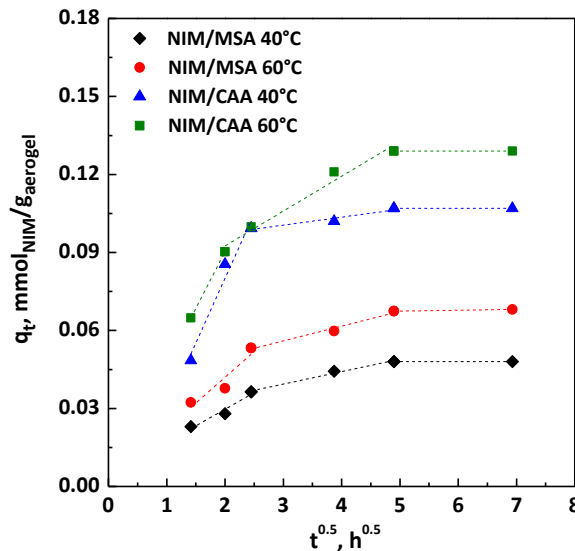


Figure V.11 Intraparticle diffusion plot for the impregnation of NIM in MSA and CAA.

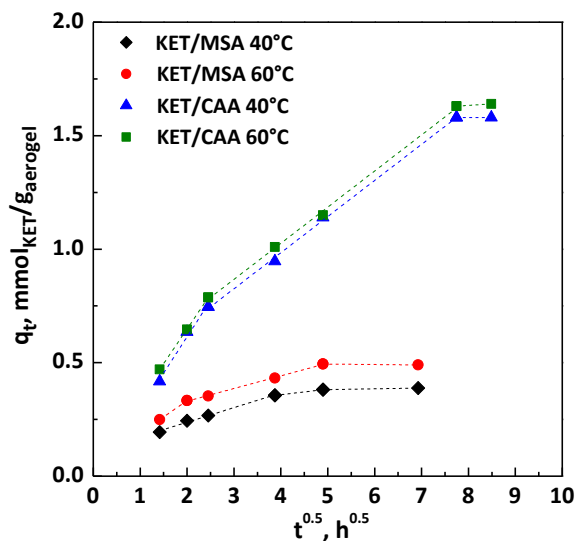


Figure V.12 Intraparticle diffusion plot for the impregnation of KET in MSA and CAA.

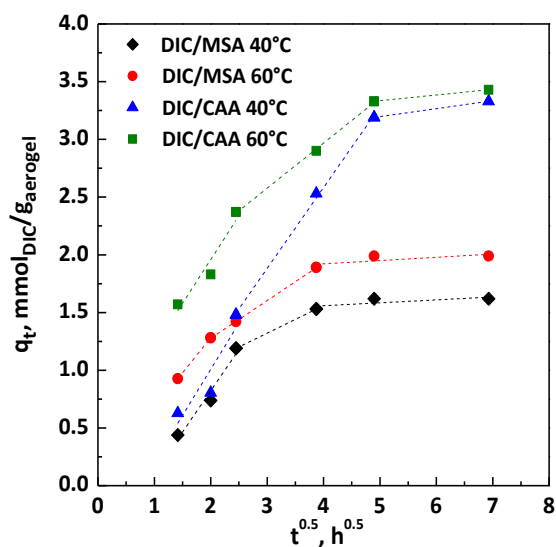


Figure V.13 Intraparticle diffusion plot for the impregnation of DIC in MSA and CAA.

It can be observed in **Table V.3** that $K_{1d} > K_{2d} > K_{3d}$ in all the cases studied, which means that at the beginning the impregnation is controlled by film diffusion and that the drug was impregnated on the outer surface of the aerogel. The impregnation rate is fast at this early stage, since the aerogel is not loaded. Thus, the drug is also impregnated on the inner surface of the aerogel and the diffusion rate decreased due to an increase in diffusion resistance; in this phase, the impregnation process is controlled by pore

diffusion (Sun and Yang, 2003). The diffusion rate becomes increasingly lower as the concentration of NSAIDs in scCO₂ decreases (as shown by the K_{3d} values); i.e., the diffusion process tends towards the final equilibrium stage.

Table V.3 Pore diffusion rate parameters for NSAID/aerogel systems.

Sample	T °C	K _{1d} mmol g ⁻¹ h ^{-0.5}	K _{2d} mmol g ⁻¹ h ^{-0.5}	K _{3d} mmol g ⁻¹ h ^{-0.5}
NIM/MSA	40	1.3 x 10 ⁻²	4.8 x 10 ⁻³	2.0 x 10 ⁻⁵
	60	2.0 x 10 ⁻²	5.7 x 10 ⁻³	3.0 x 10 ⁻⁴
NIM/CAA	40	5.0 x 10 ⁻²	3.0 x 10 ⁻³	1.0 x 10 ⁻⁵
	60	4.4 x 10 ⁻²	1.3 x 10 ⁻²	8.0 x 10 ⁻⁵
KET/MSA	40	6.5 x 10 ⁻²	2.5 x 10 ⁻²	3.2 x 10 ⁻³
	60	1.5 x 10 ⁻¹	5.6 x 10 ⁻²	1.0 x 10 ⁻⁵
KET/CAA	40	3.2 x 10 ⁻¹	1.6 x 10 ⁻¹	3.2 x 10 ⁻³
	60	3.1 x 10 ⁻¹	1.6 x 10 ⁻¹	1.6 x 10 ⁻²
DIC/MSA	40	7.2 x 10 ⁻¹	2.4 x 10 ⁻¹	2.4 x 10 ⁻²
	60	6.0 x 10 ⁻¹	3.3 x 10 ⁻¹	2.8 x 10 ⁻²
DIC/CAA	40	8.0 x 10 ⁻¹	7.0 x 10 ⁻¹	6.9 x 10 ⁻²
	60	7.5 x 10 ⁻¹	3.9 x 10 ⁻¹	4.9 x 10 ⁻²

V.2.4 Characterization of NSAID/aerogel composites

The morphology of MSA and CAA was observed before and after drug impregnation through the FESEM images, shown in **FigureV.14** and **FigureV.15** for MSA-based and CAA-based samples, respectively. Both aerogels consisted of a porous structure, which was preserved after the supercritical impregnation. In particular, unloaded CAA (**FigureV.15a**) is characterized by smaller pores than unloaded MSA (**FigureV.14a**). The presence of drug, which often filled/covered the porosity, can be observed in the case of impregnated samples. From the FESEM images, it is possible to observe that, when the drugs were impregnated into MSA (**FigureV.14b**, **FigureV.14c** and **FigureV.14d**), packed regions can be observed. For this reason, the variation of the specific surface areas and the pore size distributions were evaluated. In particular, the specific surface area was equal to 58.3 ± 0.5 , 46.0 ± 1.0 and 44.4 ± 0.7 m²/g for NIM/MSA, KET/MSA and DIC/MSA, respectively. The reduction of the specific surface area in the a impregnated samples with respect to the one of unloaded MSA (80 m²/g) is due to the impregnated drug that fills the aerogel porosities. Moreover, it is possible to consider that the reduction was lower in the case of NIM/MSA (27.1%) with respect to KET/MSA (42.5%) and DIC/MSA (44.5%), because of the lower amount of NIM impregnated onto MSA with respect to the other NSAIDs. The pore size distributions were evaluated in terms of mean pore size \pm standard deviation. They were $0.26 \pm$

0.27 μm for NIM/MSA, 0.26 \pm 0.22 μm for KET/MSA and 0.13 \pm 0.10 μm for DIC/MSA. The higher reduction in the pore size of DIC/MSA sample can be ascribed to the higher amount of impregnated drug with respect to the other NSAID/MSA samples. Considering the NSAIDs impregnation into CAA (**Figure V.15b**, **Figure V.15c** and **Figure V.15d**), it is possible to observe the presence of micrometric-sized drug crystals onto the aerogel external surface, thus relating to the part of the drug that has not been impregnated in the CAA pores.

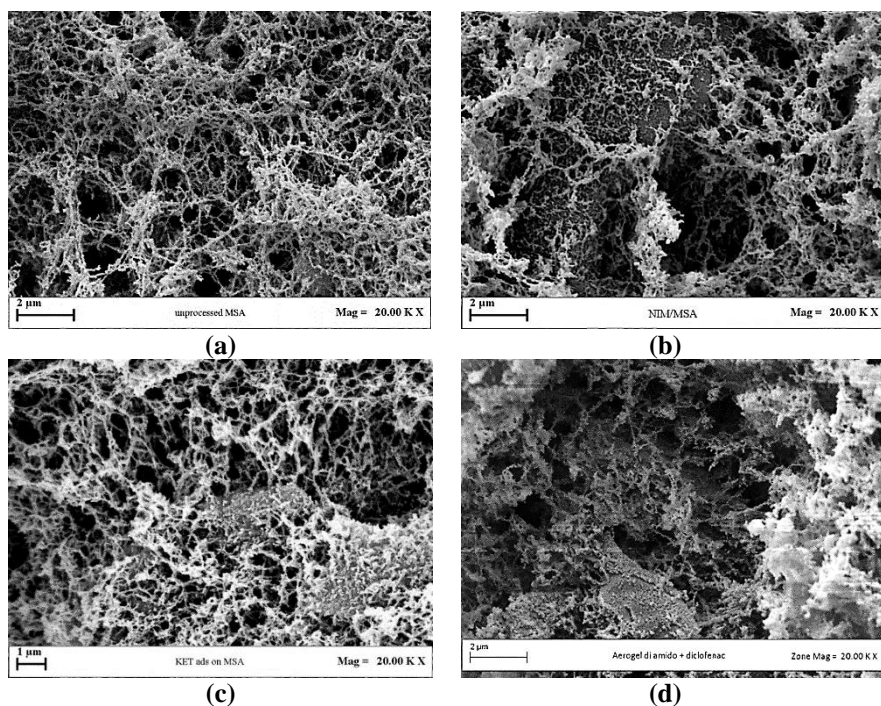
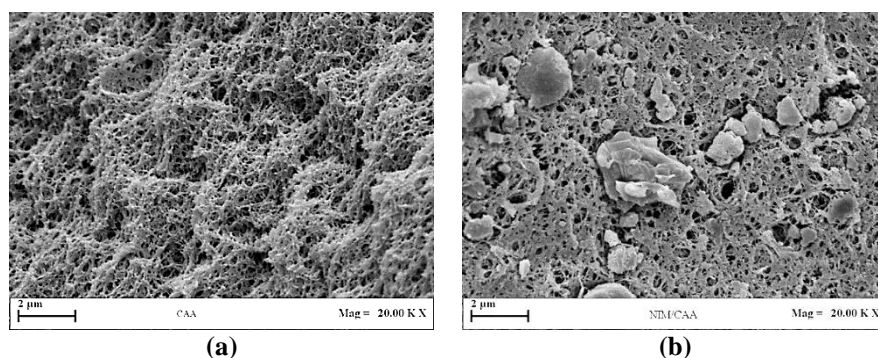


Figure V.14 FESEM images of (a) pure MSA after drying using $sc\text{CO}_2$, (b) NIM impregnated on MSA, (c) KET impregnated on MSA, (d) DIC impregnated on MSA.



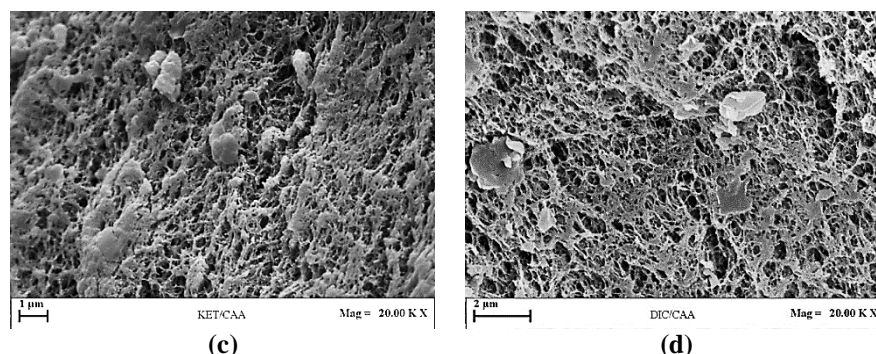


Figure V.15 FESEM images of (a) pure CAA after drying using $scCO_2$, (b) NIM impregnated on CAA, (c) KET impregnated on CAA, (d) DIC impregnated on CAA.

The FTIR spectra of pure NSAIDs, unloaded MSA and CAA, physical mixtures (NSAID+aerogel) and loaded samples are shown in **FigureV.16**, **FigureV.17** and **FigureV.18** for NIM, KET and DIC, respectively. Although the spectra of the impregnated samples and physical mixtures were similar to those of aerogels, some characteristic bands of the drug were also detected, as follows:

- With regards to the NIM/MSA and NIM/CAA systems, the spectra of impregnated samples and physical mixtures showed a characteristic peak of NIM (Chopra et al., 2007, Begum et al., 2015, Campardelli et al., 2019a); that is, the peak at 1341 cm^{-1} related to the stretching of the SO_2 . Furthermore, the spectra of NIM impregnated on CAA and of NIM/CAA physical mixture exhibited peaks at 1153 cm^{-1} also attributed to the stretching of SO_2 and at 1588 cm^{-1} corresponding to the asymmetric stretching of NO_2 .

- As regards the KET/MSA and KET/CAA systems, the spectra of impregnated samples and physical mixtures showed two peaks related to the presence of KET; i.e., at 1649 and 1697 cm^{-1} indicating the carbonyl group (Grimling et al., 2014, Al-Tahami, 2014). Besides, the KET/CAA mixture and the corresponding impregnated sample also exhibited a band at 1437 cm^{-1} ascribable to deformation of CH_3 .

- As regards the DIC/MSA and DIC/CAA systems, the spectra of impregnated samples and physical mixtures showed some typical peaks of DIC (Kebebe et al., 2010, Edavalath et al., 2011): for example, at about 1574 cm^{-1} corresponding to the stretching of $-C=O$ of the carboxyl ion, at 1450 cm^{-1} related to C-H bend, at 746 and 774 cm^{-1} for the stretching of the C-Cl bond. Furthermore, the spectra of DIC impregnated on MSA and the physical mixture DIC/MSA showed a peak at 1557 cm^{-1} due to the stretching of C=C ring.

The results just discussed clearly demonstrate the presence of the drug inside the aerogel after the impregnation process. Besides, no interactions

between polymer and drug were observed, since the presence of new peaks that belong neither to the aerogel nor to the drug was not detected.

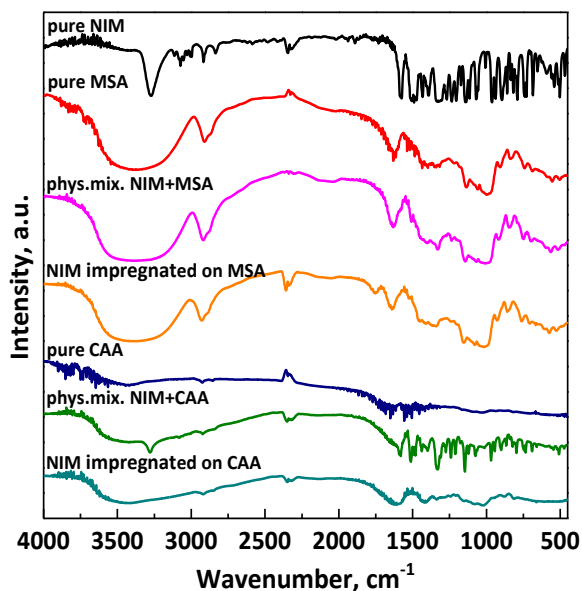


Figure V.16 FTIR spectra for pure NIM, pure MSA and CAA, physical mixture aerogel+NIM, NIM impregnated into aerogels.

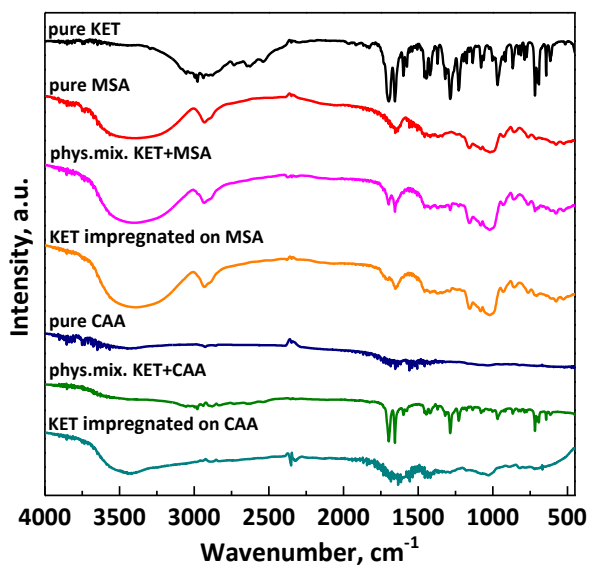


Figure V.17 FTIR spectra for pure KET, pure MSA and CAA, physical mixture aerogel+KET, KET impregnated into aerogels.

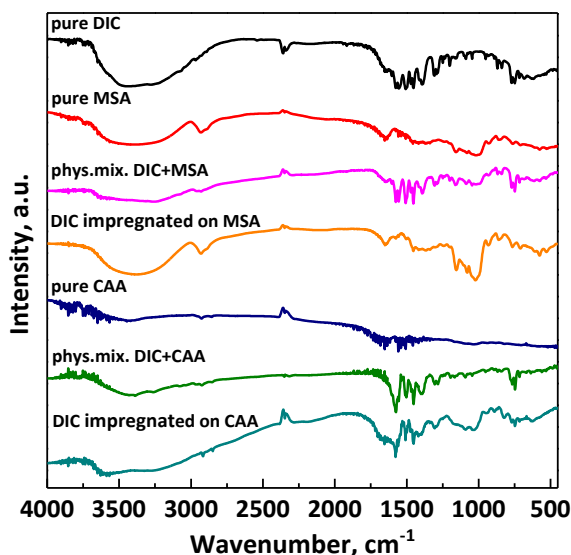


Figure V.18 FTIR spectra for pure DIC, pure MSA and CAA, physical mixture aerogel+DIC, DIC impregnated into aerogels.

DSC thermograms of NIM, KET and DIC samples are shown in **Figure V.19**, **Figure V.20** and **Figure V.21**, respectively. The NIM curve had an endothermic peak at about 150°C indicating the melting point and an exothermic peak at a higher temperature due to crystallization. The thermogram of pure KET exhibited an endothermic peak at about 95.5 °C indicating the melting point, followed by the thermal decomposition of the drug in the temperature range 250-380°C (Tița et al., 2011). The curve of pure DIC showed two endothermic peaks at about 56 and 288°C respectively due to the dehydration and melting point, followed by the thermal decomposition of the drug (Lopes et al., 2006). MSA thermogram showed a first broad endothermic peak attributed to the dehydration and gelatinization of MSA (De Marco et al., 2015a), followed by starch degradation between 260 and 350°C (Cruz et al., 2015). Instead, the CAA curve exhibited a broad endothermic peak related to dehydration (Baldino et al., 2016). As shown in the DSC thermograms, the composite systems were characterized by an amorphous shape similar to aerogels before supercritical impregnation. This outcome can be explained considering that the polymeric matrix containing the impregnated drug has an amorphous structure which, therefore, hides the peaks related to crystalline drugs.

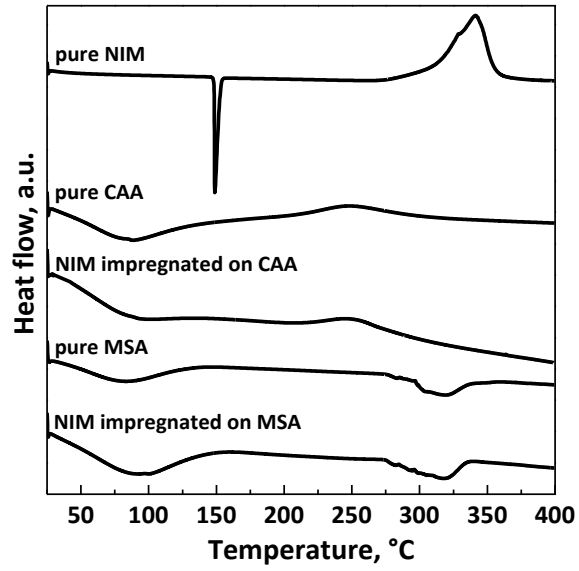


Figure V.19 DSC thermograms of pure NIM, pure MSA and CAA, NIM impregnated into aerogels.

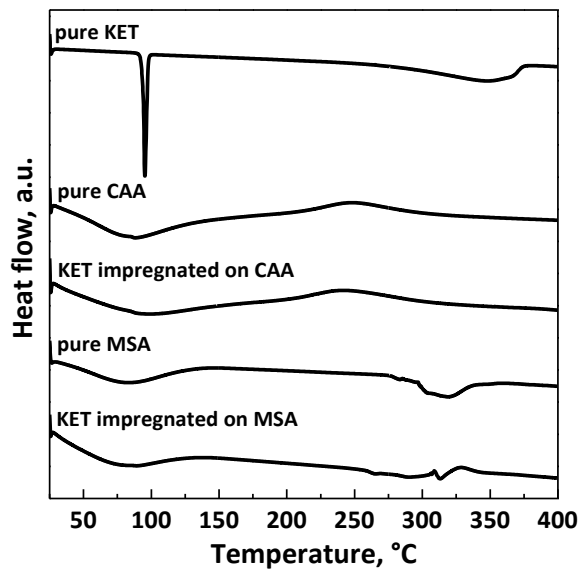


Figure V.20 DSC thermograms of pure KET, pure MSA and CAA, KET impregnated into aerogels.

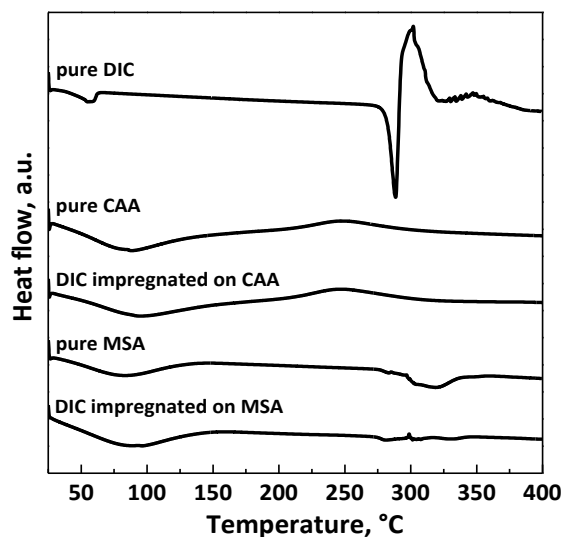


Figure V.21 DSC thermograms of pure DIC, pure MSA and CAA, DIC impregnated into aerogels.

XRD analyses were performed on each unprocessed NSAID and on aerogels before and after scCO_2 impregnation. The XRD patterns are reported in **Figure V.22**, **Figure V.23** and **Figure V.24** for NIM, KET and DIC, respectively.

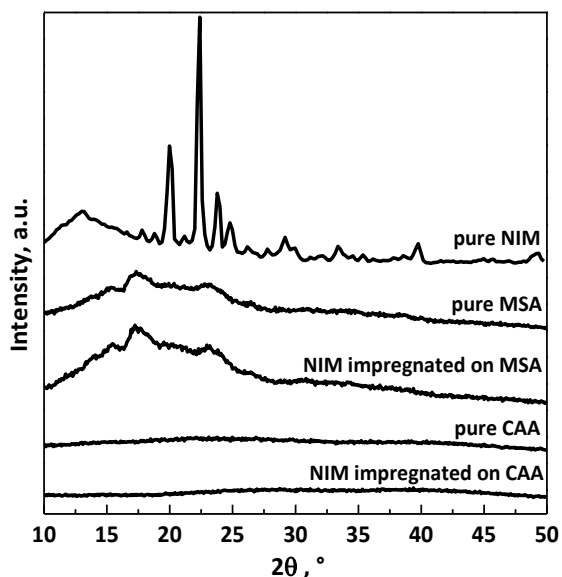


Figure V.22 XRD patterns for pure NIM, pure MSA and CAA, NIM impregnated into aerogels.

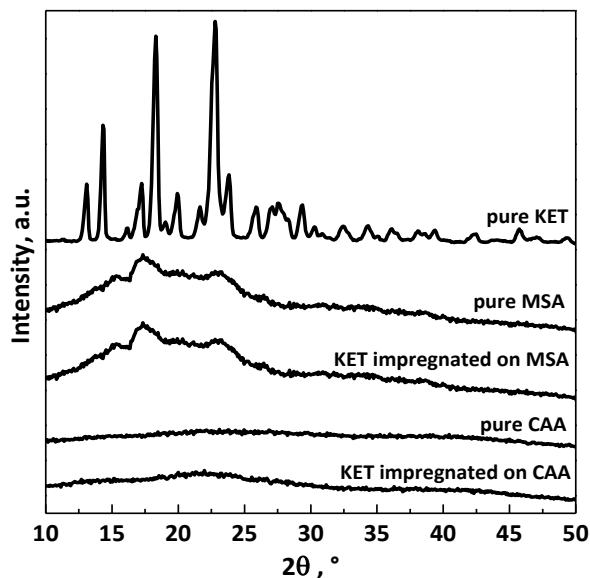


Figure V.23 XRD patterns for pure KET, pure MSA and CAA, KET impregnated into aerogels.

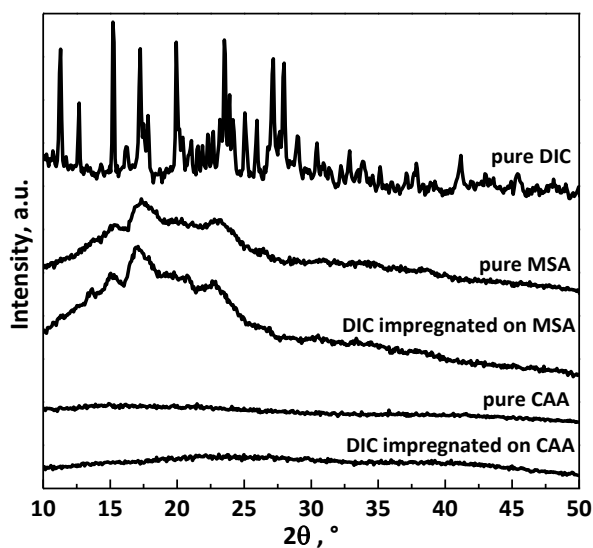


Figure V.24 XRD patterns for pure DIC, pure MSA and CAA, DIC impregnated into aerogels.

All NSAIDs were characterized by a typical crystalline structure, while MSA and CAA were amorphous as well as composite systems obtained by supercritical absorption. Several literature studies have highlighted the advantages of the amorphous form, also called *disordered*, compared to the crystalline form in the pharmaceutical field, such as the increase in drug

wettability, free energy and apparent solubility (Hancock and Parks, 2000, Gurunath et al., 2013, Dahan et al., 2013).

In vitro dissolution tests were performed on pure NSAIDs and drugs impregnated in the aerogels. The release profiles are shown in **FigureV.25**, **FigureV.26** and **FigureV.27** for NIM, KET and DIC, respectively.

For all NSAIDs considered, it was observed that the dissolution rate was faster than the pure drug when the NSAID was impregnated into MSA, while a controlled release was obtained by loading the NSAID into CAA. In particular, as regards the NIM samples, the pure NIM reached 90 % of the dissolution in about 15 h, while the physical mixture NIM/MSA and the NIM impregnated in MSA required 13 h and 10 h, respectively. Instead, the physical mixture NIM/CAA and NIM loaded in CAA achieved 90 % of release in about 18.5 h and 69 h. As regards the KET samples, 90 % of the dissolution was achieved in 1.7 h both for pure KET and for the physical mixture KET/MSA; while the release of KET was accelerated when it was impregnated on MSA, effectively reaching 90 % of the dissolution in 1.47 h. On the contrary, the dissolution of KET was prolonged thanks to CAA, achieving 90 % of release in 1.95 h and 2.7 h respectively in case of physical mixture and impregnated sample. Finally, the physical mixture DIC/MSA and DIC impregnated into MSA reached 90 % of the dissolution in about 1.6 and 1.2 h respectively, whereas the pure DIC and the physical mixture DIC/CAA took about 2 h. When DIC was impregnated in CAA, 90 % of the release was obtained in about 7 h. The results obtained from these drug release studies in PBS are of considerable interest. Summing up, the dissolution process is faster when the drug is impregnated in MSA because it is a hydrophilic carrier, so it is quickly wetted with water, with a partial collapse of the MSA structure; the drug molecules are readily surrounded by the water (Smirnova et al., 2005b). In contrast, CAA promotes a controlled drug release, as it has a hydrophobic behaviour, thus it is more stable in water than the hydrophilic aerogel. Furthermore, CAA is characterized by pores smaller than those of MSA, therefore the diffusion of the drug within the pores of the aerogel appears to be the controlling phenomenon during the dissolution process.

From a pharmaceutical point of view, in the case of NIM, the use of MSA as a hydrophilic carrier to promote fast drug release may be preferable for obtaining ODTs for inflammatory conditions such as headaches, toothache, etc. (Caputo et al., 2012, Prosapio et al., 2016b). Instead, since DIC is more suitable for the treatment of rheumatoid arthritis and osteoarthritis, its impregnation in CAA is suitable for producing tablets with a slow dissolution rate to reduce the dosage frequency (Sahoo and Mishra, 2013, Priyanka et al., 2018). Both composite systems with fast or controlled release can be considered in the case of KET (Smirnova et al., 2005b, Mazières et al., 2005, Ahmed and Fatahalla, 2007).

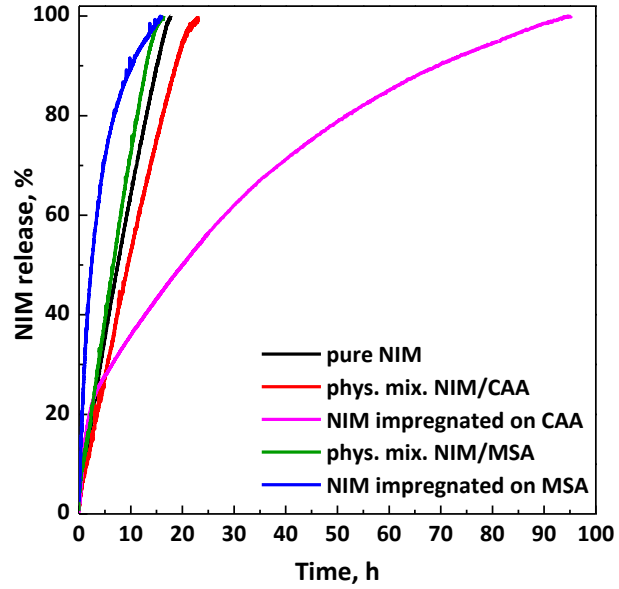


Figure V.25 Dissolution profiles of NIM in PBS at 37 °C and pH 7.4.

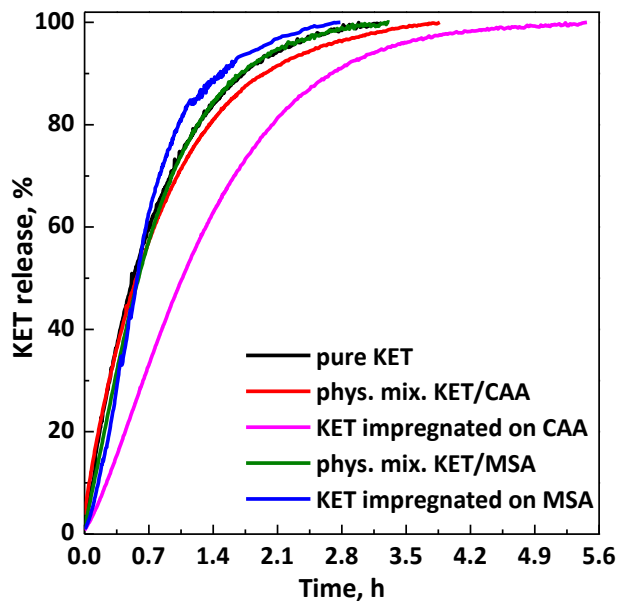


Figure V.26 Dissolution profiles of KET in PBS at 37 °C and pH 7.4.

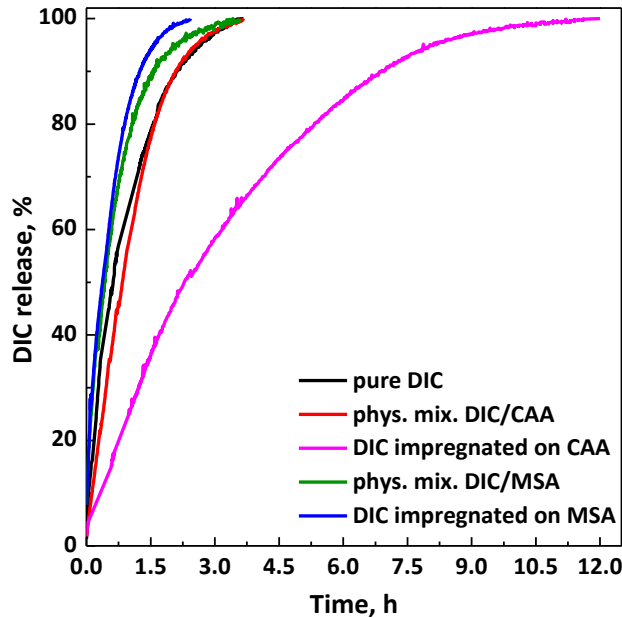


Figure V.27 Dissolution profiles of DIC in PBS at 37 °C and pH 7.4.

The Peppas equation (Ritger and Peppas, 1987) was used to compare drug release profiles, as well as to obtain quantitative information on the mechanism of aerogel-based drug delivery systems. Indeed, Peppas proposed an exponential relationship that can be used to describe the Fickian and non-Fickian release behavior of moderately swellable controlled release systems, which are prepared by drug incorporation into polymers. In general, the release of the drug from a controller-release system is strongly influenced by diffusion and/or macromolecular relaxation. The exponential dependence of the amount of drug released from time is described by the following equation:

$$\frac{M_t}{M_\infty} = kt^n \quad (6)$$

where 'M_t' is the drug released at the time 't', 'M_∞' is the total amount of loaded drug, 'k' is a constant, 'n' is a diffusional exponent that provides important information on the mechanism of drug release through the polymer. The 'n' exponent can be obtained by fitting data with $\frac{M_t}{M_\infty} < 0.6$ and gives an indication on the release mechanism (2015). The dissolution parameters obtained by fitting the dissolution data of each sample are reported in **Table V.4**.

Table V.4 Dissolution parameters obtained by Peppas equation.

Sample	K	n	R ²
NIM/MSA	0.285	0.633	0.995
NIM/CAA	0.127	0.459	0.994
KET/MSA	1.078	1.262	0.999
KET/CAA	0.467	1.014	0.999
DIC/MSA	0.881	0.713	0.999
DIC/CAA	0.263	0.747	0.993

The interpretation of the release models of the active principles from the polymeric matrices depends on the different geometries (Ritger and Peppas, 1987, Kosmidis et al., 2003, 2015). The tablets consisting of the impregnated aerogels can be assimilated to cylindrical samples, for which dependence of 'n' on the transport mechanism is as follows:

- when $n=0.45$, a pure Fickian release occurs: the drug release is governed by diffusion; i.e., the solvent diffusion into the matrix is faster than the polymer relaxation;
- when $0.45 < n < 0.89$, an anomalous or non-Fickian occurs: the mechanism of drug release is governed by both solvent diffusion and swelling/relaxation of polymeric chains that have a similar magnitude; this is the case of the samples NIM/CAA, NIM/MSA, DIC/CAA and DIC/MSA;
- when $n = 0.89$, the release mechanism is governed by swelling or relaxation of polymeric chains; i.e., the diffusion of the solvent through the system is very fast if compared to the relaxation of the polymeric interface;
- $n > 0.89$ corresponds to Super Case II transport: tension and breaking of the polymer occur due to a much faster solvent diffusion (2015); the systems KET/MSA and KET/CAA belong to in this category.

The use of the Peppas equation shows that both solvent diffusion and polymer swelling/relaxation of polymeric chains generally governed the mechanism of drug release from aerogels; however, also the coupling polymer-drug can sometimes influence the release mechanism.

V.2.5 Conclusions

The effectiveness of impregnation using $scCO_2$ to obtain ODTs was demonstrated by incorporating three different NSAIDs, namely NIM, KET and DIC, in MSA and CAA. In particular, two different types of tablets have been proposed, since, based on the specific application, a rapid or controlled release may be necessary for NSAIDs. The results on the impregnation kinetics indicated that the drug loadings were higher in the CAA compared to the MSA also due to the greater specific surface area of the CAA. The release tests showed that the MSA used as a hydrophilic carrier allows a

rapid dissolution of the NSAID, useful for producing ODTs, which quickly provide the desired therapeutic effect. In contrast, the CAA promotes a controlled release of NSAIDs, thanks to its greater stability in water and smaller pores, suitable for developing tablets of prolonged release drugs, which increase patient compliance reducing the frequency of administration and side effects.

The amounts of NSAID impregnated within the aerogel are sufficient to obtain adequate dosages to be delivered in the form of tablets. Indeed, the tablets currently on the market contain 100 mg of active principle; it means that, in the case of NIM, the tablet has to be constituted by 100 mg drug + 2 g aerogel; for KET, 100 mg drug + 330 mg aerogel; for DIC, 100 mg drug + 100 mg aerogel. These results are relevant from the pharmaceutical point of view, since it is possible to achieve a rapid or controlled release of NSAIDs based on the specific therapy desired by choosing the appropriate aerogel.

V.3 Supercritical impregnation of drugs into polymeric films

In order to develop novel topical patches, a one-step “foaming + drug impregnation” process was attempted using $scCO_2$. MSG was selected as model drug for the wound healing. The MSG impregnation was studied by firstly processing PCL granulates as received. Then, the optimum operating conditions were employed to perform the “supercritical foaming + impregnation” also on PCL film prepared by compression molding, with the aim of using composite system PCL/MSG as topical patch.

In a previous study (Campardelli et al., 2019a), the foaming conditions of PCL granules were accurately investigated, demonstrating that the best foaming of PCL was reached at the operating temperature and pressure of 35°C and 17 MPa, respectively. Therefore, these conditions were fixed to study the impregnation of MSG into PCL.

The experimental results presented in this part of the work can be divided in four main steps:

1. study of the solubility of MSG in $scCO_2$;
2. one-shot supercritical foaming+impregnation process, to know the time necessary for the equilibrium conditions;
3. development of MSG-loaded patches by using PCL film produced by compression molding as support for the impregnation at the optimized conditions;
4. characterization of samples with different analytical techniques.

V.3.1 Solubility measurements of MSG in $scCO_2$

Since there were no literature data about the solubility of MSG in $scCO_2$, it was necessary to carry out some preliminary tests. The solubility of MSG

in the scCO₂ was determined at 35°C; i.e., the best temperature for the PCL foaming using scCO₂ (Campardelli et al., 2019a). Indeed, it has to be considered that the PCL melting point is at very low temperature (about 60°C) and the exposition of a semicrystalline polymer to a compressed fluid induced the melting point depression (Fanovich and Jaeger, 2012, Lian et al., 2006). Although PCL foams with a regular porous structure were successfully obtained at 17 MPa (Campardelli et al., 2019a), it was decided to determine the solubility of MSG in the scCO₂ at different pressures (12, 15 and 17 MPa). Experimental data were reported in **Table V.5**. It can be noted that the solubility of MSG in scCO₂ enhanced as the pressure increased and it seems to reach a plateau value between 15 and 17 MPa. The preliminary studies of the solubility were essential to deduce that is possible to perform the MSG impregnation at the temperature and pressure conditions optimized in the previous work, focused on the PCL foaming; i.e., 35°C and 17 MPa (Campardelli et al., 2019a).

Table V.5 Solubility of MSG in scCO₂ at 35°C and different pressures.

P (MPa)	Solubility mol_{MSG}/mol_{CO2}
12	3.297 (± 0.071) x 10 ⁻⁶
15	4.048 (± 0.113) x 10 ⁻⁶
17	4.053 (± 0.068) x 10 ⁻⁶

V.3.2 Foaming + MSG impregnation in PCL granules

Firstly, the one step ‘foaming + impregnation’ tests were performed using PCL granules, without any pre-treatment. The impregnation kinetics were determined to know the time required for the complete impregnation of MSG in the PCL foam; i.e., to reach the maximum amount of loaded drug. The uptake was expressed as q_i ; i.e., mg of impregnated MSG per mg of foamed PCL. The experimental data were obtained at 17 MPa and 35°C, varying the contact time between the polymeric support and the MSG dissolved in scCO₂ from 2 to 48 h. The impregnation kinetic data reported in **Figure V.28** showed that the quantity of loaded MSG increased by increasing the time of impregnation, up to a maximum value of about 0.22 mg_{MSG}/mg_{PCL} reached after 24 h. Moreover, different images of PCL granules after the supercritical impregnation at various times investigated (in the range 2-24 h) were also reported in **Figure V.29**. It can be observed that the best foaming of PCL granules occurred after 24 h of impregnation.

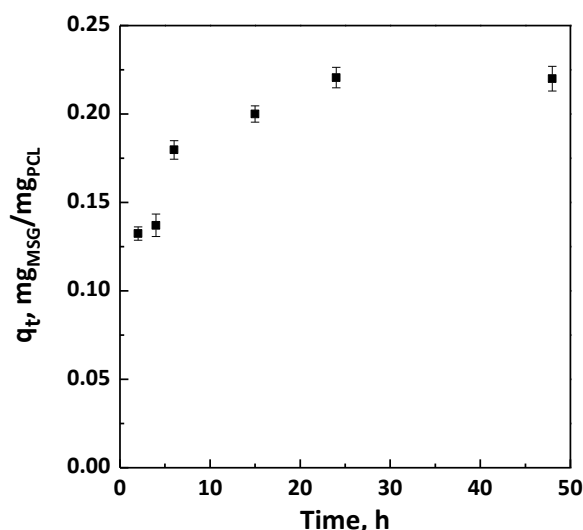


Figure V.28 Kinetic curves at 17 MPa and 35°C for the impregnation of MSG on PCL foams.



unprocessed PCL 2h adsorption 4h adsorption 6h adsorption 15h adsorption 24h adsorption

Figure V.29 Photographs of unprocessed PCL, and foamed + impregnated samples at 17 MPa, 35°C and various contact time (in the range 2 h- 24 h).

It is worth noting that the amount of MSG impregnated in the foamed PCL, in terms of polymer/drug weight ratio, is sufficient to assure an adequate dosages, which is one of the limits of conventional wound care systems (Saghazadeh et al., 2018). This outcome confirms the potential of supercritical impregnation (Kikic and Vecchione, 2003) to overcome the drawbacks of the traditional impregnation technologies in which liquid organic solvents are used; i.e., low drug loadings on/in polymeric matrices. Indeed, when a liquid solvent is used to dissolve and impregnate a drug, its penetration in polymeric support is limited not only by the geometry/surface properties of the polymer matrices (e.g., pore size) but also by the liquid bulk properties (e.g., surface tension of the liquid) (Ahuja and Pathak, 2009). Thanks to the blowing effect and to the quasi-zero surface tension of $scCO_2$, an appropriate incorporation of the active principle was reached (Kikic and Vecchione, 2003).

In order to check if the experimental and theoretical loadings are in good agreement, the experimental data of the kinetic curves were fitted both with

pseudo-first-order and pseudo-second-order models, which are obtained from the integration of the equation (3) reported in the Paragraph V.2.2. Impregnation rate constants obtained from the pseudo-first-order and pseudo-second-order kinetics are reported in **Table V.6**.

Table V.6 Impregnation rate constants obtained from the pseudo-first-order and pseudo-second-order models for MSG/PCL system.

Pseudo-first-order kinetics			Pseudo-second-order kinetics		
q_e mmol/g	k_1 1/h	R^2	q_e mmol/g	k_2 g/mmol h	R^2
0.351	0.185	0.740	0.367	1.445	0.999

It is possible to note that the pseudo-first-order kinetic did not fit the experimental data properly, since the value of R^2 is far from unity, as shown in **Table V.6**. On the contrary, the pseudo-second-order model fitted the kinetic data correctly, because R^2 is very close to unity, meaning that the experimental and theoretical loadings were in good agreement. In particular, the pseudo-second-order model (Ho, 2006) was applied according to the equation (4) reported in the Paragraph V.2.3. The plot of t/q_t versus t was shown in **Figure V.30**; q_e and k_2 were determined from slope and intercept of the fitting.

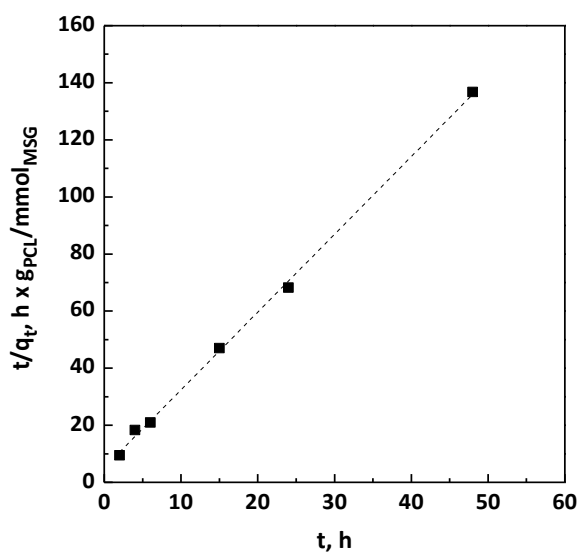


Figure V.30 Pseudo-second-order kinetics for the impregnation of MSG on PCL at 17 MPa and 35°C.

V.3.3 Mechanism of MSG impregnation

Different mechanisms can control the impregnation process; three steps are generally considered (Lazaridis and Asouhidou, 2003), namely *film diffusion*, *intraparticle or pore diffusion* and *release of the adsorbate on adsorbent active sites*, as mentioned in the Paragraph V.2.3. The last step is commonly very fast; therefore its resistance can be neglected (Kalavathy et al., 2005). When the support is a polymeric matrix, the impregnation of the drug is often governed by film diffusion at the beginning, followed by pore diffusion (De Marco and Reverchon, 2017). According to the Weber and Morris approach (Weber and Morris, 1963), the pore diffusion coefficient K_{id} can be defined by the equation (5) reported in the Paragraph V.2.3. Plotting q_t versus $t^{0.5}$ as shown in **Figure V.31**, a multi-linearity was observed and the intercept of each straight line was not equal to zero; these results indicated that different steps occurred in the impregnation process (Weber and Morris, 1963, Sun and Yang, 2003, Kalavathy et al., 2005).

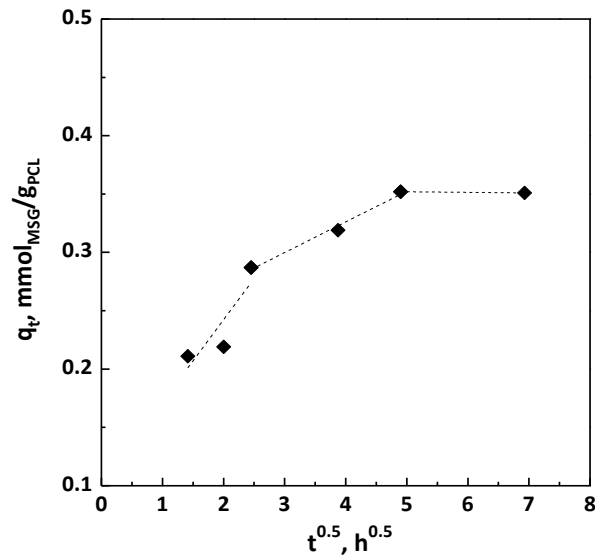


Figure V.31 Pore diffusion plot for the MSG impregnation on foamed PCL.

The slopes of the different lines, representing the different stages, are reported in **Table V.7**. It can be observed that $K_{1d} > K_{2d} > K_{3d}$, indicating that the impregnation is controlled by film diffusion at the beginning and that MSG was impregnated on the outer surface of the foamed PCL. At this initial stage, the impregnation rate is fast because the polymeric matrix is unloaded. Then, the MSG is also impregnated on the surface of the inner porosities of the foamed PCL; therefore, in this stage, the process is controlled by pore diffusion (Sun and Yang, 2003). In this step, the diffusion rate decreased due to an increase in diffusion resistance. As the amount of MSG in $scCO_2$ decreases, the diffusion rate became lower and the process

tends towards the final equilibrium stage, as proved by the very little value of K_{3d} .

Table V.7 Pore diffusion rate parameters for MSG/PCL system.

K_{1d} $\text{mmol g}^{-1} \text{h}^{-0.5}$	K_{2d} $\text{mmol g}^{-1} \text{h}^{-0.5}$	K_{3d} $\text{mmol g}^{-1} \text{h}^{-0.5}$
7.01×10^{-2}	2.64×10^{-2}	5.0×10^{-4}

V.3.4 Foaming + MSG impregnation in PCL films

Thin PCL film, characterized by a thickness of 100 μm , were produced by compression molding in order to develop topical patches. The supercritical foaming + impregnation of MSG in PCL film was performed at the optimum conditions; i.e., 35°C, 17 MPa and 24 h. Small film pieces of 1.5 cm x 1.5 cm as dimensions were used to conduct the experiments (**Figure V.32a**). At the end of the experiment, a drug loading of about 0.23 $\text{mg}_{\text{MSG}}/\text{mg}_{\text{PCL}}$ was reached; this value was similar to the MSG loading previously obtained using PCL granules. The aspect of the PCL film foamed and loaded with MSG is reported in **Figure V.32b**.

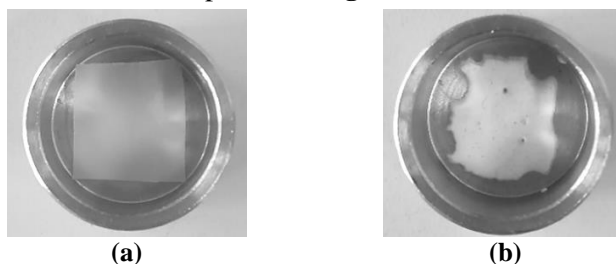


Figure V.32 Photographs of (a) unprocessed PCL film; (b) foamed PCL film after MSG impregnation.

V.2.4 Characterization of MSG/PCL composites

MSG-loaded films were characterized by different analytical techniques.

The morphology of foamed PCL was observed by FESEM analysis in absence (**Figure V.33a**) and in presence (**Figure V.33b**) of impregnated MSG. Foamed PCL film is characterized by a porous structure, as shown in **Figure V.33a**. The pore size distribution was $0.47 \pm 0.35 \mu\text{m}$. After the MSG impregnation, the crystalline drug in form of small needles filled and covered the pores (**Figure V.33b**). Unlike traditional dressings, the use of porous foams as topical forms provides a proper moist wound environment, in addition to other advantages such as good thermal insulation, better absorption of the exudate, cushioning provided by the porous structure and also a comfortable movement of the injured body part thanks to the flexibility of this material (Boateng et al., 2008, Saghadzadeh et al., 2018).

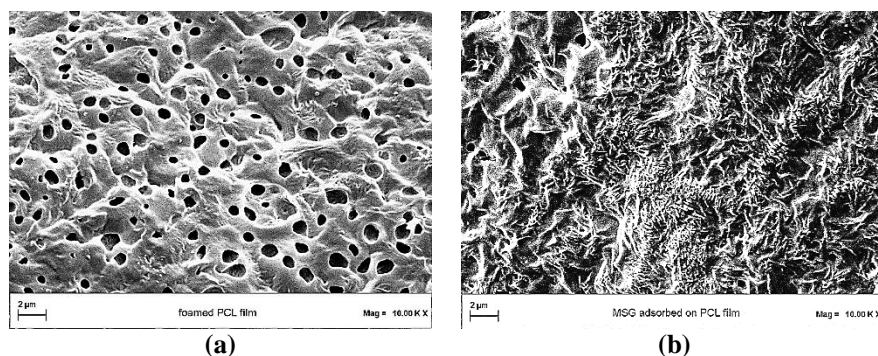


Figure V.33 FESEM images of (a) PCL film foamed by $scCO_2$; (b) MSG impregnated into/on foamed PCL film.

FTIR analyses were performed in order to verify the presence of drug into impregnated samples at the level of functional groups. FTIR spectra of unprocessed MSG, unprocessed PCL and MSG-loaded PCL film (17 MPa, 35°C and 24 h) are reported in **Figure V.34**. Spectra of impregnated sample exhibited the characteristic absorption bands both of the polymer and the drug, confirming the presence of MSG in foamed PCL.

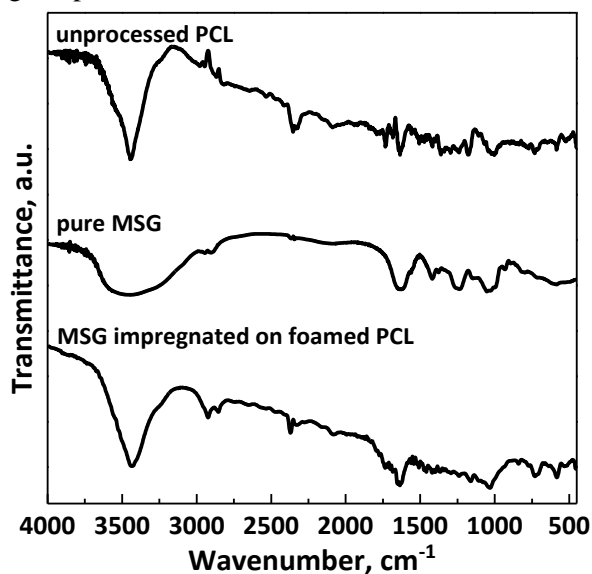


Figure V.34 FT-IR spectra for pure MSG and PCL, MSG impregnated on foamed PCL.

DSC thermograms of unprocessed MSG, unprocessed PCL and loaded PCL film (17 MPa and 35°C for a time of impregnation of 24 h) are reported in **Figure V.35**.

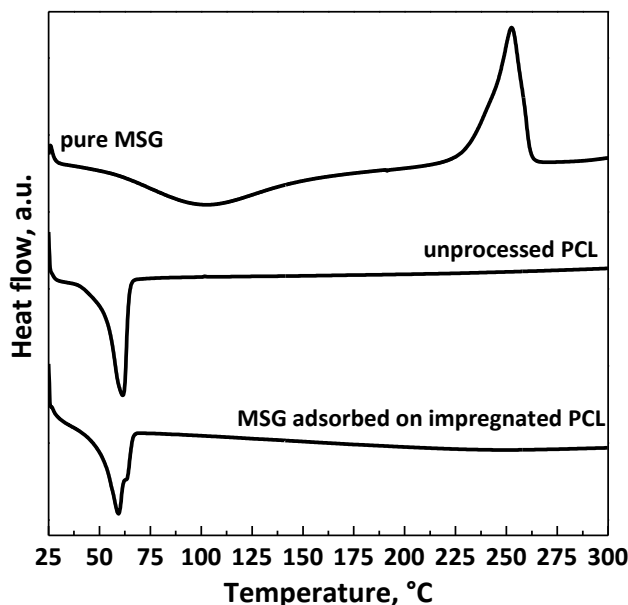


Figure V.35 DSC thermograms of pure MSG and PCL, MSG impregnated on foamed PCL.

MSG thermogram exhibited an endothermic peak due to the dehydration, and an exothermic peak at 253°C due to the crystallization. The thermogram of unprocessed PCL exhibited an endothermic melting peak at about 61°C (Can et al., 2011), which shifted at low temperature (around 59.4°C) for impregnated film due to the plasticizing effect of scCO₂ (Kishimoto and Ishii, 2000, Kikic and Vecchione, 2003). MSG adsorbed on PCL foams showed a thermal behavior similar to the PCL one; this result could be ascribed to the large presence of the polymer with respect to the drug.

The dissolution profiles in PBS at pH 7.4 of unprocessed MSG and MSG impregnated on foamed PCL film (17 MPa, 35°C and 24 h) are compared in **Figure V.36**. Pure MSG completely dissolved in less than an hour; instead, MSG impregnated on foamed PCL film took about 70 h (about 3 days). A burst-like effect (i.e., the dissolution of drug on/near the surface of the polymeric foam) of about 10% was observed in the case of MSG/PCL film system. The comparison of the dissolution profiles demonstrated that the impregnation of MSG into foamed PCL allowed to reach a prolonged release, delaying the complete dissolution of MSG up to about 70 times. Therefore, MSG/PCL system produced could offer a prolonged action on the wound for a proper regeneration of the epithelium. From a clinical point of view, the achievement of a MSG controlled release is an important goal that allows to overcome the major problem of the conventional wound care systems; i.e., the short residence times on the wound site (Boateng et al.,

2008). Indeed, the wound healing process can be improved by a controller-release delivery that assures a continuous treatment for a long period of time.

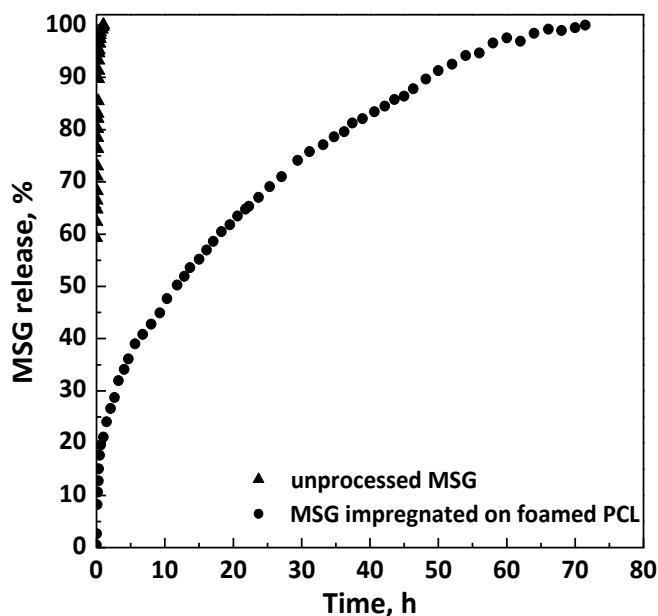


Figure V.36 Dissolution kinetics in PBS at pH 7.4 and 37°C.

V.3.5 Conclusions

In this work, a one-step supercritical foaming and impregnation process was successfully applied to obtain MSG and PCL foams. The challenge was to produce composite biopolymer/drug systems to be used as topical patches for the wound healing process. The impregnation kinetics of MSG was studied at the pressure and the temperature that guarantee the foaming of PCL; i.e., 17 MPa and 35 °C. Increasing the impregnation time, it was noted that the amount of loaded MSG increased up to a maximum value equal to 0.22 mg_{MSG}/mg_{PCL} reached after 24 h, which time also assured the best foaming of PCL granules. The modelling of kinetic data revealed that the impregnation process was properly fitted by a pseudo-second-order model, demonstrating that the experimental and theoretical loadings were in good agreement. Moreover, it was found that the impregnation process was governed by film diffusion at the beginning of the impregnation process, followed by the pore diffusion that allowed to impregnate MSG not only on the external but also on the inner surface of the foamed PCL. Then, the impregnation of MSG was also performed at the optimized conditions (17 MPa, 35°C, and 24 h) on PCL film, previously prepared by compression molding, in order to develop topical patches. As demonstrated by dissolution tests of MSG in PBS at pH 7.4, the supercritical impregnation of MSG into

foamed PCL film is effective to reach a prolonged release of the drug. Indeed, the MSG dissolution rate was 70 times slower than pure MSG when it was impregnated on foamed PCL film.

The system MSG/foamed PCL film appears very interesting for the development of topical devices designed to release MSG in a controlled-time manner. Indeed, this composite system used as topical device can offer a wound protection and a proper regeneration of the epithelium thanks to a prolonged release of MSG. Furthermore, MSG/foamed PCL film obtained by using $scCO_2$ can allow to reduce the frequency of administration in long-term therapies, avoiding high and repeated dosages and the associated side effects.

Conclusions

In this Ph.D. work, the versatility of scCO₂ in the production of different pharmaceutical forms, namely granulates, orally disintegrating tablets and topical patches, has been proven. The supercritical processes employed revealed to be effectively a valid alternative to the conventional ones. The polymer/active compound composites produced by the two scCO₂ assisted techniques, namely SAS process and supercritical impregnation, can provide an answer to the problems still concerning the pharmaceutical field. In addition to offering protection and stability for the active compound, the key role of the polymeric carrier in modifying the drug release kinetics emerged in the case of all the composite systems produced. Several pharmaceutical formulations with an accelerated or prolonged drug release have been proposed, depending on the specific therapy. Different polymers for various formulations and different drug releases have been selected, proving that carriers with a hydrophobic behaviour generally tend to extend the dissolution of the active compound, whereas hydrophilic carriers allow to increase the drug dissolution rate. Therefore, according to the clinical application, the choice of the right polymers is crucial to reduce the drug dosages and the side effects, improving the patient's compliance.

Regarding the SAS process, new carriers effective for the polymer/drug coprecipitation were identified, namely zein, Eudragit L100-55 and β -cyclodextrin. It has been demonstrated that both traditional microspheres and inclusion complexes can be prepared by SAS technique, depending on the properties of the selected carrier. In particular, the entrapment of active principles into microparticles based on zein and Eudragit L100-55 allow to prolong the drug release. It is worth noting that zein and Eudragit are less expensive than the lactic acid-based polymers (i.e., PLA and PLLA) proposed so far for the attainment of prolonged-release particles by SAS coprecipitation. On the contrary, the production of inclusion complexes by using β -CD allows to increase the dissolution rate of the active compounds incorporated into the cyclodextrin cavity. Moreover, in some cases, CDs-based inclusion complexes revealed to be more effective than PVP-based microparticles in the enhancement of the drug dissolution rate, by using a reduced amount of carrier into SAS coprecipitated powders.

SAS coprecipitation mechanisms have been also proposed in correspondence of different morphologies; i.e., nanoparticles, sub-microparticles and microparticles. For this purpose, the competition between the jet break-up and the surface tension vanishing during SAS coprecipitation has been taken into account, remembering that, when the first or the second phenomenon prevails, in general microparticles or nanoparticles precipitate, respectively. Briefly, by selecting the couple zein/diclofenac for this study, larger particles were produced by increasing the polymer/drug ratio, so passing from nanometric to micrometric size. Nanoparticles are obtained by homogeneous nucleation, so the polymer and the active compound precipitate separately and the coprecipitation fails at least partly, as similarly occurs with the attainment of sub-microparticles. Indeed, a portion of the precipitated powder is constituted by polymer nanoparticles and drug nanoparticles, whereas the residual amount of the powder can be formed by particles consisting of the materials precipitated together. Hence, the coprecipitation is achieved only in some measure, since a large aliquot of the drug dissolution is characterized by a burst effect, corresponding to drug molecules/particles freely soluble and/or located near/on the surface of particles. The burst effect decreased as the polymer/drug ratio increased; i.e., as the particle size increased, because a greater amount of drug can be entrapped and dispersed within the polymeric matrix formed after droplets drying, resulting in the formation of microspheres. This outcome is important since it demonstrates the role of the polymer, in addition to the particle size reduction, in modifying the dissolution kinetics of an active compound. This is the reason why, when a hydrophilic carrier is used, a higher dissolution rate is generally observed when composite microparticles are produced compared to that reached with nanoparticles, contrary to what can be expected. Indeed, considering a poorly-water soluble active compound, reducing its size and, consequently, increasing its specific surface area by simple SAS micronization, it is possible to speed up its dissolution in an aqueous environment. This effect is more marked the smaller the particle size, when a polymer is not employed. On the other hand, when the coprecipitation is performed with hydrophilic polymers like PVP, by increasing the quantity of carrier in the powders; i.e., the polymer/drug ratio, the drug release is often accelerated, despite the particle size increased. This result highlights the role played by the polymeric carrier in the control of the drug dissolution and it proves that SAS coprecipitation is effective when microspheres are produced. However, this trend, which links the drug release rate to the polymer quantity and to the particles size, is not always verified when inclusion complexes based on cyclodextrins are prepared by SAS coprecipitation. Indeed, due to the formation of weak interactions between the cyclodextrin and the active compound as well as to the partial or total complexation, different trends may occur.

The influence of the structure and chemical properties of the selected polymeric support on the drug release kinetics also emerged from the supercritical impregnation studies. The effectiveness of this technique in producing both orally disintegrating tablets and topical patches has been demonstrated, highlighting its versatility. By incorporating active principles into hydrophilic aerogels, such as MSA, or aerogels with a hydrophobic tendency, like CAA, the drug release is accelerated or prolonged, respectively. Briefly, the dissolution process of an active compound is faster when it is impregnated into hydrophilic aerogels, which is quickly wetted by water leading to a partial collapse of the aerogel structure; thus, the drug molecules are readily surrounded by the dissolution medium. In contrast, a more controlled drug release is reached in the case of aerogels based on hydrophobic polymers, being more stable in water than the hydrophilic aerogel. Moreover, the comparison between the use of MSA and CAA as support for the drug impregnation also highlighted the influence of the properties of the aerogel structure on the release kinetics. Indeed, aerogels like CAA characterized by very small pores promote a prolonged drug release, because the drug diffusion within the aerogel porosities is the controlling phenomenon during the dissolution process. The drug release data were fitted with Peppas model, revealing that the mechanism of drug release from aerogels is often governed by both solvent diffusion and polymer swelling/relaxation of polymeric chains. However, the results obtained from the release models show that some exceptions may occur, demonstrating that also the polymer-drug coupling can sometimes influence the release mechanism. Similarly to CAA, the use of thin films based on hydrophobic PCL as support for medicated patches promotes a controlled release of the impregnated drug. It is well known that some polymers like PCL can foam in the presence of $scCO_2$ under certain process conditions, leading to the formation of pores in the polymeric support. Therefore, using PCL as carrier, it was possible to develop a one step process consisting in the polymer foaming and the drug impregnation into the pores of the polymeric foams. By this route, it is possible to produce solvent-free pharmaceutical forms, reducing the operating times required for their preparation. It is worth noting that the supercritical impregnation of drugs into polymeric films was proposed to develop topical patches for the first time. For all the couples drug/polymeric support studied, it was noted that the impregnation kinetics were well fitted by pseudo-second-order models. The mechanisms of the drug impregnation in polymeric supports using $scCO_2$ were also investigated. In particular, it has been demonstrated that, at the beginning, the impregnation process is generally controlled by the diffusion of the drug in the bulk that surrounds the support (film diffusion), so the drug is impregnated on the outer surface of the substrate. Then, the impregnation process is controlled by pore diffusion, indeed the diffusion rate decreases due to an increase in the diffusion resistance. In this stage, the drug is also

impregnated on the inner surface of the polymeric support; i.e., into the pores. The diffusion process lastly tends towards the equilibrium stage; indeed, the diffusion rate becomes increasingly lower since the drug concentration decreases.

In conclusion, the two scCO₂ assisted techniques employed in this work can be considered effective for the preparation of various pharmaceutical forms for a controlled release of an active compound, more suited to the desired therapeutic effect. The results achieved encourage a greater application of the supercritical processes, still limited today, for the production of composite pharmaceutical systems.

References

2015. Mathematical models of drug release. *In: BRUSCHI, M. L. (ed.) Strategies to Modify the Drug Release from Pharmaceutical Systems.* Woodhead Publishing.
- ABUZAR, S. M., HYUN, S.-M., KIM, J.-H., PARK, H. J., KIM, M.-S., PARK, J.-S. & HWANG, S.-J. 2018. Enhancing the solubility and bioavailability of poorly water-soluble drugs using supercritical antisolvent (SAS) process. *International journal of pharmaceutics*, 538, 1-13.
- AHMED, I. & FATAHALLA, F. 2007. Pilot study of relative bioavailability of two oral formulations of ketoprofen 25 mg in healthy subjects. A fast-dissolving lyophilized tablet as compared to immediate release tablet. *Drug Development and Industrial Pharmacy*, 33, 505-511.
- AHUJA, G. & PATHAK, K. 2009. Porous carriers for controlled/modulated drug delivery. *Indian journal of pharmaceutical sciences*, 71, 599.
- AL-MARZOUQI, A. H., ELWY, H. M., SHEHADI, I. & ADEM, A. 2009. Physicochemical properties of antifungal drug-cyclodextrin complexes prepared by supercritical carbon dioxide and by conventional techniques. *Journal of pharmaceutical and biomedical analysis*, 49, 227-233.
- AL-TAHAMI, K. 2014. Preparation, characterization, and in vitro release of ketoprofen loaded alginate microspheres. *Int J App Pharm*, 6, 9-12.
- ALIAS, D., YUNUS, R., CHONG, G. H. & CHE ABDULLAH, C. A. 2017. Single step encapsulation process of tamoxifen in biodegradable polymer using supercritical anti-solvent (SAS) process. *Powder Technology*, 309, 89-94.
- ALTMAN, R., BOSCH, B., BRUNE, K., PATRIGNANI, P. & YOUNG, C. 2015. Advances in NSAID development: Evolution of diclofenac products using pharmaceutical technology. *Drugs*, 75, 859-877.
- ANDREATTA, A., FLORUSSE, L., BOTTINI, S. & PETERS, C. 2007a. Phase equilibria of dimethyl sulfoxide (DMSO)+ carbon dioxide, and DMSO+ carbon dioxide+ water mixtures. *The Journal of supercritical fluids*, 42, 60-68.
- ANDREATTA, A. E., FLORUSSE, L. J., BOTTINI, S. B. & PETERS, C. J. 2007b. Phase equilibria of dimethyl sulfoxide (DMSO) + carbon dioxide, and DMSO + carbon dioxide + water mixtures. *The Journal of Supercritical Fluids*, 42, 60-68.
- ARGEMÍ, A., VEGA, A., SUBRA-PATERNAL, P. & SAURINA, J. 2009. Characterization of azacytidine/poly(l-lactic) acid particles prepared by supercritical antisolvent precipitation. *Journal of Pharmaceutical and Biomedical Analysis*, 50, 847-852.

References

- ASFOUR, M. H. & MOHSEN, A. M. 2018. Formulation and evaluation of pH-sensitive rutin nanospheres against colon carcinoma using HCT-116 cell line. *Journal of Advanced Research*, 9, 17-26.
- ATTOUI-YAHIA, O., KHATMI, D., KRAIM, K. & FERKOUS, F. 2015. Hydrogen bonding investigation in Pyridoxine/ β -cyclodextrin complex based on QTAIM and NBO approaches. *Journal of the Taiwan Institute of Chemical Engineers*, 47, 91-98.
- BAGRATASHVILI, V., EGOROV, A., KROTOVA, L., MIRONOV, A., PANCHENKO, V. Y., PARENAGO, O., POPOV, V., REVELSKY, I., TIMASHEV, P. & TSYPIA, S. 2012. Supercritical fluid micronization of risperidone pharmaceutical substance. *Russian Journal of Physical Chemistry B*, 6, 804-812.
- BALDINO, L., CONCILIO, S., CARDEA, S. & REVERCHON, E. 2016. Interpenetration of natural polymer aerogels by supercritical drying. *Polymers*, 8, 106-117.
- BARRETT, A. M., DEHGhani, F. & FOSTER, N. R. 2007. Increasing the Dissolution Rate of Itraconazole Processed by Gas Antisolvent Techniques using Polyethylene Glycol as a Carrier. *Pharmaceutical Research*, 25, 1274-1289.
- BASTANTE, C. C., CARDOSO, L. C., SERRANO, C. M. & DE LA OSSA, E. M. 2017. Supercritical impregnation of food packaging films to provide antioxidant properties. *The Journal of Supercritical Fluids*, 128, 200-207.
- BEGUM, S. G., SWAMY, P. V., KALEPU, S., KONDURI, P., MANTENA, M. V. & BETHA, S. 2015. Dissolution rate enhancement of nimesulide using electrospinning and cogrinding techniques: a comparative study. *American Journal of PharmTech Research*, 5(4), 1-17.
- BELIZÓN, M., FERNÁNDEZ-PONCE, M., CASAS, L., MANTELL, C. & DE LA OSSA-FERNÁNDEZ, E. M. 2018. Supercritical impregnation of antioxidant mango polyphenols into a multilayer PET/PP food-grade film. *Journal of CO₂ Utilization*, 25, 56-67.
- BENDER, E. 1970. Equation of state exactly representing the phase behaviors of pure substances. *Proc. 5th Symposium on Thermophysical Properties. Am. Soc. Of Mech. Eng.*, 227-235.
- BETTINI, R., BERTOLINI, G., FRIGO, E., ROSSI, A., CASINI, I., PASQUALI, I. & GIORDANO, F. 2004. Interaction of pharmaceutical hydrates with supercritical CO₂. *Journal of thermal analysis and calorimetry*, 77, 625-638.
- BOATENG, J. S., MATTHEWS, K. H., STEVENS, H. N. & ECCLESTON, G. M. 2008. Wound healing dressings and drug delivery systems: a review. *Journal of pharmaceutical sciences*, 97, 2892-2923.
- BOSCHETTO, D. L., ARANHA, E. M., DE SOUZA, A. A. U., SOUZA, S. M. A. G. U., FERREIRA, S. R. S., PRIAMO, W. L. & OLIVEIRA,

- J. V. 2014. Encapsulation of bixin in PHBV using SEDS technique and in vitro release evaluation. *Industrial Crops and Products*, 60, 22-29.
- BOSCHETTO, D. L., DALMOLIN, I., DE CESARO, A. M., RIGO, A. A., FERREIRA, S. R. S., MEIRELES, M. A. A., BATISTA, E. A. C. & VLADIMIR OLIVEIRA, J. 2013. Phase behavior and process parameters effect on grape seed extract encapsulation by SEDS technique. *Industrial Crops and Products*, 50, 352-360.
- BOUCHARD, A., JOVANOVIĆ, N., JISKOOT, W., MENDES, E., WITKAMP, G.-J., CROMMELIN, D. J. & HOFLAND, G. W. 2007. Lysozyme particle formation during supercritical fluid drying: Particle morphology and molecular integrity. *The Journal of supercritical fluids*, 40, 293-307.
- BRUNAUER, S., DEMING, L. S., DEMING, W. E. & TELLER, E. 1940. On a theory of the van der Waals adsorption of gases. *Journal of the American Chemical society*, 62, 1723-1732.
- BRZEZIŃSKI, M., KOST, B., WEDEPOHL, S., SOCKA, M., BIELA, T. & CALDERÓN, M. 2019. Stereocomplexed PLA microspheres: Control over morphology, drug encapsulation and anticancer activity. *Colloids and Surfaces B: Biointerfaces*, 184, 110544.
- CAMPARDELLI, R., FRANCO, P., REVERCHON, E. & DE MARCO, I. 2019a. Polycaprolactone/nimesulide patches obtained by a one-step supercritical foaming+ impregnation process. *The Journal of Supercritical Fluids*, 146, 47-54.
- CAMPARDELLI, R., REVERCHON, E. & DE MARCO, I. 2017a. Dependence of SAS particle morphologies on the ternary phase equilibria. *The Journal of Supercritical Fluids*, 130, 273-281.
- CAMPARDELLI, R., REVERCHON, E. & DE MARCO, I. 2017b. Dependence of SAS particle morphologies on the ternary phase equilibria. *The Journal of Supercritical Fluids*, 130, 273-281.
- CAMPARDELLI, R., REVERCHON, E. & DE MARCO, I. 2019b. PVP microparticles precipitation from acetone-ethanol mixtures using SAS process: Effect of phase behavior. *The Journal of Supercritical Fluids*, 143, 321-329.
- CAN, E., UDENIR, G., KANNECI, A. I., KOSE, G. & BUCAK, S. 2011. Investigation of PLLA/PCL Blends and Paclitaxel Release Profiles. *AAPS PharmSciTech*, 12(4), 1442-1453.
- CANNAVÀ, C., CRUPI, V., FICARRA, P., GUARDO, M., MAJOLINO, D., STANCANELLI, R. & VENUTI, V. 2008. Physicochemical characterization of coumestrol/ β -cyclodextrins inclusion complexes by UV-vis and FTIR-ATR spectroscopies. *Vibrational Spectroscopy*, 48, 172-178.
- CAPUTO, G. 2013. Supercritical fluid adsorption of domperidone on silica aerogel.

References

- CAPUTO, G., SCOGNAMIGLIO, M. & DE MARCO, I. 2012. Nimesulide adsorbed on silica aerogel using supercritical carbon dioxide. *Chemical Engineering Research and Design*, 90, 1082-1089.
- CARDEA, S., BALDINO, L., DE MARCO, I., PISANTI, P. & REVERCHON, E. 2013. Supercritical gel drying of polymeric hydrogels for tissue engineering applications. *Chem. Eng.*, 32.
- CARDOSO, M. T., GERALDES, V., CABRAL, J. & PALAVRA, A. 2008a. Characterization of minocycline powder micronized by a supercritical antisolvent (SAS) process. *The Journal of Supercritical Fluids*, 46, 71-76.
- CARDOSO, M. T., MONTEIRO, G., CARDOSO, J., PRAZERES, T., FIGUEIREDO, J., MARTINHO, J., CABRAL, J. & PALAVRA, A. 2008b. Supercritical antisolvent micronization of minocycline hydrochloride. *The Journal of Supercritical Fluids*, 44, 238-244.
- CARELLI, S., HEBDA, D. M., TRAVERSA, M. V., MESSAGGIO, F., GIULIANI, G., MARZANI, B., BENEDUSI, A., DI GIULIO, A. M. & GORIO, A. 2012. A specific combination of zeaxanthin, spermidine and rutin prevents apoptosis in human dermal papilla cells. *Experimental dermatology*, 21, 953-955.
- CAZAROLLI, L. H., ZANATTA, L., ALBERTON, E. H., FIGUEIREDO, B., REIS, M. S., FOLADOR, P., DAMAZIO, R. G., PIZZOLATTI, M. G., SILVA, B. & MENA, F. R. 2008. Flavonoids: prospective drug candidates. *Mini reviews in medicinal chemistry*, 8, 1429-1440.
- CEBALLOS, A., CIRRI, M., MAESTRELLI, F., CORTI, G. & MURA, P. 2005. Influence of formulation and process variables on in vitro release of theophylline from directly-compressed Eudragit matrix tablets. *Il Farmaco*, 60, 913-918.
- CEJUDO BASTANTE, C., CASAS CARDOSO, L., MANTELL SERRANO, C. & MARTÍNEZ DE LA OSSA, E. J. 2017. Supercritical impregnation of food packaging films to provide antioxidant properties. *Journal of Supercritical Fluids*, 128, 200-207.
- CHAMPEAU, M., THOMASSIN, J.-M., TASSAING, T. & JÉRÔME, C. 2015. Drug loading of polymer implants by supercritical CO₂ assisted impregnation: A review. *Journal of controlled release*, 209, 248-259.
- CHANG, S.-C., LEE, M.-J. & LIN, H.-M. 2008a. The influence of phase behavior on the morphology of protein α -chymotrypsin prepared via a supercritical anti-solvent process. *The Journal of Supercritical Fluids*, 44, 219-229.
- CHANG, Y.-P., TANG, M. & CHEN, Y.-P. 2008b. Micronization of sulfamethoxazole using the supercritical anti-solvent process. *Journal of materials science*, 43, 2328-2335.

- CHEN, A. Z., PU, X. M., KANG, Y. Q., LIAO, L., YAO, Y. D. & YIN, G. F. 2006. Preparation of 5-Fluorouracil-Poly (L-lactide) Microparticles Using Solution-Enhanced Dispersion by Supercritical CO₂. *Macromolecular Rapid Communications*, 27, 1254-1259.
- CHEN, L.-F., XU, P.-Y., FU, C.-P., KANKALA, R. K., CHEN, A.-Z. & WANG, S.-B. 2020. Fabrication of Supercritical Antisolvent (SAS) Process-Assisted Fisetin-Encapsulated Poly (Vinyl Pyrrolidone)(PVP) Nanocomposites for Improved Anticancer Therapy. *Nanomaterials*, 10, 322.
- CHEN, M., WU, Q., JIANG, J., JIN, X., LIU, S., WANG, M. & ZHAO, C. 2017. Preparation, characterization and in vivo evaluation of a formulation of dantrolene sodium with hydroxypropyl- β -cyclodextrin. *Journal of pharmaceutical and biomedical analysis*, 135, 153-159.
- CHEN, Y.-M., TANG, M. & CHEN, Y.-P. 2010. Recrystallization and micronization of sulfathiazole by applying the supercritical antisolvent technology. *Chemical Engineering Journal*, 165, 358-364.
- CHHOUK, K., KANDA, H., KAWASAKI, S.-I. & GOTO, M. 2018. Micronization of curcumin with biodegradable polymer by supercritical anti-solvent using micro swirl mixer. *Frontiers of Chemical Science and Engineering*, 12, 184-193.
- CHOPRA, S., KISHORE SAINI, R. & NATH SANYAL, S. 2007. Intestinal toxicity of non-steroidal anti-inflammatory drugs with differential cyclooxygenase inhibition selectivity. *Nutricion hospitalaria*, 22.
- CHULLASAT, K., NURERK, P., KANATHARANA, P., DAVIS, F. & BUNKOED, O. 2018. A facile optosensing protocol based on molecularly imprinted polymer coated on CdTe quantum dots for highly sensitive and selective amoxicillin detection. *Sensors and Actuators B: Chemical*, 254, 255-263.
- CRUZ, L. C. D., MIRANDA, C. S. D., SANTOS, W. J. D., GONÇALVES, A. P. B., OLIVEIRA, J. C. D. & JOSÉ, N. M. 2015. Development of starch biofilms using different carboxylic acids as plasticizers. *Materials Research*, 18, 297-301.
- CUADRA, I. A., ZAHRAN, F., MARTÍN, D., CABAÑAS, A. & PANDO, C. 2019. Preparation of 5-fluorouracil microparticles and 5-fluorouracil/poly(l-lactide) composites by a supercritical CO₂ antisolvent process. *The Journal of Supercritical Fluids*, 143, 64-71.
- CURIA, S., DE FOCATIIS, D. S. & HOWDLE, S. M. 2015. High-pressure rheological analysis of CO₂-induced melting point depression and viscosity reduction of poly (ϵ -caprolactone). *Polymer*, 69, 17-24.
- DA FONSECA MACHADO, A. P., REZENDE, C. A., RODRIGUES, R. A., BARBERO, G. F., E ROSA, P. D. T. V. & MARTÍNEZ, J. 2018. Encapsulation of anthocyanin-rich extract from blackberry

References

- residues by spray-drying, freeze-drying and supercritical antisolvent. *Powder technology*, 340, 553-562.
- DAHAN, A., BEIG, A., IOFFE-DAHAN, V., AGBARIA, R. & MILLER, J. M. 2013. The twofold advantage of the amorphous form as an oral drug delivery practice for lipophilic compounds: increased apparent solubility and drug flux through the intestinal membrane. *The AAPS journal*, 15, 347-353.
- DAVIS, M. E. & BREWSTER, M. E. 2004. Cyclodextrin-based pharmaceuticals: past, present and future. *Nature reviews Drug discovery*, 3, 1023-1035.
- DE MARCO, I., BALDINO, L., CARDEA, S. & REVERCHON, E. 2015a. Supercritical gel drying for the production of starch aerogels for delivery systems. *Chemical Engineering Transactions*, 43, 307-312.
- DE MARCO, I., PROSAPIO, V., CICE, F. & REVERCHON, E. 2013. Use of solvent mixtures in supercritical antisolvent process to modify precipitates morphology: Cellulose acetate microparticles. *The Journal of Supercritical Fluids*, 83, 153-160.
- DE MARCO, I. & REVERCHON, E. 2008. Supercritical antisolvent micronization of cyclodextrins. *Powder Technology*, 183, 239-246.
- DE MARCO, I. & REVERCHON, E. 2011. Influence of pressure, temperature and concentration on the mechanisms of particle precipitation in supercritical antisolvent micronization. *The Journal of Supercritical Fluids*, 58, 295-302.
- DE MARCO, I. & REVERCHON, E. 2017. Starch aerogel loaded with poorly water-soluble vitamins through supercritical CO₂ adsorption. *Chemical Engineering Research and Design*, 119, 221-230.
- DE MARCO, I., ROSSMANN, M., PROSAPIO, V., REVERCHON, E. & BRAEUER, A. 2015b. Control of particle size, at micrometric and nanometric range, using supercritical antisolvent precipitation from solvent mixtures: application to PVP. *Chemical Engineering Journal*, 273, 344-352.
- DI CAPUA, A., ADAMI, R., IZZO, L. & REVERCHON, E. 2017a. Luteolin/dextran-FITC fluorescent microspheres produced by supercritical assisted atomization. *The Journal of Supercritical Fluids*, 130, 97-104.
- DI CAPUA, A., ADAMI, R. & REVERCHON, E. 2017b. Production of luteolin/biopolymer microspheres by supercritical assisted atomization. *Industrial & Engineering Chemistry Research*, 56, 4334-4340.
- DI MAIO, E. & KIRAN, E. 2018. Foaming of polymers with supercritical fluids and perspectives on the current knowledge gaps and challenges. *The Journal of Supercritical Fluids*, 134, 157-166.
- DJERAFI, R., SWANEPOEL, A., CRAMPON, C., KALOMBO, L., LABUSCHAGNE, P., BADENS, E. & MASMOUDI, Y. 2017.

- Supercritical antisolvent co-precipitation of rifampicin and ethyl cellulose. *European Journal of Pharmaceutical Sciences*, 102, 161-171.
- DUARTE, A. R. C., ROY, C., VEGA-GONZÁLEZ, A., DUARTE, C. M. & SUBRA-PATERNAULT, P. 2007. Preparation of acetazolamide composite microparticles by supercritical anti-solvent techniques. *International journal of pharmaceutics*, 332, 132-139.
- EDAVALATH, S., SHIVANAND, K., PRAKASAM, K., RAO, B. P. & DIVAKAR, G. 2011. Formulation development and optimization of controlled porosity osmotic pump tablets of diclofenac sodium. *International Journal of Pharmacy and Pharmaceutical Sciences*, 3, 80-87.
- ELVASSORE, N., BERTUCCO, A. & CALICETI, P. 2001. Production of protein-loaded polymeric microcapsules by compressed CO₂ in a mixed solvent. *Industrial & engineering chemistry research*, 40, 795-800.
- ERLUND, I., KOSONEN, T., ALFTHAN, G., MÄENPÄÄ, J., PERTTUNEN, K., KENRAALI, J., PARANTAINEN, J. & ARO, A. 2000. Pharmacokinetics of quercetin from quercetin aglycone and rutin in healthy volunteers. *European journal of clinical pharmacology*, 56, 545-553.
- FANOVICH, M. A. & JAEGER, P. 2012. Sorption and diffusion of compressed carbon dioxide in polycaprolactone for the development of porous scaffolds. *Materials Science and Engineering: C*, 32, 961-968.
- FERNÁNDEZ-PONCE, M. T., MASMOUDI, Y., DJERAFI, R., CASAS, L., MANTELL, C., DE LA OSSA, E. M. & BADENS, E. 2015. Particle design applied to quercetin using supercritical anti-solvent techniques. *The Journal of Supercritical Fluids*, 105, 119-127.
- FRANCESCHI, E., DE CEZARO, A., FERREIRA, S. R. S., KUNITA, M. H., MUNIZ, E. C., RUBIRA, A. F. & OLIVEIRA, J. V. 2010. Co-precipitation of beta-carotene and bio-polymer using supercritical carbon dioxide as antisolvent. *Open Chemical Engineering Journal*, 4, 11-20.
- GANESHPURKAR, A. & SALUJA, A. K. 2017. The pharmacological potential of rutin. *Saudi pharmaceutical journal*, 25, 149-164.
- GARCÍA-GONZÁLEZ, C., ALNAIEF, M. & SMIRNOVA, I. 2011. Polysaccharide-based aerogels—Promising biodegradable carriers for drug delivery systems. *Carbohydrate Polymers*, 86, 1425-1438.
- GARCÍA-GONZÁLEZ, C. A. & SMIRNOVA, I. 2013. Use of supercritical fluid technology for the production of tailor-made aerogel particles for delivery systems. *The Journal of Supercritical Fluids*, 79, 152-158.

References

- GAZI, A. S. & KRISHNASAILAJA, A. 2019. Preparation and Characterization of Methotrexate Loaded Polymeric Nanoparticles by Nanoprecipitation Technique. *Nano Biomed. Eng*, 11, 351-360.
- GLENN, G. M. & IRVING, D. W. 1995. Starch-based microcellular foams. *Cereal chemistry*, 72, 155-161.
- GOUGH, C. R., BESSETTE, K., XUE, Y., MOU, X. & HU, X. 2020. Air-Jet Spun Corn Zein Nanofibers and Thin Films with Topical Drug for Medical Applications. *International Journal of Molecular Sciences*, 21, 5780.
- GRIMLING, B., GÓRNIK, A., MELER, J. & SZCZEŚNIAK, M. 2014. Characterisation and dissolution properties of ketoprofen in binary solid dispersion with chitosan. *Progress on Chemistry and Application of Chitin and its Derivatives*, 19, 23-31.
- GUHA, R., VINJAMUR, M. & MUKHOPADHYAY, M. 2011. Demonstration of mechanisms for coprecipitation and encapsulation by supercritical antisolvent process. *Industrial & engineering chemistry research*, 50, 1079-1088.
- GUNASEKARAN, S., VARADHAN, S. & KARUNANIDHI, N. 1996. Qualitative analysis on the infrared bands of tetracycline and ampicillin. *PROCEEDINGS-INDIAN NATIONAL SCIENCE ACADEMY PART A*, 62, 309-316.
- GUNEY, O. & AKGERMAN, A. 2002. Synthesis of controlled-release products in supercritical medium. *AIChE Journal*, 48, 856-866.
- GUPTA, A. & BAH, M. 2016. NSAIDs in the Treatment of Postoperative Pain. *Current Pain and Headache Reports*, 20.
- GURUNATH, S., KUMAR, S. P., BASAVARAJ, N. K. & PATIL, P. A. 2013. Amorphous solid dispersion method for improving oral bioavailability of poorly water-soluble drugs. *Journal of pharmacy research*, 6, 476-480.
- HA, E.-S., CHOO, G.-H., BAEK, I.-H., KIM, J.-S., CHO, W., JUNG, Y. S., JIN, S.-E., HWANG, S.-J. & KIM, M.-S. 2015a. Dissolution and bioavailability of lercanidipine-hydroxypropylmethyl cellulose nanoparticles with surfactant. *International Journal of Biological Macromolecules*, 72, 218-222.
- HA, E.-S., KIM, J.-S., BAEK, I.-H., HWANG, S.-J. & KIM, M.-S. 2015b. Enhancement of dissolution and bioavailability of ezetimibe by amorphous solid dispersion nanoparticles fabricated using supercritical antisolvent process. *Journal of Pharmaceutical Investigation*, 45, 641-649.
- HA, E.-S., PARK, H., LEE, S.-K., SIM, W.-Y., JEONG, J.-S., BAEK, I.-H. & KIM, M.-S. 2020. Pure Trans-Resveratrol Nanoparticles Prepared by A Supercritical Antisolvent Process Using Alcohol and Dichloromethane Mixtures: Effect of Particle Size on Dissolution and Bioavailability in Rats. *Antioxidants*, 9, 342.

- HA, E. S., KIM, J. S., BAEK, I. H., YOO, J. W., JUNG, Y., MOON, H. R. & KIM, M. S. 2015c. Development of megestrol acetate solid dispersion nanoparticles for enhanced oral delivery by using a supercritical antisolvent process. *Drug Design, Development and Therapy*, 9, 4269-4277.
- HANCOCK, B. C. & PARKS, M. 2000. What is the true solubility advantage for amorphous pharmaceuticals? *Pharmaceutical research*, 17, 397-404.
- HASAN, S., AL ALI, H., AL-QUBAISI, M., HUSSEIN, M. Z., ISMAIL, M., ZAINAL, Z. & HAKIM, M. N. 2012. Controlled-release formulation of antihistamine based on cetirizine zinc-layered hydroxide nanocomposites and its effect on histamine release from basophilic leukemia (RBL-2H3) cells. *International Journal of Nanomedicine*, 7, 3351.
- HIENDRAWAN, S., VERIANSYAH, B., WIDJOJOKUSUMO, E., SOEWANDHI, S., WIKARSA, S. & TJANDRAWINATA, R. R. 2016. Simultaneous cocrystallization and micronization of paracetamol-dipicolinic acid cocrystal by supercritical antisolvent (SAS). *Int J Pharm Pharm Sci*, 8, 89-98.
- HO, Y.-S. 2006. Review of second-order models for adsorption systems. *Journal of hazardous materials*, 136, 681-689.
- HU, D., LIN, C., LIU, L., LI, S. & ZHAO, Y. 2012. Preparation, characterization, and in vitro release investigation of lutein/zein nanoparticles via solution enhanced dispersion by supercritical fluids. *Journal of food engineering*, 109, 545-552.
- HUANG, Y., ZU, Y., ZHAO, X., WU, M., FENG, Z., DENG, Y., ZU, C. & WANG, L. 2016. Preparation of inclusion complex of apigenin-hydroxypropyl- β -cyclodextrin by using supercritical antisolvent process for dissolution and bioavailability enhancement. *International journal of pharmaceuticals*, 511, 921-930.
- JADHAV, N. R., GAIKWAD, V. L., NAIR, K. J. & KADAM, H. M. 2014. Glass transition temperature: Basics and application in pharmaceutical sector. *Asian Journal of Pharmaceuticals (AJP): Free full text articles from Asian J Pharm*, 3.
- JERMAIN, S. V., BROUGH, C. & WILLIAMS III, R. O. 2018. Amorphous solid dispersions and nanocrystal technologies for poorly water-soluble drug delivery—An update. *International journal of pharmaceuticals*, 535, 379-392.
- JIA, J., ZHANG, K., ZHOU, X., ZHOU, D. & GE, F. 2018. Precise Dissolution Control and Bioavailability Evaluation for Insoluble Drug Berberine via a Polymeric Particle Prepared Using Supercritical CO₂. *Polymers*, 10, 1198.
- JIN, H. Y., XIA, F. & ZHAO, Y. P. 2012. Preparation of hydroxypropyl methyl cellulose phthalate nanoparticles with mixed solvent using

References

- supercritical antisolvent process and its application in coprecipitation of insulin. *Advanced Powder Technology*, 23, 157-163.
- JUN, S. W., KIM, M.-S., KIM, J.-S., PARK, H. J., LEE, S., WOO, J.-S. & HWANG, S.-J. 2007. Preparation and characterization of simvastatin/hydroxypropyl- β -cyclodextrin inclusion complex using supercritical antisolvent (SAS) process. *European journal of pharmaceuticals and biopharmaceutics*, 66, 413-421.
- JUNG, I.-I., HAAM, S., LIM, G. & RYU, J.-H. 2012. Preparation of peptide-loaded polymer microparticles using supercritical carbon dioxide. *Biotechnology and Bioprocess Engineering*, 17, 185-194.
- KALANTARIAN, P., HARIRIAN, I., NAJAFABADI, A. R., SHOKRGOZAR, M. A. & VATANARA, A. 2011. Entrapment of 5-fluorouracil into PLGA matrices using supercritical antisolvent processes. *Journal of Pharmacy and Pharmacology*, 63, 500-506.
- KALAVATHY, M. H., KARTHIKEYAN, T., RAJGOPAL, S. & MIRANDA, L. R. 2005. Kinetic and isotherm studies of Cu (II) adsorption onto H₃PO₄-activated rubber wood sawdust. *Journal of colloid and interface science*, 292, 354-362.
- KALOGIANNIS, C. G., MICHAILOF, C. M. & PANAYIOTOU, C. G. 2006. Microencapsulation of amoxicillin in poly (l-lactic acid) by supercritical antisolvent precipitation. *Industrial & engineering chemistry research*, 45, 8738-8743.
- KALOGIANNIS, C. G., PAVLIDOU, E. & PANAYIOTOU, C. G. 2005. Production of amoxicillin microparticles by supercritical antisolvent precipitation. *Industrial & engineering chemistry research*, 44, 9339-9346.
- KARKI, S., KIM, H., NA, S.-J., SHIN, D., JO, K. & LEE, J. 2016. Thin films as an emerging platform for drug delivery. *asian journal of pharmaceutical sciences*, 11, 559-574.
- KARTHIKEYAN, K., LAKRA, R., RAJARAM, R. & KORRAPATI, P. S. 2012. Development and characterization of zein-based micro carrier system for sustained delivery of aceclofenac sodium. *AAPS PharmSciTech*, 13, 143-149.
- KEBEBE, D., BELETE, A. & GEBRE-MARIAM, T. 2010. Evaluation of two olibanum resins as rate controlling matrix forming excipients in oral sustained release tablets. *Ethiopian Pharmaceutical Journal*, 28, 95-109.
- KESAVAN, J. G. & PECK, G. E. 1996. Solid-state stability of theophylline anhydrous in theophylline anhydrous-polyvinylpyrrolidone physical mixtures. *Drug development and industrial pharmacy*, 22, 189-199.
- KI, H. & PARK, O. O. 2001. Synthesis, characterization and biodegradability of the biodegradable aliphatic–aromatic random copolyesters. *Polymer*, 42, 1849-1861.

- KIKIC, I. & VECCHIONE, F. 2003. Supercritical impregnation of polymers. *Current Opinion in Solid State and Materials Science*, 7, 399-405.
- KILLEDAR, S. G. & NALE, A. B. 2014. Isolation, characterization, and evaluation of Cassia fistula Linn. seed and pulp polymer for pharmaceutical application. *International journal of pharmaceutical investigation*, 4, 215.
- KIM, M.-S., JIN, S.-J., KIM, J.-S., PARK, H. J., SONG, H.-S., NEUBERT, R. H. & HWANG, S.-J. 2008. Preparation, characterization and in vivo evaluation of amorphous atorvastatin calcium nanoparticles using supercritical antisolvent (SAS) process. *European journal of pharmaceuticals and biopharmaceutics*, 69, 454-465.
- KIM, M.-S., LEE, S., PARK, J.-S., WOO, J.-S. & HWANG, S.-J. 2007. Micronization of cilostazol using supercritical antisolvent (SAS) process: effect of process parameters. *Powder Technology*, 177, 64-70.
- KIRAN, E. 2010. Foaming strategies for bioabsorbable polymers in supercritical fluid mixtures. Part I. Miscibility and foaming of poly (l-lactic acid) in carbon dioxide+ acetone binary fluid mixtures. *The Journal of Supercritical Fluids*, 54, 296-307.
- KISHIMOTO, Y. & ISHII, R. 2000. Differential scanning calorimetry of isotactic polypropene at high CO₂ pressures. *Polymer*, 41, 3483-3485.
- KOSMIDIS, K., ARGYRAKIS, P. & MACHERAS, P. 2003. Fractal kinetics in drug release from finite fractal matrices. *The Journal of chemical physics*, 119, 6373-6377.
- KUMAR SINGH YADAV, H. & SHIVAKUMAR, H. 2012. In vitro and in vivo evaluation of pH-sensitive hydrogels of carboxymethyl chitosan for intestinal delivery of theophylline. *ISRN pharmaceuticals*, 2012.
- LANG, Z. M., HONG, H. L., HAN, L. M., ZHU, N. & SUO, Q. L. 2012. Preparation of emodin-polyethylene glycol composite microparticles using a supercritical antisolvent process. *Chemical Engineering and Technology*, 35, 362-368.
- LAZARIDIS, N. & ASOUHIDOU, D. 2003. Kinetics of sorptive removal of chromium (VI) from aqueous solutions by calcined Mg-Al-CO₃ hydrotalcite. *Water Research*, 37, 2875-2882.
- LEE, C.-W., KIM, S.-J., YOUN, Y.-S., WIDJOJOKUSUMO, E., LEE, Y.-H., KIM, J., LEE, Y.-W. & TJANDRAWINATA, R. R. 2010. Preparation of bitter taste masked cetirizine dihydrochloride/ β -cyclodextrin inclusion complex by supercritical antisolvent (SAS) process. *The Journal of Supercritical Fluids*, 55, 348-357.
- LEE, S. Y., ABDULLAH, L. C., RAHMAN, R. A., ABAS, F. & CHONG, G. H. 2019. Role of polymers as crystal growth inhibitors in

References

- coprecipitation via solution-enhanced dispersion by supercritical fluids (SEDS) to improve andrographolide dissolution from standardized *Andrographis paniculata* extract. *Journal of Drug Delivery Science and Technology*, 50, 145-154.
- LENGSFELD, C., DELPLANQUE, J., BAROCAS, V. & RANDOLPH, T. 2000. Mechanism governing microparticle morphology during precipitation by a compressed antisolvent: atomization vs nucleation and growth. *The Journal of Physical Chemistry B*, 104, 2725-2735.
- LESTARI, S. D., MACHMUDAH, S., WINARDI, S., KANDA, H. & GOTO, M. 2019. Particle micronization of Curcuma mangga rhizomes ethanolic extract/biopolymer PVP using supercritical antisolvent process. *The Journal of Supercritical Fluids*, 146, 226-239.
- LI, W., LIU, G., LI, L., WU, J., LÜ, Y. & JIANG, Y. 2012. Effect of Process Parameters on Co-precipitation of Paclitaxel and Poly(L-lactic Acid) by Supercritical Antisolvent Process. *Chinese Journal of Chemical Engineering*, 20, 803-813.
- LIAN, Z., EPSTEIN, S. A., BLENK, C. W. & SHINE, A. D. 2006. Carbon dioxide-induced melting point depression of biodegradable semicrystalline polymers. *The Journal of supercritical fluids*, 39, 107-117.
- LIN, H.-L., HSU, P.-C. & LIN, S.-Y. 2013. Theophylline–citric acid co-crystals easily induced by DSC–FTIR microspectroscopy or different storage conditions. *asian journal of pharmaceutical sciences*, 8, 19-27.
- LIN, Q., LIU, G., ZHAO, Z., WEI, D., PANG, J. & JIANG, Y. 2017. Design of gefitinib-loaded poly (l-lactic acid) microspheres via a supercritical anti-solvent process for dry powder inhalation. *International journal of pharmaceuticals*, 532, 573-580.
- LIU, G., HU, M., ZHAO, Z., LIN, Q., WEI, D. & JIANG, Y. 2019. Enhancing the stability of astaxanthin by encapsulation in poly (l-lactic acid) microspheres using a supercritical anti-solvent process. *Particuology*, 44, 54-62.
- LIU, G., LI, S., HUANG, Y., WANG, H. & JIANG, Y. 2016. Incorporation of 10-hydroxycamptothecin nanocrystals into zein microspheres. *Chemical Engineering Science*, 155, 405-414.
- LIU, M., LIU, Y., GE, Y., ZHONG, Z., WANG, Z., WU, T., ZHAO, X. & ZU, Y. 2020. Solubility, Antioxidation, and Oral Bioavailability Improvement of Mangiferin Microparticles Prepared Using the Supercritical Antisolvent Method. *Pharmaceutics*, 12, 90.
- LOPES, L. B., SCARPA, M. V., PEREIRA, N. L., OLIVEIRA, L. C. D. & OLIVEIRA, A. G. 2006. Interaction of sodium diclofenac with freeze-dried soya phosphatidylcholine and unilamellar liposomes. *Revista Brasileira de Ciências Farmacêuticas*, 42, 497-504.

- LU, Y., ZHANG, X., LAI, J., YIN, Z. & WU, W. 2009. Physical characterization of meloxicam- β -cyclodextrin inclusion complex pellets prepared by a fluid-bed coating method. *Particuology*, 7, 1-8.
- MACHADO, F. R. S., TREVISOL, T. C., BOSCHETTO, D. L., BURKERT, J. F. M., FERREIRA, S. R. S., OLIVEIRA, J. V. & BURKERT, C. A. V. 2016. Technological process for cell disruption, extraction and encapsulation of astaxanthin from *Haematococcus pluvialis*. *Journal of Biotechnology*, 218, 108-114.
- MACHMUDAH, S., WINARDI, S., WAHYUDIONO, KANDA, H. & GOTO, M. 2020. Formation of Fine Particles from Curcumin/PVP by the Supercritical Antisolvent Process with a Coaxial Nozzle. *ACS omega*, 5, 6705-6714.
- MACNAUGHTON, S. J., KIKIC, I., FOSTER, N. R., ALESSI, P., CORTESI, A. & COLOMBO, I. 1996. Solubility of anti-inflammatory drugs in supercritical carbon dioxide. *Journal of Chemical and Engineering Data*, 41, 1083-1086.
- MAHMOOD, A., AHMAD, M., SARFRAZ, R. M. & MINHAS, M. U. 2016. β -CD based hydrogel microparticulate system to improve the solubility of acyclovir: Optimization through in-vitro, in-vivo and toxicological evaluation. *Journal of Drug Delivery Science and Technology*, 36, 75-88.
- MAJEED, A., RANJHA, N. M., HANIF, M., ABBAS, G. & KHAN, M. A. 2017. Development and evaluation of ivabradine HCl-loaded polymeric microspheres prepared with Eudragit L100-55 (methacrylic acid-ethyl acrylate copolymer) and ethyl cellulose for controlled drug release. *Acta poloniae pharmaceutica*, 74, 565-578.
- MAJERIK, V., CHARBIT, G., BADENS, E., HORVÁTH, G., SZOKONYA, L., BOSC, N. & TEILLAUD, E. 2007. Bioavailability enhancement of an active substance by supercritical antisolvent precipitation. *The Journal of supercritical fluids*, 40, 101-110.
- MAMMUCARI, R., DEGHANI, F. & FOSTER, N. R. 2006. Dense gas processing of micron-sized drug formulations incorporating hydroxypropylated and methylated beta-cyclodextrin. *Pharmaceutical Research*, 23, 429-437.
- MANDEEP, K., RANA, A. & NIMRATA, S. 2013. Fast Dissolving Films: An Innovative Drug Delivery System. *International Journal of Pharmaceutical Research & Allied Sciences*, 2.
- MANIAR, K. H., JONES, I. A., GOPALAKRISHNA, R. & VANGSNES, C. T. 2018. Lowering side effects of NSAID usage in osteoarthritis: recent attempts at minimizing dosage. *Expert Opinion on Pharmacotherapy*, 19, 93-102.
- MARCINIEC, B., PŁOTKOWIAK, Z., WACHOWSKI, L., KOZAK, M. & POPIELARZ-BRZEZIŃSKA, M. 2002. Analytical study of β -

References

- irradiated antibiotics in the solid state. *Journal of thermal analysis and calorimetry*, 68, 423-436.
- MARRA, F., DE MARCO, I. & REVERCHON, E. 2012. Numerical analysis of the characteristic times controlling supercritical antisolvent micronization. *Chemical Engineering Science*, 71, 39-45.
- MARTIN, T. M., BANDI, N., SHULZ, R., ROBERTS, C. B. & KOMPPELLA, U. B. 2002. Preparation of budesonide and budesonide-PLA microparticles using supercritical fluid precipitation technology. *AAPS PharmSciTech*, 3, 16-26.
- MASMOUDI, Y., AZZOUK, L. B., FORZANO, O., ANDRE, J.-M. & BADENS, E. 2011. Supercritical impregnation of intraocular lenses. *The Journal of Supercritical Fluids*, 60, 98-105.
- MATOS, R. L., LU, T., PROSAPIO, V., MCCONVILLE, C., LEEKE, G. & INGRAM, A. 2019. Coprecipitation of curcumin/PVP with enhanced dissolution properties by the supercritical antisolvent process. *Journal of CO2 Utilization*, 30, 48-62.
- MAZIÈRES, B., ROUANET, S., VELICY, J., SCARSI, C. & REINER, V. 2005. Topical ketoprofen patch (100 mg) for the treatment of ankle sprain: a randomized, double-blind, placebo-controlled study. *The American journal of sports medicine*, 33, 515-523.
- MEDEIROS, G. R., FERREIRA, S. R. & CARCIOFI, B. A. 2017. High pressure carbon dioxide for impregnation of clove essential oil in LLDPE films. *Innovative food science & emerging technologies*, 41, 206-215.
- MIGUEL, F., MARTIN, A., GAMSE, T. & COCERO, M. J. 2006. Supercritical anti solvent precipitation of lycopene: Effect of the operating parameters. *The Journal of supercritical fluids*, 36, 225-235.
- MIGUEL, F., MARTÍN, A., MATTEA, F. & COCERO, M. J. 2008. Precipitation of lutein and co-precipitation of lutein and poly-lactic acid with the supercritical anti-solvent process. *Chemical Engineering and Processing: Process Intensification*, 47, 1594-1602.
- MILOVANOVIC, S., HOLLERMANN, G., ERRENST, C., PAJNIK, J., FRERICH, S., KROLL, S., REZWAN, K. & IVANOVIC, J. 2018. Supercritical CO2 impregnation of PLA/PCL films with natural substances for bacterial growth control in food packaging. *Food Research International*, 107, 486-495.
- MIR, S. A., SHAH, M. A., DAR, B. N., WANI, A. A., GANAI, S. A. & NISHAD, J. 2017. Supercritical impregnation of active components into polymers for food packaging applications. *Food and Bioprocess Technology*, 10, 1749-1754.
- MOHAN, P. K., SREELAKSHMI, G., MURALEEDHARAN, C. & JOSEPH, R. 2012. Water soluble complexes of curcumin with

- cyclodextrins: Characterization by FT-Raman spectroscopy. *Vibrational Spectroscopy*, 62, 77-84.
- MONTES, A., GORDILLO, M. D., PEREYRA, C., DE LOS SANTOS, D. M. & MARTÍNEZ DE LA OSSA, E. J. 2014a. Ibuprofen–polymer precipitation using supercritical CO₂ at low temperature. *The Journal of Supercritical Fluids*, 94, 91-101.
- MONTES, A., GORDILLO, M. D., PEREYRA, C. & MARTÍNEZ DE LA OSSA, E. J. 2011. Co-precipitation of amoxicillin and ethyl cellulose microparticles by supercritical antisolvent process. *The Journal of Supercritical Fluids*, 60, 75-80.
- MONTES, A., GORDILLO, M. D., PEREYRA, C. & MARTÍNEZ DE LA OSSA, E. J. 2012. Polymer and ampicillin co-precipitation by supercritical antisolvent process. *The Journal of Supercritical Fluids*, 63, 92-98.
- MONTES, A., KIN, N., GORDILLO, M., PEREYRA, C. & DE LA OSSA, E. M. 2014b. Polymer–naproxen precipitation by supercritical antisolvent (SAS) process. *The Journal of Supercritical Fluids*, 89, 58-67.
- MONTES, A., KIN, N., GORDILLO, M. D., PEREYRA, C. & MARTÍNEZ DE LA OSSA, E. J. 2014c. Polymer–naproxen precipitation by supercritical antisolvent (SAS) process. *The Journal of Supercritical Fluids*, 89, 58-67.
- MONTES, A., NUNES, A., GORDILLO, M., PEREYRA, C., DUARTE, C. M. & MARTINEZ DE LA OSSA, E. J. 2013. Amoxicillin and ethyl cellulose precipitation by two supercritical antisolvent processes. *Chemical Engineering & Technology*, 36, 665-672.
- MONTES, A., WEHNER, L., PEREYRA, C. & DE LA OSSA, E. M. 2016a. Precipitation of submicron particles of rutin using supercritical antisolvent process. *The Journal of Supercritical Fluids*, 118, 1-10.
- MONTES, A., WEHNER, L., PEREYRA, C. & MARTÍNEZ DE LA OSSA, E. J. 2016b. Generation of microparticles of ellagic acid by supercritical antisolvent process. *The Journal of Supercritical Fluids*, 116, 101-110.
- MONTES, A., WEHNER, L., PEREYRA, C. & MARTÍNEZ DE LA OSSA, E. J. 2016c. Mangiferin nanoparticles precipitation by supercritical antisolvent process. *The Journal of Supercritical Fluids*, 112, 44-50.
- MOYERS-MONTOYA, E., GARCÍA-CASILLAS, P., VARGAS-REQUENA, C., ESCOBEDO-GONZÁLEZ, R., MARTEL-ESTRADA, S.-A. & MARTÍNEZ-PÉREZ, C. A. 2016. Polycaprolactone/amino-β-Cyclodextrin inclusion complex prepared by an electrospinning technique. *Polymers*, 8, 395.
- MÜLLER, V., PIAI, J. F., FAJARDO, A. R., FÁVARO, S. L., RUBIRA, A. F. & MUNIZ, E. C. 2011. Preparation and characterization of zein

References

- and zein-chitosan microspheres with great prospective of application in controlled drug release. *Journal of Nanomaterials*, 2011, 10.
- MUTHURAJAN, T., RAMMANOHAR, P., RAJENDRAN, N. P., SETHURAMAN, S. & KRISHNAN, U. M. 2015. Evaluation of a quercetin–gadolinium complex as an efficient positive contrast enhancer for magnetic resonance imaging. *RSC Advances*, 5, 86967-86979.
- NEROME, H., MACHMUDAH, S., WAHYUDIONO, FUKUZATO, R., HIGASHIURA, T., YOUN, Y. S., LEE, Y. W. & GOTO, M. 2013. Nanoparticle formation of lycopene/ β -cyclodextrin inclusion complex using supercritical antisolvent precipitation. *Journal of Supercritical Fluids*, 83, 97-103.
- OCHOA, L., IGARTUA, M., HERNANDEZ, R., GASCON, A. & PEDRAZ, J. L. 2005. Preparation of sustained release hydrophilic matrices by melt granulation in a high-shear mixer. *Journal of pharmacy & pharmaceutical sciences: a publication of the Canadian Society for Pharmaceutical Sciences, Societe canadienne des sciences pharmaceutiques*, 8, 132-140.
- OLARU, A., BORODI, G., KACSO, I., VASILESCU, M., BRATU, I. & COZAR, O. 2009. Spectroscopic studies of the inclusion compound of lisinopril with β -cyclodextrin. *Spectroscopy*, 23, 191-199.
- PANTIĆ, M., KNEZ, Ž. & NOVAK, Z. 2016. Supercritical impregnation as a feasible technique for entrapment of fat-soluble vitamins into alginate aerogels. *Journal of non-crystalline solids*, 432, 519-526.
- PARK, H., SEO, H. J., HONG, S.-H., HA, E.-S., LEE, S., KIM, J.-S., BAEK, I.-H., KIM, M.-S. & HWANG, S.-J. 2020. Characterization and therapeutic efficacy evaluation of glimepiride and L-arginine co-amorphous formulation prepared by supercritical antisolvent process: influence of molar ratio and preparation methods. *International Journal of Pharmaceutics*, 119232.
- PARK, H. J., YOON, T. J., KWON, D. E., YU, K. & LEE, Y.-W. 2017. Coprecipitation of hydrochlorothiazide/PVP for the dissolution rate improvement by precipitation with compressed fluid antisolvent process. *The Journal of Supercritical Fluids*, 126, 37-46.
- PARK, J., CHO, W., CHA, K.-H., AHN, J., HAN, K. & HWANG, S.-J. 2013. Solubilization of the poorly water soluble drug, telmisartan, using supercritical anti-solvent (SAS) process. *International journal of pharmaceutics*, 441, 50-55.
- PARK, J., PARK, H. J., CHO, W., CHA, K.-H., KANG, Y.-S. & HWANG, S.-J. 2010. Preparation and pharmaceutical characterization of amorphous cefdinir using spray-drying and SAS-process. *International journal of pharmaceutics*, 396, 239-245.
- PATOMCHAIWAT, V., PAERATAKUL, O. & KULVANICH, P. 2008. Formation of inhalable rifampicin–poly (L-lactide) microparticles by

- supercritical anti-solvent process. *AAPS PharmSciTech*, 9, 1119-1129.
- PRIYANKA, K., ABHISHEK, S., AMAN, POOJA, P. & C, B. 2018. Formulation and evaluation of transdermal patch of diclofenac sodium. *Global Journal of Pharmacy & Pharmaceutical Science*, 44, 555647.
- PROSAPIO, V., DE MARCO, I. & REVERCHON, E. 2016a. PVP/corticosteroid microspheres produced by supercritical antisolvent coprecipitation. *Chemical Engineering Journal*, 292, 264-275.
- PROSAPIO, V., DE MARCO, I. & REVERCHON, E. 2018. Supercritical antisolvent coprecipitation mechanisms. *The Journal of Supercritical Fluids*, 138, 247-258.
- PROSAPIO, V., DE MARCO, I., SCOGNAMIGLIO, M. & REVERCHON, E. 2015a. Folic acid–PVP nanostructured composite microparticles by supercritical antisolvent precipitation. *Chemical Engineering Journal*, 277, 286-294.
- PROSAPIO, V., REVERCHON, E. & DE MARCO, I. 2015b. Coprecipitation of polyvinylpyrrolidone/ β -carotene by supercritical antisolvent processing. *Industrial & Engineering Chemistry Research*, 54, 11568-11575.
- PROSAPIO, V., REVERCHON, E. & DE MARCO, I. 2016b. Formation of PVP/nimesulide microspheres by supercritical antisolvent coprecipitation. *The Journal of Supercritical Fluids*, 118, 19-26.
- PROSAPIO, V., REVERCHON, E. & DE MARCO, I. 2017. Incorporation of liposoluble vitamins within PVP microparticles using supercritical antisolvent precipitation. *Journal of CO₂ Utilization*, 19, 230-237.
- REVERCHON, E., ADAMI, R., CAPUTO, G. & DE MARCO, I. 2008a. Spherical microparticles production by supercritical antisolvent precipitation: interpretation of results. *The Journal of Supercritical Fluids*, 47, 70-84.
- REVERCHON, E. & CARDEA, S. 2007. Production of controlled polymeric foams by supercritical CO₂. *The Journal of Supercritical Fluids*, 40, 144-152.
- REVERCHON, E. & DE MARCO, I. 2006. Supercritical antisolvent precipitation of cephalosporins. *Powder Technology*, 164, 139-146.
- REVERCHON, E. & DE MARCO, I. 2011. Mechanisms controlling supercritical antisolvent precipitate morphology. *Chemical Engineering Journal*, 169, 358-370.
- REVERCHON, E., DE MARCO, I., ADAMI, R. & CAPUTO, G. 2008b. Expanded micro-particles by supercritical antisolvent precipitation: interpretation of results. *The Journal of Supercritical Fluids*, 44, 98-108.

References

- REVERCHON, E., DE MARCO, I. & TORINO, E. 2007. Nanoparticles production by supercritical antisolvent precipitation: a general interpretation. *The Journal of Supercritical Fluids*, 43, 126-138.
- REVERCHON, E., DELLA PORTA, G. & FALIVENE, M. 2000. Process parameters and morphology in amoxicillin micro and submicro particles generation by supercritical antisolvent precipitation. *The journal of supercritical fluids*, 17, 239-248.
- RITGER, P. L. & PEPPAS, N. A. 1987. A simple equation for description of solute release II. Fickian and anomalous release from swellable devices. *Journal of controlled release*, 5, 37-42.
- ROGERS, T. L., JOHNSTON, K. P. & WILLIAMS III, R. O. 2001. Solution-based particle formation of pharmaceutical powders by supercritical or compressed fluid CO₂ and cryogenic spray-freezing technologies. *Drug development and industrial pharmacy*, 27, 1003-1015.
- ROJAS, A., CERRO, D., TORRES, A., GALOTTO, M. J., GUARDA, A. & ROMERO, J. 2015. Supercritical impregnation and kinetic release of 2-nonanone in LLDPE films used for active food packaging. *The journal of supercritical fluids*, 104, 76-84.
- SAGHAZADEH, S., RINOLDI, C., SCHOT, M., KASHAF, S. S., SHARIFI, F., JALILIAN, E., NUUTILA, K., GIATSIDIS, G., MOSTAFALU, P. & DERAKHSHANDEH, H. 2018. Drug delivery systems and materials for wound healing applications. *Advanced drug delivery reviews*, 127, 138-166.
- SAHOO, B. J. & MISHRA, A. N. 2013. Formulation and evaluation of transdermal patches of diclofenac. *World Journal of Pharmacy and Pharmaceutical Sciences*, 2, 4965-4971.
- SINGH, S., SHARDA, N. & MAHAJAN, L. 1999. Spectrophotometric determination of pKa of nimesulide. *International journal of pharmaceuticals*, 176, 261-264.
- SMIRNOVA, I., MAMIC, J. & ARLT, W. 2003. Adsorption of drugs on silica aerogels. *Langmuir*, 19, 8521-8525.
- SMIRNOVA, I., SUTTIRUENGWONG, S. & ARLT, W. 2005a. Aerogels: tailor-made carriers for immediate and prolonged drug release. *KONA Powder and Particle Journal*, 23, 86-97.
- SMIRNOVA, I., SUTTIRUENGWONG, S., SEILER, M. & ARLT, W. 2005b. Dissolution rate enhancement by adsorption of poorly soluble drugs on hydrophilic silica aerogels. *Pharmaceutical development and technology*, 9, 443-452.
- SOLTANI, S., ZAKERI-MILANI, P., BARZEGAR-JALALI, M. & JELVEHGARI, M. 2016. Comparison of different nanosuspensions as potential ophthalmic delivery systems for ketotifen fumarate. *Advanced pharmaceutical bulletin*, 6, 345.

- STEBBINS, N. D., OUI MET, M. A. & UHRICH, K. E. 2014. Antibiotic-containing polymers for localized, sustained drug delivery. *Advanced drug delivery reviews*, 78, 77-87.
- STELLA, V. J. & RAJEWSKI, R. A. 1997. Cyclodextrins: Their future in drug formulation and delivery. *Pharmaceutical Research*, 14, 556-567.
- SULTANOVA, Z., KALELI, G., KABAY, G. & MUTLU, M. 2016. Controlled release of a hydrophilic drug from coaxially electrospun polycaprolactone nanofibers. *International journal of pharmaceuticals*, 505, 133-138.
- SUN, J., HONG, H., ZHU, N., HAN, L. & SUO, Q. 2019. Response surface methodology to optimize the preparation of tosylloxacin tosylate/hydroxypropyl- β -cyclodextrin inclusion complex by supercritical antisolvent process. *Journal of Molecular Structure*, 1198, 126939.
- SUN, Q. & YANG, L. 2003. The adsorption of basic dyes from aqueous solution on modified peat-resin particle. *Water research*, 37, 1535-1544.
- TENORIO, A., GORDILLO, M., PEREYRA, C. & DE LA OSSA, E. M. 2007a. Controlled submicro particle formation of ampicillin by supercritical antisolvent precipitation. *The Journal of supercritical fluids*, 40, 308-316.
- TENORIO, A., GORDILLO, M. D., PEREYRA, C. & MARTINEZ DE LA OSSA, E. J. 2007b. Controlled submicro particle formation of ampicillin by supercritical antisolvent precipitation. *Journal of Supercritical Fluids*, 40, 308-316.
- TITA, B., FULIAS, A., BANDUR, G., LEDETI, I. & TITA, D. 2011. Application of thermal analysis to study the compatibility of sodium diclofenac with different pharmaceutical excipients. *Revista de Chimie*, 62, 443-454.
- TIȚA, D., FULIAȘ, A. & TIȚA, B. 2011. Thermal stability of ketoprofen—active substance and tablets: Part 1. Kinetic study of the active substance under non-isothermal conditions. *Journal of thermal analysis and calorimetry*, 105, 501-508.
- TKALEC, G., PANTIĆ, M., NOVAK, Z. & KNEZ, Ž. 2015. Supercritical impregnation of drugs and supercritical fluid deposition of metals into aerogels. *Journal of materials science*, 50, 1-12.
- TSIVINTZELIS, I., ANGELOPOULOU, A. G. & PANAYIOTOU, C. 2007. Foaming of polymers with supercritical CO₂: an experimental and theoretical study. *Polymer*, 48, 5928-5939.
- TSIVINTZELIS, I., SANXARIDOU, G., PAVLIDOU, E. & PANAYIOTOU, C. 2016. Foaming of polymers with supercritical fluids: A thermodynamic investigation. *The Journal of Supercritical Fluids*, 110, 240-250.

References

- UZUN, İ. N., SIPAHIGIL, O. & DINÇER, S. 2011. Coprecipitation of Cefuroxime Axetil–PVP composite microparticles by batch supercritical antisolvent process. *The Journal of Supercritical Fluids*, 55, 1059-1069.
- VAN KONYNENBURG, P. & SCOTT, R. 1980. Critical lines and phase equilibria in binary van der Waals mixtures. *Philosophical Transactions of the Royal Society of London. Series A, Mathematical and Physical Sciences*, 298, 495-540.
- VEGA GONZALEZ, A., TUFEU, R. & SUBRA, P. 2002. High-Pressure Vapor–Liquid Equilibrium for the Binary Systems Carbon Dioxide + Dimethyl Sulfoxide and Carbon Dioxide + Dichloromethane. *Journal of Chemical & Engineering Data*, 47, 492-495.
- VERT, M., SCHWARCH, G. & COUDANE, J. 1995. Present and future of PLA polymers. *Journal of Macromolecular Science, Part A: Pure and Applied Chemistry*, 32, 787-796.
- VILLEGAS, C., TORRES, A., RIOS, M., ROJAS, A., ROMERO, J., DE DICASTILLO, C. L., VALENZUELA, X., GALOTTO, M. J. & GUARDA, A. 2017. Supercritical impregnation of cinnamaldehyde into polylactic acid as a route to develop antibacterial food packaging materials. *Food Research International*, 99, 650-659.
- VISENTIN, A., RODRÍGUEZ-ROJO, S., NAVARRETE, A., MAESTRI, D. & COCERO, M. J. 2012. Precipitation and encapsulation of rosemary antioxidants by supercritical antisolvent process. *Journal of Food Engineering*, 109, 9-15.
- WANG, W., LIU, G., WU, J. & JIANG, Y. 2013. Co-precipitation of 10-hydroxycamptothecin and poly (l-lactic acid) by supercritical CO₂ anti-solvent process using dichloromethane/ethanol co-solvent. *The Journal of Supercritical Fluids*, 74, 137-144.
- WEBER, W. J. & MORRIS, J. C. 1963. Kinetics of adsorption on carbon from solution. *Journal of the Sanitary Engineering Division*, 89, 31-60.
- WIDJOJOKUSUMO, E., VERIANSYAH, B. & TJANDRAWINATA, R. R. 2013. Supercritical anti-solvent (SAS) micronization of Manilkara kauki bioactive fraction (DLBS2347). *Journal of CO₂ Utilization*, 3-4, 30-36.
- WON, D.-H., KIM, M.-S., LEE, S., PARK, J.-S. & HWANG, S.-J. 2005. Improved physicochemical characteristics of felodipine solid dispersion particles by supercritical anti-solvent precipitation process. *International journal of pharmaceuticals*, 301, 199-208.
- WU, K., LI, J., WANG, W. & WINSTEAD, D. A. 2009. Formation and characterization of solid dispersions of piroxicam and polyvinylpyrrolidone using spray drying and precipitation with compressed antisolvent. *Journal of Pharmaceutical Sciences*, 98, 2422-2431.

- YADAV, P. S., KUMAR, V., SINGH, U. P., BHAT, H. R. & MAZUMDER, B. 2013. Physicochemical characterization and in vitro dissolution studies of solid dispersions of ketoprofen with PVP K30 and d-mannitol. *Saudi Pharmaceutical Journal*, 21, 77-84.
- YANG, J., GUO, J. & YUAN, J. 2008a. In vitro antioxidant properties of rutin. *LWT-Food Science and Technology*, 41, 1060-1066.
- YANG, R., WANG, Y., ZHENG, X., MENG, J., TANG, X. & ZHANG, X. 2008b. Preparation and evaluation of ketoprofen hot-melt extruded enteric and sustained-release tablets. *Drug development and industrial pharmacy*, 34, 83-89.
- YODA, S., SATO, K. & OYAMA, H. T. 2011. Impregnation of paclitaxel into poly (DL-lactic acid) using high pressure mixture of ethanol and carbon dioxide. *RSC advances*, 1, 156-162.
- YOSHIDA, V. M. H., BALCÃO, V. M., VILA, M. M. D. C., OLIVEIRA JÚNIOR, J. M., ARANHA, N., CHAUD, M. V. & GREMIÃO, M. P. D. 2015. Zidovudine-Poly(l-Lactic Acid) Solid Dispersions with Improved Intestinal Permeability Prepared by Supercritical Antisolvent Process. *Journal of Pharmaceutical Sciences*, 104, 1691-1700.
- ZAHARAN, F., CABAÑAS, A., CHEDA, J. A. R., RENUNCIO, J. A. R. & PANDO, C. 2014. Dissolution rate enhancement of the anti-inflammatory drug diflunisal by coprecipitation with a biocompatible polymer using carbon dioxide as a supercritical fluid antisolvent. *The Journal of Supercritical Fluids*, 88, 56-65.
- ZHANG, H.-X., WANG, J.-X., ZHANG, Z.-B., LE, Y., SHEN, Z.-G. & CHEN, J.-F. 2009. Micronization of atorvastatin calcium by antisolvent precipitation process. *International journal of pharmaceutics*, 374, 106-113.
- ZHANG, Y., KANG, D., AINDOW, M. & ERKEY, C. 2005. Preparation and characterization of ruthenium/carbon aerogel nanocomposites via a supercritical fluid route. *Journal of Physical Chemistry B*, 109, 2617-2624.
- ZHAO, C., WANG, L., ZU, Y., LI, C., LIU, S., YANG, L., ZHAO, X. & ZU, B. 2011a. Micronization of Ginkgo biloba extract using supercritical antisolvent process. *Powder technology*, 209, 73-80.
- ZHAO, X., CHEN, X., ZU, Y., JIANG, R. & ZHAO, D. 2012. Recrystallization and micronization of taxol using the supercritical antisolvent (SAS) process. *Industrial & engineering chemistry research*, 51, 9591-9597.
- ZHAO, X., ZU, Y., JIANG, R., WANG, Y., LI, Y., LI, Q., ZHAO, D., ZU, B., ZHANG, B. & SUN, Z. 2011b. Preparation and physicochemical properties of 10-hydroxycamptothecin (HCPT) nanoparticles by supercritical antisolvent (SAS) process. *International journal of molecular sciences*, 12, 2678-2691.

References

- ZHONG, Q., JIN, M., DAVIDSON, P. M. & ZIVANOVIC, S. 2009. Sustained release of lysozyme from zein microcapsules produced by a supercritical anti-solvent process. *Food chemistry*, 115, 697-700.
- ZHONG, Q., JIN, M., XIAO, D., TIAN, H. & ZHANG, W. 2008. Application of supercritical anti-solvent technologies for the synthesis of delivery systems of bioactive food components. *Food biophysics*, 3, 186-190.
- ZHOU, R., WANG, F., GUO, Z. & ZHAO, Y. 2012. Preparation and characterization of resveratrol/hydroxypropyl- β -cyclodextrin inclusion complex using supercritical antisolvent technology. *Journal of Food Process Engineering*, 35, 677-686.
- ZIZOVIC, I. 2020. Supercritical Fluid Applications in the Design of Novel Antimicrobial Materials. *Molecules*, 25, 2491.
- ZU, Y., ZHANG, Q., ZHAO, X., WANG, D., LI, W., SUI, X., ZHANG, Y., JIANG, S., WANG, Q. & GU, C. 2012. Preparation and characterization of vitexin powder micronized by a supercritical antisolvent (SAS) process. *Powder technology*, 228, 47-55.

List of Symbols

ASES: Aerosol Solvent Extraction System
AMOXI: Amoxicillin trihydrate
AMPI: Ampicillin sodium salt
 β -CD: β -cyclodextrin
BET: Brunauer, Emmett and Teller
C: crystals
CAA: calcium alginate aerogel
CD: cyclodextrin
cMP: coalescent microparticles
cSMP: coalescing sub-microparticles
 C_{tot} : total concentration
CTZ: cetirizine dihydrochloride
D: nozzle diameter
DIC: diclofenac sodium salt
DMSO: dimethylsulfoxide
DSC: differential scanning calorimetry
EMP: expanded microparticles
EtOH: ethanol
EUD: Eudragit L100-55
FTIR: Fourier-transform infrared
GAS: supercritical gas antisolvent
HCl: hydrochloric acid
HP- β -CD: hydroxypropyl- β -cyclodextrin
KET: ketoprofen
KTF: ketotifen fumarate salt
M: morphology
MCP: mixture critical point
m.d.: mean diameter
MP: microparticles
MSA: maize starch aerogel
MSG: mesoglycan
NIM: nimesulide
NMP: N-methyl-2-pyrrolidone
NP: nanoparticles
NSAID: non-steroidal anti-inflammatory drug
ODT: oral disintegrating tablet
Oh: Ohsenorge number
P: pressure
PBS: phosphate buffer solution
PCL: polycaprolactone
PLA: polylactic acid
PLLA: poly (L-lactic acid)

References

PSD: particle size distribution
PVP: polyvinylpyrrolidone
 Re : Reynolds number
RUT: rutin hydrate
SAS: supercritical antisolvent
scCO₂: supercritical carbon dioxide
s.d.: standard deviation
SEDS: solution enhanced dispersion by supercritical fluids
SMP: sub-microparticles
T: temperature
THEOP: theophylline
 t_{JB} : time of jet break-up
 t_{STV} : time of surface tension vanishing
 v : fluid velocity
VLEs: vapor liquid equilibria
 We : Weber
XRD: X-ray diffraction
 σ : surface tension
 μ : viscosity of the mixture CO₂-solution
 ρ : fluid density

